Creative Thermal Solutions, Inc.
2209 N. Willow Rd., Urbana IL 61802
Phone: (217) 344-7663, Fax: (217) 344-7552

DOE Award Number:	DE-EE0003981
Recipient:	Creative Thermal Solutions, Inc.
DataItem:	Final Scientific/ Technical Report
Project Title:	High Efficiency R-744 Commercial Heat Pump Water Heaters
Principal Investigator:	Stefan Elbel
Teaming Members:	AO Smith Corporation
Reporting Period:	Aug. 09, 2010 to Feb. 08, 2013

Executive summary

The project investigated the development and improvement process of a R744 (CO_2) commercial heat pump water heater (HPWH) package of approximately 35 kW. The improvement process covered all main components of the system. More specific the heat exchangers (Internal heat exchanger, Evaporator, Gas cooler) as well as the expansion device and the compressor were investigated. In addition, a comparison to a commercially available baseline R134a unit of the same capacity and footprint was made in order to compare performance as well as package size reduction potential.

The project added to the understanding of R744 HWPH by investigating the effects of improving different system components on the overall system COP. As described earlier the heat exchangers, the expansion device and the compressor were investigated. This improvement process covering all main system components for one system has not been documented in the literature before. Therefore it was possible to evaluate the different effects of the components on the system performance and their extent.

The goal of the improvement process was a combined COP of heating and cooling of up to 8 which was achieved and the performance of the R134a system was reached and even exceeded in many conditions. The system efficiency improvement was as high as 35.5% of the next generation system over the baseline system and therefore exceeded the anticipated improvement of 20% by far. A bill of materials for the R134a system and the R744 system were prepared with the project subcontractor and the economical feasibility was shown.

The project showed the successful application of the natural refrigerant R744 in a HPWH unit of the same capacity as a comparable R134a unit. In comparison to R134a, R744 has a 1340 times lower global warming potential which shows the more sustainable characteristic. A simultaneous benefit by using R744 in possible energy savings compared to the currently used gas, electric resistance and HFC heat pump water heaters and less impact on the environment could be realized.

Comparison of project goals and actual accomplishments

The goal of the project was to develop a commercial heat pump water heater (HPWH) using the natural refrigerant R744 that can reach a combined (heating and cooling) system COP of up to 8 within the same footprint as a comparable R134a unit. The proposed cycle efficiency improvements (anticipated to be 20% higher than the baseline R744 system) shall be achieved through utilization of ejectors, improved electric motors and high performance gas coolers. An R134a HPWH shall be experimentally investigated in an environmental chamber to provide a complete baseline of current technology with conventional HFC refrigerants. A baseline R744 HPWH shall then be designed and fabricated by retrofitting the components of the R134a HPWH with current R744 components and placed in the same package as the R134a unit.

The first step of the development process was to measure baseline data for the R134a and R744 HPWH systems. In this first step the beneficial properties of R744 that has a high volumetric capacity were demonstrated by reducing the HPWH unit height significantly while keeping the same capacity. During the improvement process of the next generation R744 heat pump water heater the all main system components were investigated. On the heat exchanger side an internal heat exchanger (IHX) was installed which transfers heat between high pressure side after the gas cooler and the low pressure side after the evaporator. Also the evaporator of the system was enlarged to use the unit housing volume provided by the R134a unit and obtain better component performance and therefore improve the system COP. Finally the gas cooler was improved by using a staged heat transfer process by using multiple heat exchangers. After investigating the heat exchangers the throttling losses that occur in the expansion device were reduced by using an ejector. The last aspect of the improvement process was modification of the compressor with an interior permanent magnet motor.

The system efficiency improvements were as high as 35.5% of the next generation system over the baseline system and therefore exceeded the anticipated improvement of 20% by far. The goal of a combined COP of up to 8 was reached and the performance of the R134a system was reached and even exceeded in many conditions. By using the experimental data the system performance for large temperature lifts was investigated. It was shown that especially for high water outlet temperatures which are required for sanitation by the FDA the R744 HPWH showed performance improvement over R134a of 22% at a water outlet temperature of 95°C.

Publications

Bowers, C.D., Elbel, S., Petersen, M., Hrnjak, P.S., Performance improvements in commercial heat pump water heaters using carbon dioxide, 23rd International Institute of Refrigeration, International Congress of Refrigeration, Prague, Czech Republic, August, 21-26, 2011

Bowers, C., Petersen, M., Elbel, S., Hrnjak, P., Next generation commercial heat pump water heater using carbon dioxide using different improvement approaches, 10th Gustav Lorentzen Conference on Natural Refrigerants, Delft, The Netherlands, 2012

Petersen, M., Bowers, C., Elbel, S., Hrnjak, P., Development of High Efficiency Carbon Dioxide Commercial Heat Pump Water Heater, International Refrigeration and Air Conditioning Conference at Purdue, July 16-19, 2012

Petersen, M., Bowers, C., Elbel, S., Hrnjak, P., Development of High Efficiency Carbon Dioxide Commercial Heat Pump Water Heater, HVAC&R Research, 2013, (*Submitted and currently under review)*

Buildings R&D Breakthroughs: Technologies and Products Supported by the Building Technologies Program, Department of Energy, April 2012
http://apps1.eere.energy.gov/buildings/publications/pdfs/corporate/rd_breakthroughs.pdf

Table of Contents

List of figures

List of tables

1 HPWH System Modeling

In order to obtain a better understanding of the HPWH system and to predict its behavior during variable operating conditions different modeling efforts were accomplished. A steady state system model and a Computational Fluid Dynamics (CFD) model of the water storage tank to determine the internal fluid flow and the temperature stratification characteristics were developed. The influence of the temperature stratification inside the tank on the performance of the system is of special interest. A schematic of the tank with the thermocouple tree and the corresponding model of the tank are shown in Figure 1-1.

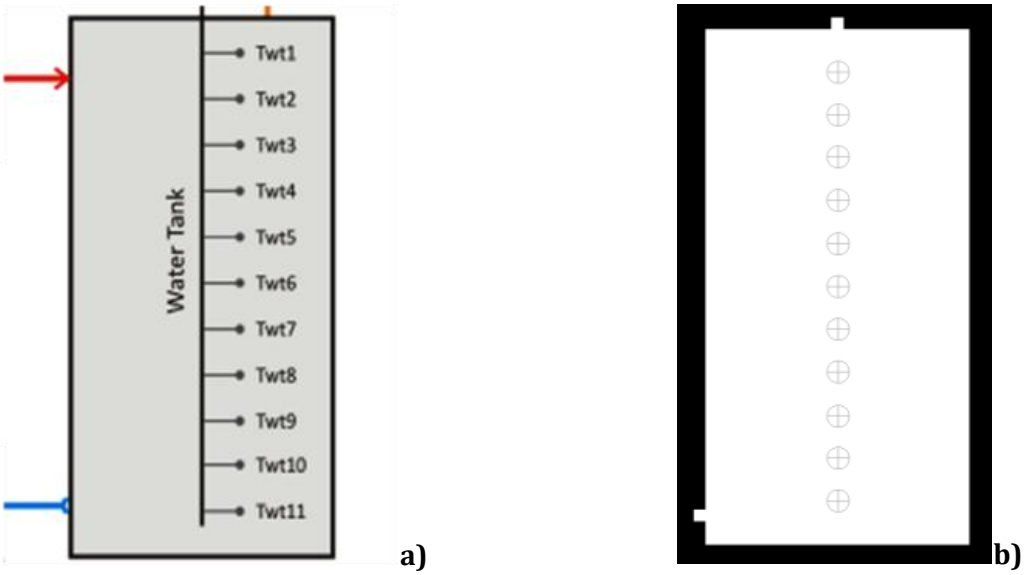

Figure 1-1: Hot Water Storage Tank with Thermocouple Tree a) and Corresponding Model b)

The tree consists of eleven thermocouples. Six thermocouples are located at positions specified by the DOE testing procedures for hot water tanks. The other five thermocouples are positioned between them. This data is very important for the validation of the CFD model.

To simulate the hot water storage tank of the heat pump a simplified two-dimensional model is used. This model consists of the water inlet, the tank body and the water outlet. The calculation of the fluid flow and heat transfer inside the tank demands a mesh that is built of cells. Different cell geometries like triangular or quadrangular cells can be used for two-dimensional models. In this case a combination of both represents the mesh (Figure 1-2).

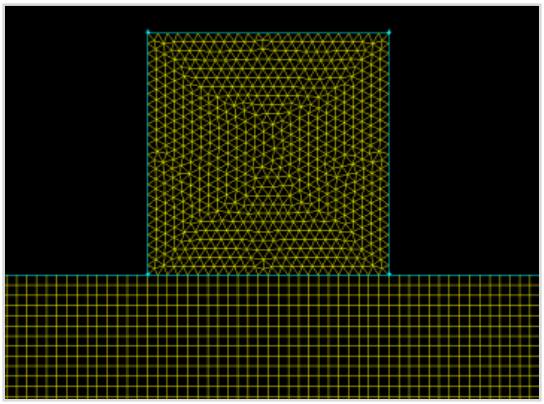

Figure 1-2: Combination of Triangular and Quadrangular Cells

The relevant differential equations are solved for each cell. The boundary conditions are the known parameters for the cells and the results of the calculations are the inlet conditions for the surrounding cells. The resolution of the mesh is very important. A high resolution offers more information but at the same time the complexity and duration of the calculation increases significantly. Therefore only in regions where large gradients are likely to occur a higher resolution is necessary. An example of this is the area close to the boundaries. These boundary layers (Figure 1-3) are very important to minimize the loss of information.

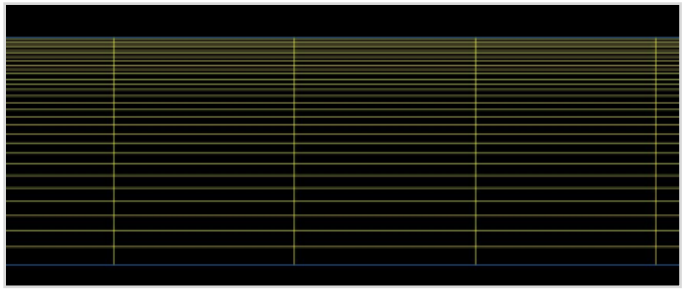

Figure 1-3: Boundary Layer

Figure 1-4 shows the 2D layer of the tank geometry and the mesh that is needed for the calculation.

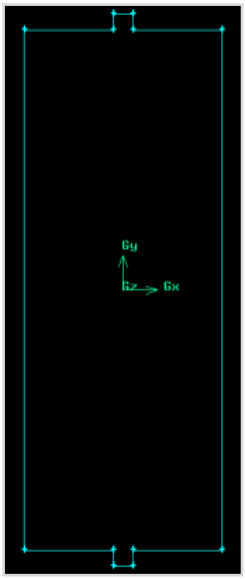

a)

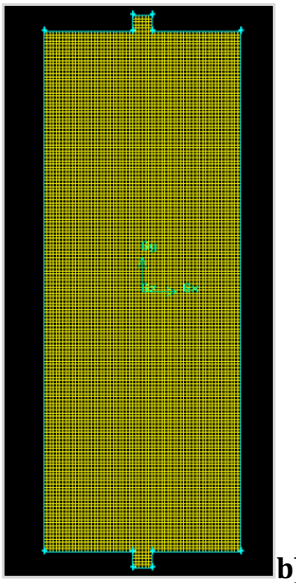

b)

Figure 1-4: 2D Tank Model: Layer a) and Mesh b)

This mesh is the basis of the following calculation. The heat transfer inside the tank between the warm water mass flow that enters the tank and the colder initial water filling is of special interest. An example of the simulation results can be seen in Figure 1-5.

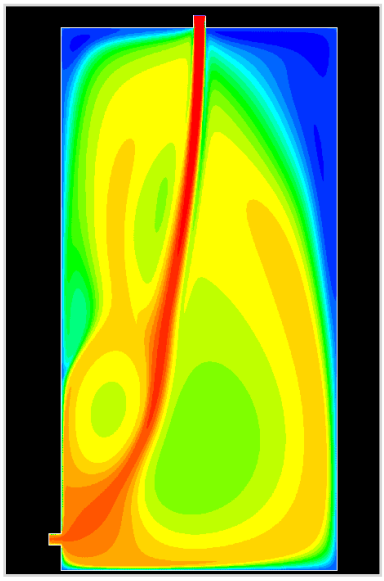

Figure 1-5: Contours of Static Temperature

1.1 1D system simulation

The first step in the HPWH modeling is to be able to predict the R134a systems currently manufactured by A. O. Smith (AOS). Therefore, an air source commercial HPWH sizing program has been developed based on the available models and tank sizes from AOS. Given the location (state), daily hot water usage, inlet water temperature, final tank temperature, air temperature and humidity, the model uses libraries of system performance and unit cost data to give a recommended system that achieves the minimum payback time.

The output windows and tables list a recommended model, or for larger applications, up to 2 units of the same size; the heating capacity of the selected unit at the design conditions entered in the input cells; a calculated tank storage size—rounded up; a yearly cost of operation for the heat pump; an estimated cost for installation—unit and tank; and a simple pay back calculation.

The assumptions that were used for this program are as follows:

1. 16 hours of unit operation
2. 2 hour peak in which 40% of total daily hot water used is consumed during peak
3. Retail electric rates are for May 2010, from www.eia.gov/cneaf/electricity/epm/table5_6.html. By selecting a city name, the program automatically searches electricity price from a given Lookup Table
4. Storage tank pricing from A.O. Smith commercial electric tank pricing
5. Assumed install cost breakdown: installing the heat pump is 50% of the unit price, installing the storage tank and piping is 20% of the unit price and wiring the electrical and controls is 20% of the unit price
6. Payback is calculated as the cost difference between buying and installing commercial electric units and a HPWH and storage tank divided by the yearly cost savings to run the heat pump instead of a commercial electric water heater.

The following window shows all the inputs needed to operate the model. These inputs include:

- Hot water usage per day in gallons
- Inlet (street or well) water temperature in F
- Outlet (or final tank) water temperature in F
- Ambient temperature in F
- Ambient relative humidity in %
- Select the geographic location (state) that the heat pump unit will be installed
- Electric price adjustment factor. The program will automatically select the electric retail price for the given state. If a more recent or more local price is known, this can be adjusted.

The output section includes the following:

- Recommended AOS commercial HPWH model, and number of units

- Nominal heating capacity of the recommended model
- Recommended storage tank size
- Estimated recovery rate
- Approximate installed cost
- Annual operating electricity cost
- Daily electricity use
- Price of electricity used for the calculation
- Annual savings compared to a commercial electric water heater
- Pay back compared with electric commercial water heater
- Overall system dimensions, plotted on the unit schematics

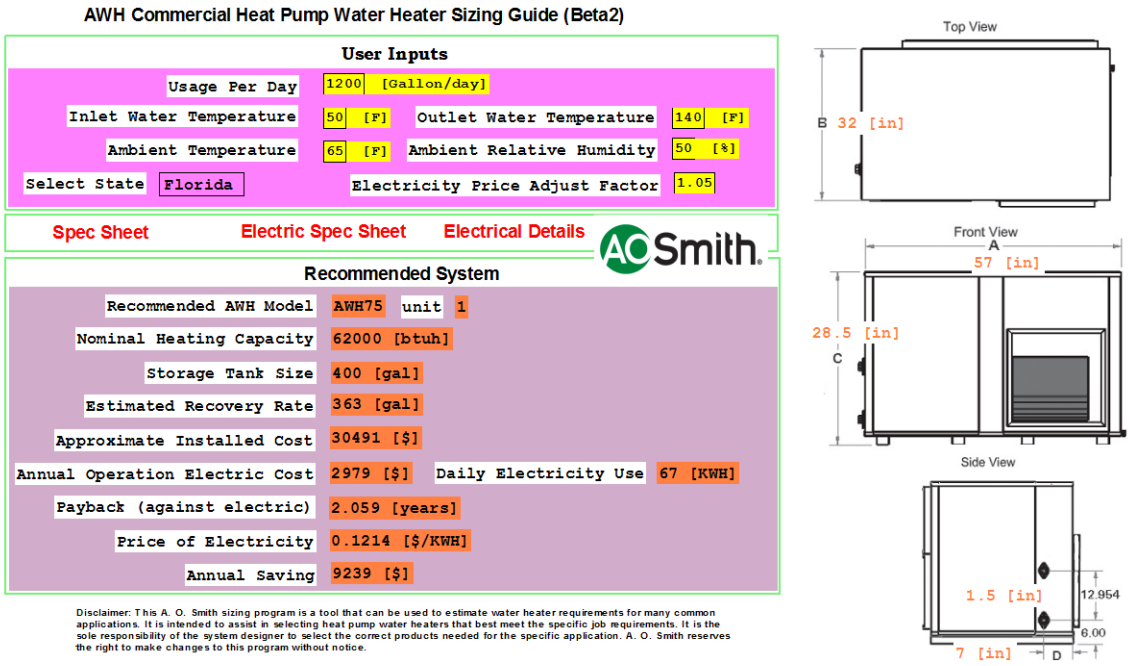

Figure 1-6: GUI Generated for the R134a Commercial HPWH

Figure 1-6 shows the Graphical User Interface (GUI) used for the model, with inputs at the top and outputs at the bottom. Example: state is “Florida”, daily water usage is 1200 gallons, water inlet temperature is set at 50°F, hot water temperature is set at 140°F, ambient is 65°F, ambient humidity is 50%. Based on all of these inputs, the program recommends using a single unit of model number of “AWH75” (see http://www.hotwater.com/lit/spec/c-hp.html). The recommended tank size is about 400 gallons and the pay back is about 2 years. There are 3 other windows shown in red type on Figure 1-6. These windows show the following:

Specification Sheet: Figure 1-7 shows the window that opens once this is clicked. This provides all the basic information about AOS commercial heat pump water heater systems.

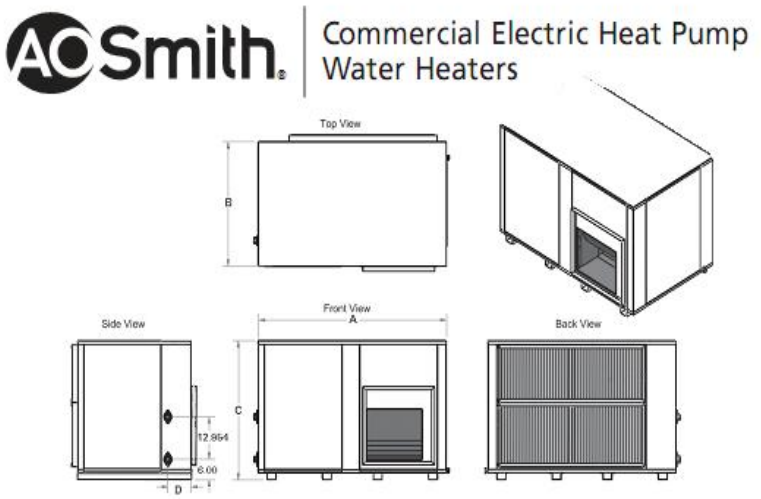

SPECIFICATION TABLE A. O. SMITH AWH AIR-TO-WATER HEATP PUMP WATER HEATERS

MODEL NUMBER	PERFORMANCE					DIMENSION					APPROX. SHIPPING WEIGHT (LBS)
	Water Heating Btu/H	Cooling Capacity Btu/H	Air Volume CFM	C.O.P	G.P.M	Inlet/Outlet (FPT)	Width A	Depth B	Height C	D	
AWH-35	35,500	27,500	1040	3.9	7	1.0"	40"	26"	24.75"	7	315
AWH-55	58,000	45,500	1650	4.1	11	1.0"	47"	32"	28.5"	7	405
AWH-75	76,000	59,000	2150	3.9	15	1.5"	57"	32"	28.5"	7	485
AWH-100	98,000	78,000	3200	4.2	20	1.5"	63"	38"	42.5"	8	660
AWH-115	113,000	89,000	3200	4.2	23	1.5"	63"	38"	42.5"	8	665
AWH140	142,000	110,000	3800	3.9	28	2.0"	63"	38"	42.5"	8	725
AWH-170	171,000	133,000	4900	3.9	34	2.0"	75"	46"	42.5"	8	880

Performance rating at 75F, 55% Relative Humidity and 100F incoming water temperature
Blower design at 0.3" external static pressure
C.O.P: coefficient of performance
All models standard 208/230V, 3-phase, 60Hz
Optional: 460V, 3-phase, 60Hz
Optional: 240V, 1-phase, 60Hz available on AWH-35 and AWH-55 only

Figure 1-7: Basic Spec Sheet for AOS's R134a Commercial HPWHs

Electric Specification Sheet: Figure 1-8 shows the spec sheet related to the electric parts of the commercial heat pump water heaters.

COMMERCIAL HEAT PUMP ELECTRICAL PERFORMANCE TABLE										
Model	V / Ph / Hz	COMPRESSOR			BLOWER MOTOR		PUMP (230V/1PH)		MCA	MFS
		RLA	LRA	MCC	FLA	HP	FLA	HP		
AWH-35	208-230/1/60	18.6	100	29	3.6	1/2	0.88	1/8	28	45
AWH-35	208-230/3/60	10.9	77	17	2.3-2.4	1/2	0.88	1/8	17	25
AWH-35	460/3/60	5.4	39	8.5	1.2	1/2	0.88	1/8	9	12
AWH-55	208-230/1/60	27.9	175	43.5	5.3	3/4	0.88	1/8	42	60
AWH-55	208-230/3/60	19.9	115	31	2.9-3	3/4	0.88	1/8	29	45
AWH-55	460/3/60	8.7	63	13.5	1.5	3/4	0.88	1/8	13	20
AWH-75	208-230/3/60	24	196	37.5	3.5-3.6	1	0.88	1/8	35	50
AWH-75	460/3/60	11.5	100	18	1.8	1	0.88	1/8	17	25
AWH-100	208-230/3/60	28.2	225	44	3.5-3.6	1	0.88	1/8	40	60
AWH-100	460/3/60	14.1	114	22	1.8	1	0.88	1/8	20	30
AWH-115	208-230/3/60	35.3	239	55	3.5-3.6	1	1	1/6	49	80
AWH-115	460/3/60	17.9	125	28	1.8	1	1	1/6	25	40
AWH-140	208-230/3/60	48.1	300	75	4.8-4.8	1 1/2	1	1/6	66	110
AWH-140	460/3/60	21.8	150	34	2.4	1 1/2	1	1/6	31	50
AWH-170	208-230/3/60	52.6	340	82	6.2-6.2	2	2.5	1/2	75	125
AWH-170	460/3/60	25.6	173	40	3.1	2	2.5	1/2	37	60

RLA = Running Load Amps LRA = Locked Rotor Amps MCC = Maximum Continuous Current FLA = Full Load Amps MCA = Minimum Circuit Ampacity MFS = Maximum Fuse Size

Figure 1-8: Electric Spec Sheet for AOS's R134a Commercial HPWHs

Electric Details: Figure 1-9 shows all the options available for the compressors that can be used in the AOS R134a commercial heat pump water heaters. For some models, there are 3 options related to the voltage, phase, and frequency. For others, there are only 2 options (option 3 and 2 are the same).

Selected Model: AWH75

# of Unit: 1

	Compressor Options		
	Option 1	Option 2	Option 3
V/Ph/Hz:	208-230/3/60	460/3/60	460/3/60
Running Load Amps (RLA):	24	11.5	11.5
Loaked Rotor Amps (LRA):	196	100	100
Max. Continuous Current (MCC):	37.5	18	18
	Blower Motor		
Full Load Amps: (FLA):	3.5-3.6	1.8	1.8
HP:	1		
	Pump (230V/1PH)		
Full Load Amps (FLA):	0.88		
HP:	0.125		
Min. Circuit Ampacity (MCA):	35	17	17
Max. Fuse Size (MFS):	50	25	25

Figure 1-9: Compressor Options for AOS's R134a Commercial HPWHs

There are many other outputs that are listed in the Parametric Table. This table lists all the potential options for this particular application. Here are the definitions of the variables in the Parametric Table:

- DailyUsage: Daily hot water usage
- Tin: Water inlet temperature
- Tout: Water exit/storage temperature
- Tamb: Ambient air temperature
- RH: Ambient air relative humidity
- State$: Name of the State
- ElectricPriceAdjustFactor: A factor used to adjust the price for the electricity
- HPunit$: Name for the system model
- N_unit: Number of units
- ElectricityPrice_adjusted: Adjusted price for electricity
- HeatingCapacity_Nominal: Nominal heating capacity for the unit
- UnitSize$: Unit size (N/A means too small; OK means possible)
- MinimumStorage: Required minimum storage tank size
- HPCostperyear: Heat pump system annual operation electricity cost

- HPUnitPrice: Heat pump system unit price
- HPTankPrice: Storage tank price
- HPinstallCost: Heat Pump system installation cost
- HPTotalInstalledCost: Total cost of the complete installed system
- ElectricTankSize: Estimated minimum electric tank size
- ElectricResistTankCost: Cost of the storage tank if using electric resistance water heater
- ElectricResistTankInstallCost: Installation cost for the electric water heater system
- ElectricResitSystemCost: Price for the complete electric water heater system
- Costperyear_resistance: Annual electricity cost if using electric resistance water heater
- HPsystemPayBack: Pay back years for the heat pump water heater system

Detailed component model

A performance prediction model for the commercial heat pump water heater with R134a as working fluid has been developed. This model is based on the detailed performance models for each of the components of the system. By giving the basic geometries of the components and operating conditions, the model can be used to predict the overall system performance.

Figure 1-10 shows the main system setup diagram window. There are several ‘child’ windows that are linked to this diagram, such as Evaporator, Condenser etc. By clicking on these text boxes, the program will open windows to display more details about the specific components for the system. All basic dimensions for each of the components are listed in the lookup table. These lookup tables are designed to set up the basics for each of the components, and within each lookup table, many different designs can be tried.

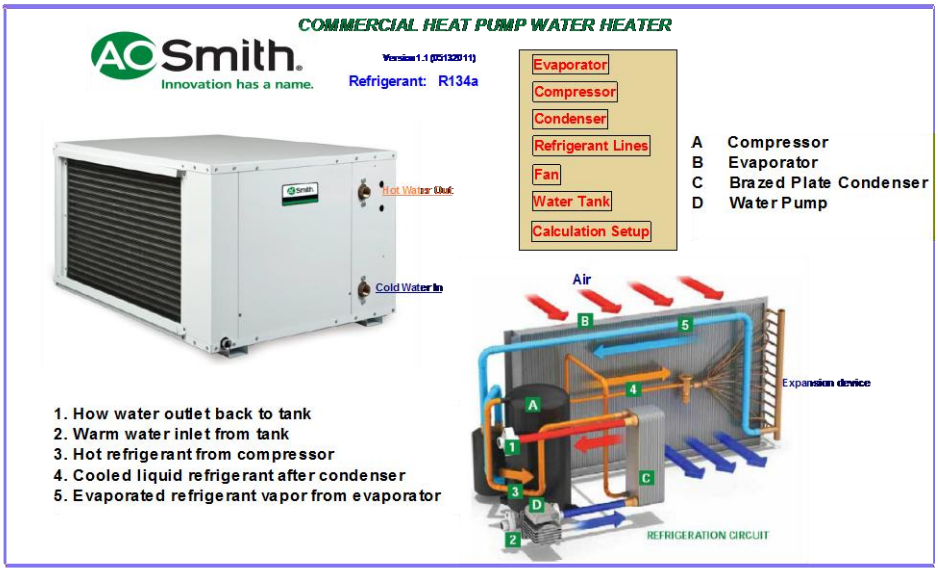

Figure 1-10: Main diagram window for the R134a commercial HPWH

Figure 1-11 shows an example for the evaporator. In this case, the 1st design (or Row 1) in the lookup table of "Evaporators" is selected for this system.

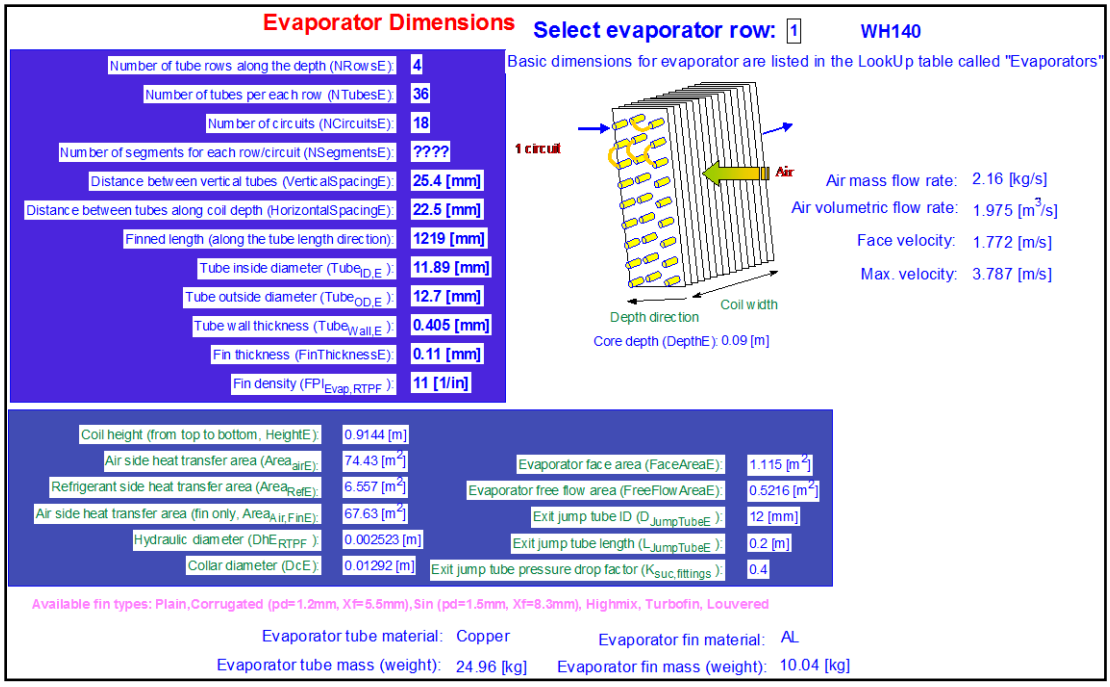

Figure 1-11: Look-Up Window for the Evaporator of the System

The model was set up based on the detailed dimensions for the evaporator, overall dimensions for the condenser and refrigerant lines. The only thing we currently know about the compressor is that it was made by Copeland (model number: ZB95KCE-TW5), the displacement is about 209cm^3 and the rpm is about 3500. At this stage, we are therefore still adding certain details about some of the components, such as the performance map for the compressor; detailed configuration of the plate condenser; diameters and lengths for the capillary tubes, blower curve and power draw, etc. Currently, we are using the test data from CTS to calibrate the model.

Given this limited information, the model was forced to match the test results to get the performance map for the compressor. Figure 1-12 and Figure 1-13 respectively show the isentropic and volumetric efficiencies for this compressor. As shown in the plots, the trend matches well with compressor maps for typical compressors. For the isentropic efficiency, the motor efficiency is included.

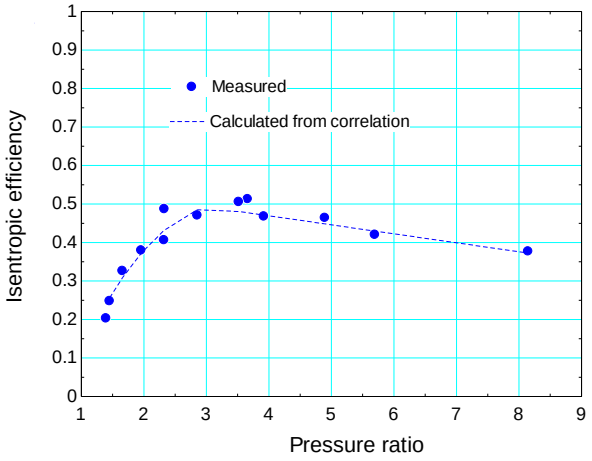

Figure 1-12: Isentropic Efficiency of the Compressor (Backed out from experimental data)

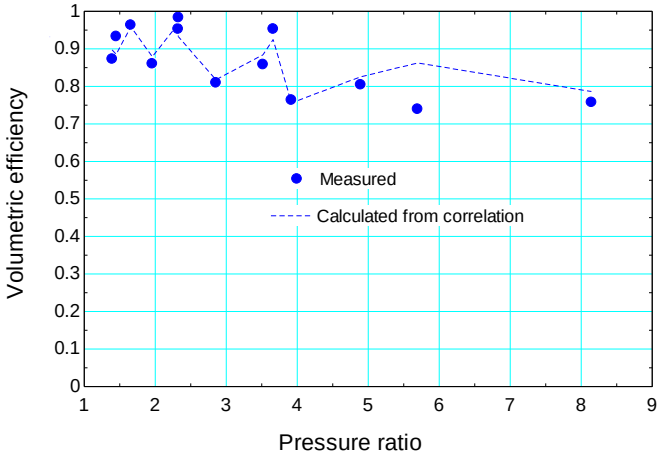

Figure 1-13: Volumetric Efficiency of the Compressor (Backed out from experimental data)

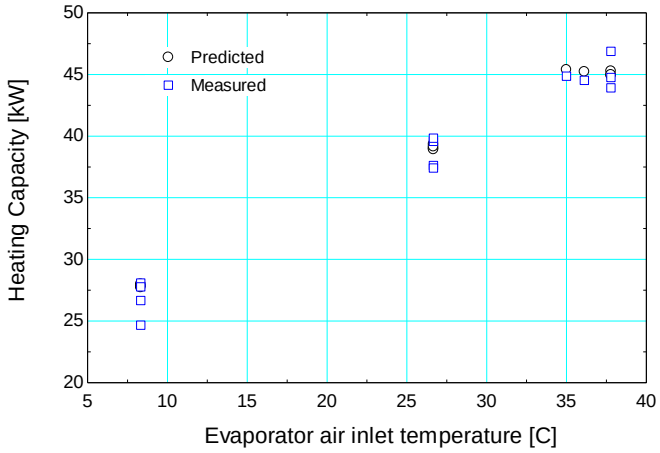

Figure 1-14: Look-Up window for the evaporator of the system

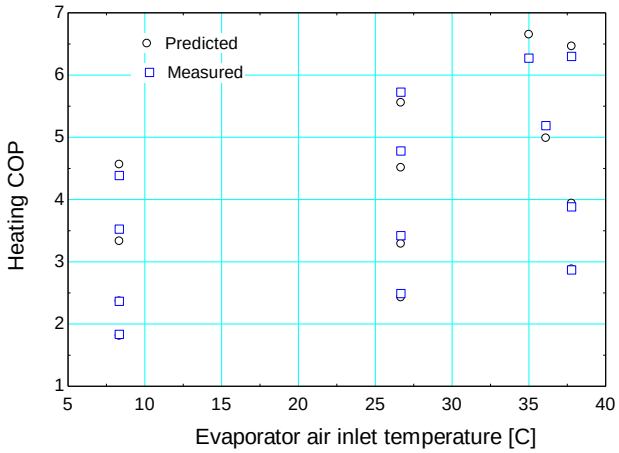

Figure 1-15: Look-Up window for the evaporator of the system

Figure 1-14 and Figure 1-15 respectively show the comparison between experimental and predicted heating capacity and COP. As shown in the plots, the model can predict the heating capacity and heating COP with ±6%.

The improvement of the HPWH vapor compression cycle performance is the key in obtaining maximum efficiency of the overall system. This improvement is accomplished in several steps investigating different aspects of the HPWH. In order to obtain a comparison of the different potential savings of each step, a simulation file was used to compare the baseline system, the system with internal heat exchanger and the system with an ejector as the expansion device. For each concept an ideal cycle is investigated neglecting aspects like pressure drop in the components and lines. The test conditions were chosen for the rating water mass flow rate of 28 gallons per minute at a water and air inlet temperature of 26.7°C. For the pressures of the high and low side of the cycle actual data was used that was recorded during R744 baseline tests. Table 1-1 gives an overview of the simulation boundary conditions.

Table 1-1: Simulation boundary conditions

Inlet temperature in ˚C		*Fluid flow*		*Pressure in kPa*	
Water	*Air*	*Water flow rate m_W in gal/min*	*Refrigerant mass flow m_r in g/s*	*Compressor outlet*	*Evaporator inlet*
26.7	26.7	28	192.3	7627	3780

The simulation was used to analyze the performance of the cycles as well as to visualize the cycles in the relevant property diagrams. The results for the pressure- specific enthalpy and temperature- entropy diagrams of the IHX and baseline system are shown in Figure 1-16 and Figure 1-17.

The baseline cycle (blue) starts at state point 1 which is the suction side of the compressor. After the compression (2) the fluid is cooled down (3) and then expanded into the two-phase area where it enters the evaporator (4). After the evaporator the fluid enters the compressor and the cycle is complete.

The IHX cycle (red) is characterized by its heat transfer between the liquid (8,9) and suction line (5,6) which increases the enthalpy difference in the evaporator and gas cooler due to a higher compressor outlet temperature.

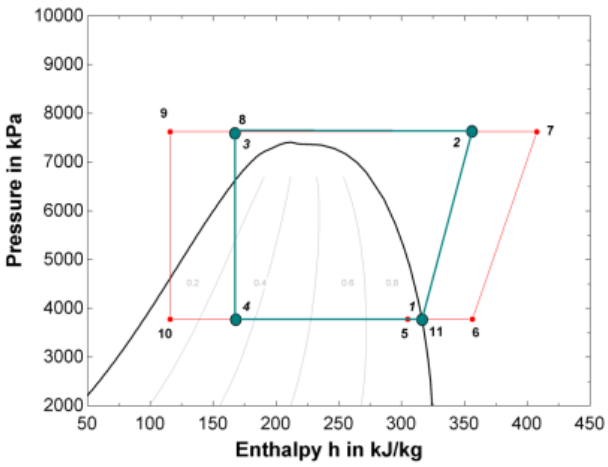

Figure 1-16: Pressure- specific enthalpy diagram of HPWH without (blue) and with (red) internal heat exchanger (IHX)

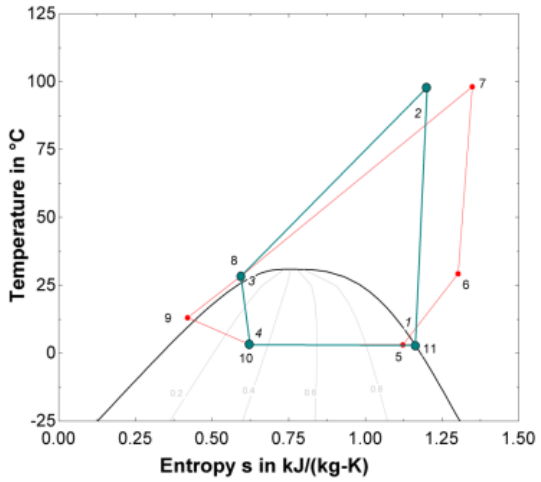

Figure 1-17: Temperature- entropy diagram of HPWH without (blue) and with (red) IHX

An ejector can be beneficially used in a vapor compression system to increase the suction pressure and therefore reduce the compressor power consumption. Some of the throttling losses that cannot be avoided when using an expansion device are recovered when operating with an ejector. The system schematic shown in Figure 1-18 describes the different set up of an ejector system compared to regular vapor compression systems.

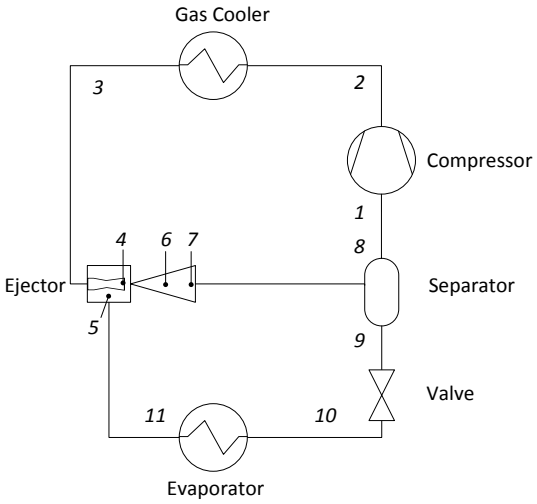

Figure 1-18: Ejector vapor compression system schematic

The fluid is compressed from the low pressure (1) to the high pressure level (2) and enters the gas cooler where it rejects heat. The colder fluid then enters the ejector and crosses the motive nozzle (4). The motive stream entrains the suction stream from the low pressure side (5). Both streams mix in the mixing section of the ejector (6) and leave the diffuser (7) before entering the separator. The fluid is separated into vapor (8) and liquid phase (9). After the expansion the low quality two-phase fluid crosses the evaporator (10, 11) before entering the suction side of the ejector to complete the cycle. The results of the pressure- specific enthalpy and temperature-entropy diagrams of the ejector cycle are shown in Figure 1-19 and Figure 1-20.

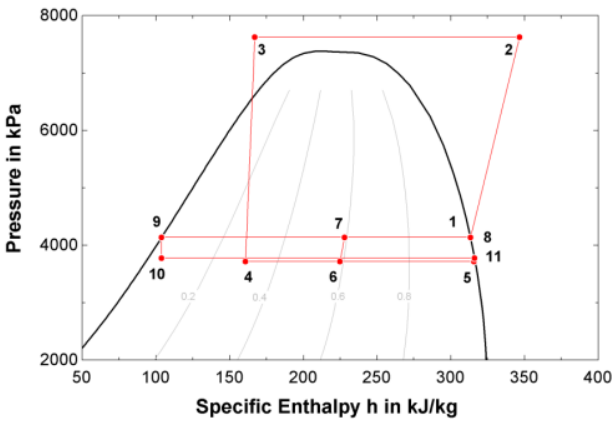

Figure 1-19: Pressure- specific enthalpy diagram of the HPWH for an ideal ejector cycle

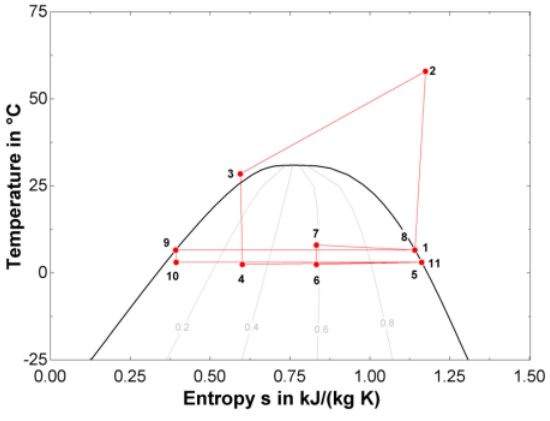

Figure 1-20: Temperature- entropy diagram of the HPWH for an ideal ejector cycle

The investigation of the system performance of the three systems is accomplished for the relevant capacities and COP's. The heating and cooling capacities as well as the compressor power consumption are calculated using the relevant enthalpy differences and the refrigerant mass flow rate. Table 1-2 gives an overview of the state points that are used for the calculation.

Table 1-2: State points used for capacity calculation

	Q_c	Q_h	Wt
Baseline	1-4	2-3	2-1
IHX	5-10	7-8	7-6
Ejector	11-10	2-3	2-1

The COP of the baseline system and the ejector cycle are calculated using the useful output (cooling, heating) divided by the compressor power consumption. The COP of the IHX system is calculated using a correlation defined by Domanski who describes the relationship between a system without and with internal heat exchanger as follows.

$$COP_{IHX} = COP \cdot \left(1 + \frac{\Delta q}{q} + \frac{\Delta w_t}{w_t}\right) \qquad (1)$$

The results of the performance determination are shown in Figure 1-21 and Figure 1-22.
It can be seen that the capacities are the highest for the IHX system. The baseline and ejector cycle are just slightly different. More evident is the difference in the compressor power which is the lowest for the ejector cycle and therefore beneficial for the COP's. Interestingly the IHX system COP's are worse compared to the baseline system because the rise in cooling and heating capacity does not compensate the increased compressor power.
It must be pointed out that the relatively high capacity and COP values are based on ideal system assumptions. These performance improvements may not be fully reached in real operation but they offer an idea about the relative behavior of the different system in comparison to each other.

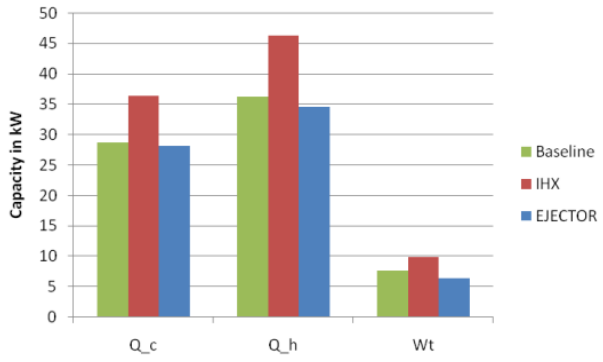

Figure 1-21: Capacity comparison for ideal baseline, IHX and Ejector cycle

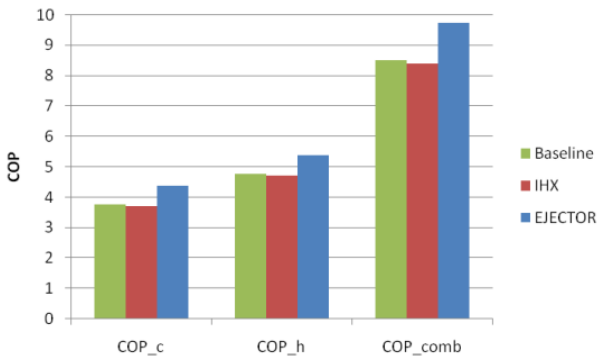

Figure 1-22: COP comparison for ideal baseline, IHX and Ejector cycle

1.2 R744 Detailed Component Model

The R744 HPWH uses a piston type compressor. Figure 1-23, Figure 1-24 and Figure 1-25 show the cooling capacity, power consumption and cooling COP respectively for this compressor at a given evaporation temperature and condenser (subcritical)/gas cooler (transcritical) exit temperature based on 10°C suction superheating and no sub-cooling from the condenser. As shown in the plot, this compressor has very high COP's at lower condenser/gas cooler exit temperatures, but the COP decreases with increasing condenser/gas cooler exit temperatures.

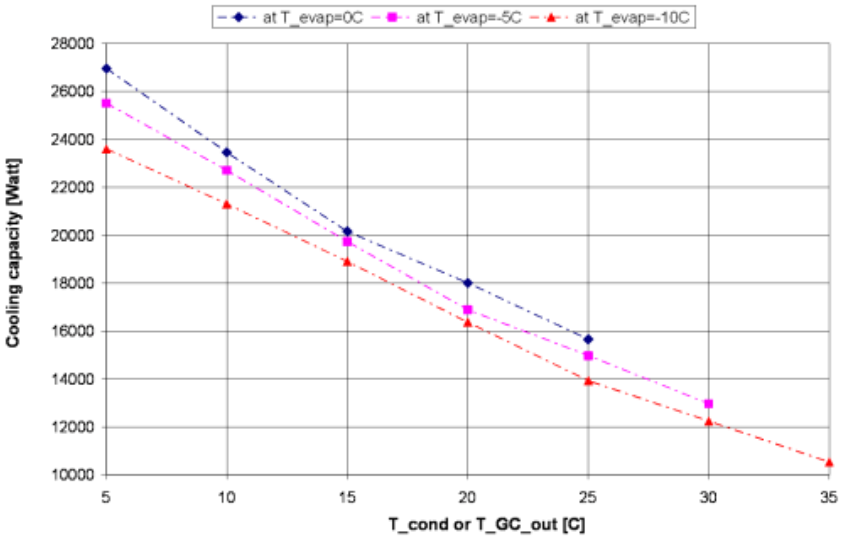

Figure 1-23: R744 compressor cooling capacity

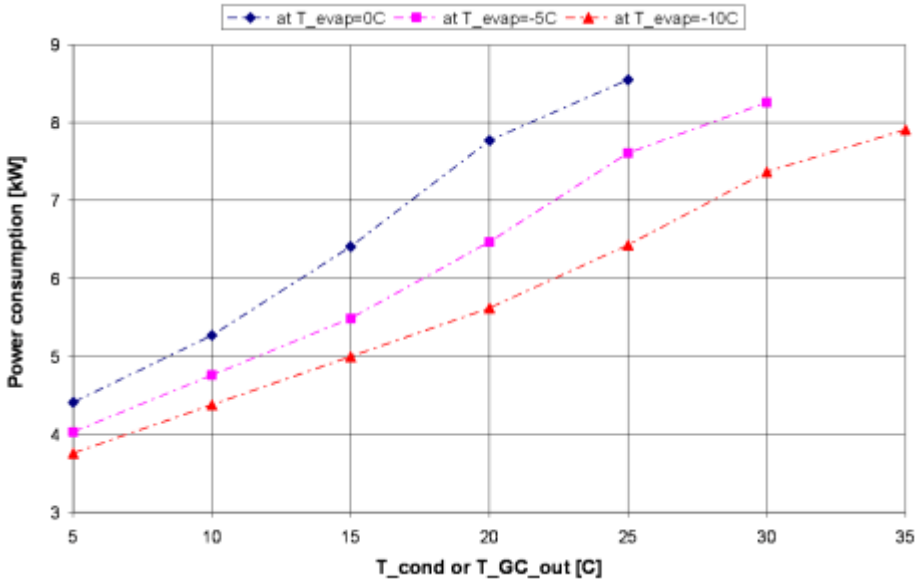

Figure 1-24: R744 compressor power consumption

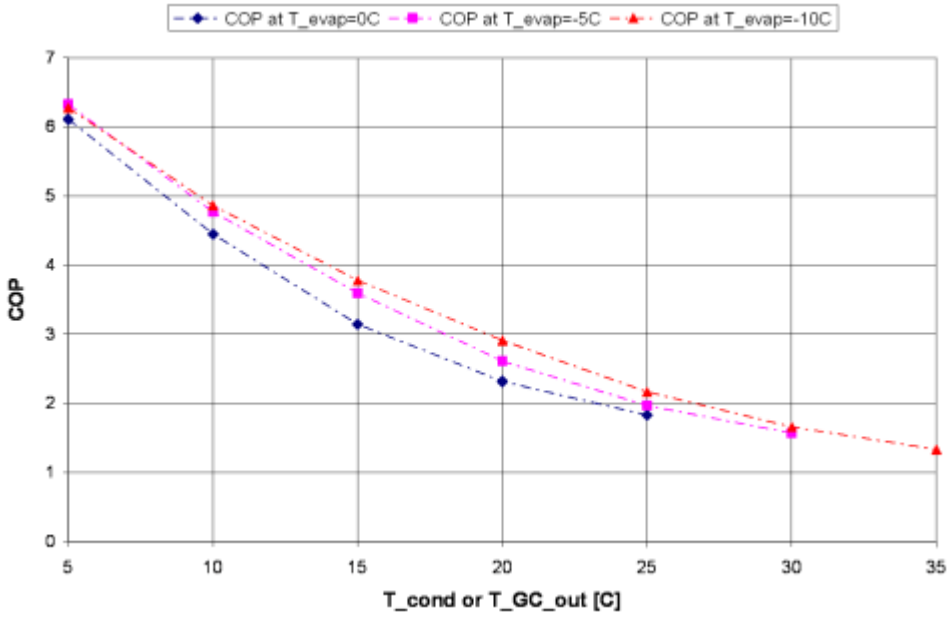

Figure 1-25: R744 compressor cooling COP

Based on the above performance curves and the specs for this compressor, a model was created to back out the compressor efficiency in a format that can be used in the performance model. Figure 1-26 and Figure 1-27 respectively show the isentropic and volumetric efficiencies

for this compressor. For most of the pressure ratio conditions, the efficiency can be correlated into a single curve fit.

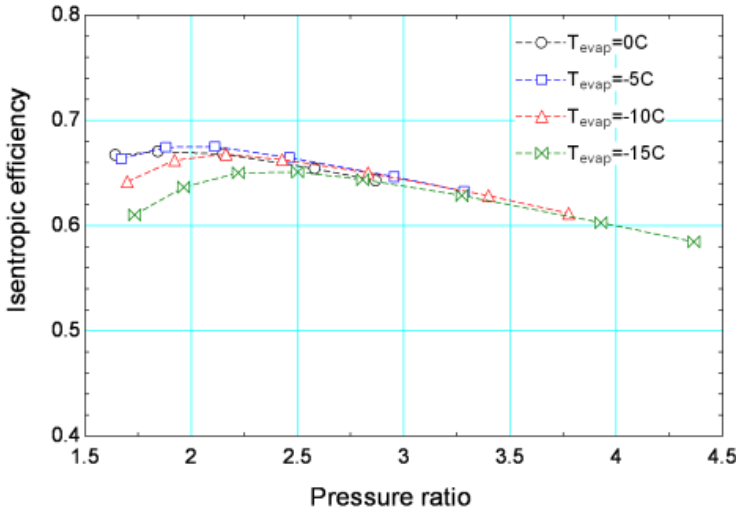

Figure 1-26: R744 compressor isentropic efficiency

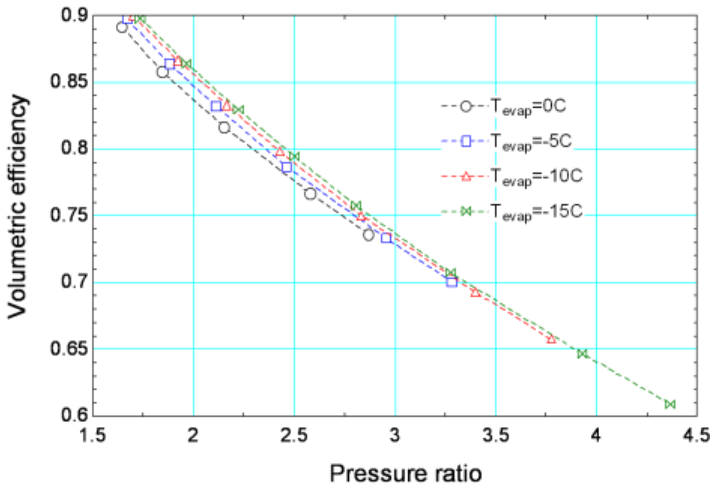

Figure 1-27: R744 compressor volumetric efficiency

The heat exchangers of the system are a brazed plate gas cooler and a round tube plate fin evaporator.

A simple model was created to check the test results from CTS. Based on the measurements of temperatures, pressures, flow rates and compressor power, the compressor efficiency can be backed out from these tests. Figure 1-28 shows the results for the compressor isentropic efficiency versus the pressure ratio. For most of the test conditions, the results show that the compressor never performed up to its potential. Figure 1-29 shows the results for the volumetric

efficiency versus the pressure ratio and the conclusions are very similar to the isentropic efficiency. To back out the compressor efficiency, the cooling capacities are needed. These were calculated based on the heating capacity (QC) and compressor power (Wcomp): the cooling capacity equals the heating capacity minus compressor power.

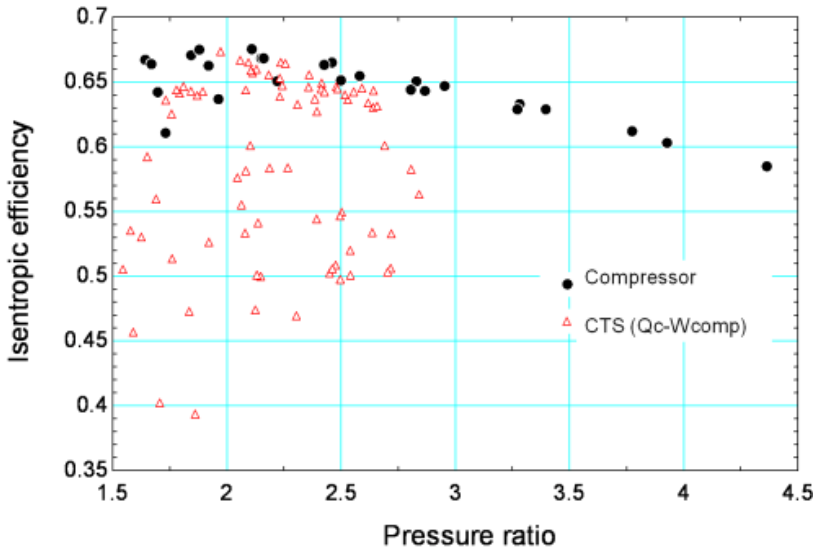

Figure 1-28: Compressor Isentropic Efficiencies vs Pressure Ratio

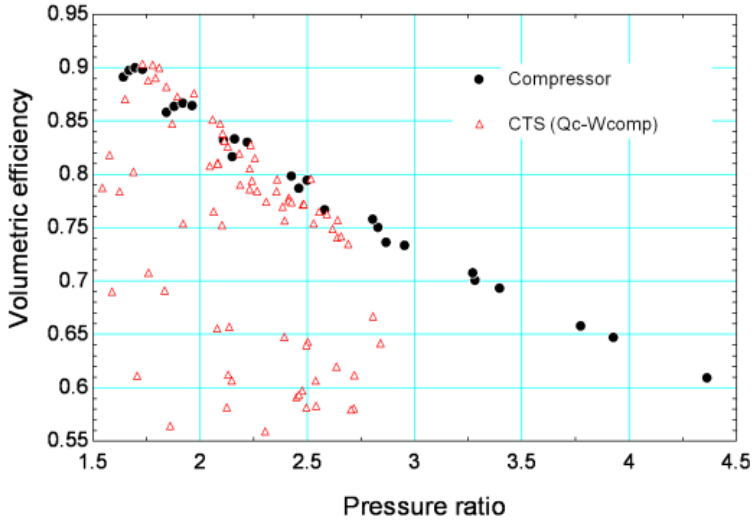

Figure 1-29: Compressor Volumetric Efficiencies vs. Pressure Ratio

Figure 1-30 and Figure 1-31 respectively show the isentropic and volumetric efficiencies plotted against the refrigerant quality at evaporator inlet. As shown in the plots, when the evaporator inlet quality is lower than 0.6 (or 60%), the compressor efficiencies from the manufacturer and

CTS tests are very close, but for qualities higher than 0.6, the differences get larger with increasing quality. These results clearly show that, the high quality entering the evaporator (and hence poor performance of the evaporator) leads to the poor performance of the compressor.

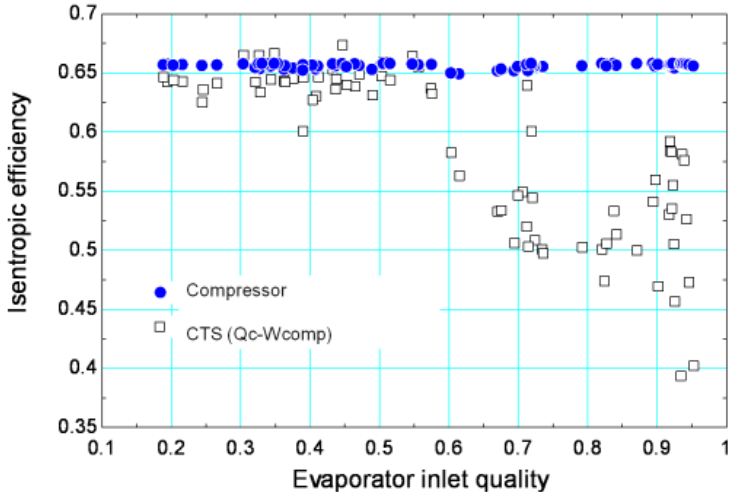

Figure 1-30: Compressor Isentropic Efficiencies vs. Evaporator Inlet Quality

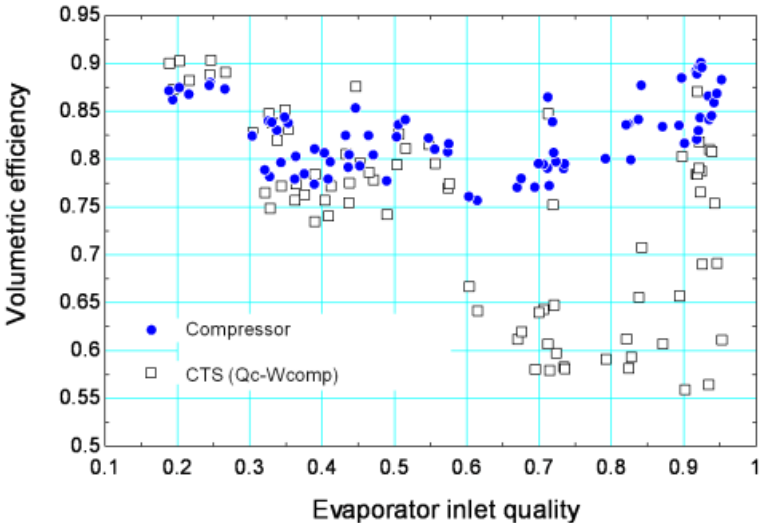

Figure 1-31: Compressor Volumetric Efficiencies vs. Evaporator Inlet Quality

Figure 1-32 shows one of the test points on a T-h diagram; as shown in the plot, the evaporator inlet quality is very high (over 80%), resulting in a very short two-phase evaporation region (mostly in the dry-out region), and a poor performance of the evaporator.

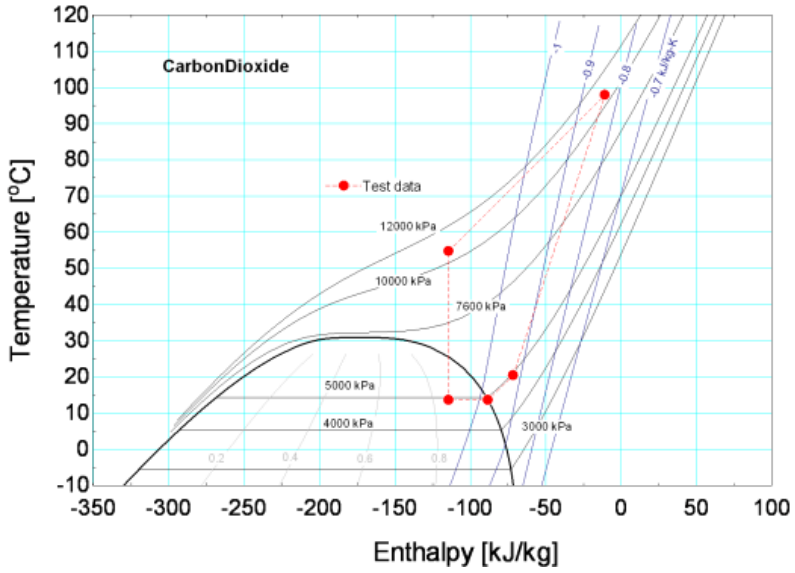

Figure 1-32: R744 T-h Diagram for One Test Point

Another variable that can be used to tell how good the compressor is doing is the difference between measured and calculated compressor discharge temperature. The cooling of the compressor can cause some difference between the measured and calculated discharge temperature, but most of the differences are caused by the refrigerant oil. As shown in Figure 1-33, for most of the test conditions, the measured compressor discharge temperatures are lower than the calculated ones. However, the differences are very consistent, which indicates a relatively constant oil circulation rate. For some points, it does look like the compressor was pumping a lot of oil.

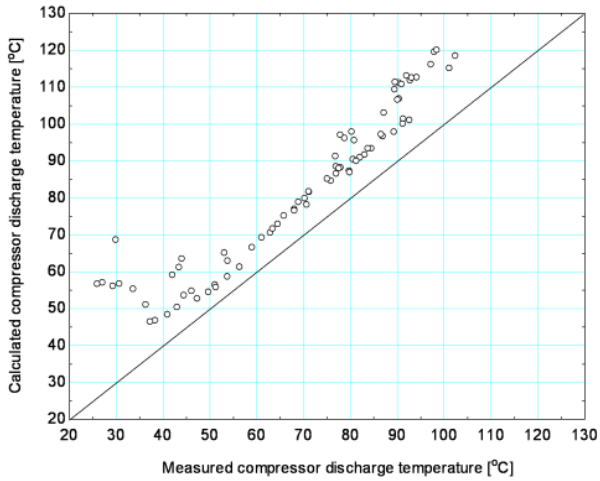

Figure 1-33: Compressor Discharge Temperature

In order to have a very efficient R744 HPWH, the gas cooler performance is very important. Ideally the approaching temperature difference (R744 temperature at gas cooler exit minus the water inlet temperature) should be as low as possible. Figure 1-34 shows the approaching temperature differences from the CTS tests, and clearly shows that the gas cooler has room for further improvement.

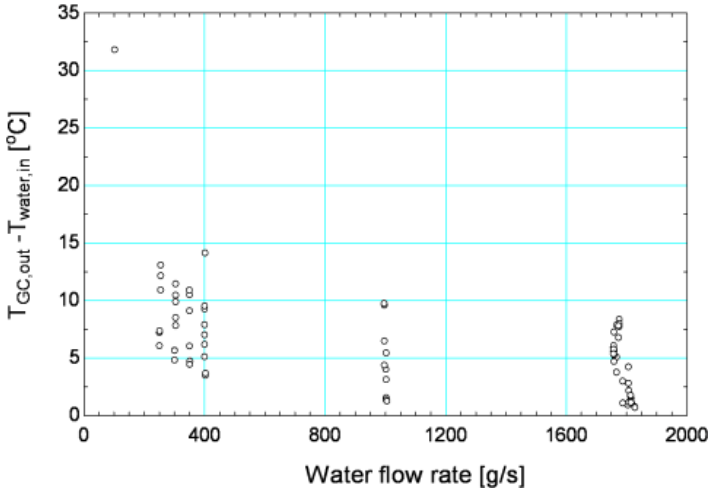

Figure 1-34: Gas Cooler Approaching Temperature Differences

As discussed in the above sections, the high inlet quality to the evaporator probably causes very poor distribution on the refrigerant side, which makes certain areas of the evaporator perform very poorly. However, it is very difficult to quantify this with modeling. These results indicate that it is very important to design a R744 water heating system that always operates in conditions such that the evaporator inlet quality is lower than 60% (or the evaporator needs to be re-designed to take care of the high inlet quality).

2 Facility Modifications and Baseline R134a HPWH Testing

The baseline R134a unit is a packaged air-source heat pump water heater with a nominal heating capacity of 142,100Btu/hr and COP of 3.9. A picture and schematic of the R134a baseline unit is shown in Figure 2-1.

Figure 2-1: Baseline R134a System

Modifications to the baseline unit included the addition of appropriate instrumentation to obtain all of the state points within the heat pump cycle. A schematic of the instrumentation installed in the baseline unit and the test facility is shown in Figure 2-2.

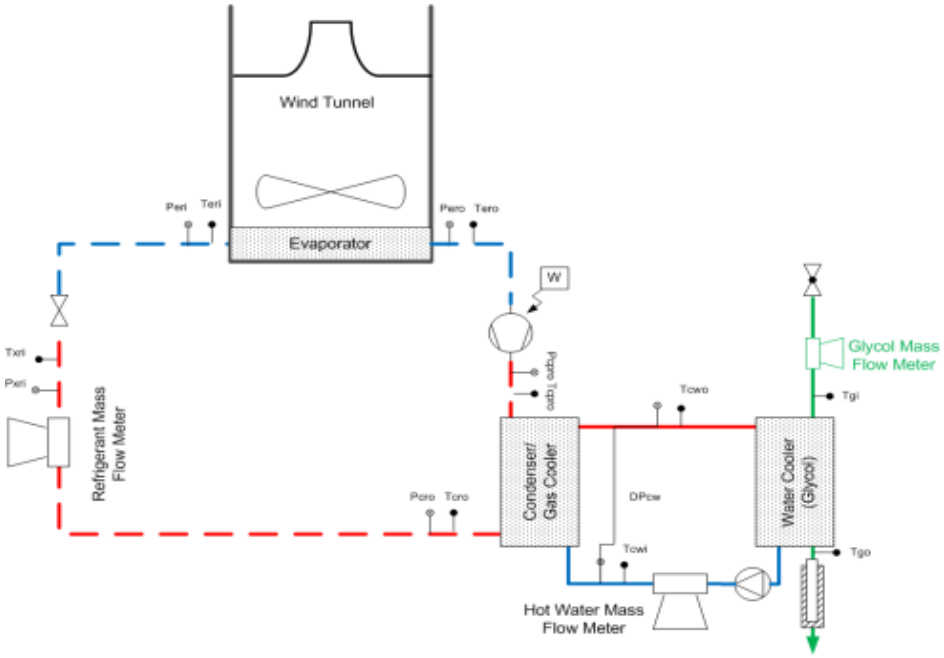

Figure 2-2: Test Facility Schematic

The heat pump system was instrumented in such a way as to achieve five separate energy balances, two on the cooling side of the cycle, and three on the heating side of the cycle. On the cooling side of the cycle the two balances were achieved on the air stream and the refrigerant stream, respectively. Determination of the cooling capacity on the air stream was determined using a separate wind tunnel directly connected to the evaporator air discharge of the heat pump unit. This wind tunnel was built and instrumented according to ASHRAE Standard 37-2005, as shown in Figure 2-3. While the heat pump unit was equipped with a blower to provide air flow over the evaporator, this blower was not strong enough to provide the pressure header required to overcome the pressure drop caused by the flow nozzles used to determine air flow rate. For this reason, a “helper” blow was installed at the exit of the wind tunnel to provide the additional pressure lift required to maintain the flow rate provided by the blower integrated into the heat pump water heater unit.

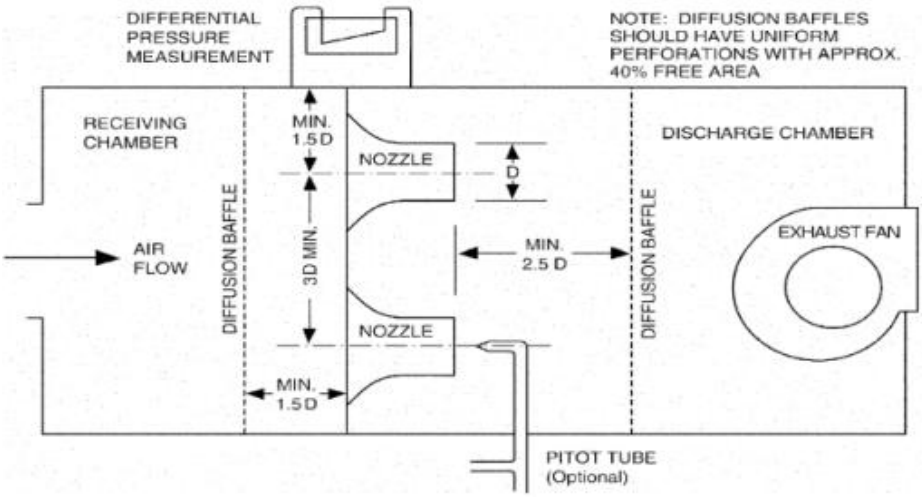

Figure 2-3: Airflow Measurement Wind Tunnel from ASHRAE 37-2005

The second determination of the cooling capacity of the system was through measurements obtained on the refrigerant flow stream. Adding these measurement points to the system required minor modifications to the refrigerant piping. Most of these modifications consisted of only adding ports for temperature and pressure instrumentation. However, in order to obtain a measurement of the refrigerant mass flow, a coriolis type mass flow meter was placed in the liquid line of the refrigerant loop. This required removing a small section of piping and the addition of the appropriate mating connections between the mass flow meter and the copper

liquid lines. A photograph showing some of the added instrumentation on the high pressure side of the system can be seen in Figure 2-5.

Figure 2-4: Evaporator Wind Tunnel Connected to Baseline R134a System

Figure 2-5: High Pressure Side of HPWH with Added Instrumentation

On the heating side of the system, three different energy determination methods were employed. Using the instrumentation on the refrigerant cycle described above, the heating capacity was determined from the temperatures, pressures, and mass flow values in the condenser. The second heating capacity determination was made using temperature and mass flow measurements on the water stream. This was in accordance with the testing of Type IV heat pump water heaters specified in ASHRAE Standard 118.1, as shown in Figure 2-6. In order to obtain a good understanding of the bottlenecks of the heat pump system performance the "once through" design of a Type IV unit was investigated.

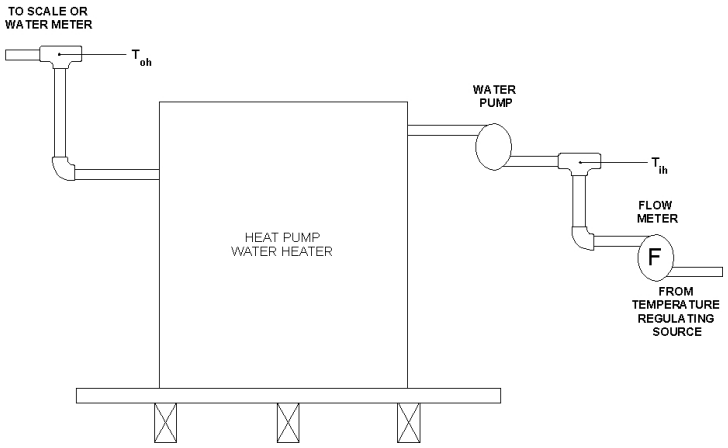

Figure 2-6: ASHRAE 118.1 Type IV Heat Pump Water Heater Test Configuration

The heat rejection was achieved by using a water to glycol heat exchanger. The third determination of heating capacity was made on this glycol stream. A special facility was designed and constructed to provide a heat transfer mechanism between the hot water and the glycol. Heat transfer between the hot water stream and the cold glycol stream was achieved through a brazed plate heat exchanger installed in the glycol/pump facility shown in Figure 2-7. In addition to the brazed plate heat exchanger, the cart was also equipped with two mass flow meters, one for each fluid stream, trim heaters, and pump to control the water flow rate.

Figure 2-7: Water/Glycol Measurement Cart

Upon completion of the instrumentation of the heat pump water heater, initial shakedown testing of the unit was started. These shakedown tests included system functionality testing, calibration

of instrumentation, and testing of system controls. A pressure – specific enthalpy (P-h) diagram of the state points for the baseline R134a unit running during one of the shakedown tests is shown in Figure 2-8. Such P-h diagrams were plotted online during testing in order to see immediate system response to operating conditions. They also offered insight into important system parameters such as evaporator exit superheat, compressor discharge temperature, condenser subcooling, and evaporation temperatures.

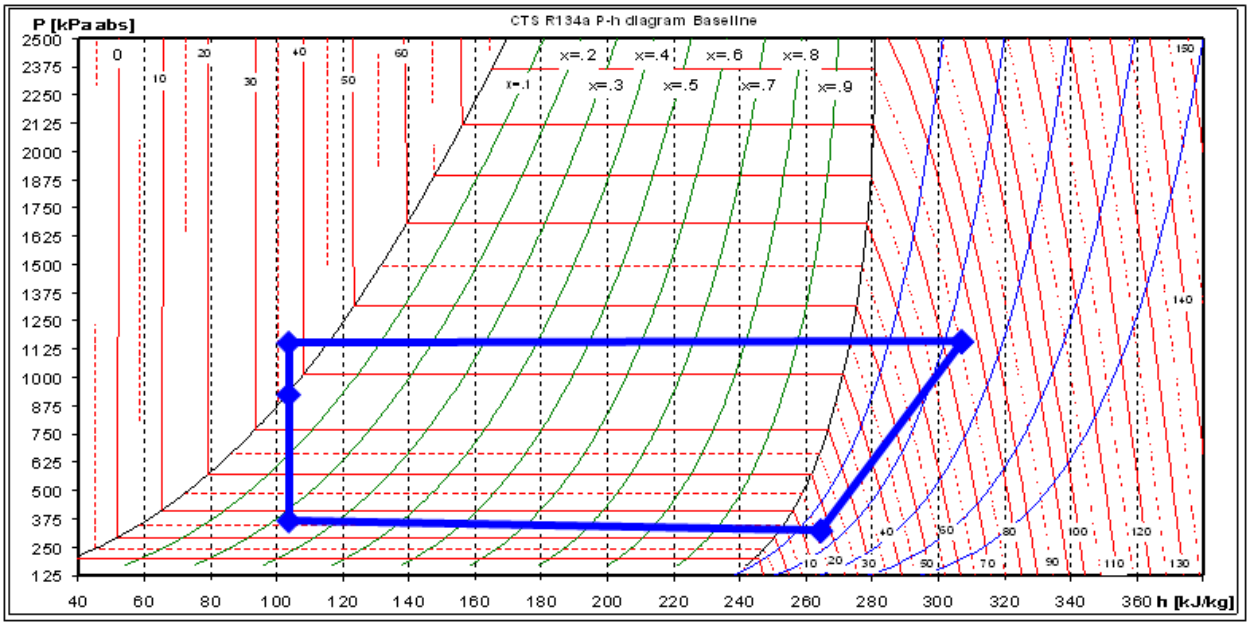

Figure 2-8: R134a Baseline P-h Diagram

ASHRAE Standard 118.1 on the analysis of Type IV Heat Pump Water Heater Test Configurations requires one energy balance for the whole heat pump water heater including the cooling capacity in order to evaluate the system performance.

$$EB = \frac{[\dot{Q}_h - (\dot{Q}_c + \dot{W}_t)]}{\dot{Q}_h} \qquad (2)$$

Where:

$\dot{Q}_h$: HPWH water heating capacity in kW

$\dot{Q}_c$: HPWH total cooling capacity in kW

$\dot{W}_t$: HPWH power input in kW

The HPWH was instrumented with various sensors to obtain the relevant state points for a total of five separate energy balances (Figure 2-9). Two cooling balances for the refrigerant and the air side and three heating balances on the refrigerant the glycol and the water sides.

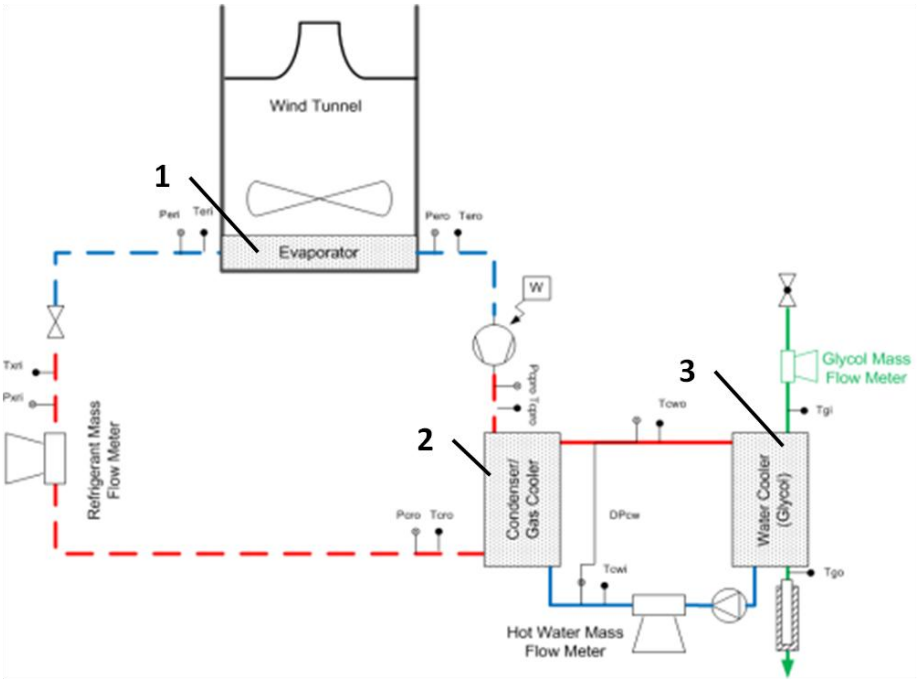

Figure 2-9: Test Facility Schematic with Energy Balances

These five balances offer more information and make the system analysis more reliable. The cooling balances were achieved for the air stream and the refrigerant mass flow crossing the evaporator (Figure 2-9: 1).

$$\dot{Q}_{ea} = \dot{m}_a \cdot (h_{eao} - h_{eai}) \qquad (3)$$

Where:

$\dot{Q}_{ea}$: Cooling capacity of the air stream in kW

$\dot{m}_a$: Air mass flow in kg/s

h_{eao} : Enthalpy of air at outlet of evaporator in kJ/kg

h_{eai} : Enthalpy of air at inlet of evaporator in kJ/kg

$$\dot{Q}_{er} = \dot{m}_r \cdot (h_{ero} - h_{eri}) \qquad (4)$$

Where:

$\dot{Q}_{er}$: Cooling capacity of the refrigerant stream in kW

$\dot{m}_r$: Refrigerant mass flow in kg/s

h_{ero} : Enthalpy of refrigerant at outlet of evaporator in kJ/kg

h_{eri} : Enthalpy of refrigerant at inlet of evaporator in kJ/kg

The heating balances were accomplished in the condenser (R134a) or gas cooler (R744) depending on the working fluid (Figure 2-9: 2). The refrigerant rejects the heat to the cooling water. Therefore a refrigerant and water balance can be obtained.

$$\dot{Q}_{cr} = \dot{m}_r \cdot (h_{cro} - h_{cri}) \quad (5)$$

Where:

$\dot{Q}_{cr}$: Heating capacity of the refrigerant stream in kW

$\dot{m}_r$: Refrigerant mass flow in kg/s

h_{cro} : Enthalpy of refrigerant at outlet of condenser/ gas cooler in kJ/kg

h_{cri} : Enthalpy of refrigerant at inlet of condenser/ gas cooler in kJ/kg

$$\dot{Q}_h = \dot{m}_w \cdot c_{pw} \cdot (T_{wo} - T_{wi}) \quad (6)$$

Where:

$\dot{Q}_h$: Water heating capacity of the HPWH in kW

$\dot{m}_w$: Water mass flow in kg/s

c_{pw} : Specific heat of the water stream in kJ/(kg K)

T_{wo} : Temperature of water at outlet of condenser/ gas cooler in K

T_{wi} : Temperature of water at inlet of condenser/ gas cooler in K

The third heating balance was the heat rejection from the cooling water to the glycol stream (Figure 2-9: 3).

$$\dot{Q}_g = \dot{m}_g \cdot c_{pg} \cdot (T_{go} - T_{gi}) \quad (7)$$

Where:

$\dot{Q}_g$: Glycol heating capacity of the HPWH in kW

$\dot{m}_g$: Glycol mass flow in kg/s

c_{pg} : Specific heat of the glycol stream in kJ/(kg K)

T_{go} : Enthalpy of glycol at outlet of condenser/ gas cooler in K

T_{gi} : Enthalpy of glycol at inlet of condenser/ gas cooler in K

The initial baseline testing of the R134a system was carried out according to the test matrix shown in Table 2-1.

Table 2-1: Test Matrix for Heat Pump Testing

Inlet Water Temperature	Ambient Temperature		
8°C (46.4°F)	5°C (41°F)	10°C (50°F)	22.2°C (72°F)
37.8°C (100°F)	5°C (41°F)	10°C (50°F)	22.2°C (72°F)

Water inlet temperature and ambient air temperature were of special interest. The water inlet temperature was specified as the water inlet condition of the condenser of the system. The ambient temperature was the temperature of the surrounding air of the unit that went through the evaporator. The humidity during the tests was kept very low to avoid frosting during 5 °C and 10 °C ambient air temperature operation. This behavior can be seen in Figure 2-10.

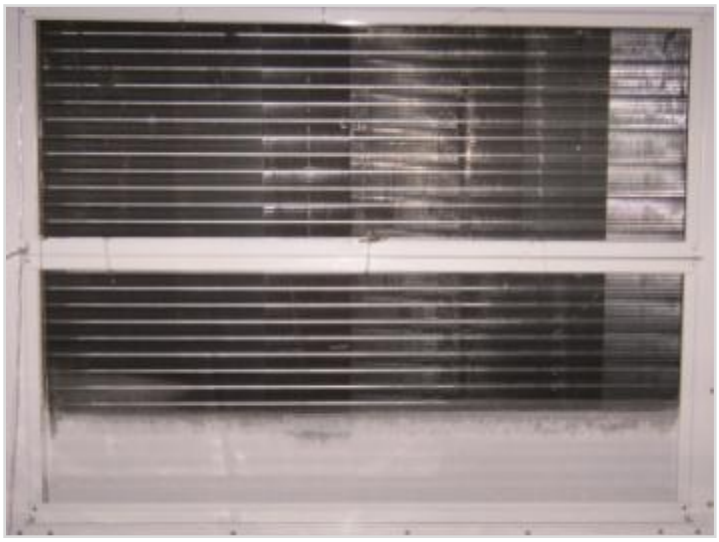

Figure 2-10: Frosting of Evaporator

Figure 2-11 shows a pressure –specific enthalpy diagram for the case with an inlet water temperature of 8°C and an ambient temperature of 10°C. In this case, the cooling capacity was determined to be 20.5 kW and the heating capacity was 25 kW (Figure 2-13). This resulted in a COP for cooling of 3.8 and 4.6 for heating (Figure 2-14). A pressure – specific enthalpy diagram for the case with an inlet water temperature of 8 °C and an ambient temperature of 5 °C is shown in Figure 2-12. In this case, the cooling capacity was determined to be 15.8 kW and the heating capacity was 21.5 kW. This resulted in a COP for cooling of 3.1 and 4.2 for heating respectively.

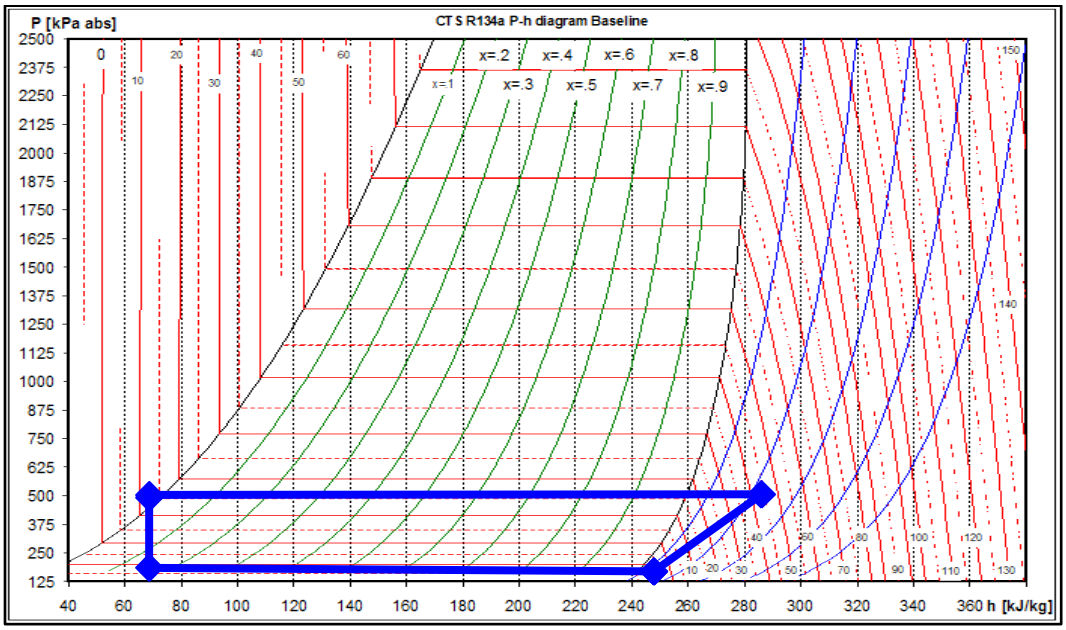

Figure 2-11: Pressure-Enthalpy Diagram for Baseline Heat Pump System with Water inlet Temperature of 8°C and Ambient Temperature of 10°C

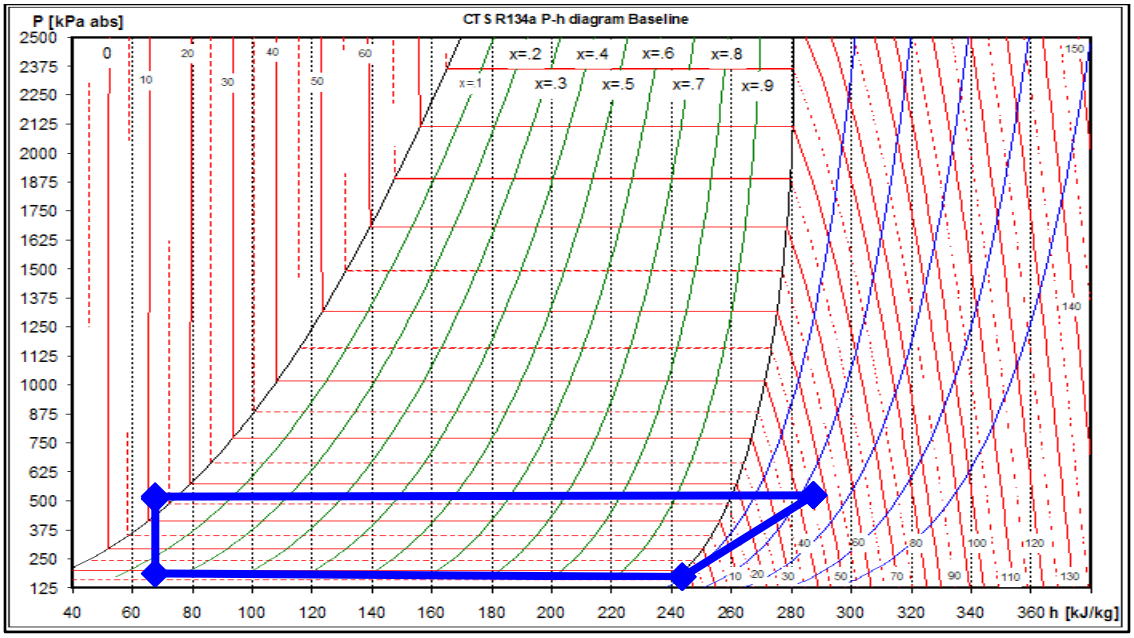

Figure 2-12: Pressure-Enthalpy Diagram for Baseline Heat Pump System with Water inlet Temperature of 8°C and Ambient Temperature of 5°C

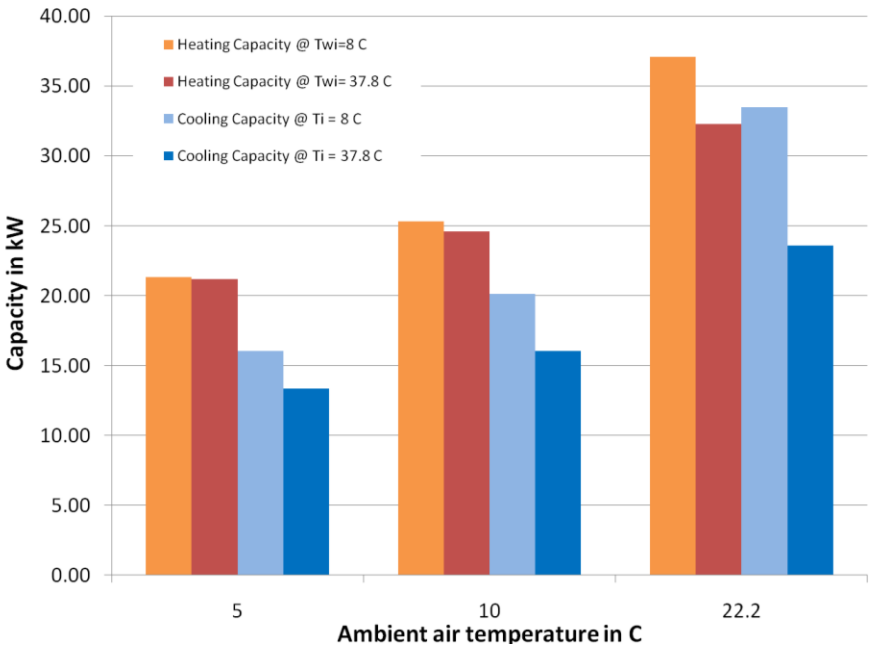

Figure 2-13: Cooling and Heating Capacity

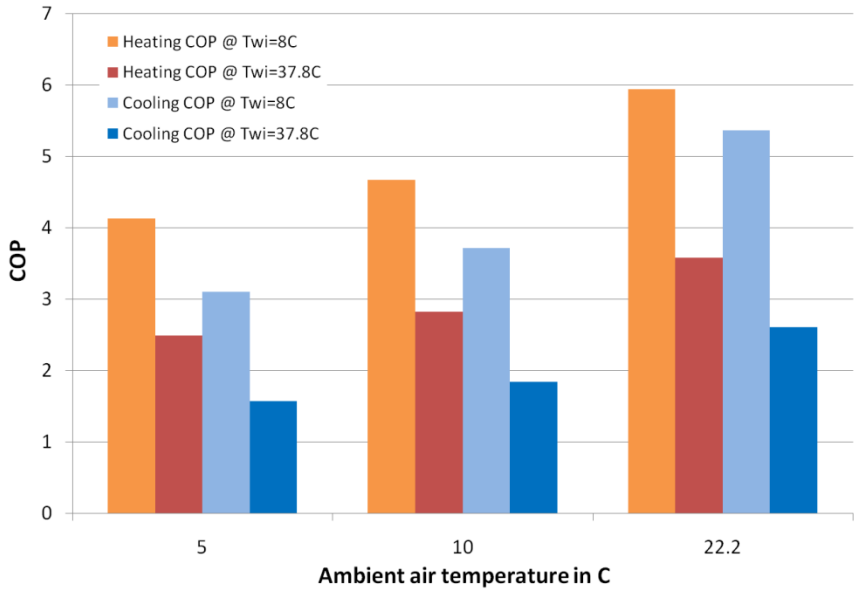

Figure 2-14: Cooling and Heating COP

The initial baseline testing was done according to the test matrix Table 2-1. However for further testing a broader range of conditions was used to investigate the system. Therefore extended test conditions with variations of the water inlet condition of the condenser as well as the ambient temperature were accomplished as shown in Table 2-2.

Table 2-2: Extended Test Matrix for Heat Pump Testing

Inlet Water Temperature	8°C (46.4°F)	12°C (53.6°F)	26°C (78.8°F)	37.8°C (100°F)	43°C (109.4°F)	60°C (140°F)

Ambient Temperature	5°C (41°F)	8°C (46.4°F)	10°C (50°F)	22.2°C (72°F)	26.7°C (80°F)	35°C (95°F)	37.8°C (100°F)

The following pressure specific enthalpy diagrams represents several of the different conditions that were investigated (Figure 2-15 to Figure 2-19).

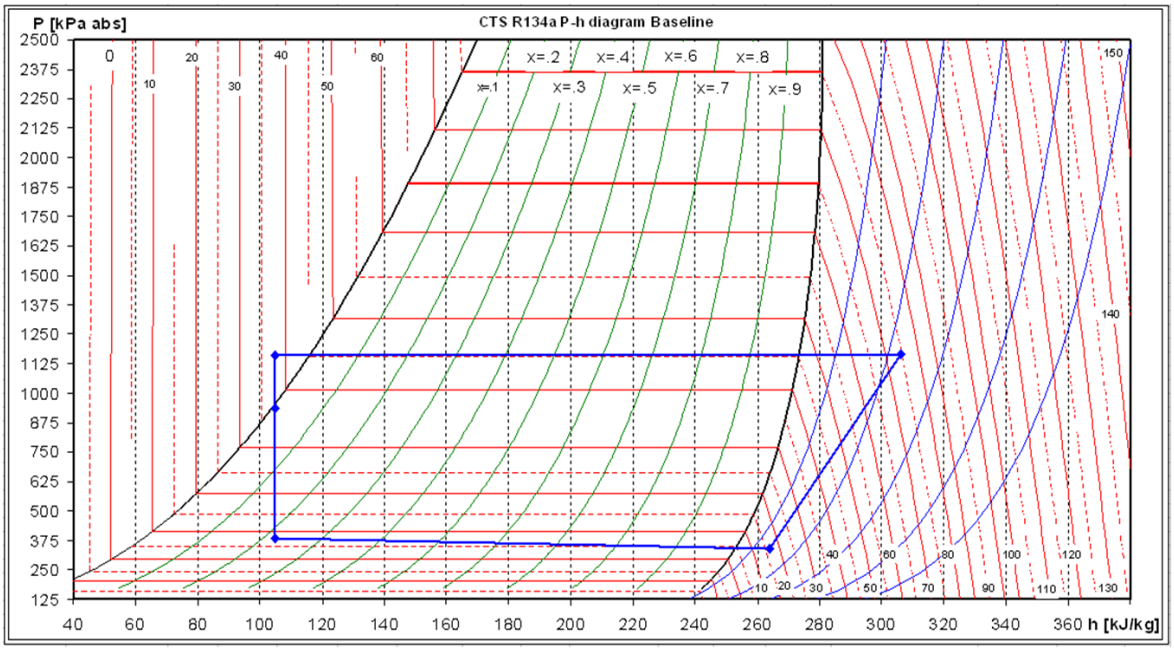

Figure 2-15: Pressure- Specific Enthalpy Diagram for Baseline Heat Pump System with Water Inlet Temperature of 37.8 ˚C and Ambient Temperature of 22.2 ˚C

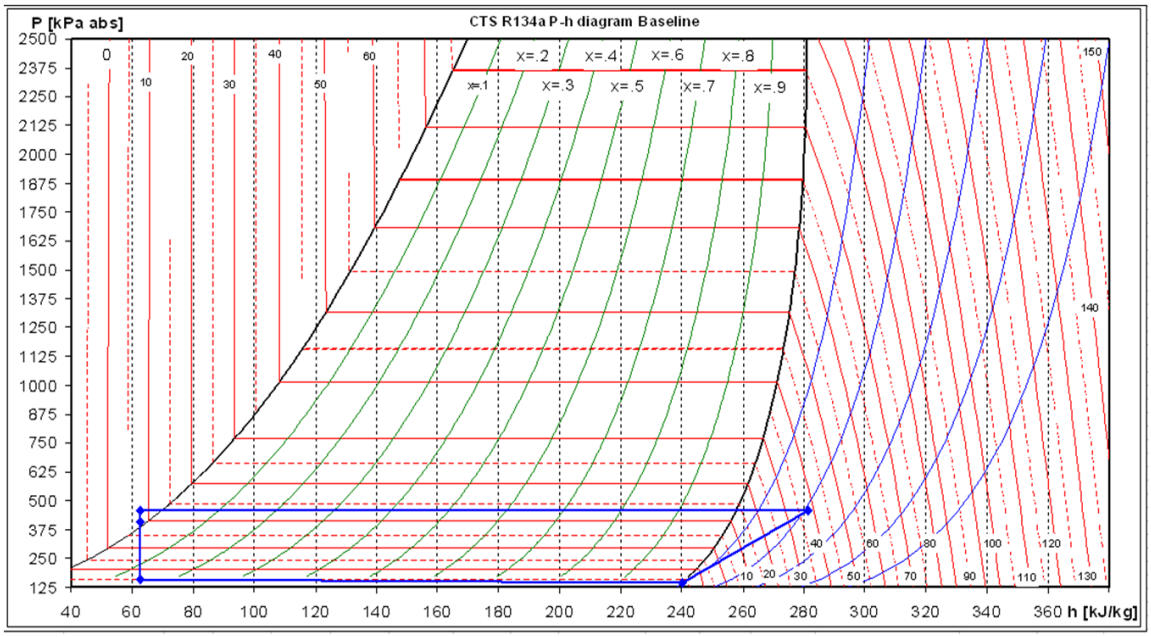

Figure 2-16: Pressure- Specific Enthalpy Diagram for Baseline Heat Pump System with Water Inlet Temperature of 8 ˚C and Ambient Temperature of 22.2 ˚C

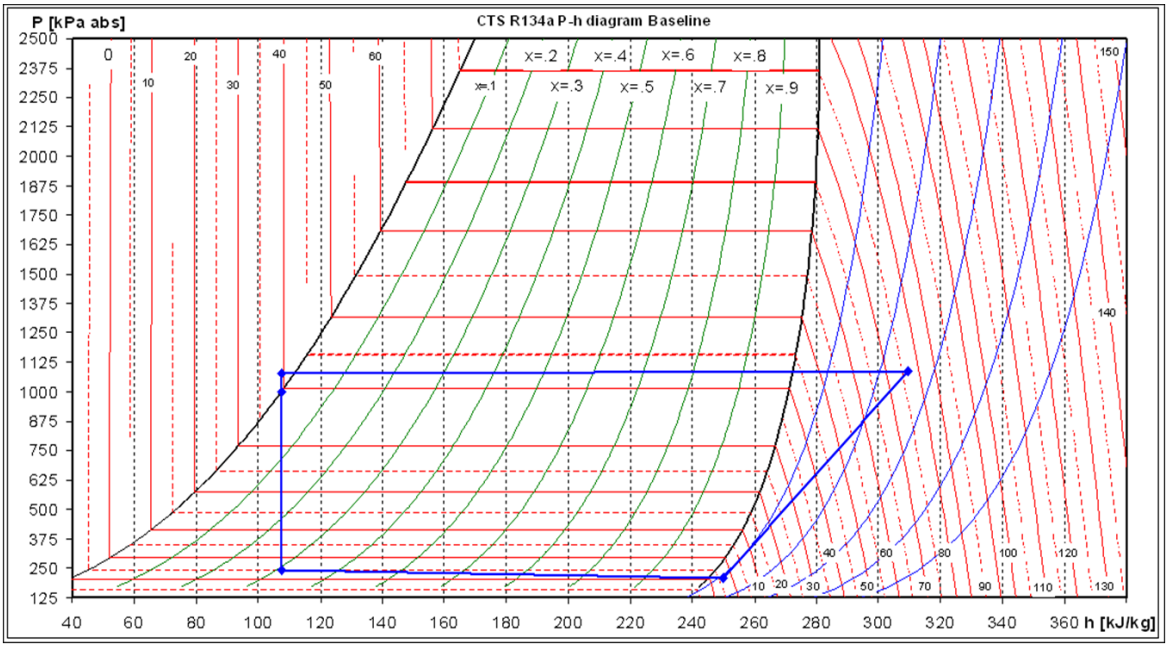

Figure 2-17: Pressure- Specific Enthalpy Diagram for Baseline Heat Pump System with Water Inlet Temperature of 37.8 ˚C and Ambient Temperature of 5 ˚C

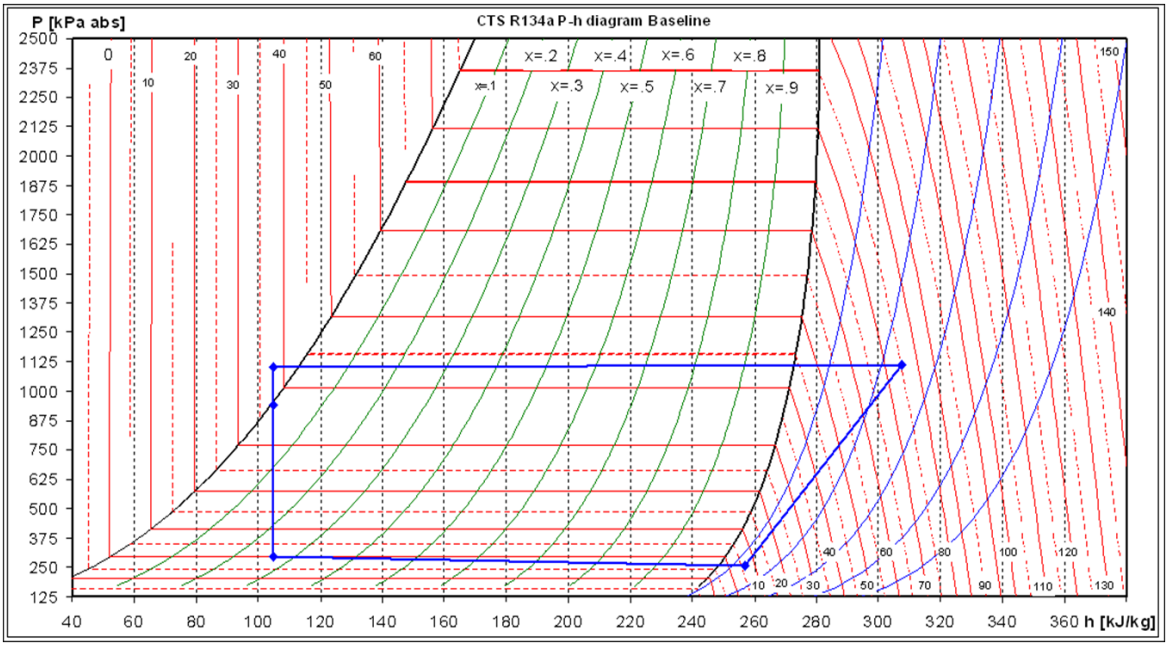

Figure 2-18: Pressure- Specific Enthalpy Diagram for Baseline Heat Pump System with Water Inlet Temperature of 37.8 ˚C and Ambient Temperature of 10 ˚C

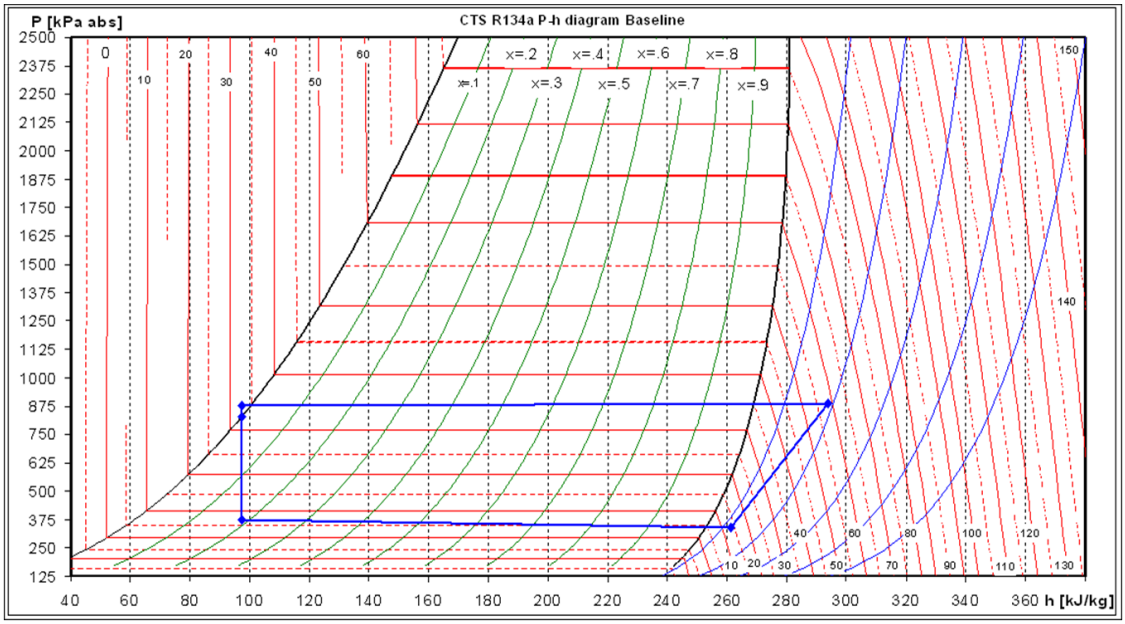

Figure 2-19: Pressure- Specific Enthalpy Diagram for Baseline Heat Pump System with Water Inlet Temperature of 26.3 ˚C and Ambient Temperature of 26.7 ˚C

The recorded measurements were used to examine the performance of the HPWH. The heating and cooling characteristics were the most important aspects of the investigation. Therefore the relevant capacities and COP's are presented (Figure 2-20 to Figure 2-24).

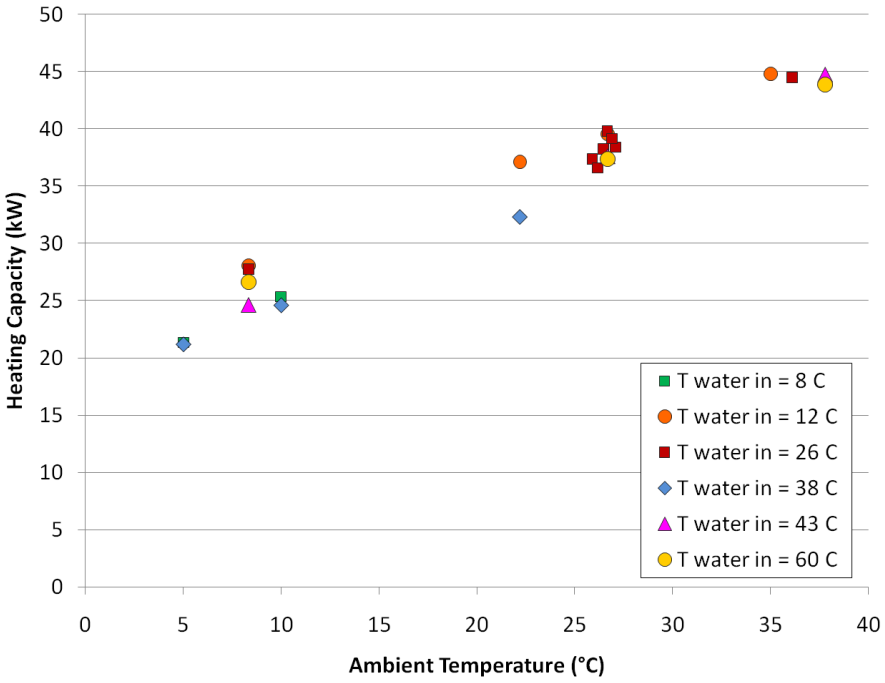

Figure 2-20: Heating Capacity as a function of Water inlet and Ambient Air Temperature

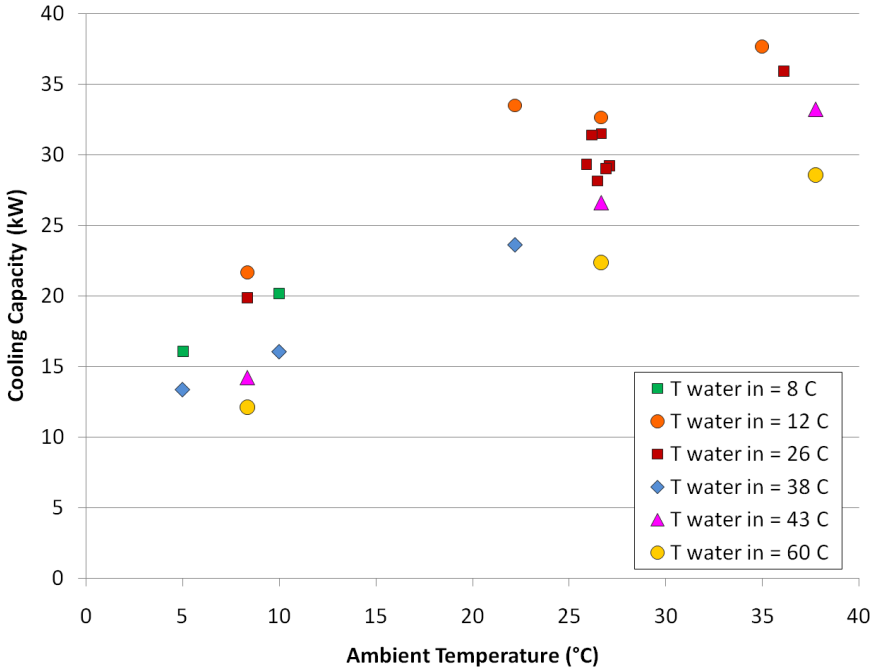

Figure 2-21: Cooling Capacity as a function of Water inlet and Ambient Air Temperature

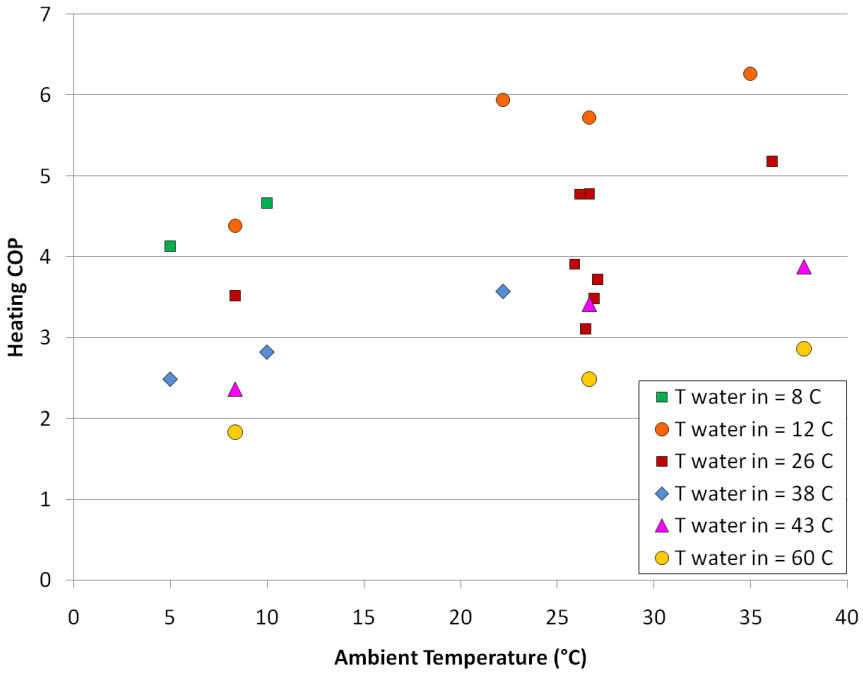

Figure 2-22: Heating COP as a function of Water inlet and Ambient Air Temperature

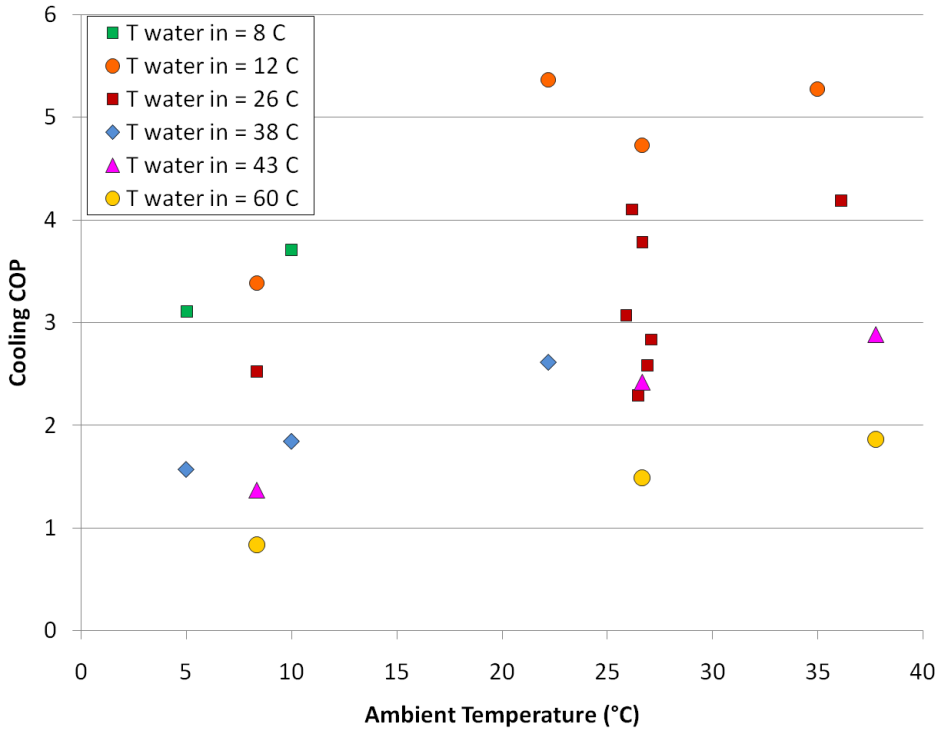

Figure 2-23: Cooling COP as a function of Water inlet and Ambient Air Temperature

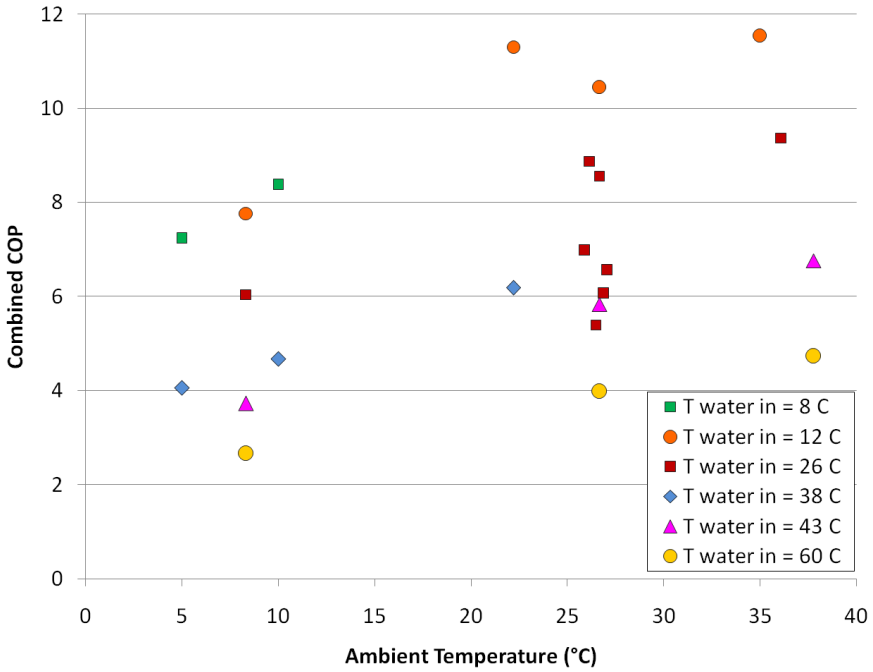

Figure 2-24: Combined COP as a function of Water inlet and Ambient Air Temperature

In addition to temperature variations of the inlet conditions of the air and water side of the system water mass flow variations were also investigated (Figure 2-25). A variation between 28 gallons per minute (gpm) and 4.66 gpm was carried out which resulted in a heating COP of 4.8 (28 gpm) and 3.4 (4.66 gpm) respectively.

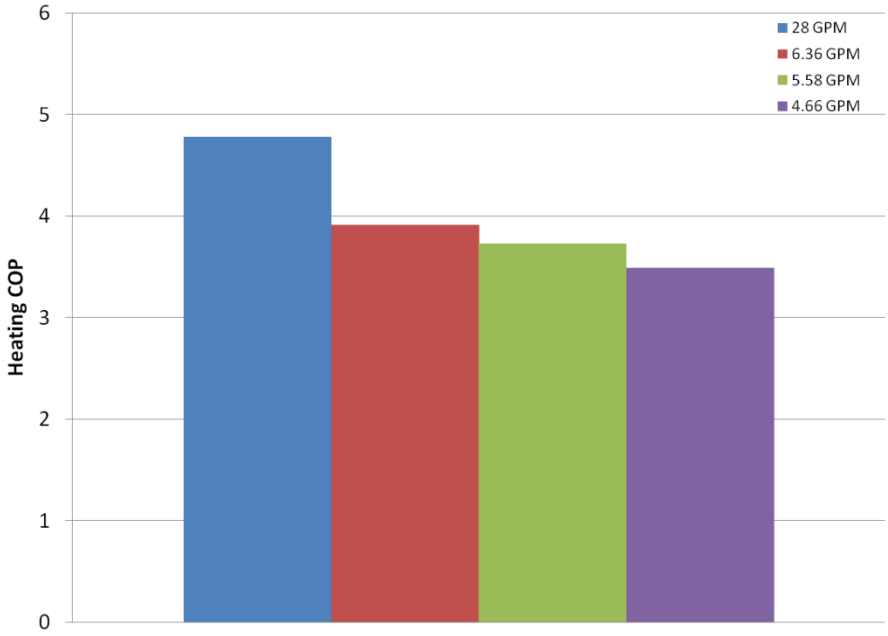

Figure 2-25: Heating COP as a function of Water Mass Flow Rate

In order to obtain a better understanding of the qualitative influence of the water inlet temperature and the ambient temperature on the capacities and the COP's of the HPWH three dimensional plots were created corresponding to the two dimensional plots described before (Figure 2-20 to Figure 2-24). They allowed a better view of the overall behavior of the system as shown in Figure 2-26 to Figure 2-30.

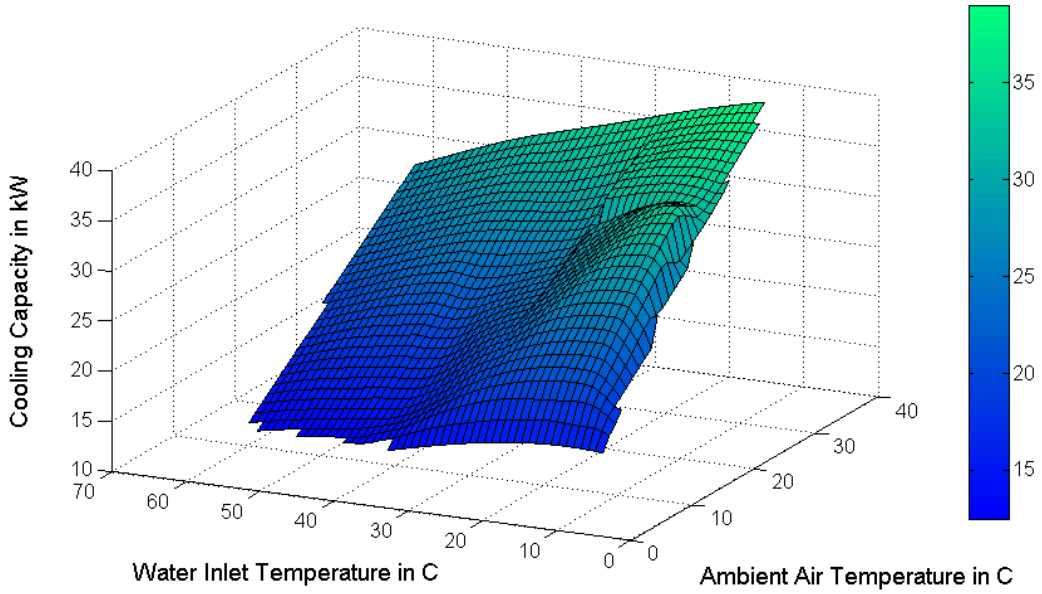

Figure 2-26: Cooling Capacity as a Function of Water Inlet and Ambient Air Temperature

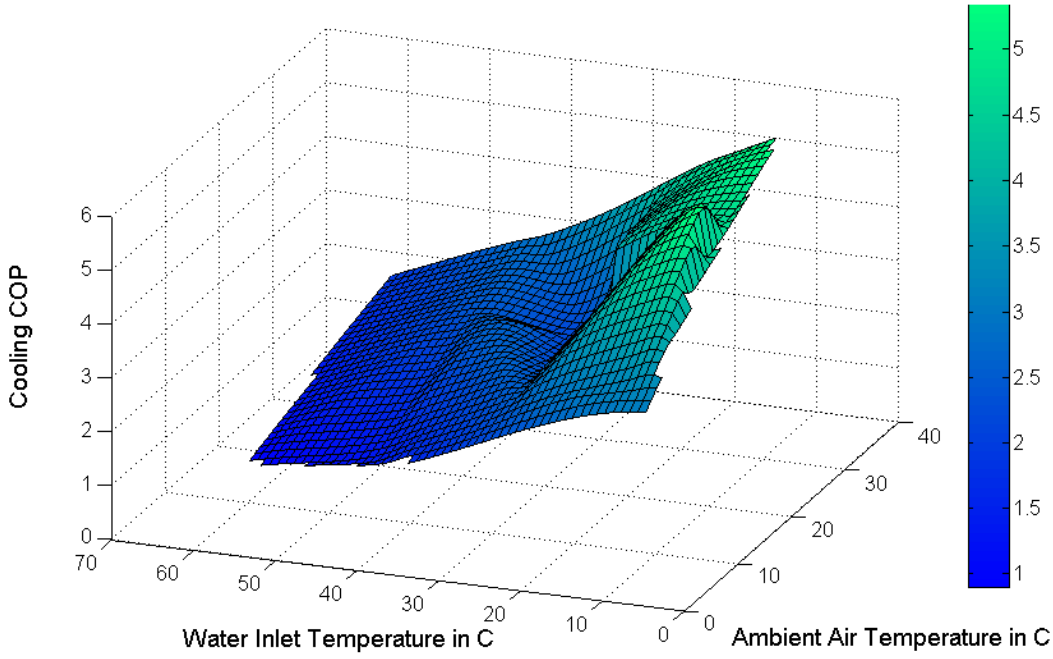

Figure 2-27: Cooling COP as a Function of Water Inlet and Ambient Air Temperature

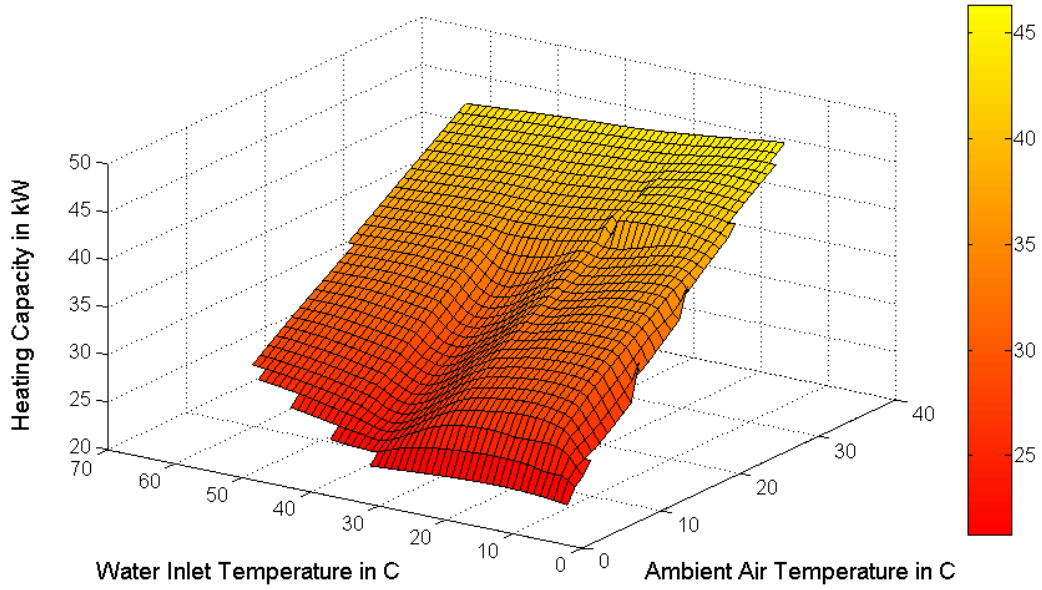

Figure 2-28: Heating Capacity as a Function of Water Inlet and Ambient Air Temperature

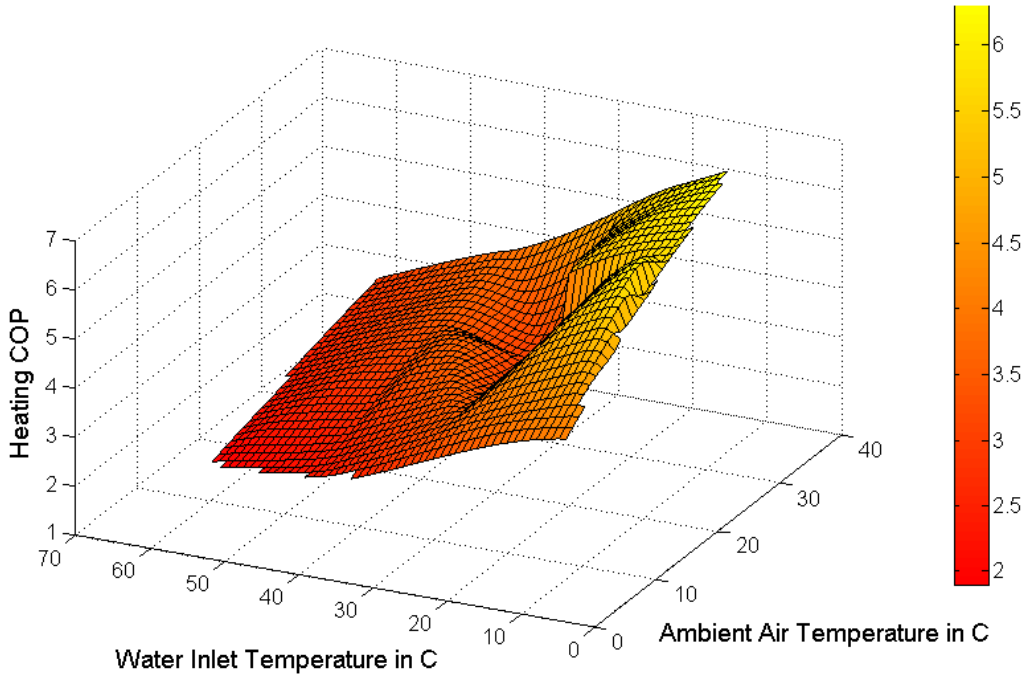

Figure 2-29: Heating COP as a Function of Water Inlet and Ambient Air Temperature

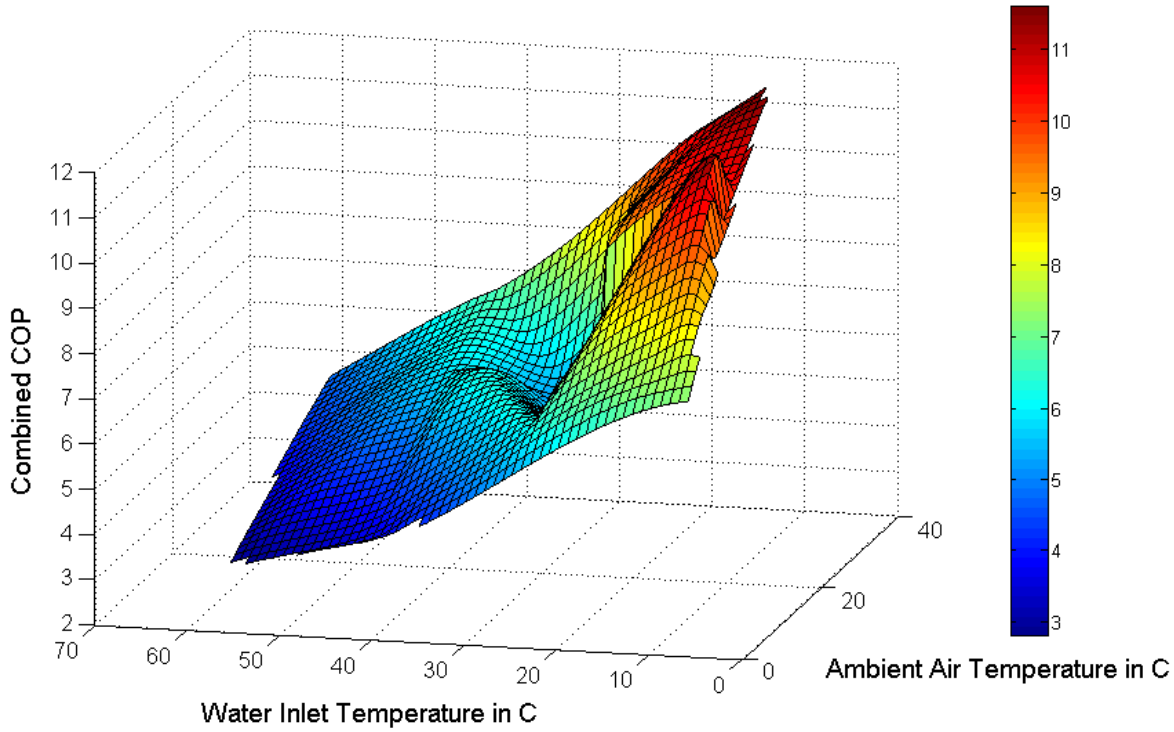

Figure 2-30: Combined COP as a Function of Water Inlet and Ambient Air Temperature

The testing of the R134a and R744 HPWH was accomplished to obtain information about the different performances of the two working fluids. Capacities and COP's were the characterizing parameters of this analysis. In addition to the evaluation of the performance the development of control strategies for the next generation HPWH was an important aspect to realize an optimum in efficiency. Therefore the possible water lift during variable water flow rates was of special interest. The baseline R134a performance represented the reference state which is shown in Figure 2-31.

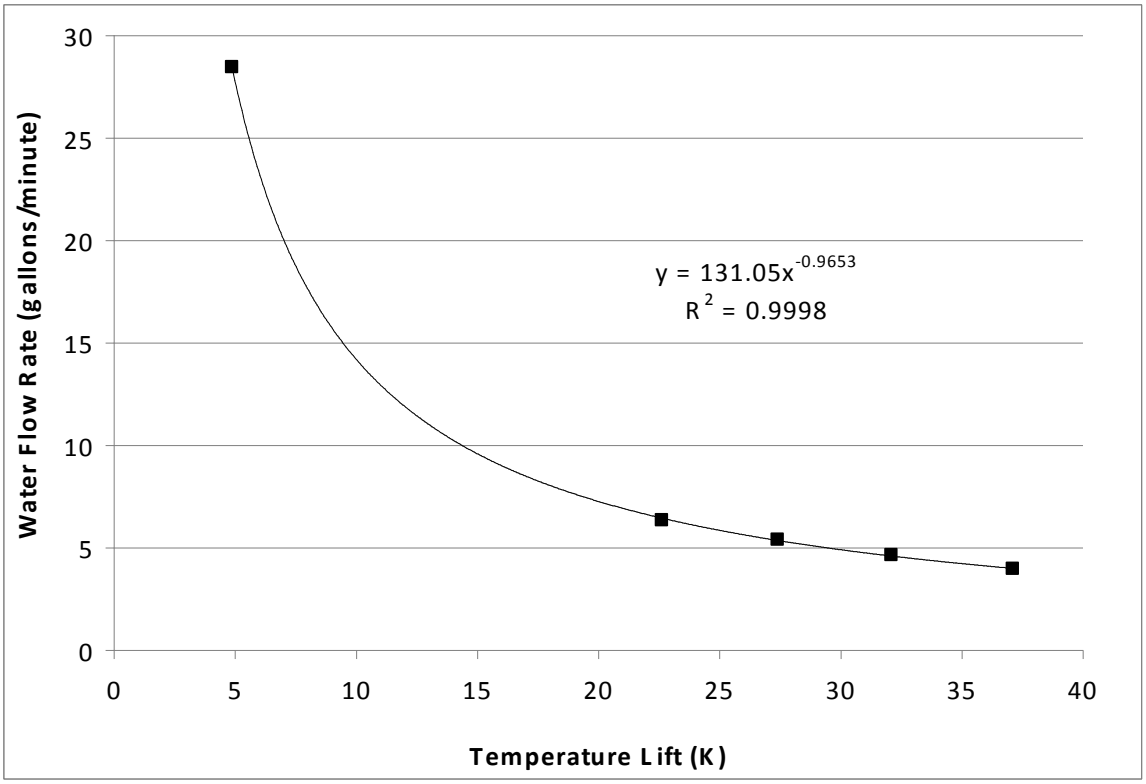

Figure 2-31: Water flow rate vs. Temperature lift

The temperature lift is the requested heating of the cooling water which occured in the condenser or gas cooler of the HPWH depending on the working fluid.

Further analysis of the R134a heat pump water heater data was performed. This analysis focused on potential savings presented by the use of heat pumps in water heating, with specific attention paid to water heated to temperatures appropriate for sanitary use (80°C and higher). This was one of the areas of greatest potential for the use of CO_2 in water heating, due to the unique characteristics of transcritical heat rejection. Based upon the experimental data, performance curves of the R134a HPWH were constructed. Several of these curves are shown in Figure 2-32. Specifically shown in Figure 2-32 is the water flow rate required to achieve a given outlet temperature with an inlet temperature of 26.7°C and an air temperature of 26.7°C. Also shown is the COP of the R134a heat pump for outlet temperatures below 81°C and a hybrid COP when the outlet temperature was above 81°C. A limit on the compressor discharge temperature was the reason why the R134a heat pump could not be used to bring the temperature of the water above 81°C. This hybrid COP took into account the fact that the heat

pump was used to bring the temperature up to 81°C and the rest of the required heating was done with a finish electric heater with a COP of 1. The results show that even with resistance heaters, the hybrid approach can achieve an average COP of 1.5 and higher.

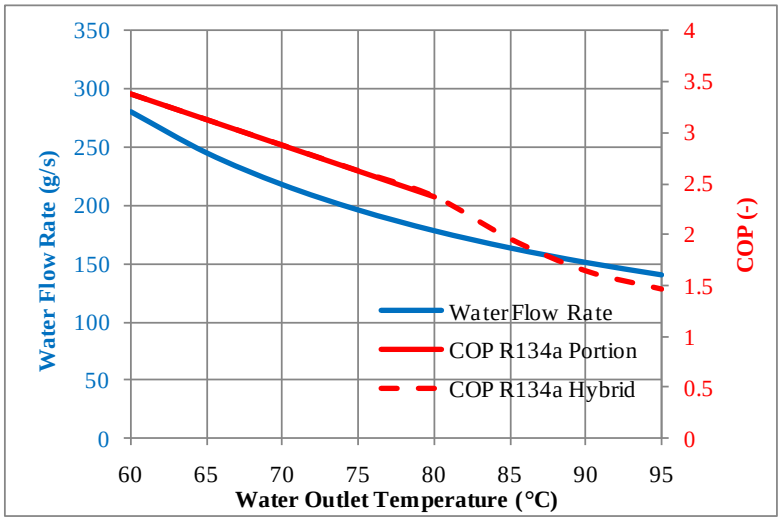

Figure 2-32: Water Flow Rate, R134a COP, and R134a Hybrid COP Curves Based Upon Experimental Data (Air and Water Inlet Temperature of 26.7°C)

Using the performance curves mentioned above, the energy consumption was calculated for given cases. The graph shown in Figure 2-33 shows the calculated energy consumption of an electric resistance heater and the R134a heat pump, with finish electric heater when needed, to bring 500 gallons of water from 26.7°C to the outlet temperatures shown, at an ambient temperature of 26.7°C

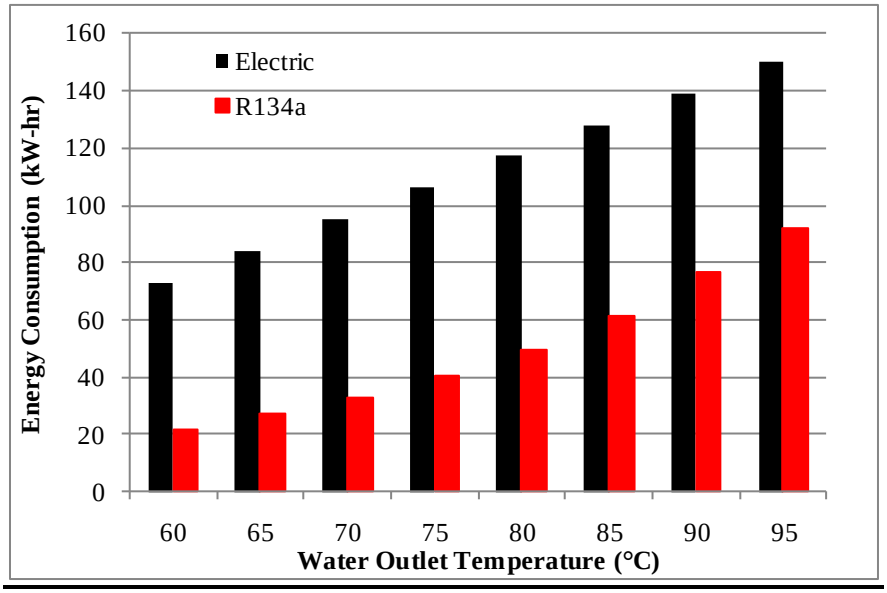

Figure 2-33: Energy Consumption of R134a Heat Pump Unit and Electrical Resistance Heat as a Function of Hot Water Outlet Temperature (Air and Water Inlet Temperature of 26.7°C)

Having calculated the energy consumption of the two methods of heating, resistance and heat pump, the savings of using heat pump was determined. The percentage savings from using the R134a heat pump instead of an electric resistance heater to bring 500 gallons of water from 26.7°C to various outlet temperatures at an ambient temperature of 26.7°C is shown in Figure 2-34. This figure shows that the use of a hybrid R134a heat pump/electric heater resulted in 40% to 70% savings over only electric heat. The drop off in savings above 81°C was caused by the fact that the heat pump did not operated at outlet water temperatures higher than this. This drop off led to higher potential savings when CO_2 was used as the working fluid.

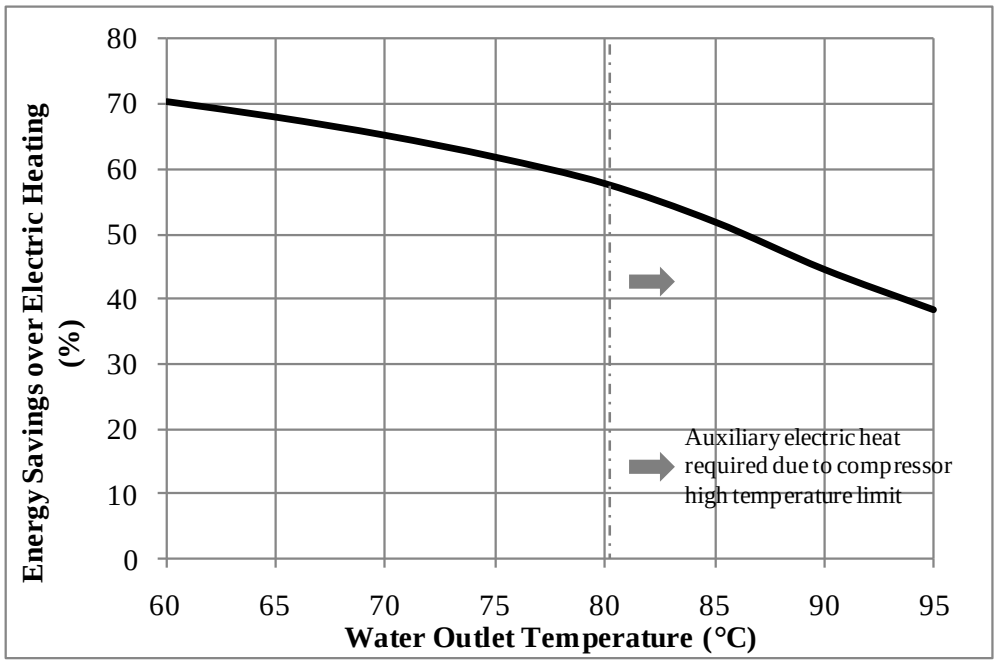

Figure 2-34: Energy Savings of Using R134a Heat Pump Instead of Electric Heating as a Function of Hot Water Outlet Temperature (Air and Water Inlet Temperature of 26.7°C)

3 Baseline R744 HPWH System Development

Design of the baseline R744 was progressing in parallel to the testing of the baseline R134a unit. In addition to performance enhancements that R744 as the working fluid in a heat pump water heater offered, the high volumetric efficiency of R744 systems offered a chance for unit package volume reduction. The plan was to use the same housing for the baseline R744 system as for the baseline R134a system. A second heat pump frame, blower, and sheet metal were acquired from the manufacturer. This allowed the buildup of a baseline R744 unit to continue in parallel with the testing of the baseline R134a unit. The expected reduction in system volume was demonstrated through a reduction in the overall height of the system package. A rendering from the three dimensional CAD model of the proposed baseline R744 unit is shown in Figure 3-1.

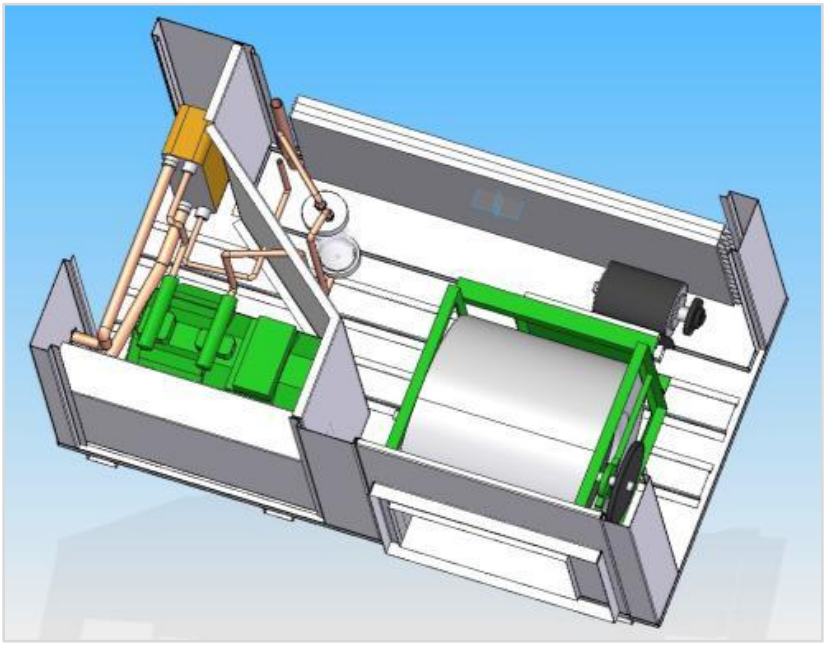

Figure 3-1: Proposed Baseline R744 Unit Design

One of the key components in demonstrating the compactness of the R744 unit was the evaporator. Based upon initial simulations, an evaporator of similar round tube design only required approximately 60% of the face area of the evaporator in the baseline R134a system. This evaporator is shown in Figure 3-2. In addition to the reduction in size, the placement of the

distributor to the evaporator in comparison to the compressor chamber of the unit had also been modified. In the baseline unit, the distributor was on the far side of the evaporator from the compressor. This necessitated a long liquid line, which increased charge. In the proposed design for the R744 unit, the distributor was placed on the near side of the evaporator to both reduce charge and the amount of piping in the system. In another attempt to underscore the reduction in package height using R744, the motor on the evaporator blower was moved from the top of the blower frame to the side as seen in Figure 3-3.

Figure 3-2: Evaporator for Baseline R744 Heat Pump Water Heater

The situation in the baseline R134a HPWH with the blower motor located on top of the blower can be seen in Figure 3-3.

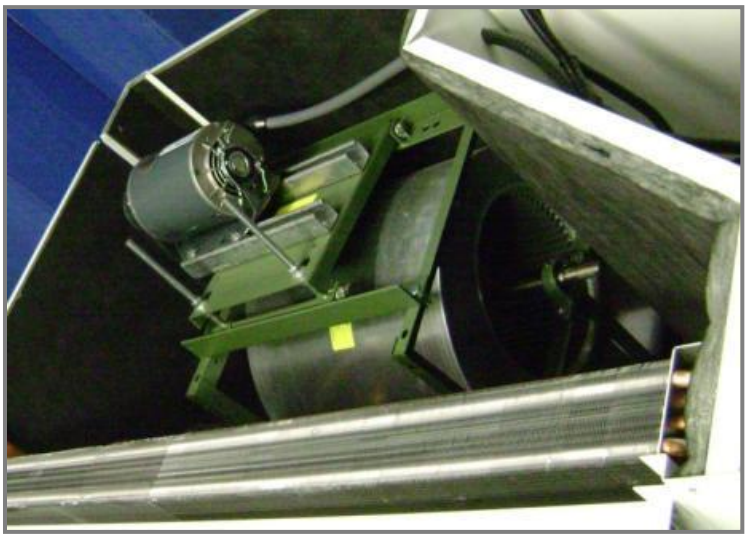

Figure 3-3: R134a System Blower Motor Position

The reduction in the necessary evaporator volume of the R744 unit allowed a lowering of the overall HPWH height. For that purpose the blower motor of the HPWH was moved beside the blower (Figure 3-4).

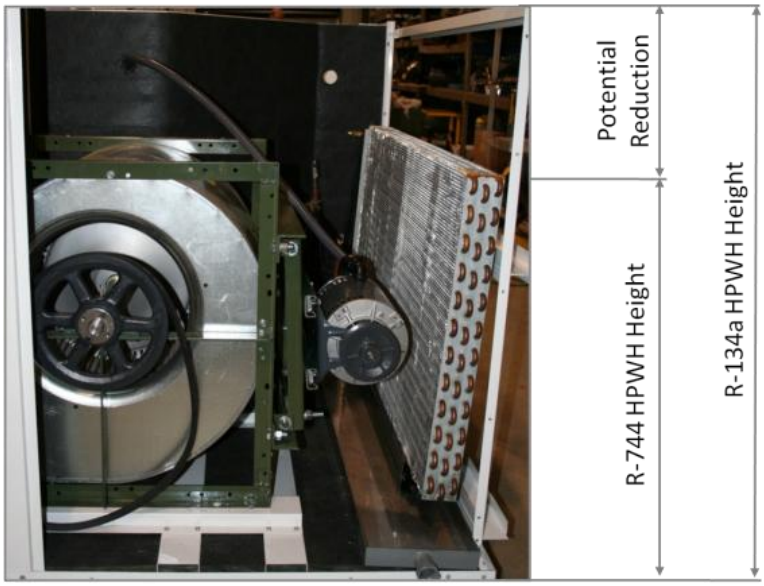

Figure 3-4: R744 System Blower Motor Position and Potential Reduction

The situation with the mounted R744 evaporator and moved blower motor visualizes the possible potential of volume economization.

The baseline R134a unit was equipped with a condenser of brazed plate design. A schematic of how a typical brazed plate heat exchanger functions is shown in Figure 3-5. In order to offer a good comparison between the baseline R134a and R744 systems a brazed plate gas cooler was used for the baseline R744. This gas cooler was of a similar capacity (~40kW), had a maximum working pressure of 140bar, and was designed in such a way to have low pressure drop in both fluid streams.

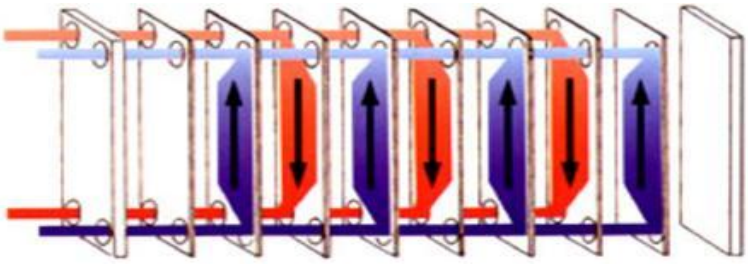

Figure 3-5: Typical Brazed Plate Heat Exchanger Design

The compact design of the unit allowed the integration of the R744 compressor into the R134a housing. A drawing of the compressor can be seen in Figure 3-6.

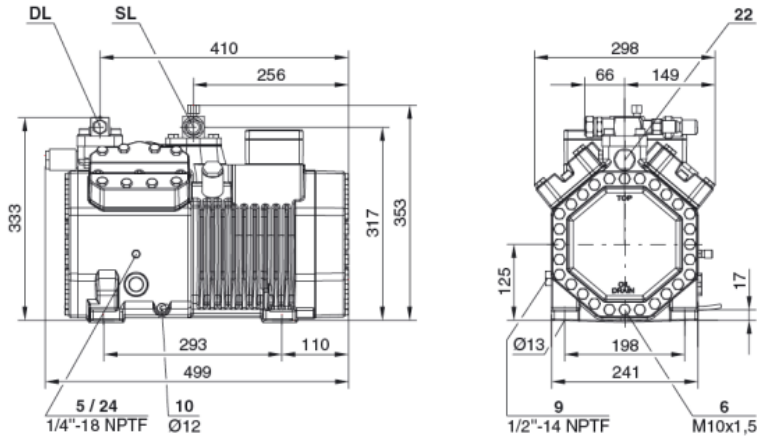

Figure 3-6: R744 Compressor Dimensions

The capacity was in the same range as the R134a system which allowed a good comparison between the two cycles. The dimensions of the compressor were suitable for the R134a heat pump housing. Due to the increased weight compared to the R134a compressor small structural support was added to the housing. Also minor modifications of the control panel were arranged for the higher voltage. Figure 3-7 shows the mounted R744 compressor inside the heat pump housing.

Figure 3-7: R744 Compressor in Heat Pump Housing

The HPWH had to operate at various water inlet conditions depending on the water supply for temperature and flow rate. These parameters have a strong influence on the high side pressure of the R744 HPWH system. The ability to store refrigerant mass during various operating modes on the high pressure side of the system was limited. In order to ensure safe operation during these changing conditions an accumulator offered additional system volume to store refrigerant mass. In addition to that the compressor was protected from possible wet suction conditions which could have caused damage due to incompressibility of the working fluid. The prototype accumulator design is shown in Figure 3-8.

Figure 3-8: R744 Accumulator Design

The accumulator was fabricated and pressure tested up to 2000 psi which guaranteed safe operation. The accumulator parts and the assembly are shown in Figure 3-9 and Figure 3-10.

Figure 3-9: R744 Accumulator Parts

Figure 3-10: R744 Accumulator Assembly

As mentioned earlier CTS had sourced an R744 evaporator that was more compact than the R134a evaporator (Figure 3-11).

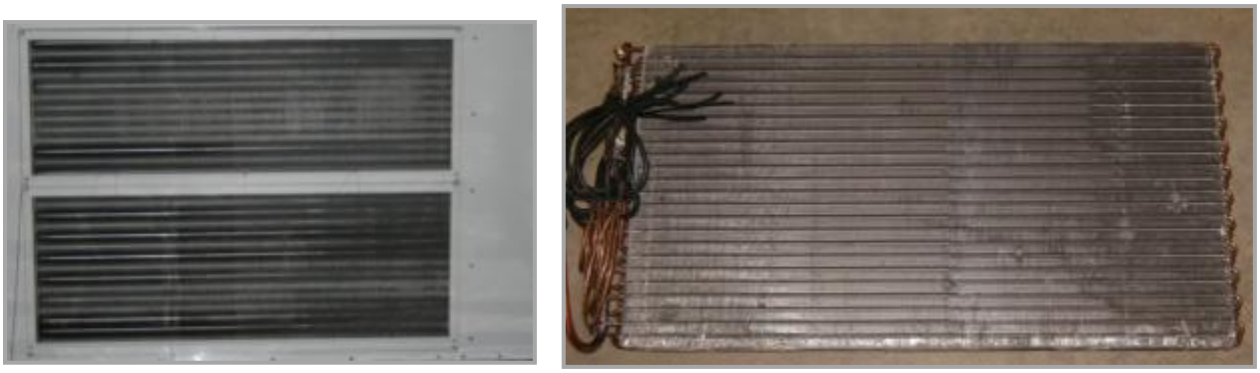

a) *b)*

Figure 3-11: R134a (a) and R744 (b) Evaporator

A comparison of the dimensions of the two heat exchangers points out the amount of volume reduction that was achieved (Figure 3-12).

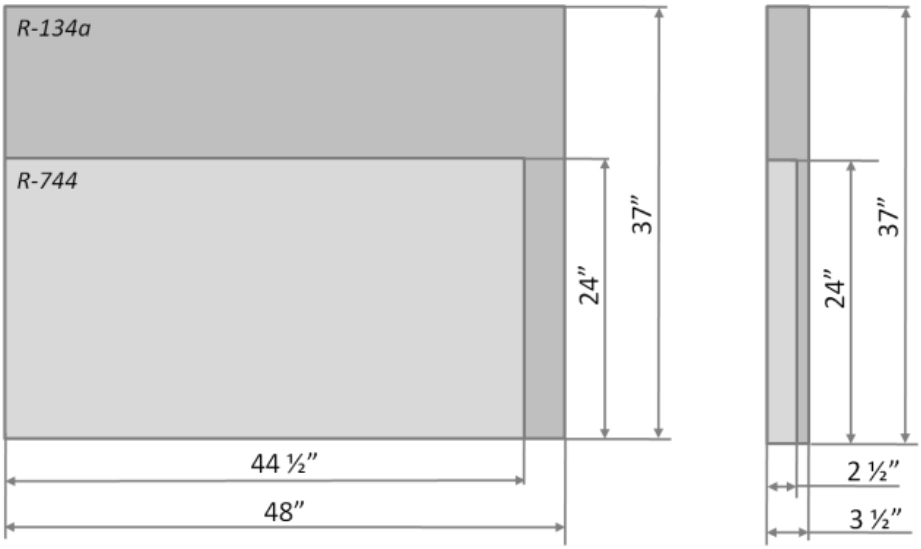

Figure 3-12: Comparison of R134a and R744 Evaporator sizes (Front and Side View)

The reduction of the evaporator face area from R134a to R744 was 40% and the reduction of the evaporator volume was even 57%. The condenser of the R134a system was a brazed plate heat exchanger which can be seen in mounted position in Figure 3-13.

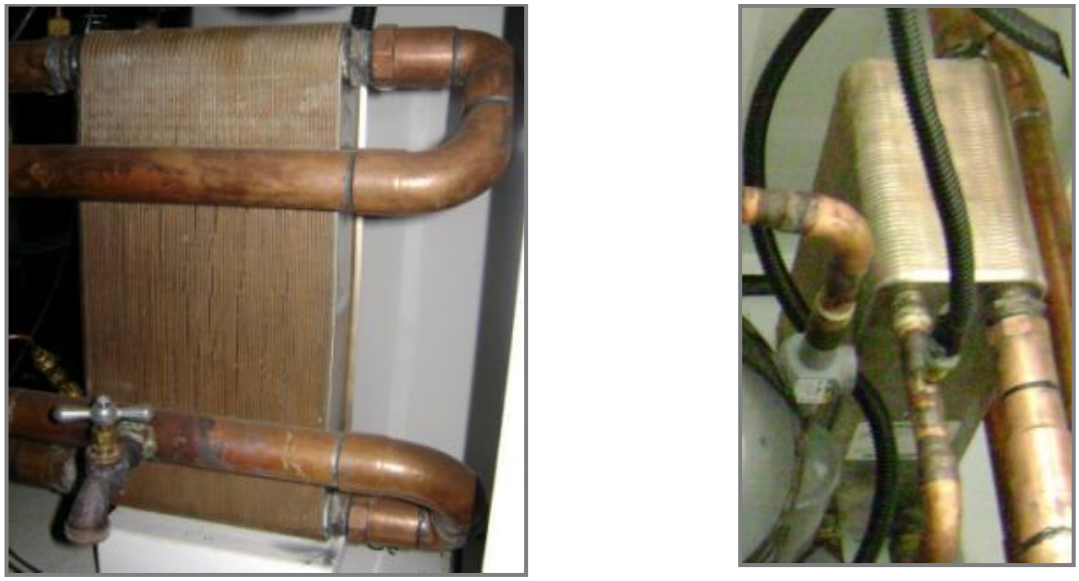

Figure 3-13: R134a Brazed Plate Condenser

For the R744 system CTS sourced a R744 gas cooler with comparable performance which allowed a good comparison between the two systems (Figure 3-14).

Figure 3-14: R744 Brazed Plate Gas Cooler

A comparison of the dimensions of the two heat exchangers makes the amount of volume reduction clear (Figure 3-15).

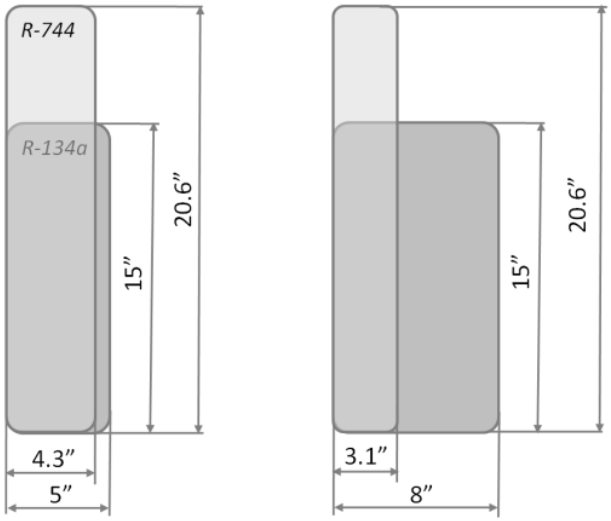

Figure 3-15: Comparison of Gas cooler/Condenser sizes (Front and Side View)

The R744 gas cooler was designed narrower compared to the R134a condenser. The reduction of the gas cooler volume from R134a to R744 was 54%. In addition to this volume reduction the design of the R744 gas cooler was beneficial since the fluid inlet and outlet connectors were located on one side of the component. This meant less piping and room for installation was needed. The following schematic gives an overview of the main components and their location in the HPWH (Figure 3-16).

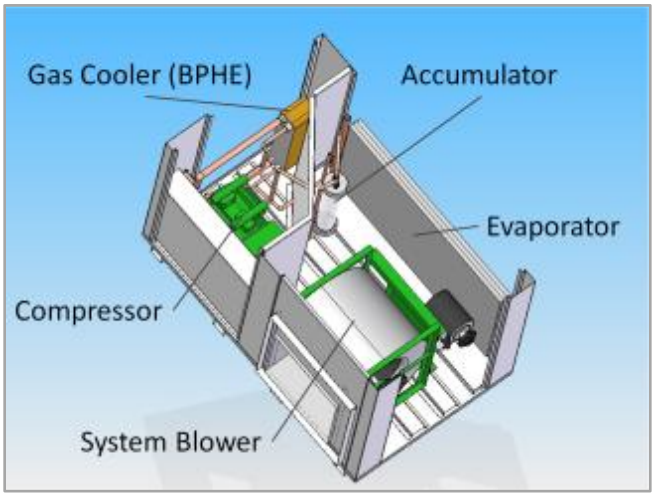

Figure 3-16: HPWH with its Main Components

In order to allow easy access to the installation space inside the HPWH, the inner dividing wall between air side and compressor/gas cooler was removed. The main components like compressor, evaporator, accumulator, and gas cooler were installed in the HPWH as seen in Figure 3-17.

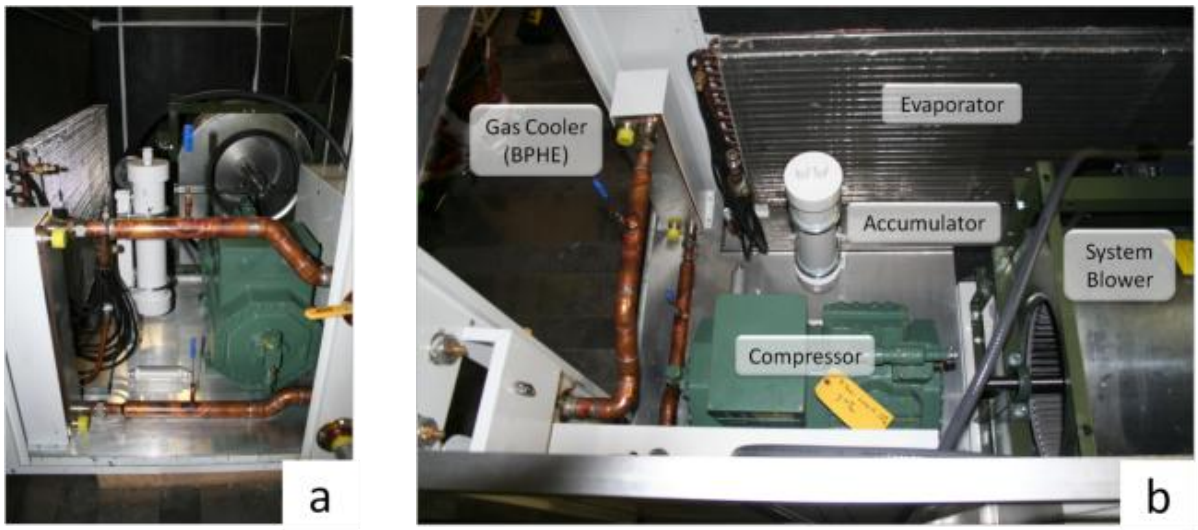

Figure 3-17: HPWH with the mounted R744 Main Components in Side a) and Top View b)

The different necessary tasks that were accomplished for the components are described in the following section.

The evaporator was mounted at the front of the HPWH. Due to the higher compactness of the component, the HPWH housing was adjusted to fit the smaller face area. The evaporator was fastened on the side to assure its position. A stainless steel tray was used to drain water in case of condensation.

The accumulator was painted after its fabrication to prevent corrosion. In order to achieve a compact system design, the accumulator was located behind the evaporator in terms of air flow direction. To ensure its functionality the accumulator was mounted vertically. The used steel channel guarantees a minimum of vibration during operation. The mounted situation in top and side view is shown in Figure 3-18.

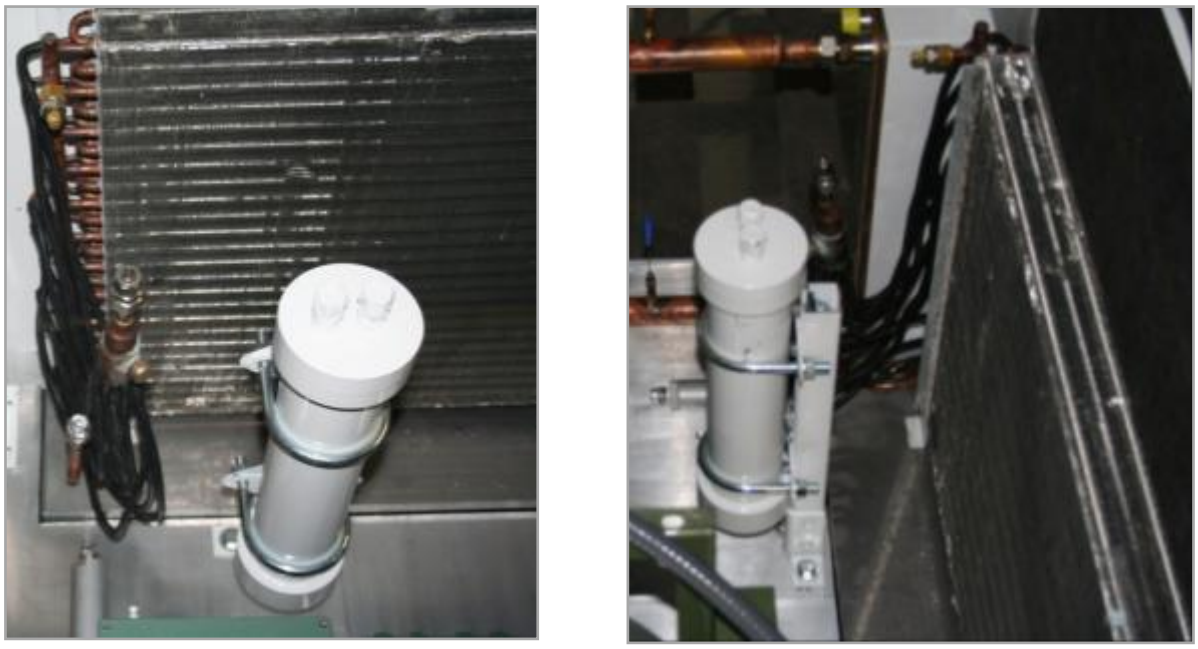

Figure 3-18: Accumulator and Evaporator with its Refrigerant Distributor

The next step in integrating the accumulator into the HPWH system was the connection between the compressor and the evaporator on the refrigerant side. Therefore, the inlet and outlet of the component were connected with stainless steel tubing due to the higher operating pressures compared to R134a. The bottom refrigerant line of the accumulator was equipped with a valve to regulate the oil return to the compressor. The connected accumulator is shown in Figure 3-19.

Figure 3-19: Connected accumulator

The gas cooler of the HPWH being an interface between water and refrigerant side was integrated into the two cycles. Therefore the water side was realized with brazed copper lines which connect the water adapters of the system with the gas cooler. The connection of the HPWH water side to the glycol/water measurement cart was realized with flexible plastic hoses. The overall heat rejection cycle is visualized in Figure 3-20.

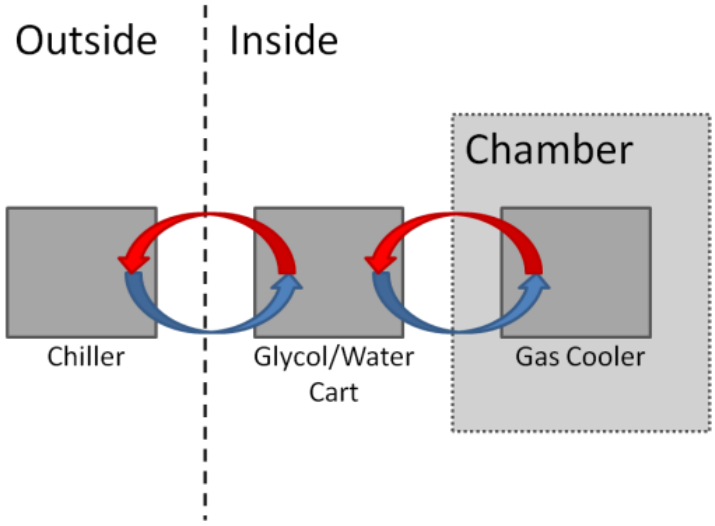

Figure 3-20: Heat Rejection Cycle

The heat rejection was accomplished with two secondary fluid cycles. On the one hand there is the water cycle which connected the HPWH gas cooler with the glycol/water measurement cart. On the other hand, there was the glycol cycle which connected the glycol/water measurement cart inside of the building with the chiller which was located outside of the building. Finally the heat was rejected to the environment. The use of glycol allowed running temperatures below 0˚C which was necessary to provide sufficient cooling capacity for low temperature test conditions.

In order to obtain the necessary performance data of the water and refrigerant side, parameters like pressures and temperatures were recorded during operation. Therefore pressure gauges and temperature immersion probes at the inlet and outlet of the gas cooler were included in the water and refrigerant lines which are shown in Figure 3-21.

Figure 3-21: Pressure and Temperature Measurement on the Water and Refrigerant Side of the Gas Cooler

After the installation of the R744 components, a new dividing wall was fabricated and installed to ensure proper airflow through the evaporator.

After finishing the installation of all components and the implementation of all necessary sensors, the HPWH was installed in the environmental chamber. The system was then connected to the wind tunnel and the helper blower which was used to overcome the additional pressure drop created by the wind tunnel. The HPWH and the whole testing set up inside the environmental chamber at CTS can be seen in Figure 3-22.

Figure 3-22: HPWH in Environmental Chamber

The change from R134a to R744 as a refrigerant in the HPWH required modifications in the data acquisition files. The necessary steps were completed which included modifications of the refrigerant property data in the online pressure specific enthalpy diagram visualization and the revision of the data analysis code. An example of the pressure specific enthalpy diagram for R744 in subcritical operation is shown in Figure 3-23.

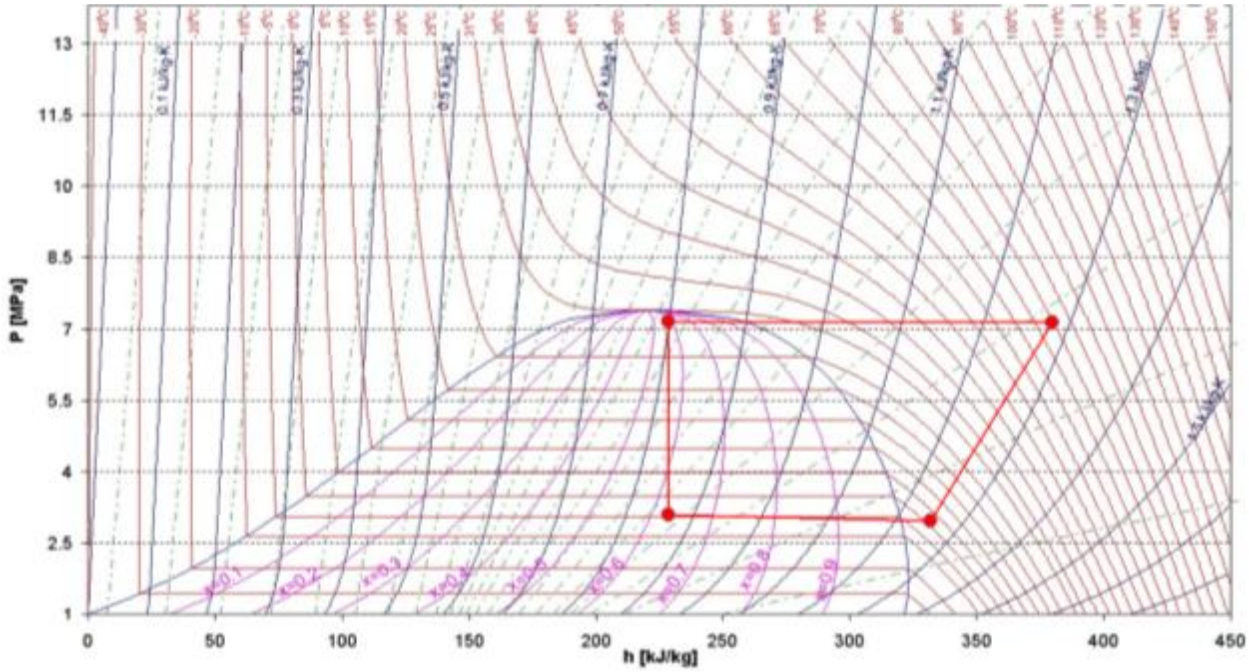

Figure 3-23: R744 Pressure Specific Enthalpy Diagram

Vapor compression cycles are distinguished by their performance and certain values depending on the application area. In order to clarify the most important characteristics of the HPWH the relevant parameters are explained in the following paragraph and the following Figure 3-24 which shows an ideal transcritical vapor compression cycle.

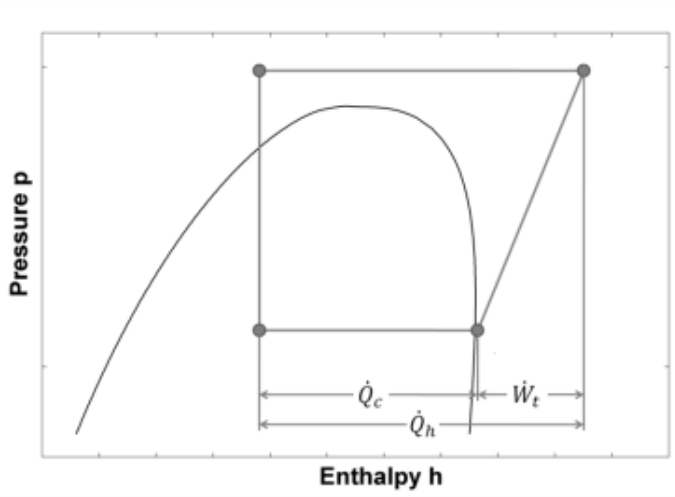

Figure 3-24: Ideal Transcritical Vapor Compression Cycle with its relevant Capacities

In general energy conversion efficiencies are defined as the ratio of useful output and necessary input. The range of this ratio is usually between 0 and 1 or 0 to 100 % respectively. In vapor compression cycles the efficiency can be greater than 1. Therefore the term COP or coefficient of performance is used. Depending on the desired useful output of the vapor compression cycle different characterizations are possible.

If the cooling output is of special interest the COP is the ratio of cooling capacity and necessary technical power input.

$$COP_c = \frac{\dot{Q}_c}{\dot{W}_t} \tag{8}$$

Where:

$\mathrm{COP_c}$: HPWH cooling COP

$\dot{Q}_c$: Cooling capacity in kW

$\dot{W}_t$: HPWH power input in kW

On the other side if the heating output is desired the heating COP is formed by the heating capacity divided by the technical power.

$$COP_h = \frac{\dot{Q}_c + \dot{W}_t}{\dot{W}_t} = \frac{\dot{Q}_h}{\dot{W}_t} \tag{9}$$

Where:

$\mathrm{COP_h}$: HPWH heating COP

$\dot{Q}_h$: Heating capacity in kW

$\dot{W}_t$: HPWH power input in kW

Another possible relationship for the HPWH which provides heating and cooling as the useful outputs simultaneously is the combined COP.

$$COP_{comb} = COP_c + COP_h = \frac{\dot{Q}_c}{\dot{W}_t} + \frac{\dot{Q}_c + \dot{W}_t}{\dot{W}_t} = \frac{2 \cdot \dot{Q}_c + \dot{W}_t}{\dot{W}_t} \tag{10}$$

Where:

$\mathrm{COP_{comb}}$: HPWH combined COP

This exceptional characteristic of the HPWH system compared to regular vapor compression cooling or heating cycles makes bigger overall COPs possible. A Sankey diagram which is used to visualize energy conversion systems (Figure 3-25) demonstrates the different situations of the heating mode of the HPWH and the combined capacity of heating and cooling.

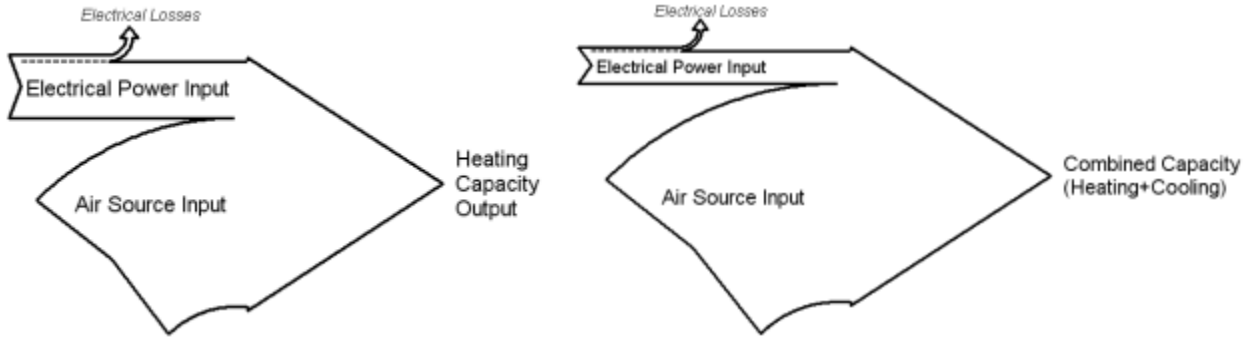

a) ***b)***

Figure 3-25: Sankey Diagram showing heating capacity a) and combined output of heating and cooling capacity b)

In the heating mode the electrical power input and the cooling capacity generated by the source input add up to the heating capacity. In the operation mode with combined capacities the cooling capacity adds up to the heating capacity, so that the overall efficiency increases.

A balance check of the first test runs was accomplished to show the reliability of the calculated energy balances. Therefore the combination of equation 1 and equation 2 show that the relationship between the heating and cooling COP is

$$COP_h = COP_c + 1 \quad . \qquad (11)$$

The resulting balance check of the recorded experimental results is shown in Figure 3-26.

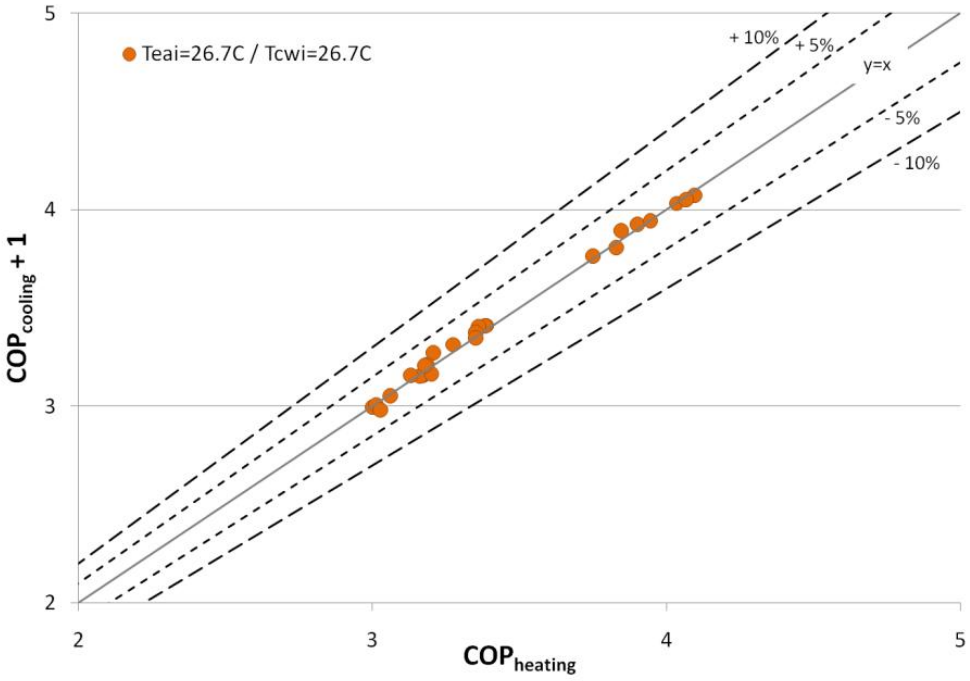

Figure 3-26: Comparison of energy balances based on experimental results

All initial results with variable water flow rate and air and water inlet conditions of 26.7 ˚C were within +/-5 % between heating COP and cooling COP plus 1. Therefore the accuracy of the measurements was confirmed.

The water flow rate variation was accomplished for 4, 4.8, 5.6, 15.9 and 28 gallons per minute at a water and ambient air inlet temperature of 26.7 ˚C to allow a comparison with R134a data at this condition. The water flow rate variation was of special interest because of its relevance for the development of an optimum control strategy of the water heater. The relationship between desired water outlet temperature and water flow rate defined this situation.

A comparison of the investigated maximum water flow rate condition and the minimum water flow rate in the logarithmic pressure specific enthalpy diagram showed the influence of different volume flows on the refrigeration cycle (Figure 3-27).

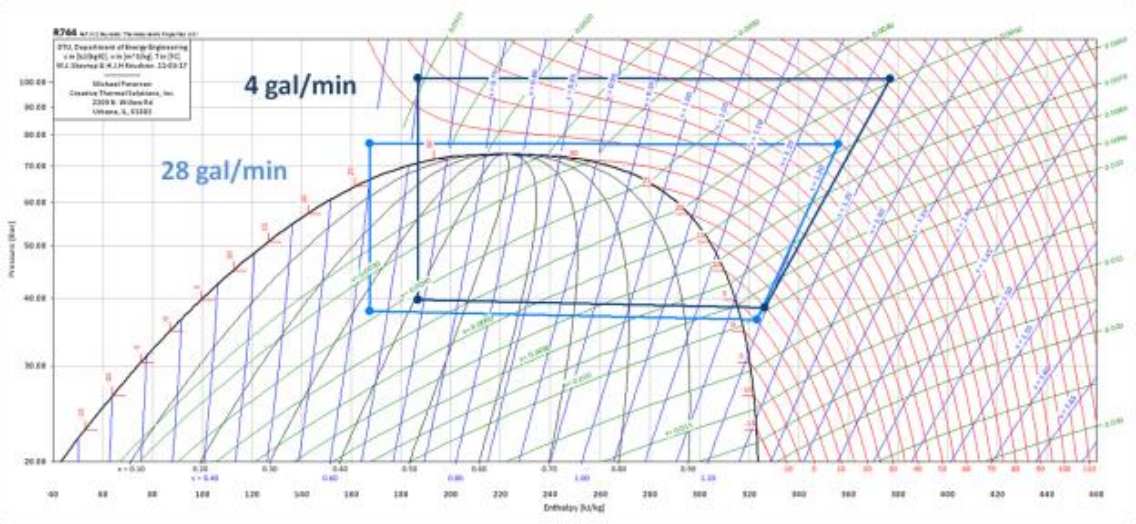

Figure 3-27: R744 log p-h Diagram with low and high water flow rate conditions

Comparing the two water flow rate conditions, the influence of the different heat transfer coefficients at 4 and 28 gallons per minute becomes apparent. At the lower flow rate, higher temperatures and therefore higher high-side pressures were achieved compared to the high flow rate. At the same time, the gas cooler outlet temperature was higher compared to the 28 gallons per minute condition. This demonstrated the varying water temperature lift possibilities at different water flow rates. While the ASHRAE and EHPA testing standards call for equipment rating at a lift of 5°C, the real energy saving potential lies in increasing the efficiency of the heat pump at higher lifts, since this is generally how the demand is seen.

A comparison of the R134a and R744 measurements was done to investigate the performance of the two systems. Therefore the water flow rate versus the water temperature lift in the condenser (R134a) and gas cooler (R744) of the systems was plotted (Figure 3-28).

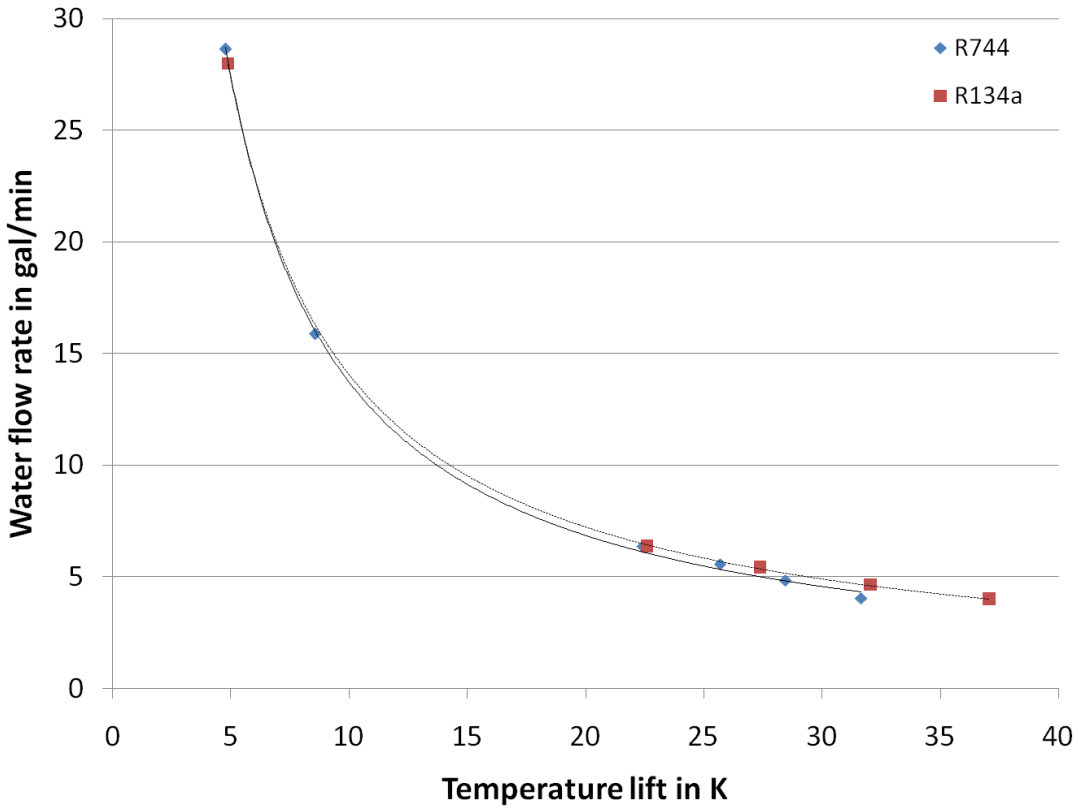

Figure 3-28: Water Flow Rate versus Temperature Lift

The results for R134a and R744 showed very good agreement between the two curves which indicated that the chosen components for the R744 system match the R134a components performance very well, at the rating condition. A good comparison between the two systems was therefore ensured. Comparing the temperature lifts for the two fluids, R134a achieved a slightly higher capacity with a maximum temperature lift of 37 K compared to 32 K for R744 at a water flow rate of 4 gallons per minute.

A comparison of the heating COP of the two systems gave another impression of their performance (Figure 3-29). Comparing the heating COP versus the temperature lift for the two working fluids R134a showed slightly higher COP than the baseline R744 system at the investigated condition.

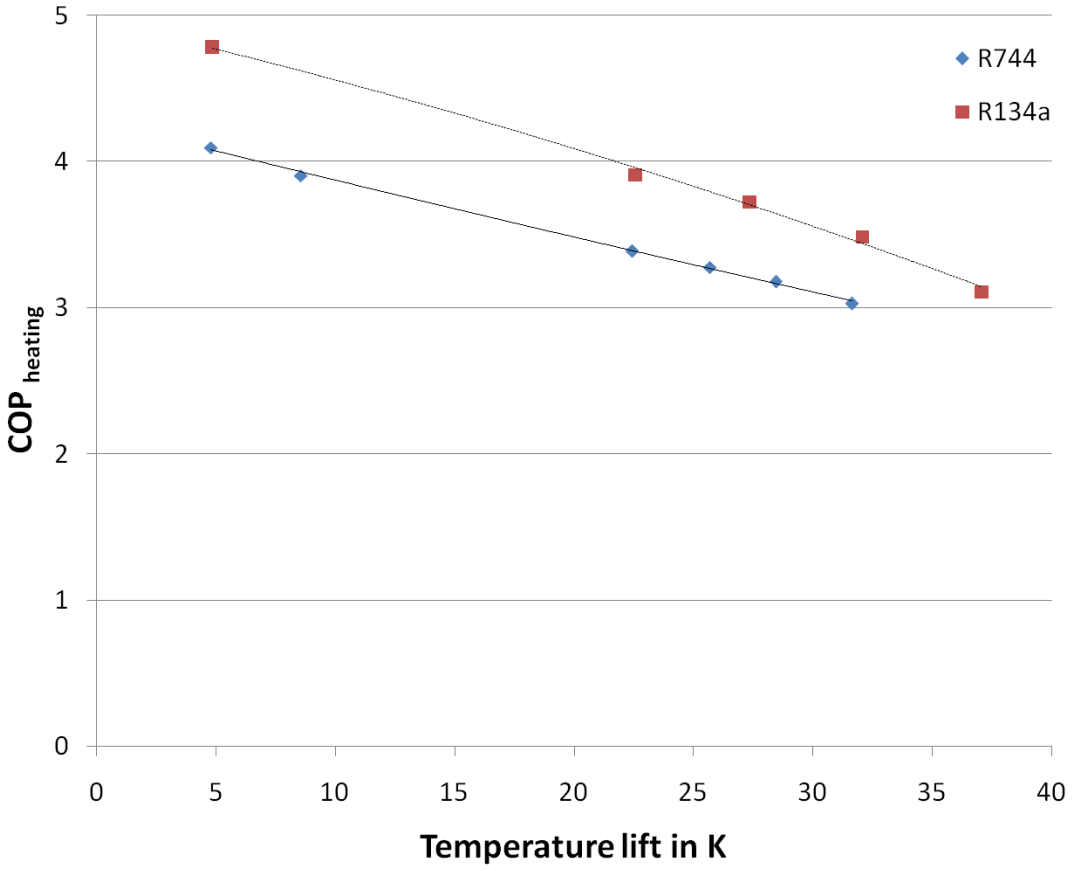

Figure 3-29: $COP_{heating}$ versus Temperature Lift

Better COP's were reached compared to the R744 system. However it must be pointed out that the operating condition of the system at 26.7 ˚C on the water and air side were not ideal for R744.

First results of the R744 baseline testing showed the potential performance of the alternative working fluid. The baseline tests were accomplished with special interest in two aspects. On the one hand water mass flow rate variation and on the other hand various water and ambient air temperature conditions at the rating water mass flow rate of 28 gallons per minute were investigated. The comparison between R134a and the baseline R744 system (Figure 3-30 to Figure 3-33) was carried out for the conditions presented in Table 3-1 at a water mass flow rate of 28 gallons per minute.

Table 3-1: Test conditions at rating water mass flow rate

Water inlet temperature in ˚C	12	26.7	8	12	26.7	60
Ambient air temperature in ˚C	8	8	10	26.7	26.7	26.7

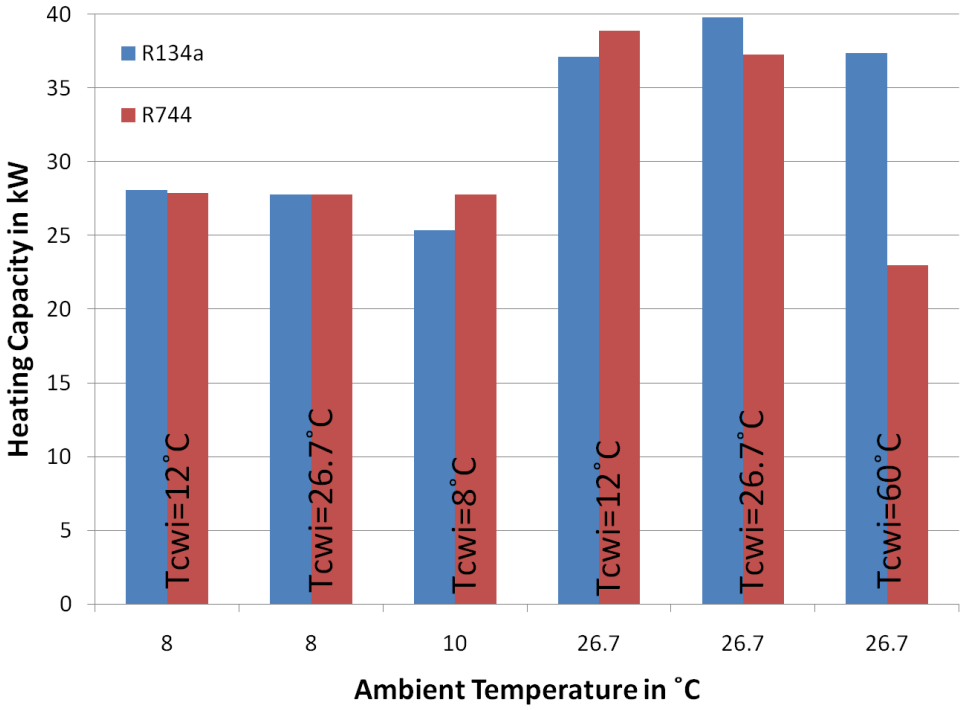

Figure 3-30: R134a vs. R744 Baseline Heating Capacity

The heating capacity was an important characteristic to determine the performance of the heat pump water heater. The comparison of the heating capacities for R134a and R744 (Figure 3-30) showed that the baseline R744 system matched the R134a heating capacity at lower ambient temperatures. Going to higher temperatures R744 even exceeded the R134a heating capacity. At higher ambient and water inlet temperatures R134a showed a better performance. The next step of the data analysis took account of the electrical input for the compressor and blower of the heat pump which defined the system heating COP (Figure 3-31).

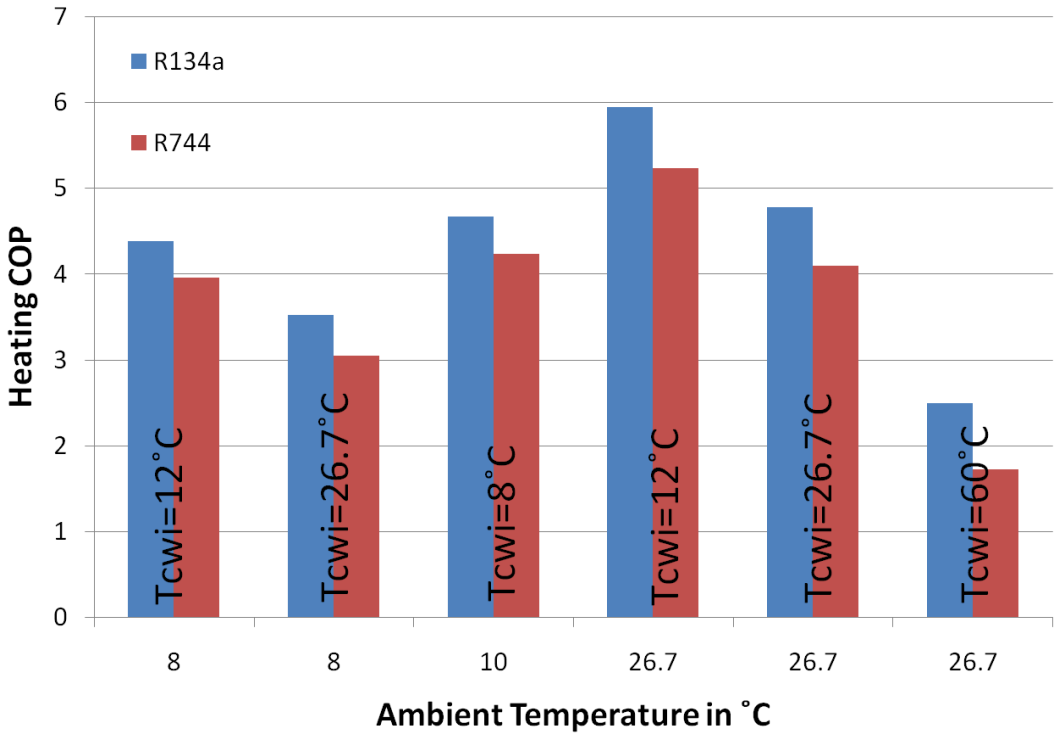

Figure 3-31: R134a vs. R744 Baseline Heating COP

When analyzing the system heating performance the situation between R744 and R134a changed. The R134a system showed a better performance throughout the test conditions due to a better ratio of heating capacity and power consumption.

The second useful output of the heat pump was the cooling capacity which is shown in Figure 3-32.

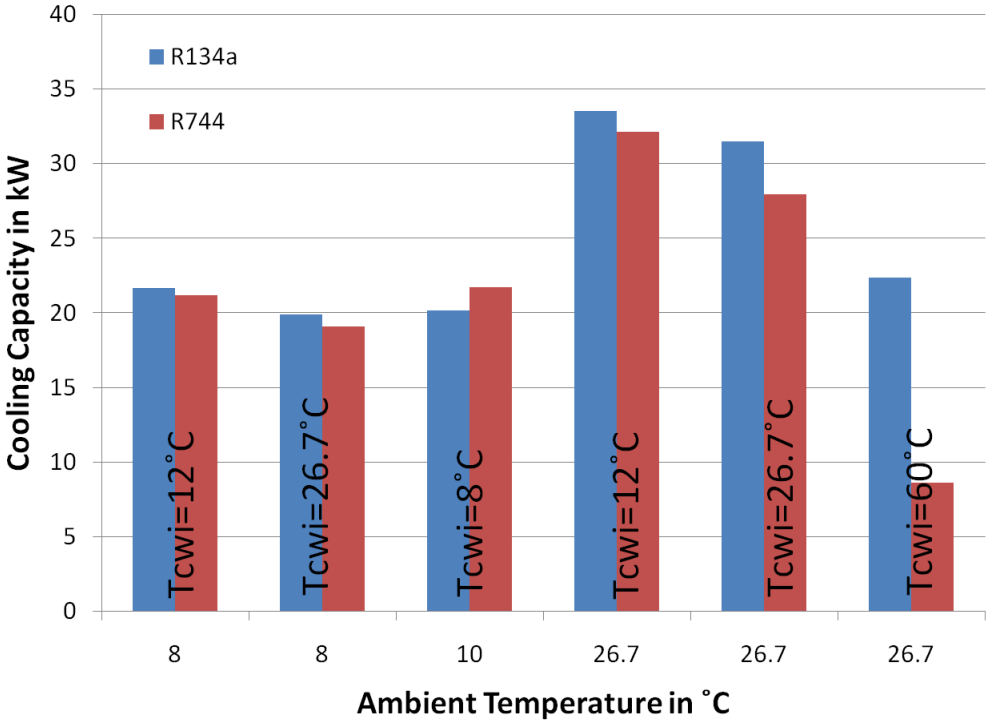

Figure 3-32: R134a vs. R744 Baseline Cooling Capacity

The results for the cooling capacity of the two working fluids was qualitative comparable to the heating capacity. The R134a performance was almost matched at low ambient air temperatures (8˚C) and even exceeded at an air temperature of 10˚C and a water inlet temperature of 8˚C. At higher ambient temperatures the R134a showed a better performance compared to R744.

In order to get an idea of the overall performance of the heat pump water heater both useful outputs of the system (heating and cooling) were considered. This combination of capacities divided by the necessary electrical power formed the combined COP. An overview of the combined COP results for R134a and R744 can be seen in Figure 3-33. The combined COP for the R134a system showed a better performance throughout the investigated test conditions. However the R744 system exceeded the goal of a combined COP of 8 at an ambient temperature of 26.7˚C and a water inlet temperature of 12˚C.

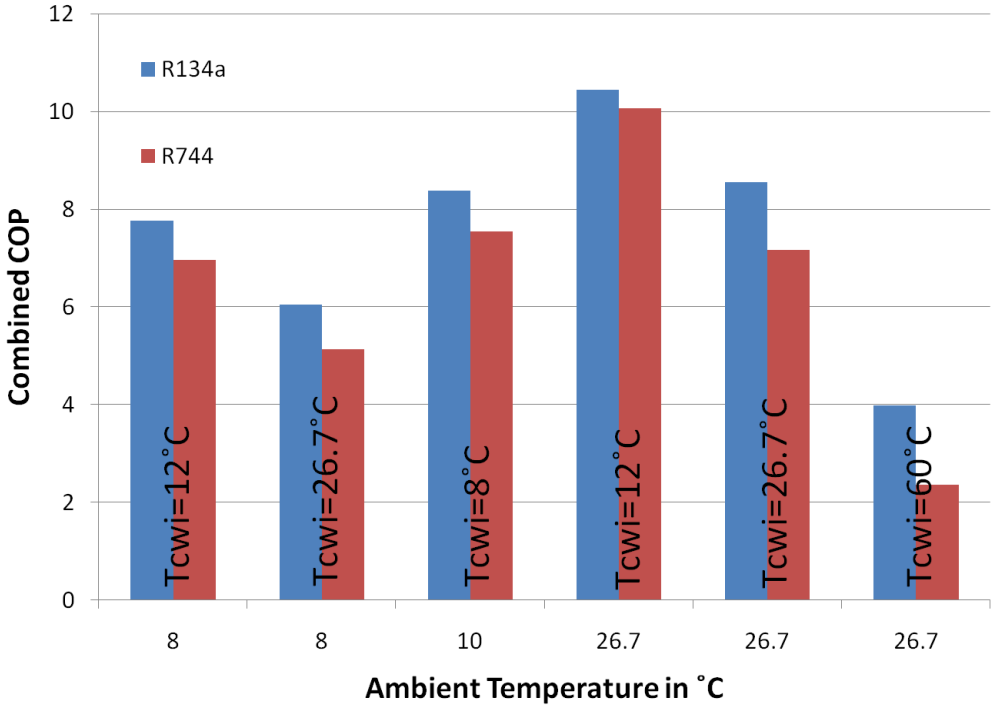

Figure 3-33: R134a vs. R744 Baseline Combined COP

A variation of the water flow rate was an important aspect of an ideal control strategy for the HPWH. Only investigating the rating condition of a water and ambient air inlet temperature of 26.7˚C at a water flow rate of 28 gallons per minute to achieve a temperature lift of 5 K was not representing the real operation requirements. When running the HPWH various situations and therefore demands of water temperatures and flow rates can be expected. Therefore a huge potential was expected in investigating the operation behavior of the HPWH at various conditions. The results can be seen in Figure 3-34.

All tests were accomplished at an ambient temperature of 26.7˚C. The water mass flow rate was varied at 28, 15.9, 6.4, 5.4, 4.7 and 4 gallons per minute. The lower water inlet temperature tests were done at 12˚C and the higher temperature tests were done at 50˚C. It became obvious that the linear COP trend decreased at higher temperature lifts and lower water mass flow rates respectively. The COP was also dependent on the water inlet temperature. At lower water inlet temperatures it decreased faster than at higher temperatures (50˚C) where lift had only a little effect on the COP.

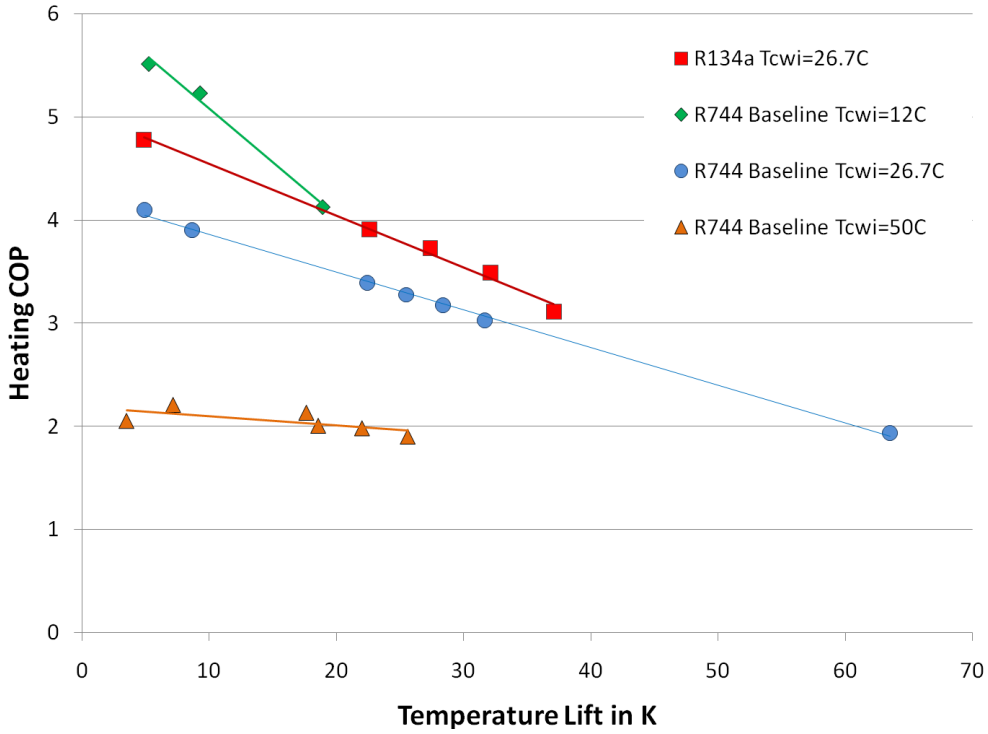

Figure 3-34: Heating COP vs. Temperature Lift

An additional condition was investigated at a water inlet temperature of 26.7˚C. At 1.6 gallons per minute a temperature lift of 63.5 K at a water outlet temperature of 91.2˚C was achieved. This high load condition showed the potential that R744 offered. Higher possible water outlet temperatures were reached in once through design of the HPWH compared to R134a. The R134a system would require additional electric heating as described starting at 81.7˚C water outlet temperature. Therefore a once through design of an R134a heat pump cycle to reach temperatures above 81.7˚C could not be realized due to a compressor discharge temperature limit of 107˚C. The comparison of the R134a and R744 water flow rate development can be seen in Figure 3-35.

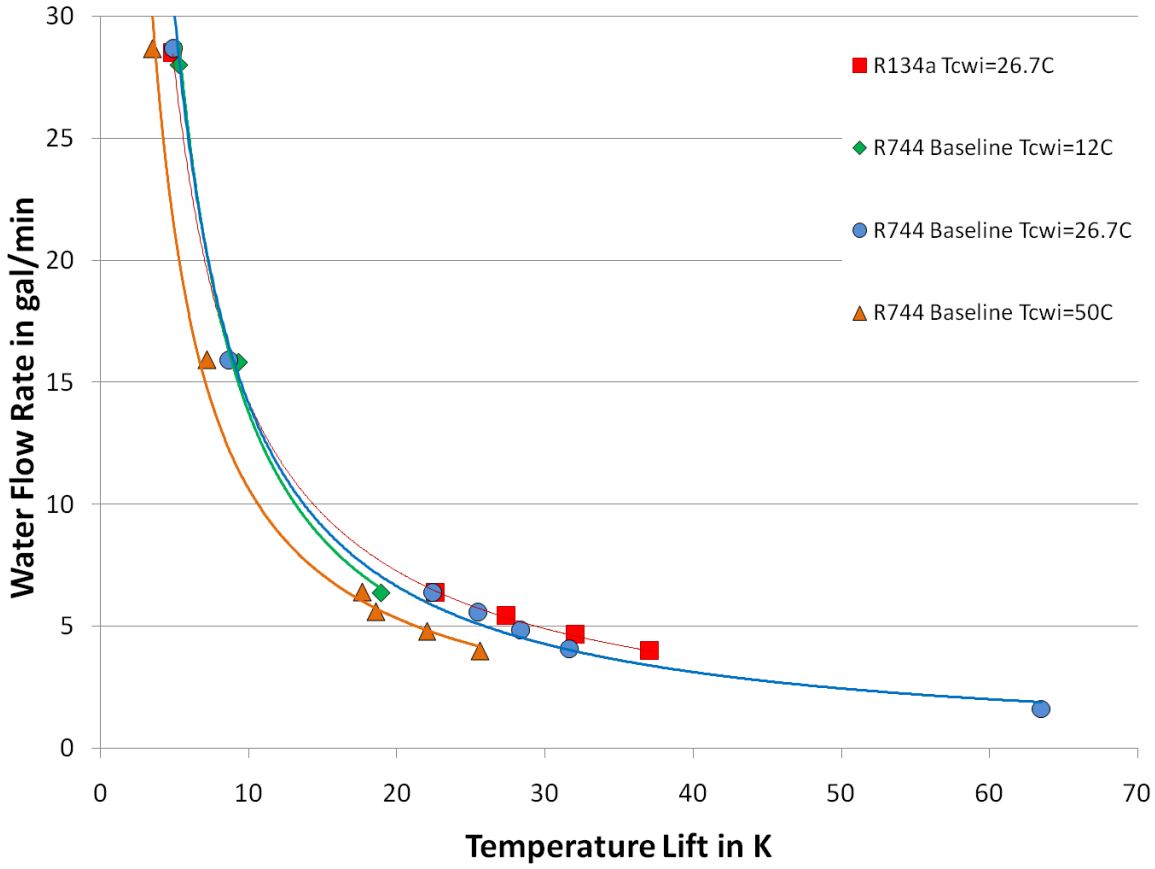

Figure 3-35: Water Flow Rate vs. Temperature Lift

The graph shows that the 12˚C water inlet condition matched the rating condition at higher water flow rates but differed at 6.4 gallons per minute. This difference in the possible temperature lifts increased for 50˚C water inlet temperature.

4 Next Generation R744 HPWH System development

In order to specify the necessary improvements to enhance the HPWH system performance the bottlenecks of the baseline R744 system were investigated. Therefore a data analysis of the R744 baseline tests was accomplished. The investigated parameters which were considered to be the most beneficial on the system performance are visualized in the following Figure 4-1.

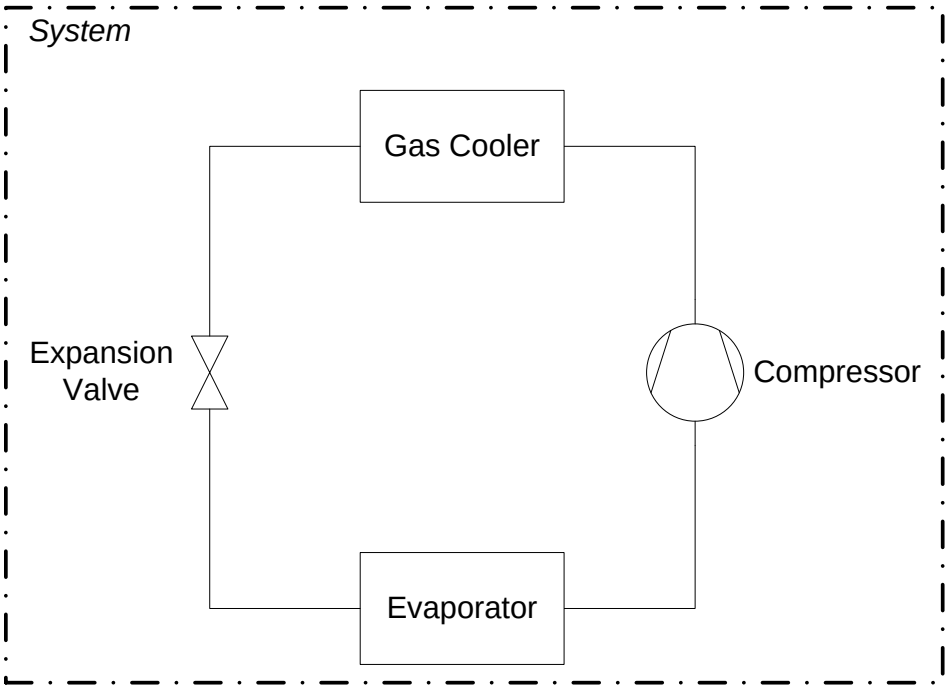

Figure 4-1: System schematic with investigated system improvement potentials

Beside the four main components of the HPWH compressor, gas cooler, expansion valve and evaporator the whole system was part of the optimization. On the component side there were different aspects that had to be considered:

Compressor The investigation of the compressor speed variation as well as the use of high efficiency motors was part of the optimization.

Heat Exchangers The gas cooler and evaporator have a certain efficiency regarding their ability to transfer heat. The characterizing parameter is the approach temperature difference which was optimized. Another aspect was the use

of an internal heat exchanger which was considered to provide a higher COP.

Expansion Valve The expansion device was changed and instead an ejector was used which allowed expansion work recovery.

System The improvement of the system was accomplished by using an enhanced control strategy. This contained the optimal strategy in heating water including parameters like water flow rate and desired temperature lift.

The bottlenecks of the system performance were determined by analyzing the data of the R744 baseline tests. The relevant aspects are described in the following paragraph.

On the heat exchanger side an important parameter in characterizing the efficiency was the approach temperature difference which should be minimized. The following Figure 4-2 visualizes the different definitions that are possible when talking about the approach temperature difference.

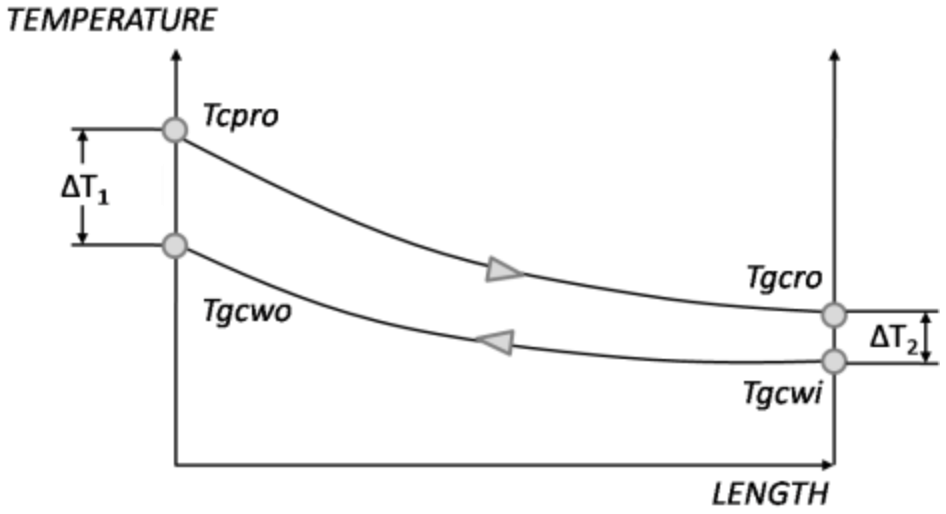

Figure 4-2: Approach temperature difference gas cooler

In regular refrigeration cycles the approach temperature difference is defined as the difference between the inlet of the coolant and the refrigerant outlet temperature. For the gas cooler of the system the refrigerant was the defining fluid. Therefore the approach of the R744 gas cooler outlet temperature to the coolant temperature was of special interest.

$$\Delta T_2 = T_{gcro} - T_{gcwi} \qquad (12)$$

This situation changed when looking at the HPWH. The water side and the possible heating of the water flow became more important. The relevant approach temperature difference was calculated between water outlet temperature and gas cooler inlet temperature.

$$\Delta T_1 = T_{cpro} - T_{gcwo} \qquad (13)$$

The results shown in Figure 4-3 visualize the determined approach temperature differences in the R744 baseline water variation tests with water inlet temperatures of 12˚C, 26.7˚C and 50˚C for the water side of the gas cooler.

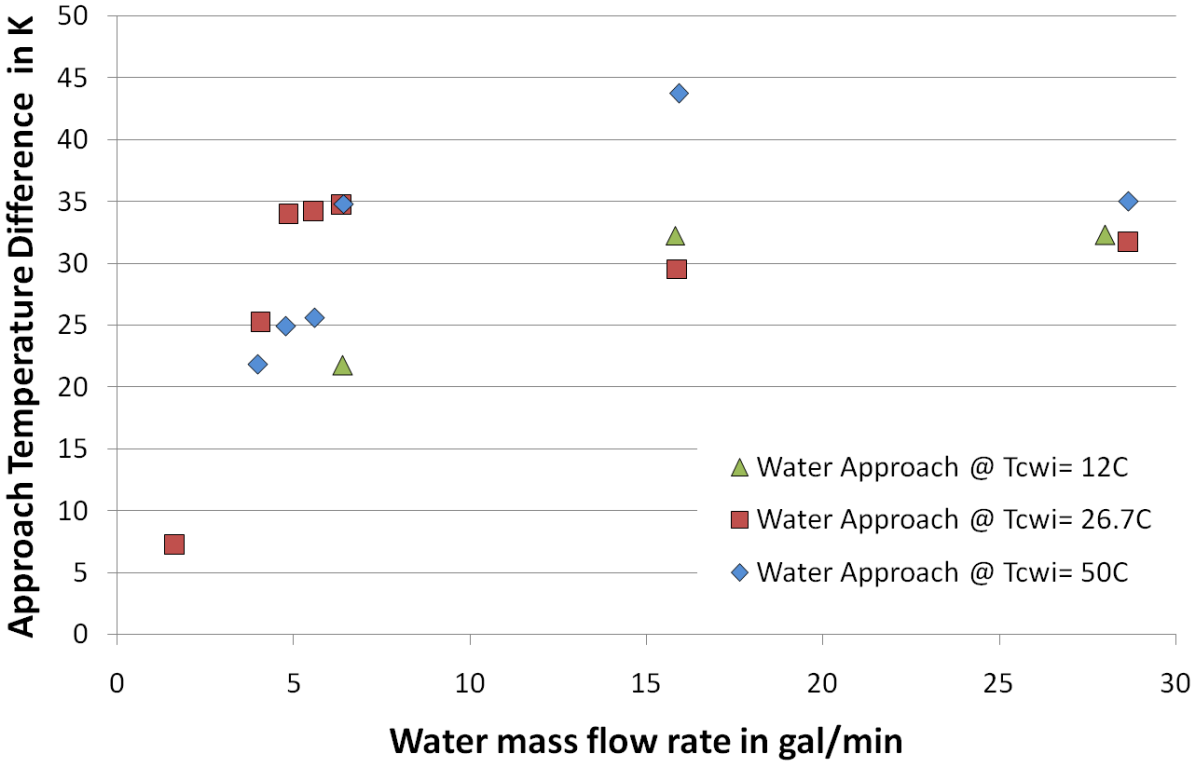

Figure 4-3: Approach temperature difference on the water side of the gas cooler

The approach temperature difference was increasing with increasing water inlet temperature. For the rating condition of 28 gallons per minute the approach temperature difference was between 32 K and 35 K for all three water inlet temperatures. This showed the potential of improvement on the gas cooler side.

The evaporator results for the refrigerant side are shown in Figure 4-4.

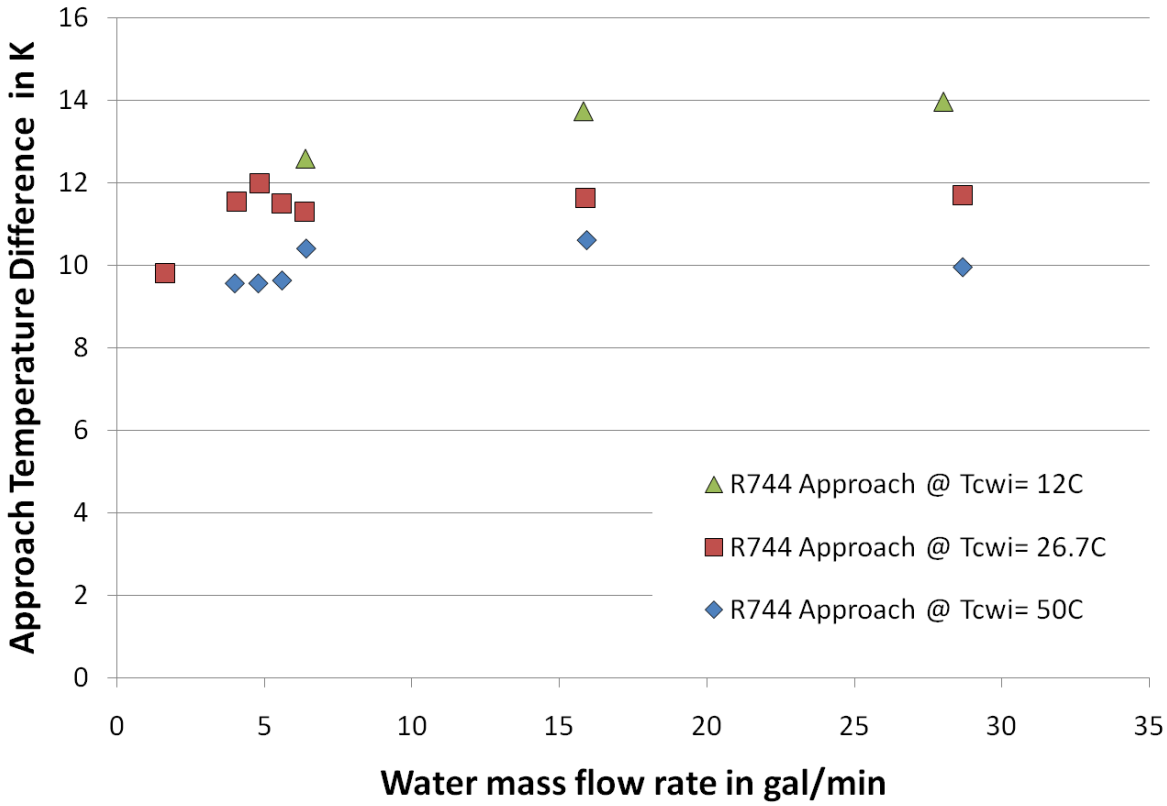

Figure 4-4: Approach temperature difference in the evaporator

It can be seen that the approach on the refrigerant side was between 9.5 K and 14 K throughout the conditions. This was caused by the constant air temperature of 26.7˚C that was used. The air flow rate through the evaporator was also kept constant. However the potential for minimizing the approach temperature was observed. Therefore an optimization of the gas cooler and evaporator was part of the improvement of the system efficiency.

4.1 Internal heat exchanger

The first aspect on the heat exchanger side was the investigation of the system improvement potential of an internal heat exchanger (IHX). A comparison of the system schematic of the HPWH with and without IHX and the corresponding pressure specific enthalpy diagram can be seen in Figure 4-5 and Figure 4-6.

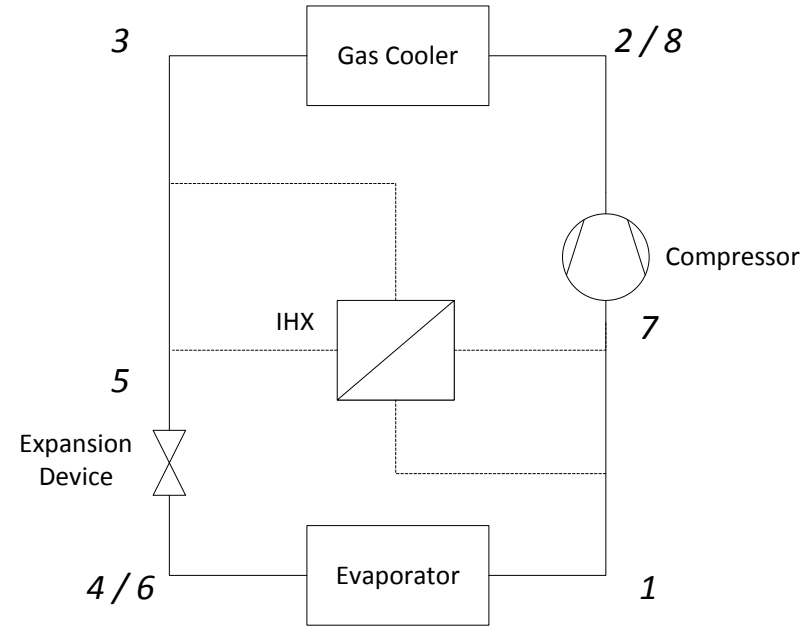

Figure 4-5: Vapor compression cycle with internal heat exchanger

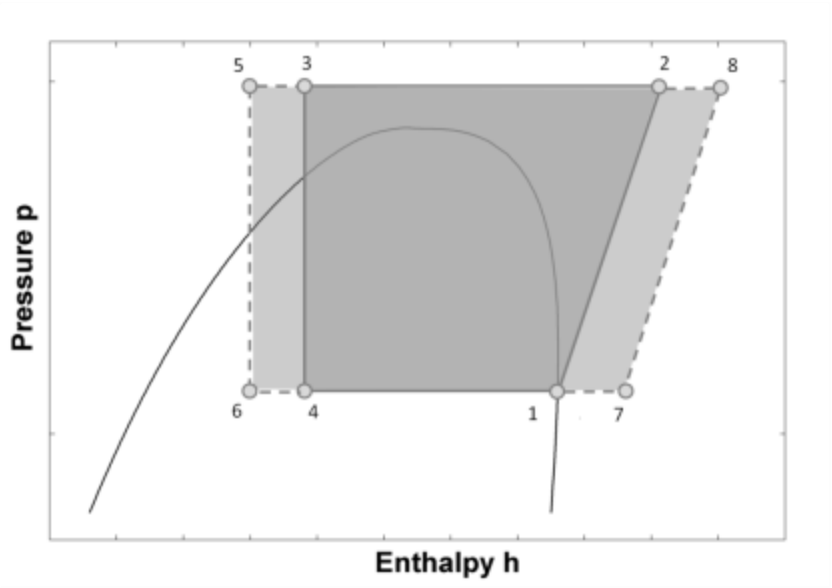

Figure 4-6: Ideal vapor compression cycle with (solid) and without (dashed) internal heat exchanger

The schematic in Figure 4-5 visualizes the changes between a conventional vapor compression cycle (solid lines, dark grey) and the enhanced one with IHX (dashed lines, light grey). It can be seen that the usage of an IHX enlarges the usable enthalpy difference on the high and low pressure side (heating and cooling). This can be realized by transferring heat from the hot high

pressure gas cooler discharge flow to the cold low pressure flow leaving the evaporator. This further sub cooling and super heating of the fluid on the high and low pressure side respectively has a beneficial influence on the system performance. It has to be pointed out that the mentioned processes are ideal. Therefore the behavior of the system in reality needs to be investigated and confirmed. The IHX that was used is a microchannel heat exchanger which is shown in Figure 4-7.

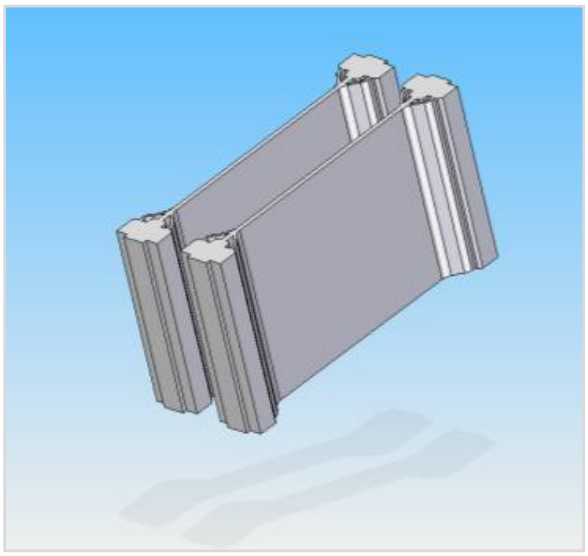

Figure 4-7: Model of Microchannel IHX

The first step in the optimization of the HPWH was the integration of this internal heat exchanger. The IHX consisted of two microchannel heat exchangers which were combined to provide sufficient capacity. The insulated heat exchangers and the assembled IHX set up are shown in Figure 4-8.

Figure 4-8: Internal heat exchanger with insulation (left) and mounted piping (right)

The insulation of the heat exchangers was used to minimize losses to the environment. For the piping, stainless steel tubing was used because of the high pressure levels that were reached when using R744 as a refrigerant. Ball valves were used to bypass one of the two heat exchangers. This offered more options during operation and made it possible to vary the effectiveness and capacity if necessary. The heat exchangers were placed in the HPWH housing above the compressor. A frame supported the IHX assembly and protected it from strong vibration which could have caused leakage and damage to the component. Figure 4-9 and Figure 4-10 show the HPWH before and after the installation of the IHX assembly.

Figure 4-9: HPWH without IHX

Figure 4-10: HPWH with installed IHX

The modification of the baseline system for IHX operation required the installation of additional pressure and temperature sensors in order to determine the effect of the IHX on the system performance. Therefore two pressure transducers and thermocouples were installed at the inlet of the electronic expansion valve and the inlet of the compressor. The instrumented system schematic of the HPWH with the water and glycol cycle is shown in Figure 4-11.

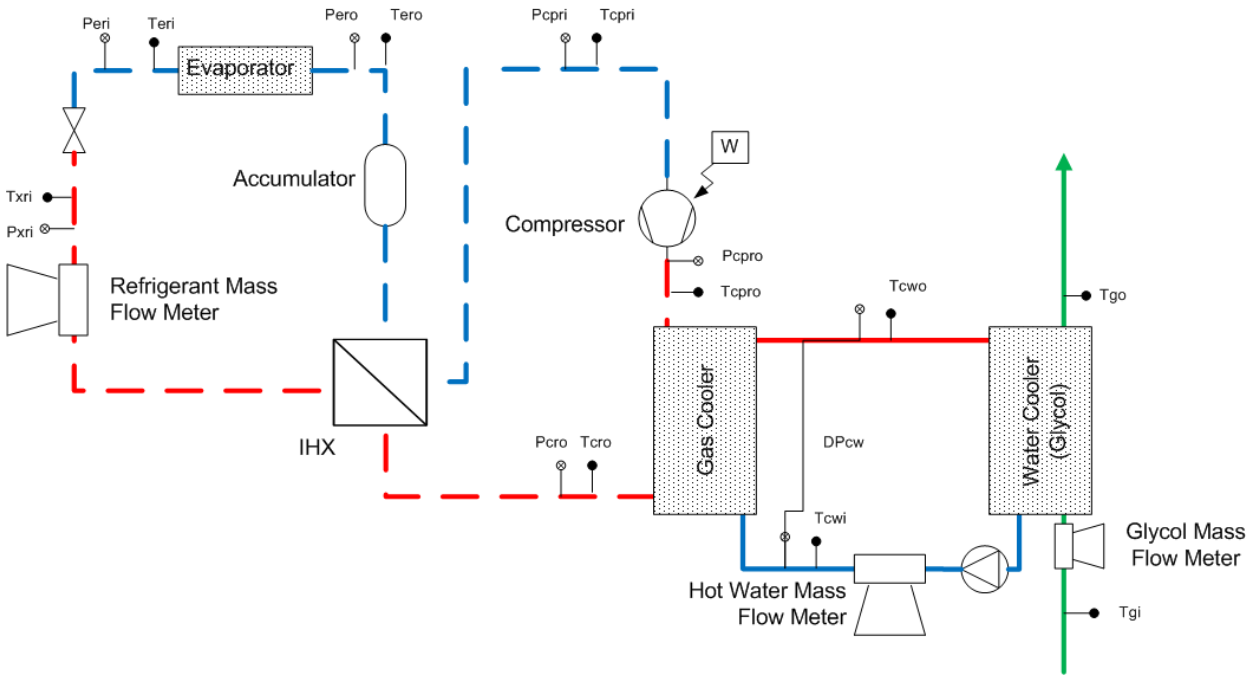

Figure 4-11: System schematic of HPWH with IHX

The IHX cycle differed from the baseline system in the additional measurement ports for the compressor inlet Pcpri/ Tcpri and the expansion valve inlet Pxri/ Txri respectively. The IHX transferred heat from the liquid line on the high pressure side to the suction line on the low pressure side of the cycle. It consisted of two microchannel heat exchangers that were combined to provide sufficient capacity. The detailed view of the IHX set-up (Figure 4-12) describes the design of the component.

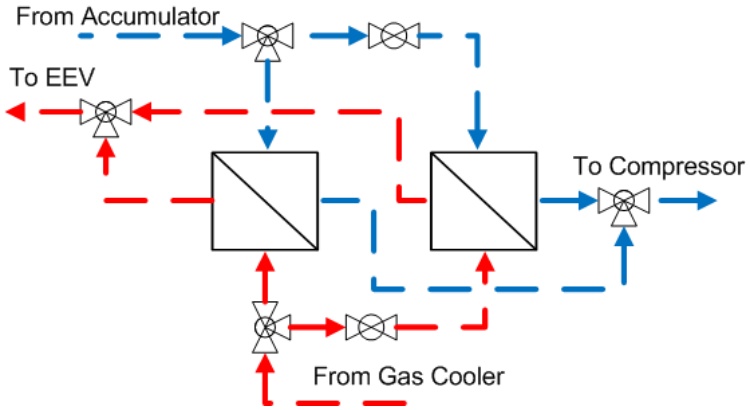

Figure 4-12: Detailed view of IHX assembly

The use of ball valves enabled the operator to regulate the capacity in a range of 50 to 100 %. When the valves were open, both IHX were used for the internal heat exchange. When the valves were closed, only one heat exchanger was used. The instrumented IHX with the pressure and temperature ports as well as the ball valves is shown in Figure 4-13.

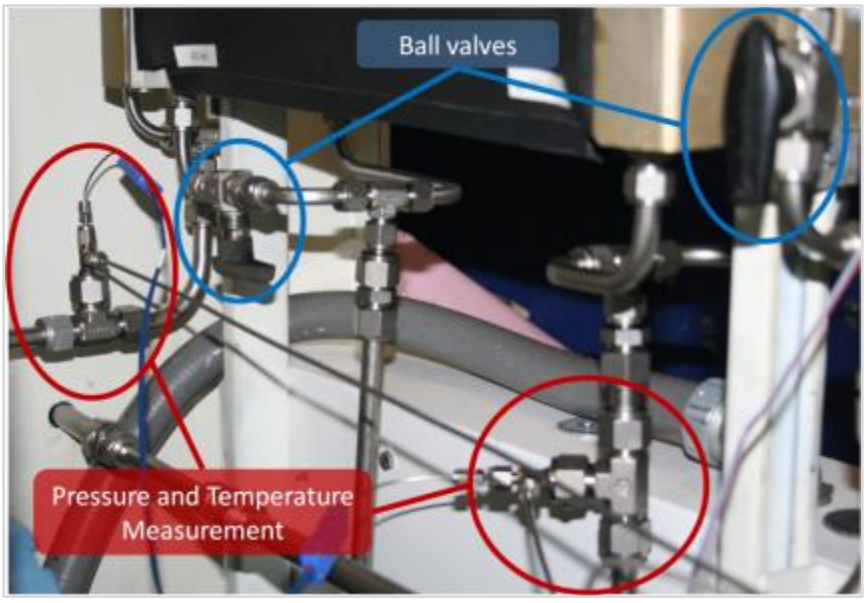

Figure 4-13: Measurement ports and valves in IHX assembly

The calibration of the additional pressure transducers Pxri and Pcpri was done according to their operating range. The resulting calibration curves are shown in Figure 4-14 and Figure 4-15.

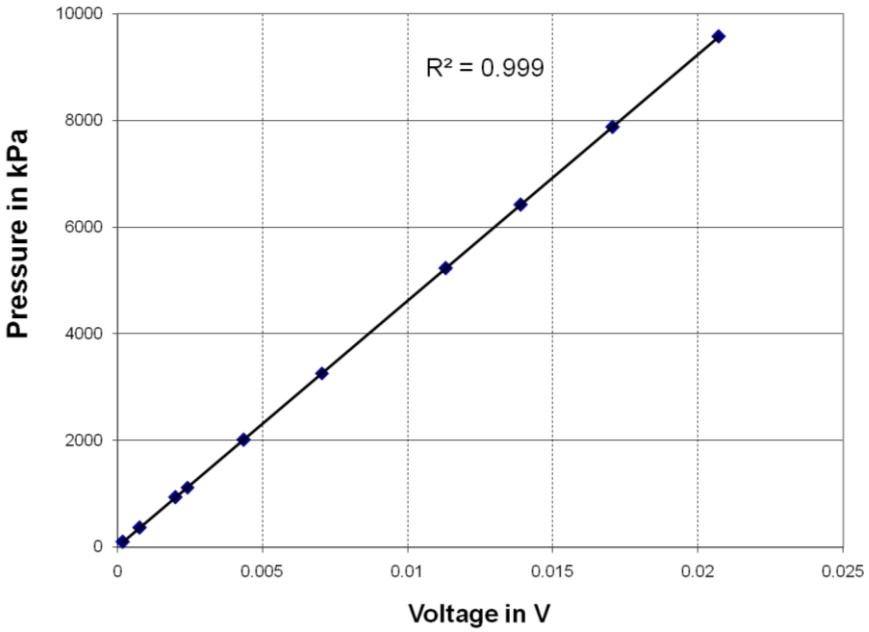

Figure 4-14: Calibration curve for expansion valve inlet pressure transducer

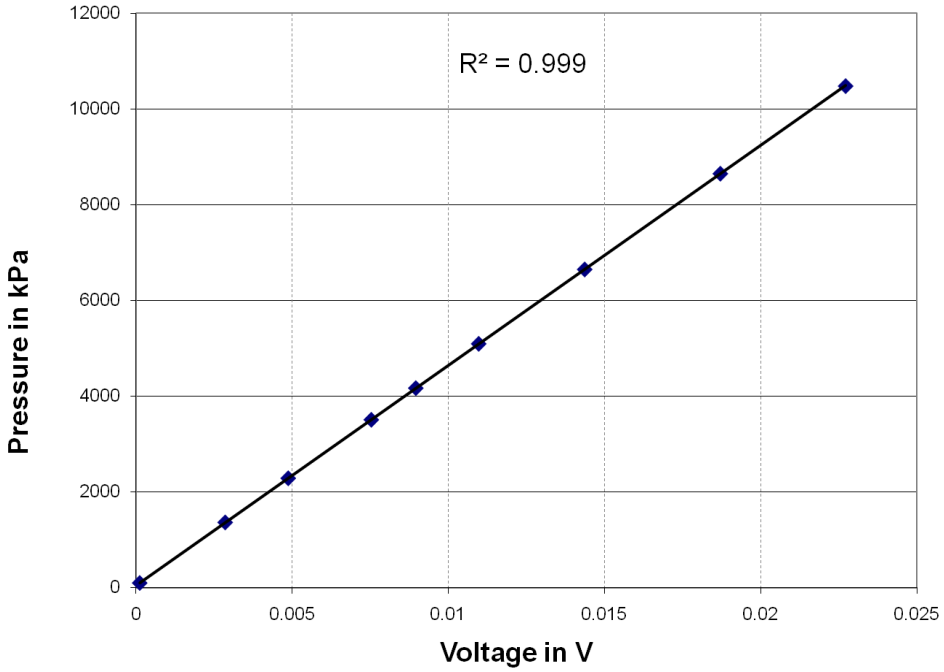

Figure 4-15: Calibration curve for compressor inlet pressure transducer

After the installation of the sensors an inline filter was installed to clean out any dirt that may have gotten into the system. The system was run for three hours and afterwards the filter was replaced with tubing. The results of the system cleaning showed just minor contamination (Figure 4-16).

Figure 4-16: Inline filter after 3h system run

The change from baseline to IHX system required modifications of the data acquisition as well as the data processing files. The additional component was integrated into the data analysis routine to determine its influence on the system performance. The online cycle visualization in the pressure- specific enthalpy diagram as an example of the modified state points is shown in Figure 4-17.

The initial shakedown testing showed good results of the functionality of the IHX and the pressure and temperature measurement.

The test results all were within an error band of +/- 5% which showed a good reliability of the measurements. A continuous check of the balances was done for all tests to verify the test quality.

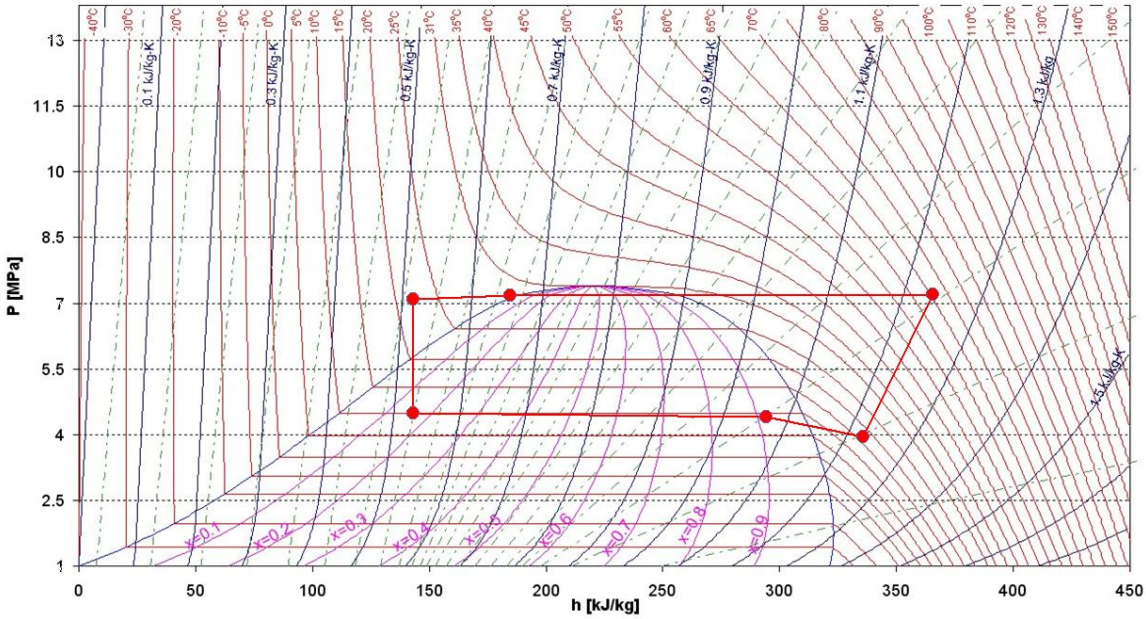

Figure 4-17: R744 pressure- specific enthalpy diagram of HPWH with IHX

In order to obtain a comparison between R134a, R744 baseline and R744 IHX tests the initial shakedown tests were done at a water and air inlet temperature of 26.7˚C with varying the water flow rate. The resulting temperature lift of the water through the condenser (R134a) and gas cooler (R744) of the system is compared in Figure 4-18. The almost matching curves for the three system concepts confirmed the well chosen components for a comparison between the systems. Especially at the rating condition of 28 gallons per minute all three systems matched very well.

The comparison of the heating COP's for the three systems gives more information of the system performances (Figure 4-19 and Figure 4-20). Therefore the heating COP was plotted as a function of the temperature lift and water flow rate respectively. It can be seen that the R134a performance was still slightly better compared to the R744 baseline and IHX system for lower temperature lifts. However the advantage of R744 being able to reach very high water outlet temperatures became obvious. The IHX also seemed to have a crossover point with R134a at higher temperature lifts.

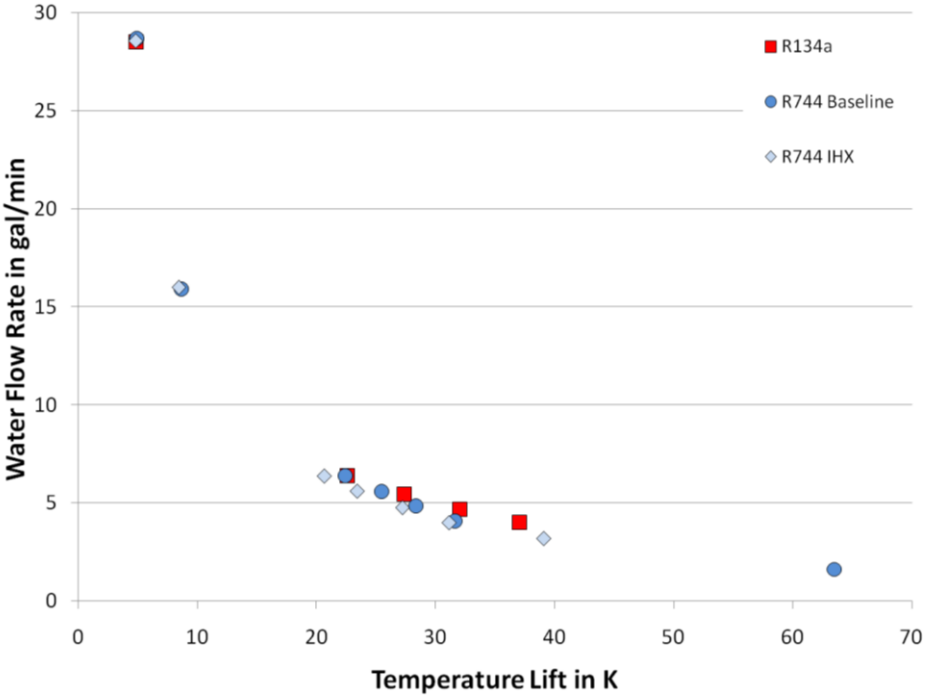

Figure 4-18: Water flow rate versus temperature lift

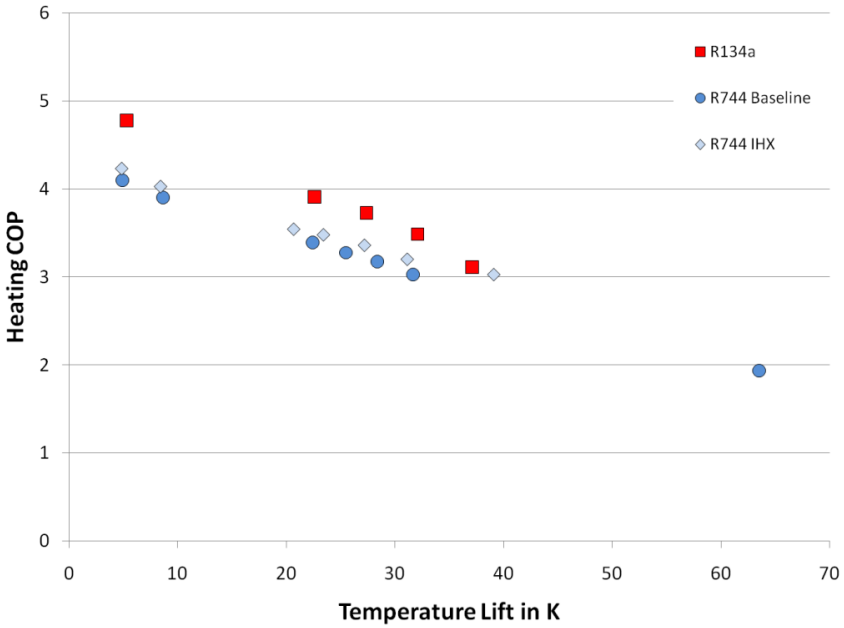

Figure 4-19: Heating COP versus Temperature lift

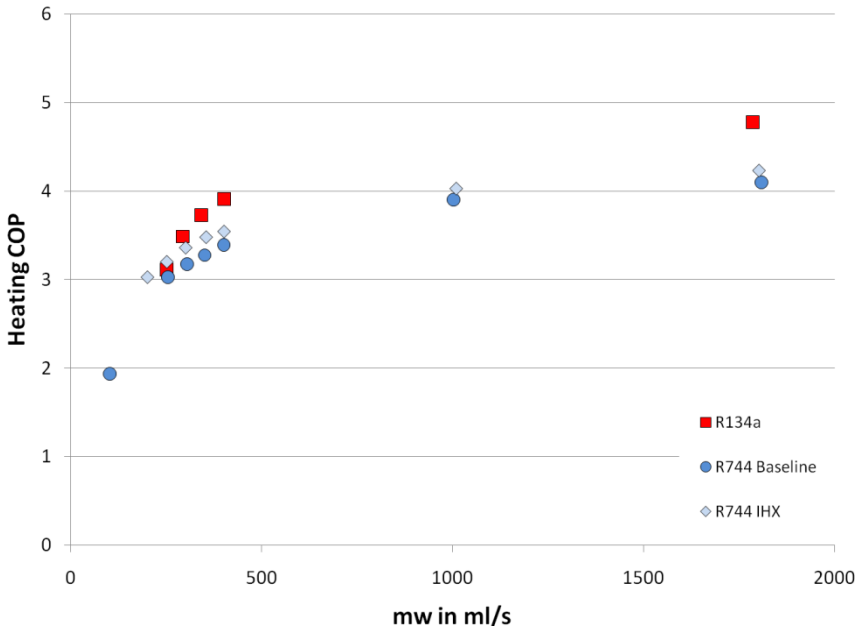

Figure 4-20: Heating COP versus water mass flow rate

The first results showed the potential improvement that was reached when using an internal heat exchanger in the next generation R744 HPWH. Further investigations were accomplished to get a better idea of the IHX system performance and to have a comparison with the R744 baseline and R134a results (Figure 4-21 to Figure 4-24). Several different water and air inlet conditions were investigated at the rating water mass flow rate of 28 gallons per minute. The investigated conditions are summarized in Table 4-1.

Table 4-1: R744 IHX test conditions

Water inlet temperature in ˚C	12	26.7	8	12	26.7	60
Ambient air temperature in ˚C	8	8	10	26.7	26.7	26.7

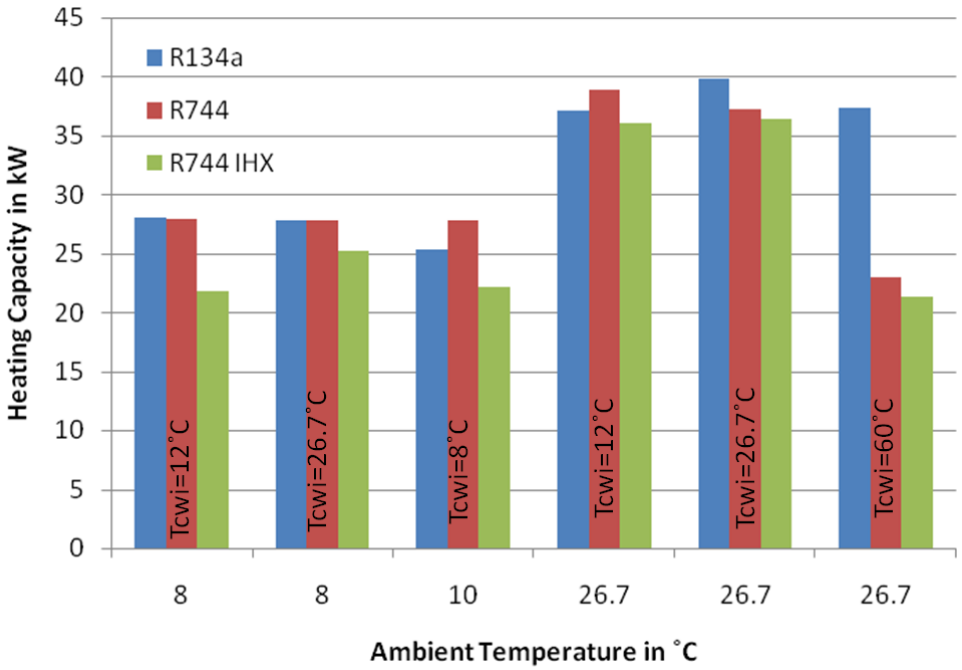

Figure 4-21: Heating capacity versus ambient temperature

It was pointed out earlier that R744 can reach or even exceed the R134a performance in several conditions. When looking at the next step in the optimization process with the R744 system with IHX it became obvious that the heating capacity was the lowest of the three systems throughout the test conditions even though the IHX made bigger enthalpy differences possible (Figure 4-21). The tests with IHX were done with an adjusted evaporator outlet quality on the refrigerant side of 0.95. This was done to have a good compromise between the necessary superheat and the discharge temperature of the compressor. The superheated state was used to prevent the compressor from sucking liquid refrigerant droplets which could have damaged the compressor due to their incompressibility. The lower refrigerant discharge temperature reduced the compressor work which was beneficial for an optimum COP. Therefore limiting the evaporator exit quality was a good approach to prevent liquid refrigerant entering the compressor but at the same time the refrigerant mass flow rate decreased which compensated the gain in enthalpy difference.

The ratio of heating capacity and necessary power input results in the heating COP which is shown in Figure 4-22.

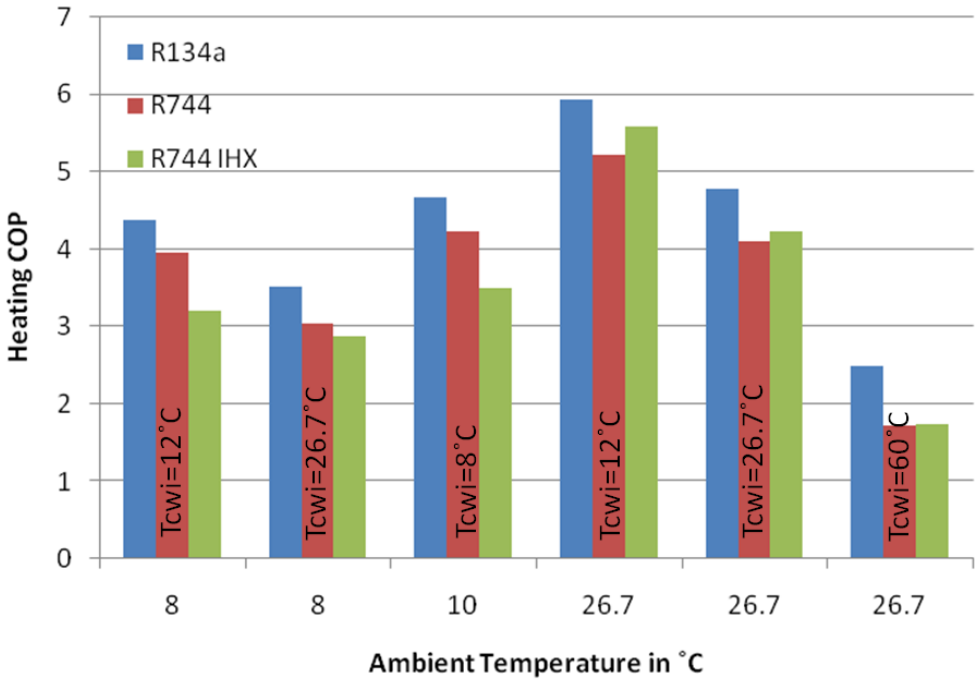

Figure 4-22: Heating COP versus ambient temperature

It can be seen that at lower ambient temperatures (8˚C, 10˚C) R134a showed the best performance while the IHX had the lowest COP. This behavior changed when going to higher ambient temperatures. The COP of the IHX system exceeded the system performance of the baseline system for all three water inlet temperatures. This showed that the loss in capacity was compensated by the savings that were achieved on the compressor side of the system which resulted in a better overall heating COP.

A comparison of the cooling capacities of the three systems is shown in Figure 4-23.

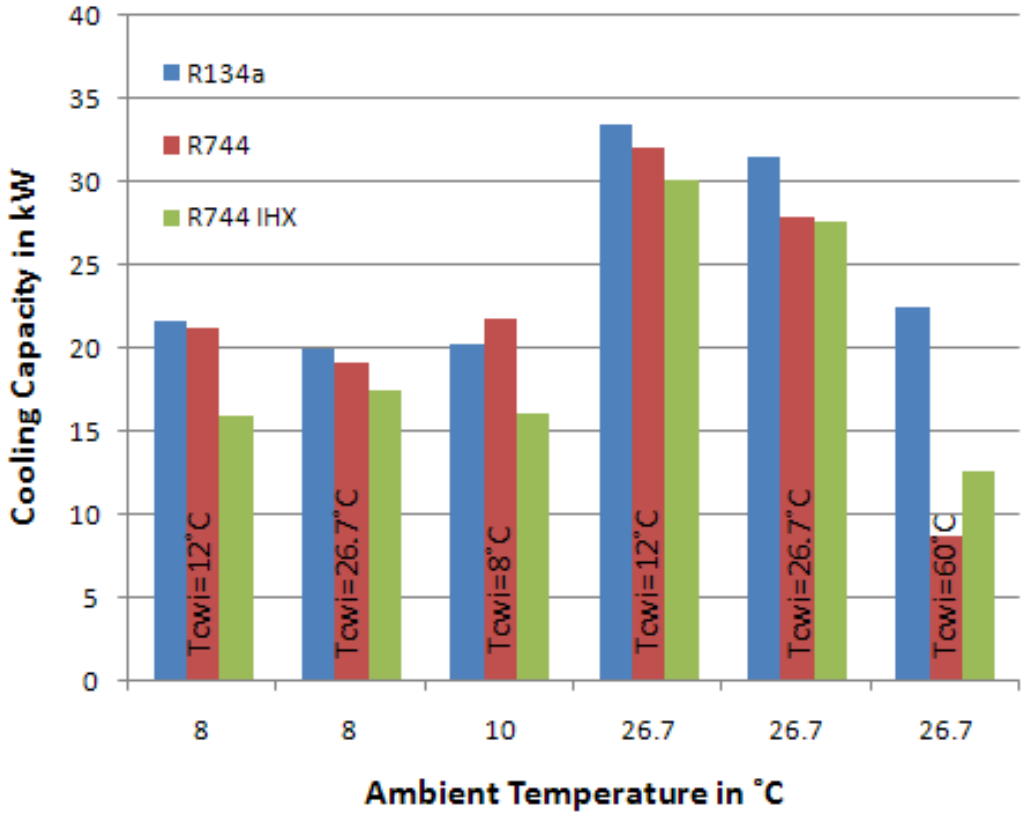

Figure 4-23: Cooling capacity versus ambient temperature

The same trend that was described for the IHX for the heating capacity was seen for the cooling capacity. The capacity was lower due to a lower refrigerant mass flow rate even though the enthalpy difference was improved. An improvement was seen at higher ambient (26.7˚C) and water inlet temperatures (60˚C).

A combination of both useful outputs of the system divided by the compressor power resulted in the combined COP which gave an idea of the overall system performance which is shown in Figure 4-24.

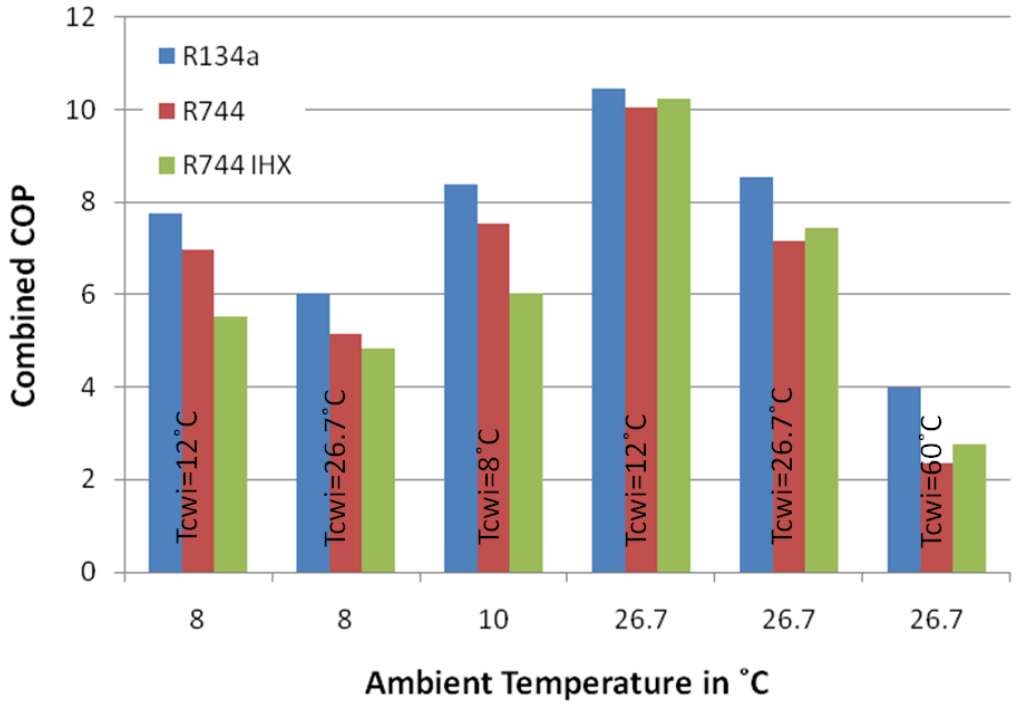

Figure 4-24: Combined COP versus ambient temperature

The goal of the optimization to reach a combined COP of 8 was reached for R744 baseline and IHX at 12˚C water and 26.7˚C air inlet temperatures. The performance of the IHX system was the lowest for low ambient temperatures (8˚C and 10˚C) but exceeded the R744 baseline results at higher ambient temperatures (26.7˚C).

Additional investigations were done for varying water flow rates at low (12˚C) and high (50˚C) water inlet temperatures. These investigations were useful for the development of the control strategy of the HPWH in order to provide the best performance in heating water. The results for the water flow rate versus the temperature lift and the heating COP versus the temperature lift are shown in Figure 4-25 and Figure 4-26 respectively.

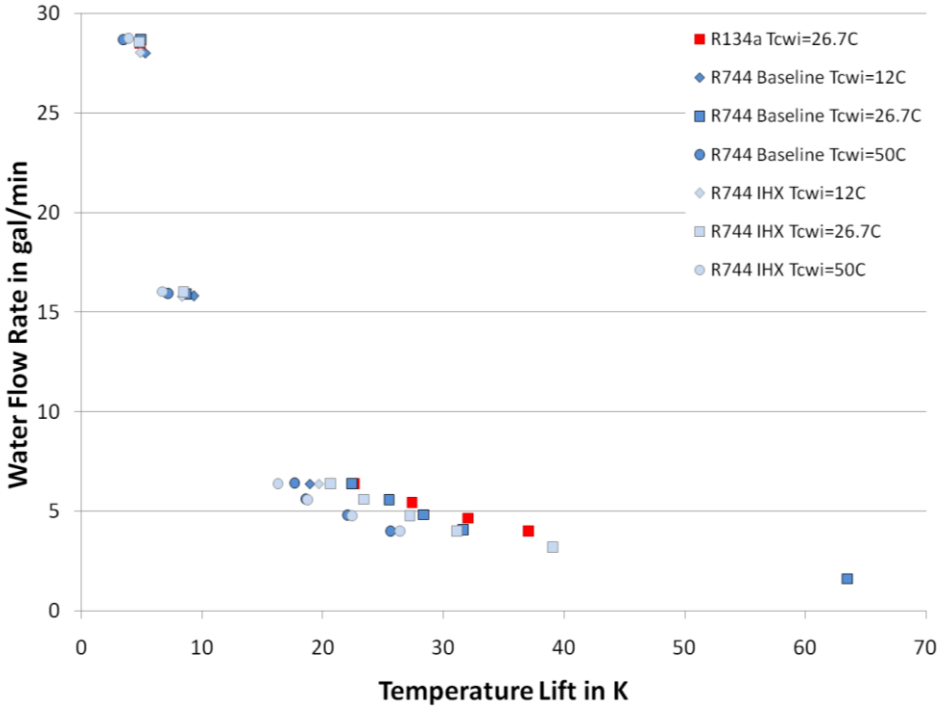

Figure 4-25: Water mass flow rate versus temperature lift

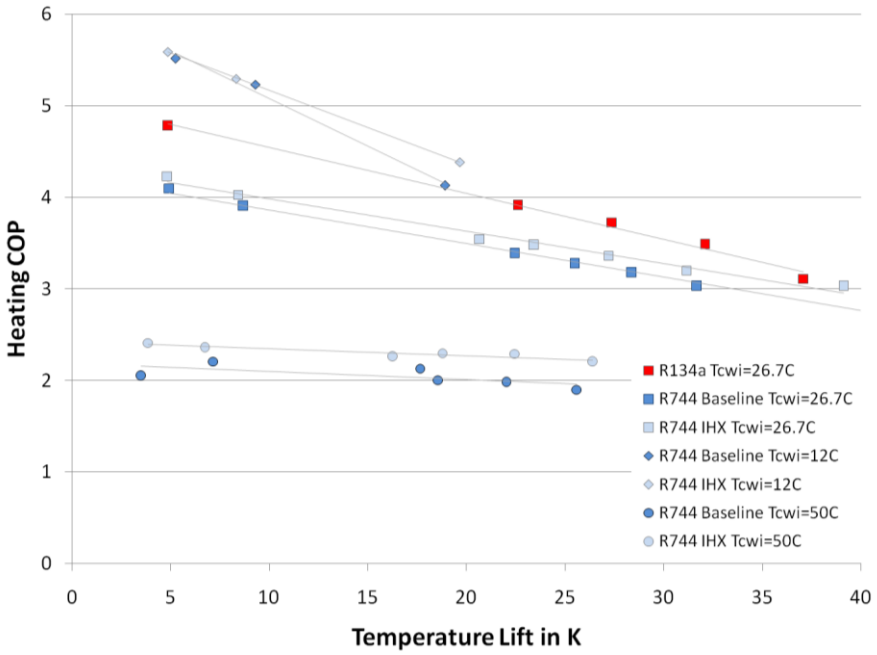

Figure 4-26: Heating COP versus temperature lift

The water flow rate variation versus the temperature lift plot shows the well chosen components of the two systems which allowed a good comparison. Further information is provided in the plot of the heating COP versus the temperature lift. It can be seen that the COP decreased faster at lower water inlet temperatures. At high water inlet temperatures the lift had just a little effect on the COP. For the water variation at a water inlet temperature of 26.7˚C a crossover point between IHX and R134a was seen. This showed the potential of the IHX system compared to the R134a system.

Additional investigations were accomplished to get more information about the behavior of the IHX system at higher water temperature lifts. Water flow rates of 1.95 gallons per minute and 2.3 gallons per minute were used to increase the achievable water outlet temperature. Water and air inlet temperatures of 26.7˚C were used for the tests. The results for the heating COP and water flow rate versus the temperature lift are shown in Figure 4-27 and Figure 4-28.

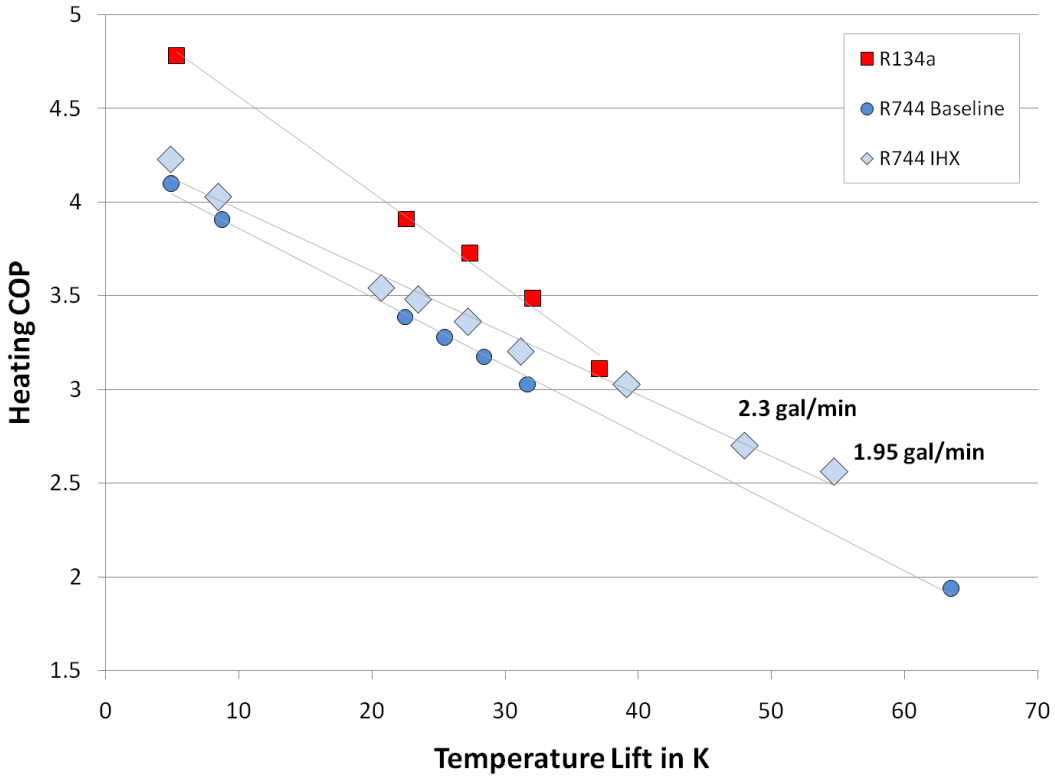

Figure 4-27: Heating COP versus Temperature lift

It can be seen that the results line up well with the test results that were recorded before. Both data points agree well with the linear curve fit that is used to describe the behavior of the IHX

system. With the additional points it also can be confirmed that there was a crossover point between R134a and the R744 IHX system. This showed that at higher temperature lifts the IHX HPWH had a better performance than the R134a system. It also can be pointed out that higher temperature lifts had a minor reducing impact on the COP compared to the R744 baseline system.

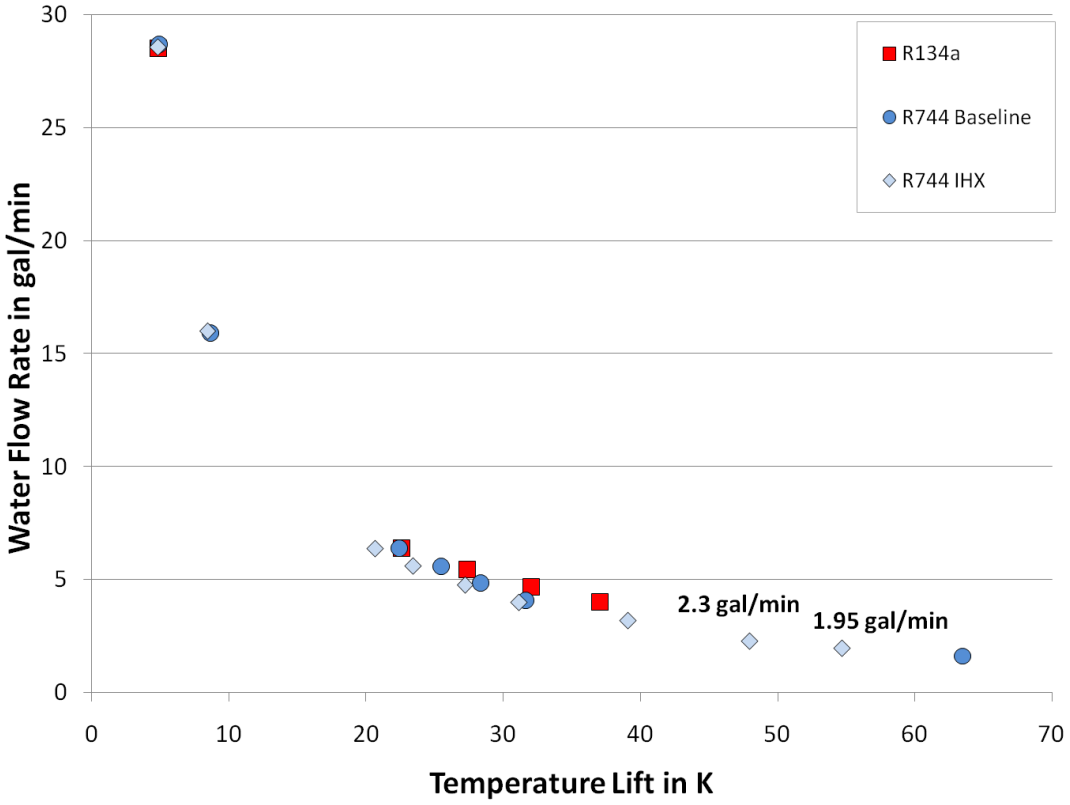

Figure 4-28: Water flow rate versus temperature lift

The visualization of the water flow rate versus the temperature lift confirmed the good accordance with the earlier test results.

With the experimental test results curve fits were generated to describe the development of the characterizing parameters with extrapolated data. Those curve fits made it possible to get an idea of the power consumption of each system and allow making a comparison between the three investigated development steps. This investigation concentrated on the potential energy savings that were achieved when using an R134a heat pump instead of electrical resistance heating. It was pointed out that R134a was limited in its maximum compressor outlet temperature of 107˚C or a maximum water outlet temperature of 81.7˚C in heat pump operation

respectively. Therefore water outlet temperatures of up to 95˚C were not reachable in heat pump mode. Additional electrical resistance heating was necessary to make up the gap between 81.7˚C and the desired water outlet temperature. Even though those restrictions had to be taken into account possible energy savings between 70% at 60˚C water outlet temperature and 38% at 95˚C in hybrid operation of combined heat pump and resistance heating were possible.

Further investigations were accomplished with the integration of the R744 baseline and the R744 IHX system. The results can be seen in Figure 4-31 to Figure 4-33.

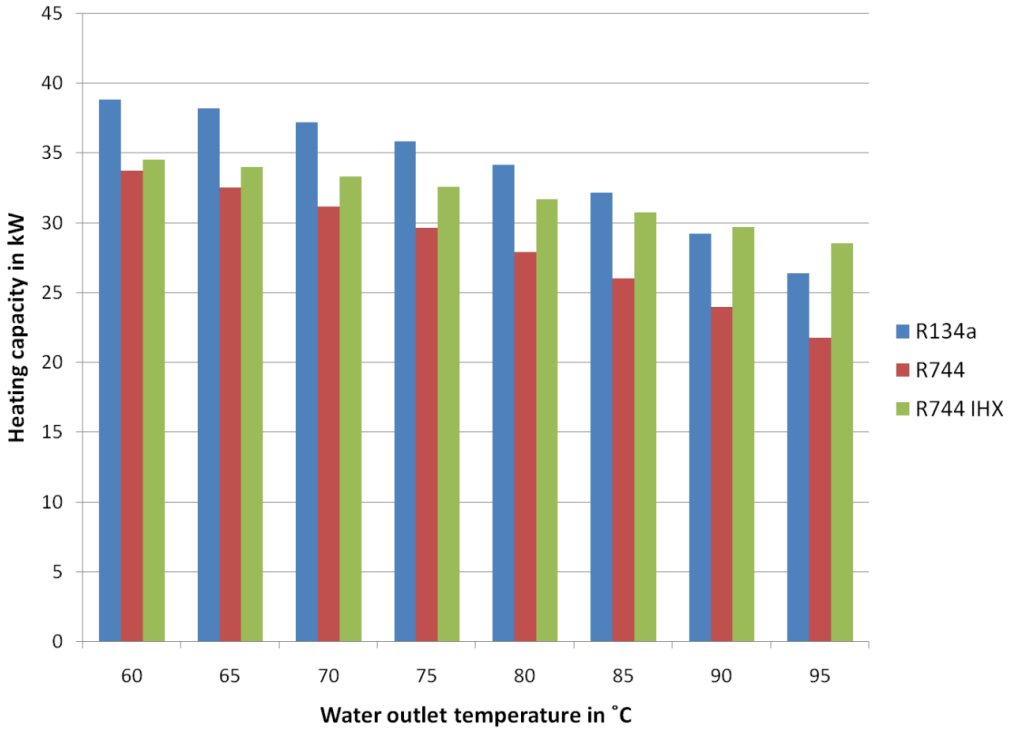

Figure 4-29: Heating capacity versus water outlet temperature

The development of the heating capacity (Figure 4-29) shows that the R744 system had a consistently lower heating capacity compared to the other two systems. Between the R134a and the IHX system a crossover were seen. Below 90˚C water outlet temperature R134a showed a better performance while going to higher water outlet temperatures the IHX system can provide higher heating capacities.

The heat pump power draw of the systems represents the power consumption of the HPWH containing compressor and system blower (Figure 4-30). The R134a system showed lower

power consumption at water outlet temperatures below 65˚C. At higher temperatures which are investigated in this graph the R744 and R744 IHX systems had lower power consumption. Even though at water outlet temperatures below 60˚C the IHX had higher power draw it can be seen that between 60˚C and 95˚C the IHX system showed the lowest power consumption.

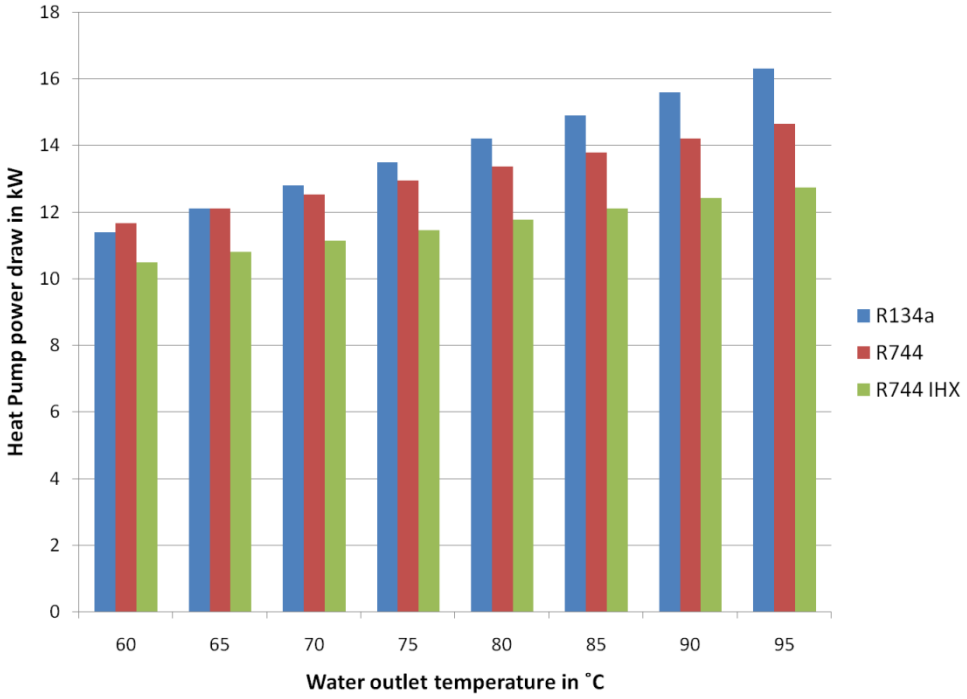

Figure 4-30: Power draw versus water outlet temperature

The combination of the heating capacity and the necessary power consumption of the system form the heating COP which characterizes the overall system performance (Figure 4-31). The R744 system showed the lowest performance throughout the investigated water outlet temperatures. Even though the IHX system had a low heating capacity the overall heating COP was higher especially at higher water outlet temperatures.

With the extrapolated information generated from experimental results the energy consumption for heating water was determined. The calculations were done for 500 gallons of water with an inlet temperature of 26.7˚C. The heating process was done in once through design to the desired water outlet temperature. The results can be seen in Figure 4-32.

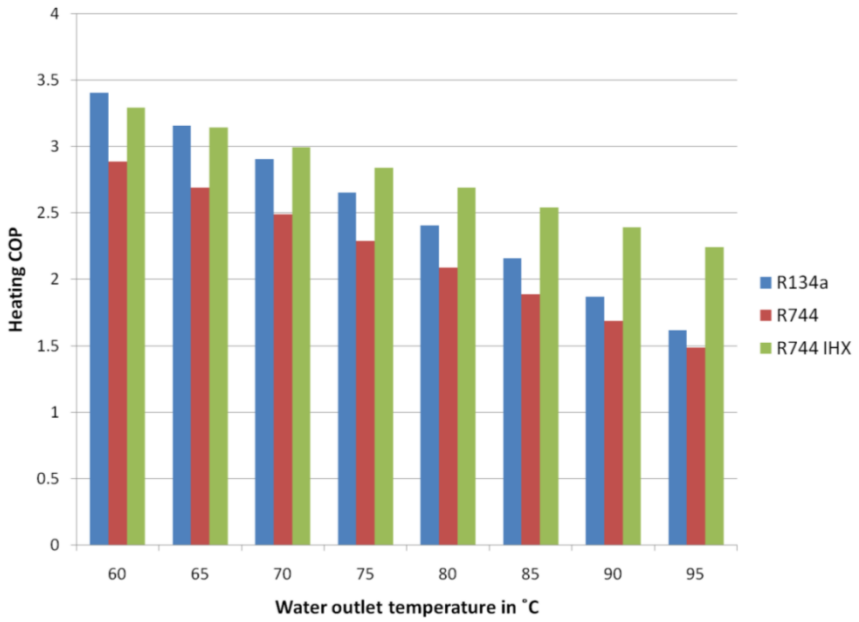

Figure 4-31: Heating COP versus water outlet temperature

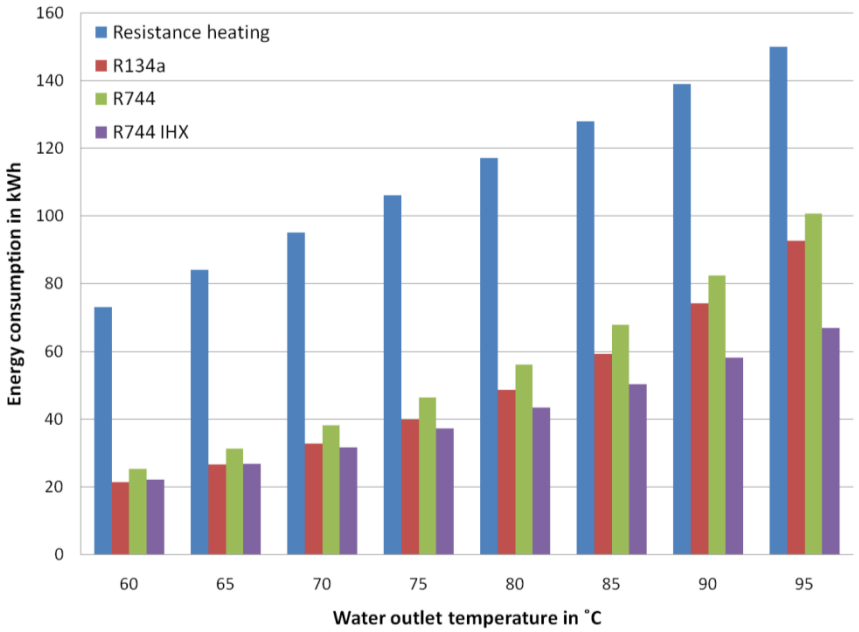

Figure 4-32: Energy consumption versus water outlet temperature

The comparison was done for resistance heating and the three heat pump systems. The resistance heating had a linear development based on its COP of 1 which means 100% of the power consumption was used for heating up the water. The heat pump systems show

exponential curves that were based on the extrapolated data. The R744 system needed the most energy for heating water among the heat pump systems. While having almost the same power consumption at lower water outlet temperatures the R134a and the IHX system diverge at higher water outlet temperatures. The IHX system showed the lowest energy consumption. With these data a comparison of the possible savings compared to resistance heating was accomplished (Figure 4-33).

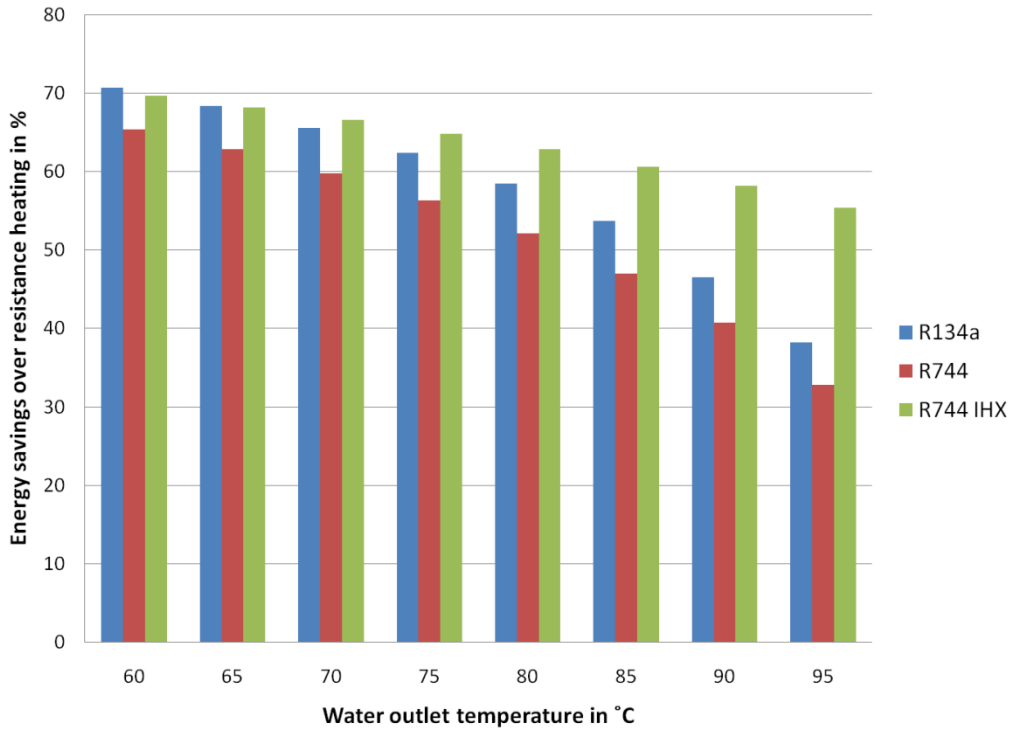

Figure 4-33: Energy savings over resistance heating versus water outlet temperature

It is shown that the R134a system had energy savings between 70% and 38% for water outlet temperatures of 60˚C and 95˚C respectively. The R744 system had the lowest energy savings over resistance heating between 65% and 33%. The IHX system showed lower performance at 60˚C compared to R134a and the same savings at 65˚C. At higher water outlet temperatures between 70˚C and 95˚C with possible savings of 66% and 55% respectively the IHX system showed the best performance.

4.2 IHX Bypass

The internal heat exchanger tests did not show the COP and especially capacity improvements that were anticipated. Therefore the baseline and IHX data were analyzed and compared by visualizing the cycles in the pressure specific enthalpy diagram (Figure 4-34).

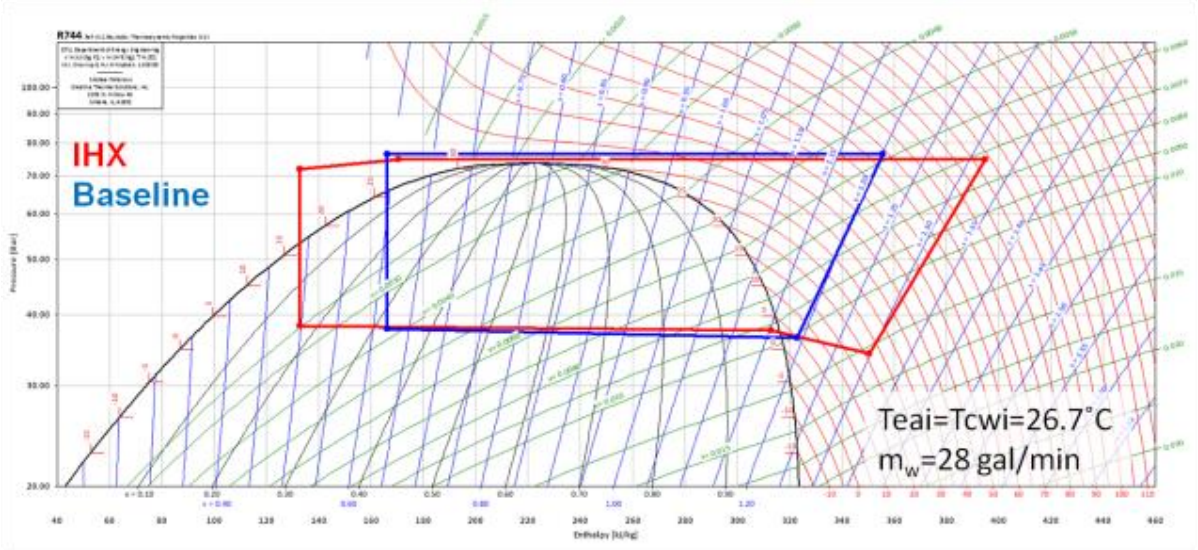

Figure 4-34: Comparison of R744 baseline and IHX system

The comparison of the two system cycles was done at the representative rating condition with a water mass flow rate of 28 gallons per minute at a water and air inlet temperature of 26.7˚C. It can be seen that both cycles almost had the same high and low pressure levels. The IHX cycle showed larger specific capacities. The heating capacity was increased due to the higher superheat at the compressor inlet which resulted in a higher compressor discharge temperature. Since both cycles almost had the same gas cooler exit temperatures the specific heating capacity was much larger. The specific cooling capacity also increased caused by the higher sub cooling and therefore lower evaporator inlet quality. Further information about the cycles can be observed when looking at the absolute performance values (
Table 4-2).

The heating capacity of the IHX system was even lower compared to the baseline system. The COP was practically the same. As described earlier the compressor discharge temperature was higher because of the higher superheat. The reason for the lower capacities was the refrigerant mass flow rate which was 19% lower compared to the baseline system. Even though the

enthalpy differences for heating and cooling were bigger this gain was negated by the low refrigerant mass flow rate.

Table 4-2: Comparison of R744 baseline and IHX system

	IHX	Baseline
Heating capacity in kW	35.53	36.23
Heating COP	3.99	3.98
Compressor discharge Temperature in ˚C	87.82	63.68
Refrigerant mass flow rate in g/s	156.6	193.2

As a next step of the modification of the HPWH bypasses were installed. This offered more flexibility when running the system. On the one hand, the choice between a system with or without IHX was given by bypassing the component. On the other hand, the effectiveness of the IHX was varied by opening the bypass and therefore varying the IHX capacity. Also the relatively high pressure drop on the low pressure side of the system was reduced and the refrigerant mass flow rate was increased.

The system schematic of the HPWH with additional bypasses on the high and low pressure side is shown in Figure 4-35.

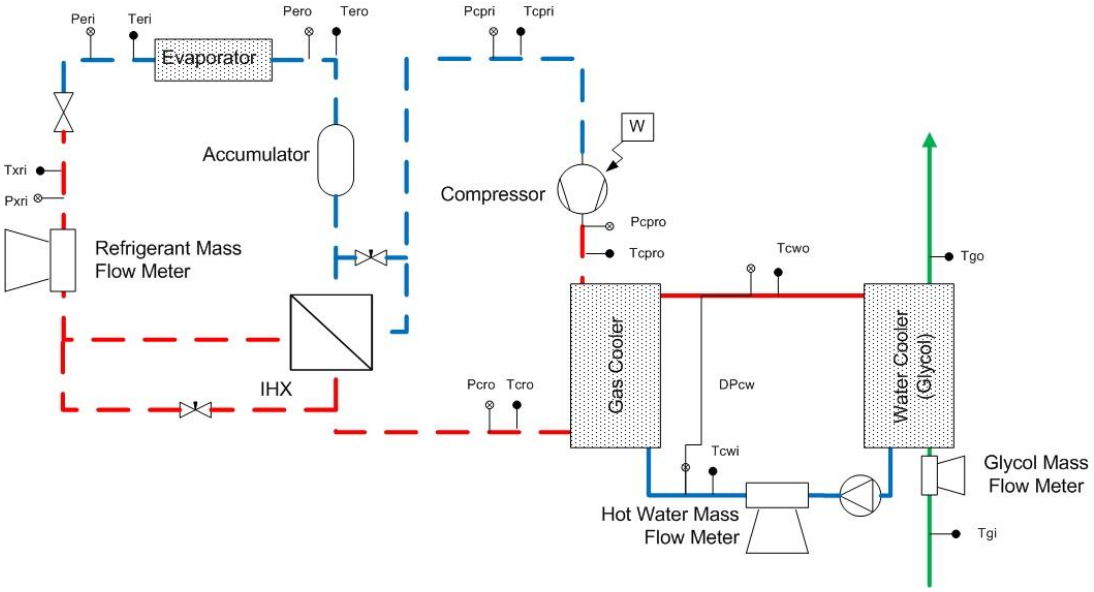

Figure 4-35: R744 IHX system with bypasses

The bypasses were realized with integral-bonnet needle valves on the high and low pressure side of the cycle. The cross sectional view of the valve and the development of the flow coefficient depending on the number of turns open show the behavior during operation (Figure 4-36).

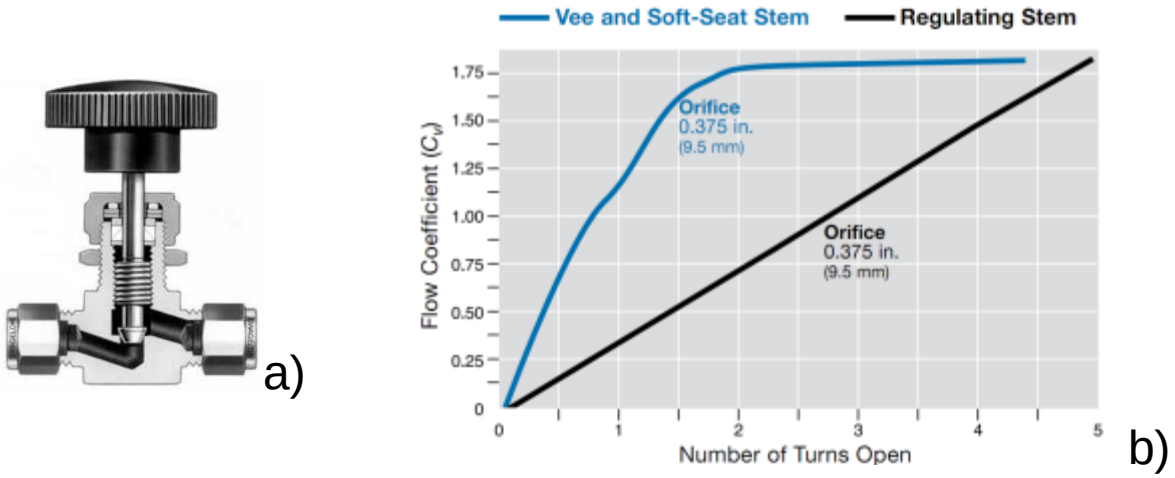

Figure 4-36: Cross section of needle valve (a) and flow coefficient versus number of turns at 100˚F (b)

The valve was equipped with a regulating stem in order to provide a linear development of the flow coefficient C_v. This ensured a more predictable behavior of the valve and an easier control of the refrigerant mass flow that was bypassed. The installed valves are shown in Figure 4-37 and Figure 4-38. Both valves had marks going from one to twelve o'clock which made it easier to orientate and to ensure the desired opening of the valve.

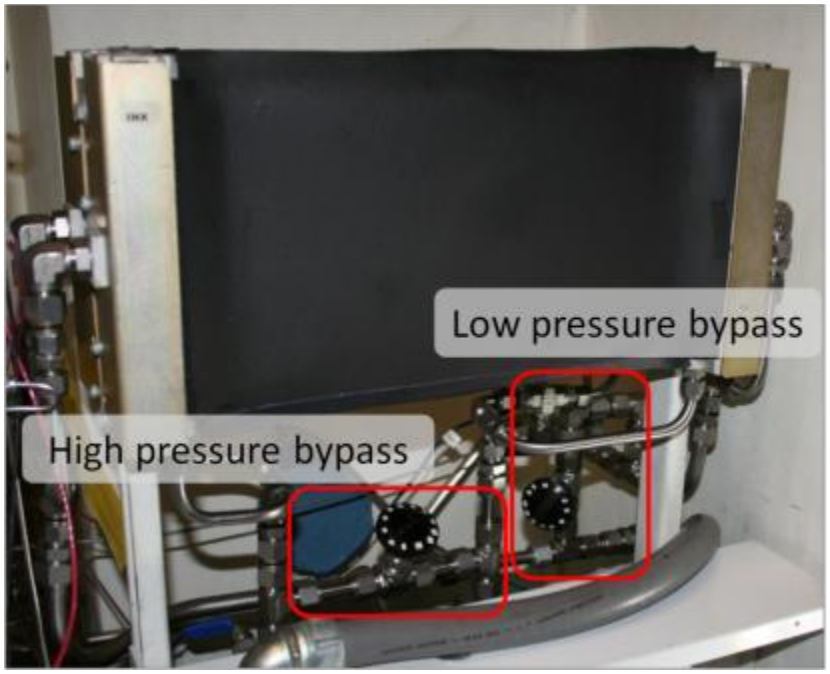

Figure 4-37: Installed IHX bypasses in HPWH (front)

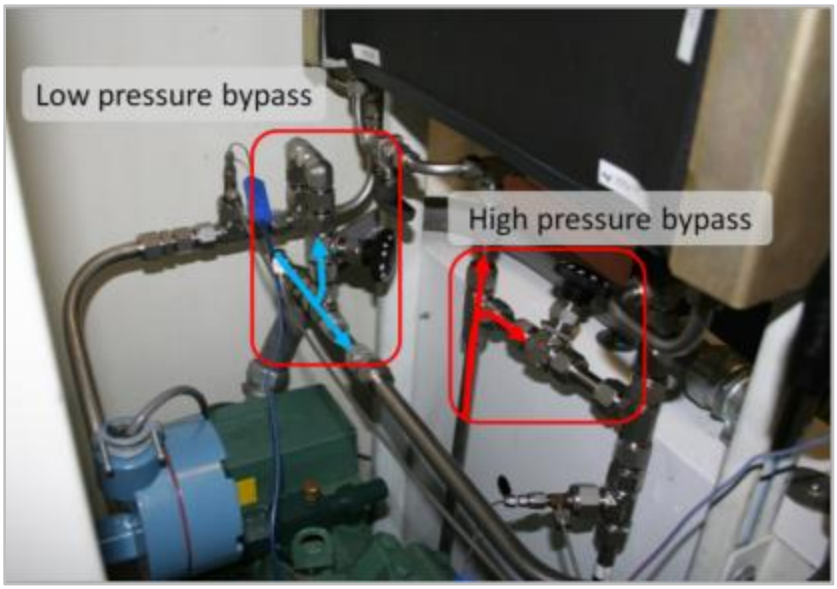

Figure 4-38: Installed IHX bypasses in HPWH (back)

Even though it was anticipated to obtain the best results with an adjustment of the low pressure bypass both sides and their influence on the HPWH performance were investigated for the sake of completeness. It turned out that the adjustment of the low pressure side at ¼ and ½ valve

turns open showed the best results. This corresponded to 7% to 14% valve opening. The investigation was done at an air inlet temperature of 26.7°C and water inlet temperature of 12°C, 26.7°C and 50°C with varying water mass flow rates. The results of the tests are shown in Figure 4-39 to Figure 4-41.

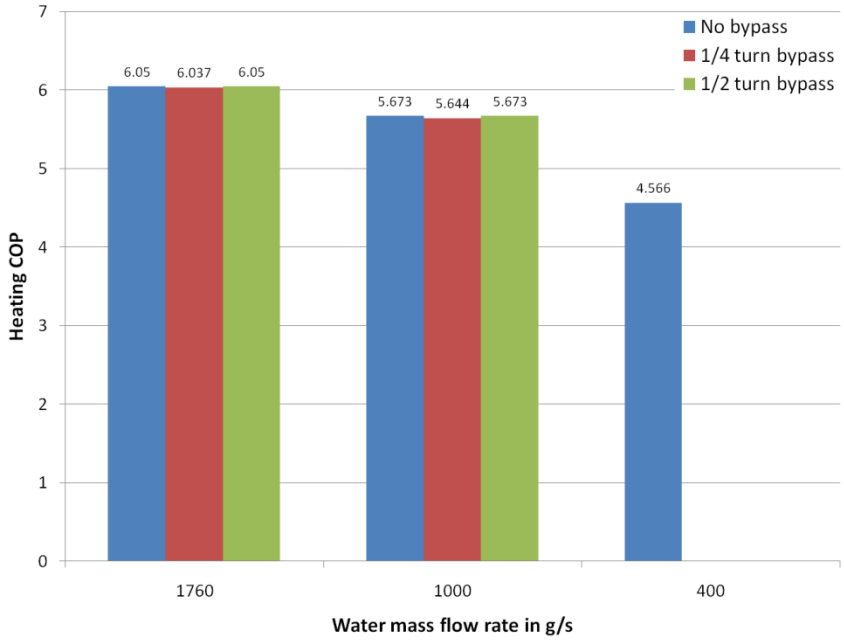

Figure 4-39: Heating COP versus water outlet temperature at a water inlet temperature of 12°C and an air inlet temperature of 26.7°C

It can be noted that the variation of the bypass opening did not affect the system performance. The minor fluctuations within 1% were normal instabilities during operation of the system which cannot be avoided. At all water inlet temperature levels of 12°C, 26.7°C and 50°C no significant improvement could be detected.

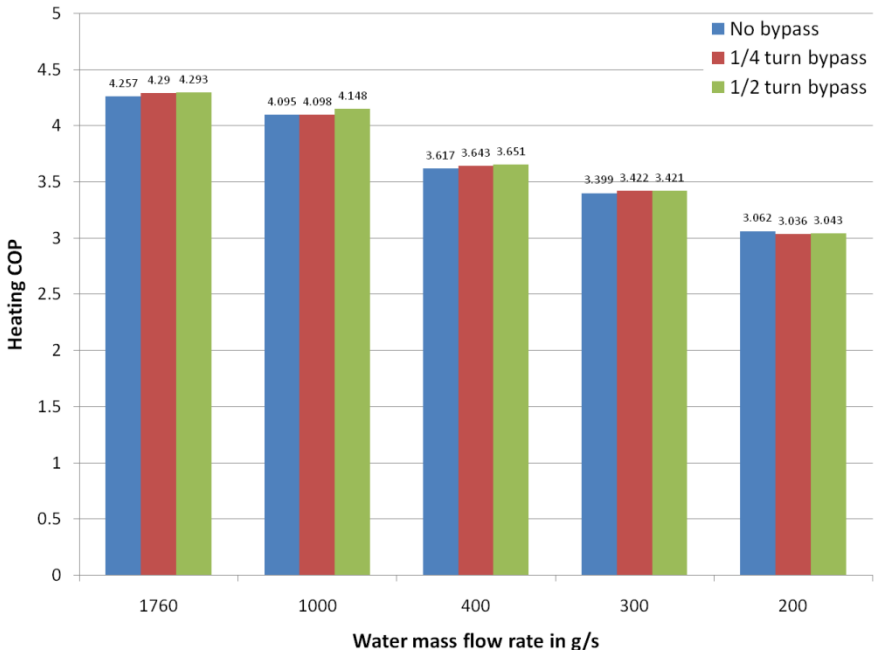

Figure 4-40: Heating COP versus water outlet temperature at a water and air inlet temperature of 26.7°C

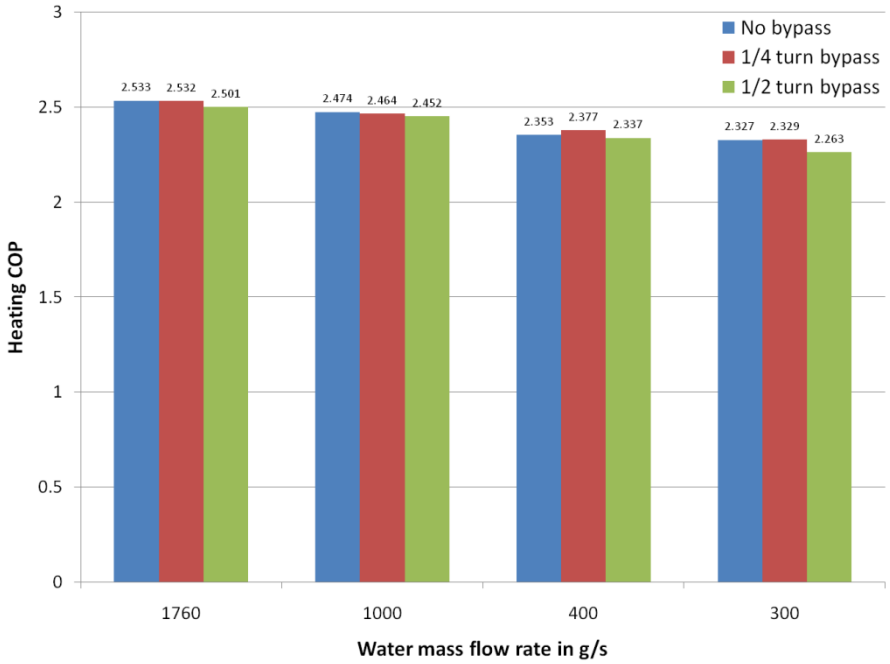

Figure 4-41: Heating COP versus water outlet temperature at a water inlet temperature of 50°C and an air inlet temperature of 26.7°C

Opening the bypass had several effects on the system behavior on the low and high pressure side of the refrigeration cycle. The pressure drop on the low pressure side was reduced and therefore the refrigerant mass flow rate increased. At the same time the IHX effectiveness and the IHX capacity decreased because a fraction of the total refrigerant mass flow was bypassed. This reduced possible cooling of the high pressure fluid leaving the gas cooler increased the high side pressure. Even though the suction pressure drop was decreased both effects compensate each other. Possible positive effects were therefore negated. The effects of opening the bypass are qualitatively visualized in Figure 4-42.

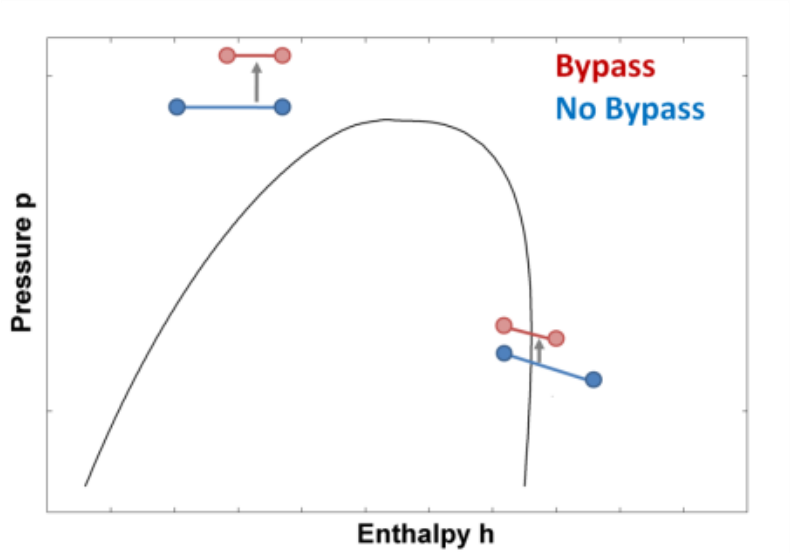

Figure 4-42: Qualitative visualization of bypass opening in a R744 p-h diagram

Another step was the improvement of the internal heat exchanger (IHX) of the system. The first IHX that was used was of microchannel (MC) design. This component offered good heat transfer characteristics but at the same time caused a relatively large pressure drop which had a negative effect on the system performance. The improved IHX component that was sourced was a brazed plate (BP) heat exchanger which had similar thermal performance but a much lower pressure drop rating. First tests with this enhanced component confirmed the lower pressure drop which is shown in Figure 4-43.

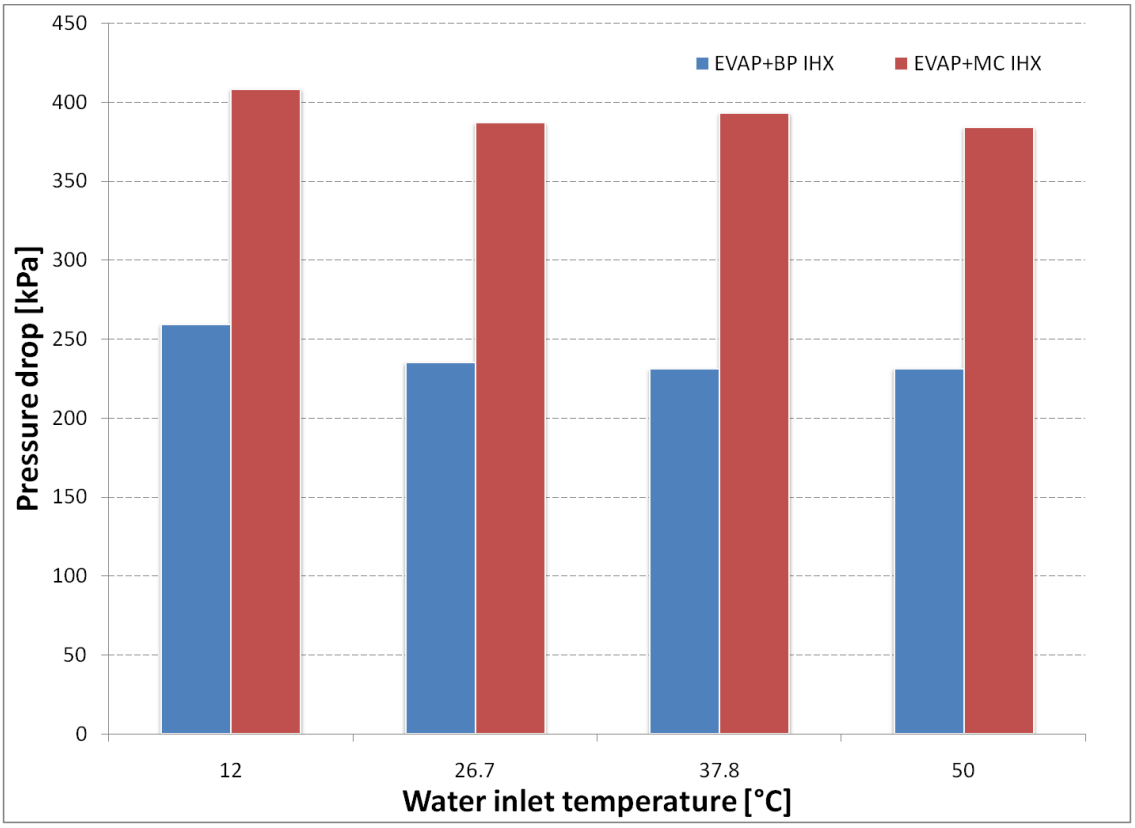

Figure 4-43: Low pressure side IHX pressure drop at various gas cooler water inlet temperatures at an ambient temperature of 26.7°C

It can be seen in Figure 4-43 that throughout the investigated water inlet temperature conditions the BP IHX showed a lower pressure drop than the MC design. A 57% to 66% lower pressure drop of the BP design compared to the MC design was seen for the 12°C and 50°C conditions respectively. In order to better evaluate the improvement the influence of differences of the refrigerant mass flow rates at the investigated conditions had to be taken into account (Figure 4-44).

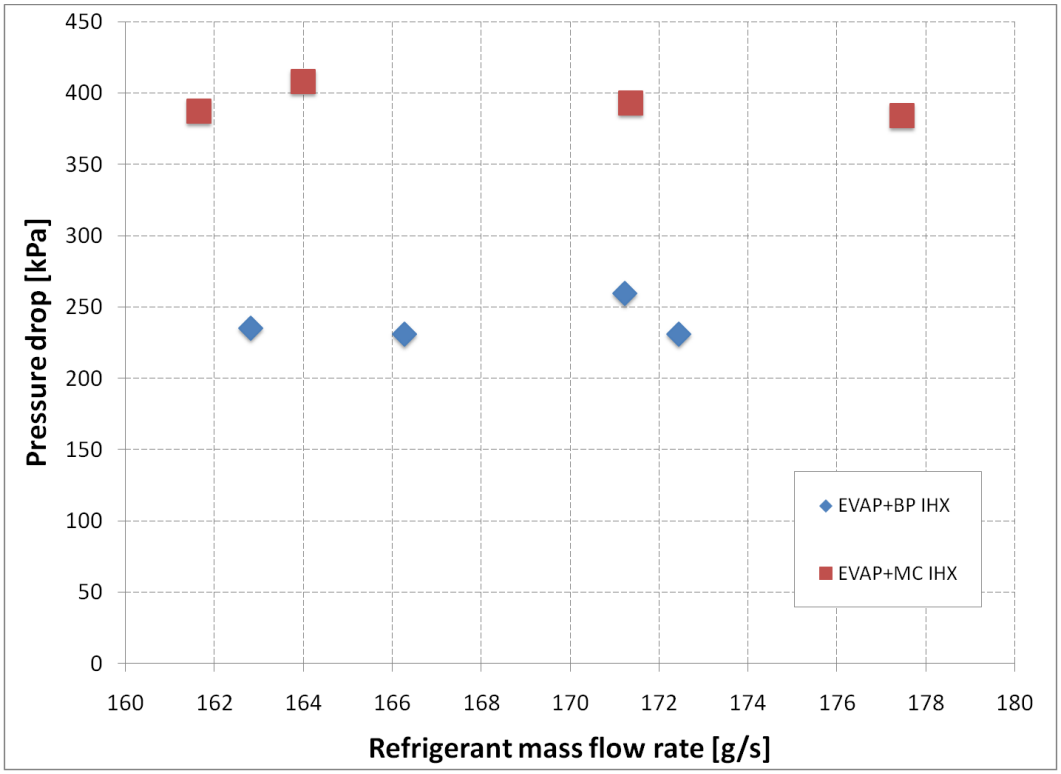

Figure 4-44: Low pressure side IHX pressure drop versus refrigerant mass flow rate at an ambient temperature of 26.7°C

The comparison of the pressure drop versus the refrigerant mass flow rates (Figure 4-44) confirmed the trend that was seen in Figure 4-43. A much lower pressure drop was seen for the BP IHX.

This lower pressure drop had a beneficial effect on the HPWH system performance. It was characterized by the combined system COP. The combined COP for various water inlet temperatures at the rating condition of 26.7°C ambient temperature and a water flow rate of 28 gallons per minute is shown in Figure 4-45.

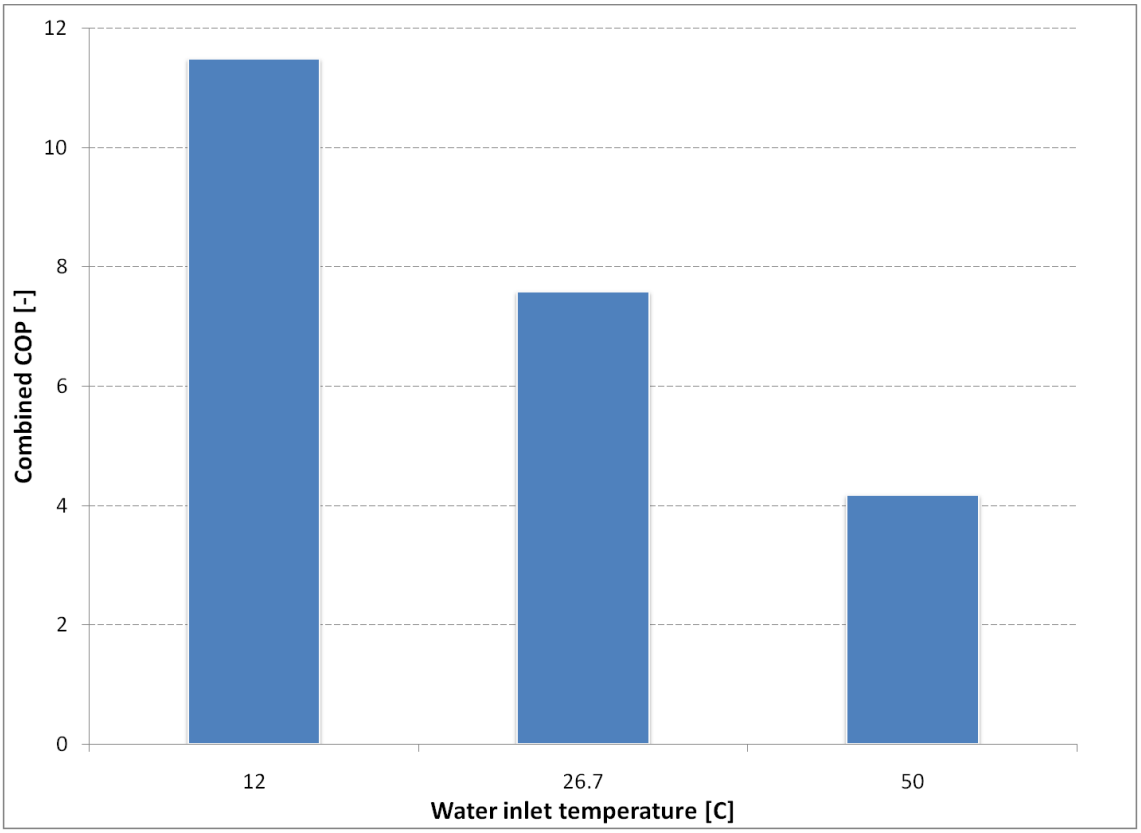

Figure 4-45: Combined COP of the BP IHX system at various water inlet temperatures and an ambient temperature of 26.7°C

The BP IHX system showed very good values for the combined COP (Figure 4-45) for all three investigated gas cooler water inlet temperatures. At 12°C, 26.7°C and 50°C the combined COP was 11.5, 7.6 and 4.2 respectively. A better idea of the overall situation offered a comparison of the BP IHX results compared to previous HPWH development steps which is shown in Figure 4-46.

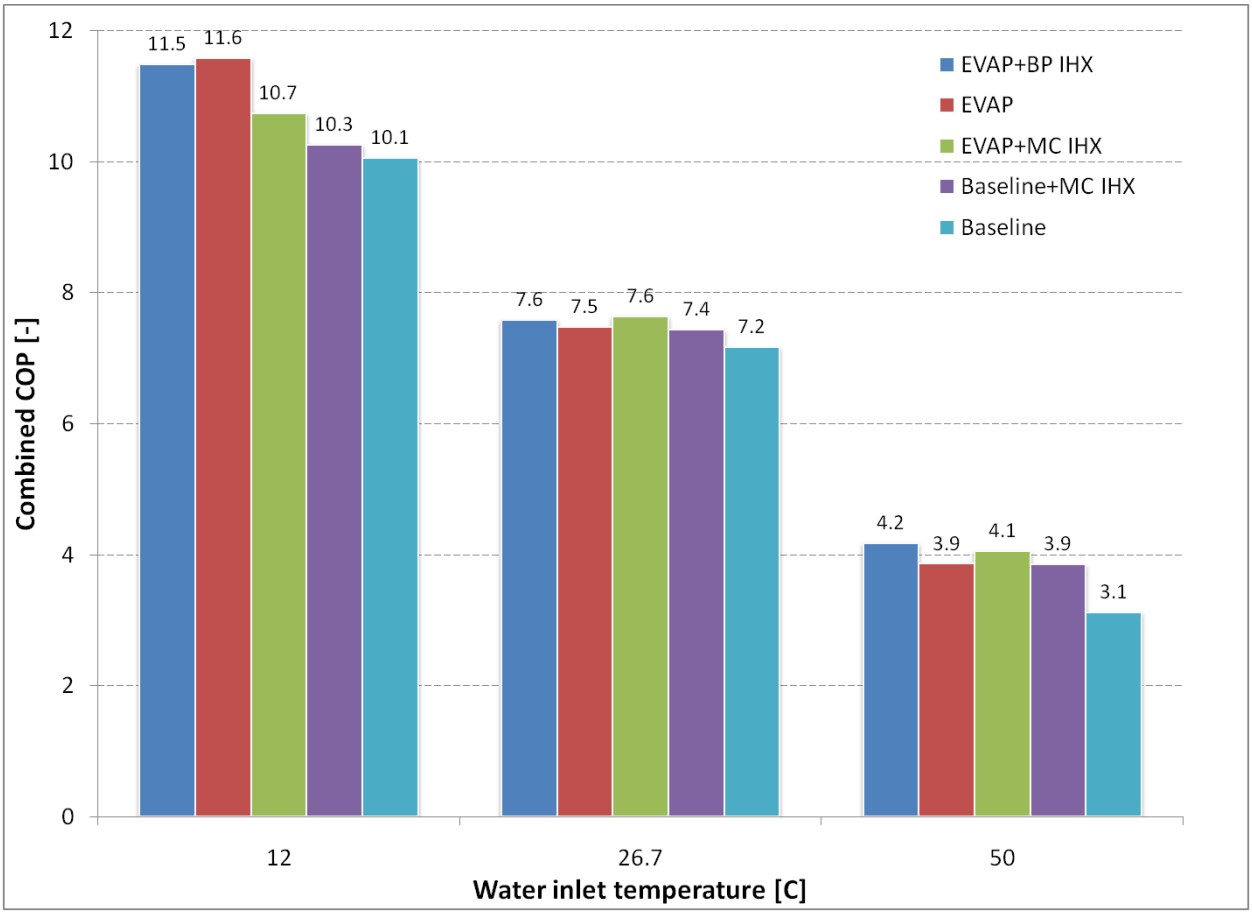

Figure 4-46: Comparison of combined COP's of different HPWH system development stages at various water inlet temperatures and an ambient temperature of 26.7°C

It can be seen that the system performance for all systems decreased with increasing gas cooler water inlet temperature. This behavior was caused by increasing compressor power consumption while the useful capacity increase became smaller during transcritical operation. The BP IHX system performed well compared to the previous development steps. It can be pointed out that the use of an IHX provided the best performance for a wide temperature range. Good results were realized at low water inlet temperatures and even better relative performance was achieved at increasing water inlet temperatures where the IHX can help in reducing the negative effect of reduced capacity improvement.

When comparing the BP IHX system to the baseline system improved results of 13.5% (12°C) 5.5% (26.7°C) and 35.5% (50°C) were achieved. This large improvement for the highest water inlet temperature fulfilled and even exceeded the proposed goal of an improvement of the next

generation HPWH compared to the baseline system of 20%. In detail the investigated improvement steps have different influence on the overall performance. Lower relative improvement values can be seen for low water inlet temperatures where all system stages achieve good performances due to the beneficial operating conditions for R744. For increasing gas cooler water inlet temperatures up to the high values of 50°C the influence of the system improvement becomes more evident due to the more challenging operating conditions for R744. That is why the usage of the MC IHX and the enhanced evaporator both achieve improved performances of 25.8%. The enhanced evaporator with MC IHX reaches a 32.3% and the enhanced evaporator with BP IHX even reaches 35.5% better combined COP.

4.3 Evaporator

One part of the system optimization process was the improvement of the heat exchangers of the HPWH. As a first step, the IHX was integrated in the system and tested. The next step in this process was the modification of the evaporator of the system. The goal was to decrease the approach temperature difference between the air and refrigerant side which had a positive effect on the system efficiency. A comparison of the three evaporator sizes used in the R134a, R744 baseline and the enhanced R744 evaporator system is shown in Figure 4-47.

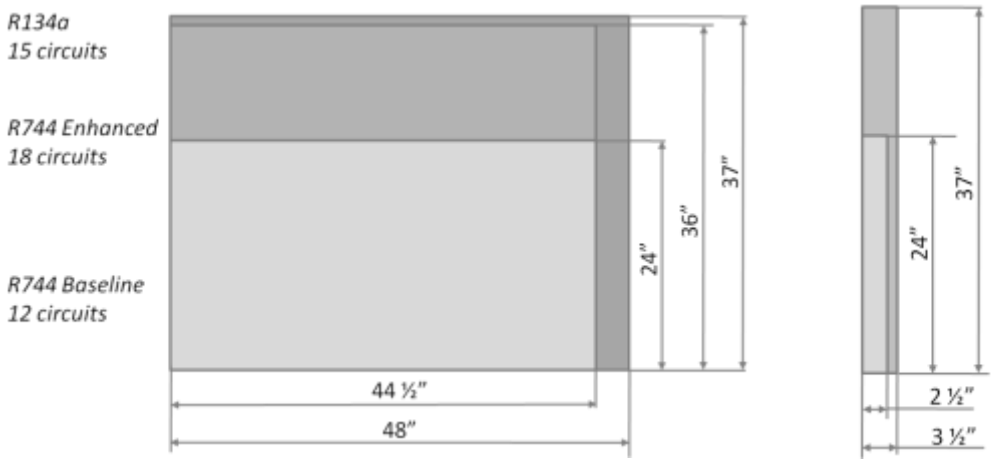

Figure 4-47: Evaporator size comparison

The R134a evaporator was the biggest of the three components. The R744 enhanced evaporator was 50% bigger than the baseline component. It consisted of 18 circuits. In order to

increase the evaporator size, the baseline component was combined with half of another evaporator (Figure 4-48).

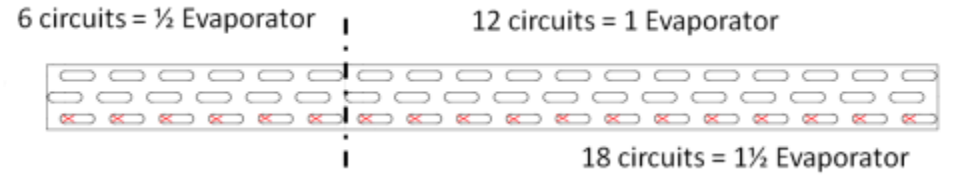

Figure 4-48: Combination of one and a half evaporator

The evaporator was cut in half with special attention to the section plane. This was done in order to minimize a potential gap between the two heat exchangers. A gap could affect the airflow through the component causing a bypass which would decrease the capacity. The cut evaporators and the section plane are shown in Figure 4-49.

Figure 4-49: Cut evaporator halves and detailed view of section plane

The modification required a new distributor because the number of circuits increased from 12 to 18. The new distributor before the connection to the feeder tubes is shown in Figure 4-50.

Figure 4-50: Distributor for enhanced evaporator

In order to combine both evaporator parts minor structural reinforcements were necessary to ensure the stability of the component. The feeder tubes of the baseline evaporator and the new half evaporator were cut and prepared for installation of the new distributor. It was made sure that all feeder tubes had the same length to verify an even refrigerant distribution in the evaporator. Each brazed feeder tube connection was visually inspected and then leak checked. The enhanced evaporator passed a pressure test at 1200 PSI or 82.73 bar which was sufficient for a component on the low pressure side of the refrigeration cycle. The assembled enhanced evaporator is shown in Figure 4-51.

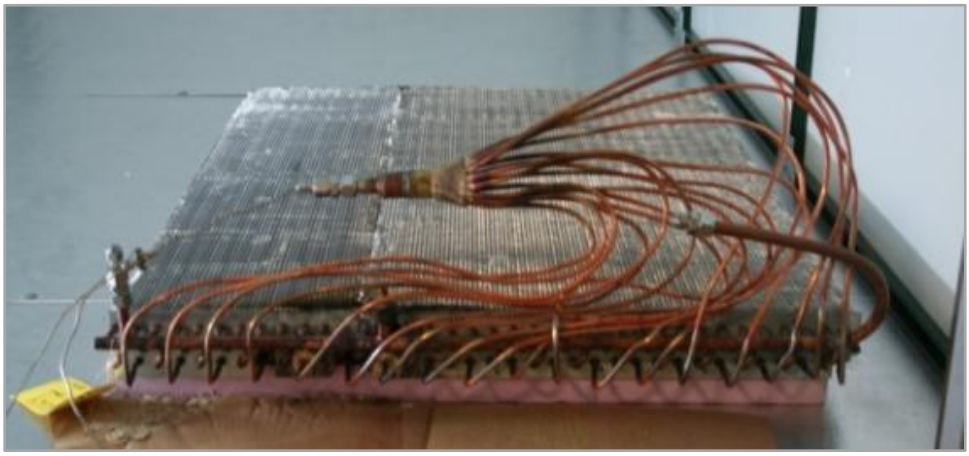

Figure 4-51: Assembled enhanced evaporator

After finishing the fabrication and pressure test of the enhanced evaporator the component was installed in the HPWH housing. Minor modifications of the brackets which hold the evaporator in place were necessary. Three additional thermocouples were installed to provide the same

number of air inlet temperature measurements per area. A comparison between the baseline evaporator (Figure 4-52) and the enhanced evaporator (Figure 4-53) is shown in the following figures.

Figure 4-52: R744 baseline evaporator

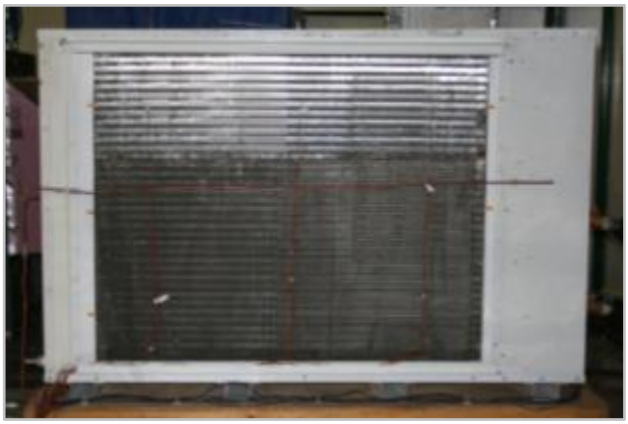

Figure 4-53: R744 enhanced evaporator

In order to allow a good comparison between the different evaporators the air flow rate was kept constant. The modified evaporator provided a 50% bigger component volume and face area. Therefore the face velocity of the air that passed the enhanced evaporator was less compared to the baseline evaporator.

After the installation the system was leak checked and a flushing run was done to clean out possible debris that could have gotten in the lines during fabrication. For this an inline filter was installed and the system was run for two and a half hours. The inline filter before (Figure 4-54) and after (Figure 4-55) the flushing run is shown in the following figures. There were no particles detected which proved the cleanliness of the system.

Figure 4-54: Inline filter before system flushing

Figure 4-55: Inline filter after system flushing

After flushing the system the inline filter was replaced with stainless steel piping and initial shakedown testing started. The system was run at a water and air inlet temperature of 26.7°C and a water mass flow rate of 28 gallons per minute. A comparison of the R744 baseline, R744 IHX and R744 IHX with enhanced evaporator can be seen in Figure 4-56.

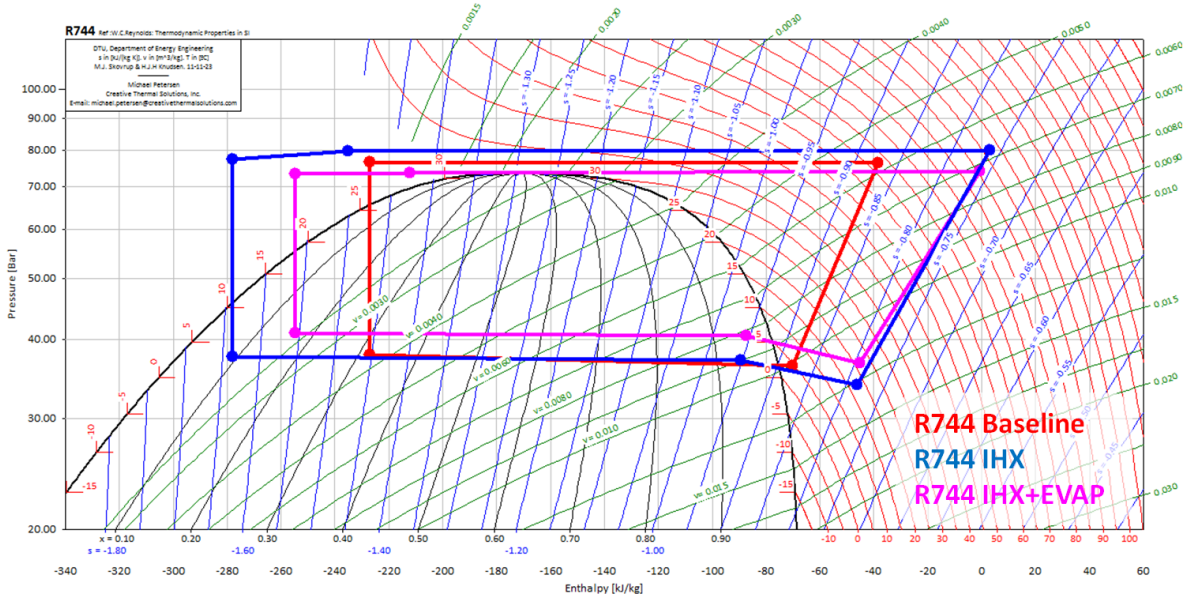

Figure 4-56: p-h-diagram comparison of R744 Baseline, IHX and IHX+EVAP systems

The comparison of the three development stages shows the influence of the IHX and the enhanced evaporator. The baseline system was run at an adjusted evaporator outlet condition. The superheat was kept constant at 3 K to 5 K in order to prevent the compressor from sucking liquid refrigerant droplets which could have caused damage to it.

The next stage with an IHX had the same low side pressure level. The evaporator refrigerant outlet quality was kept at 95%. The superheat was achieved by the internal heat exchange from the high pressure side to the low pressure side. Due to the additional sub cooling after the gas cooler and superheat after the evaporator bigger enthalpy differences were reached. At the same time the compressor discharge temperature increased which caused a higher high side pressure level.

The third development step with an IHX and enhanced evaporator increased the heat transfer area which decreased the approach temperature difference between refrigerant and air side. Consequently the low side pressure was higher which decreased the necessary compressor power. This has a beneficial effect on the system performance (COP).

Further tests were done investigating water inlet temperatures of 12°C, 26.7°C and 50°C at an air inlet temperature of 26.7°C and at various water mass flow rates. The results for the heating

COP versus the water temperature lift at a water inlet temperature of 12°C are shown in Figure 4-57.

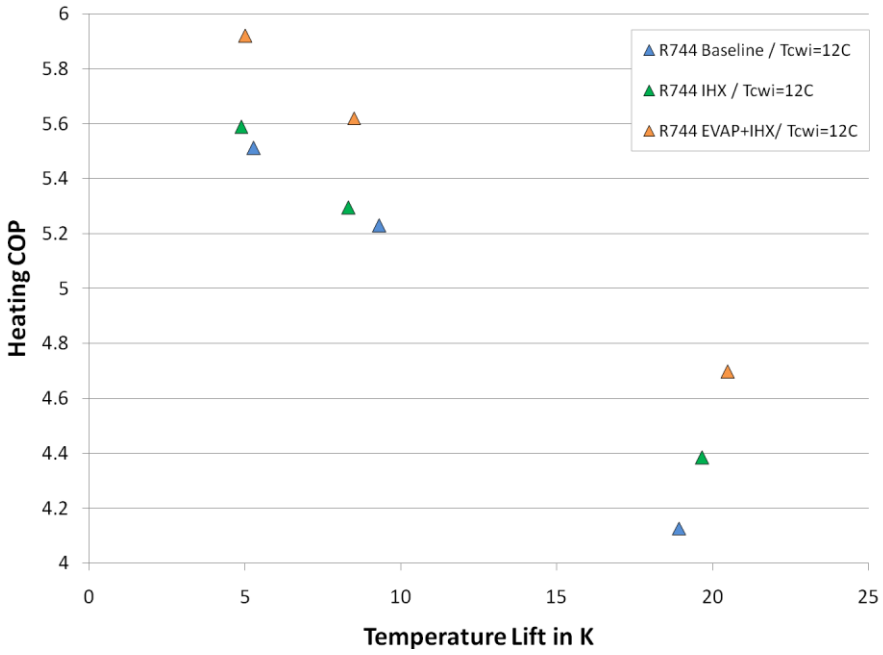

Figure 4-57: Heating COP versus water temperature lift at a water inlet temperature of 12°C

The enhanced evaporator system with IHX showed a significant improvement of the heating COP compared to the baseline and IHX system. Between water temperature lifts of 5 K and 20 K COP improvements of 5.9% and 7.3% were seen.

The results at a water inlet temperature of 26.7°C are shown in Figure 4-58. It can be noted that the enhanced evaporator system with IHX showed the best performance of the three R744 HPWH development stages. An improvement of approximately 3% compared to the IHX system was seen.

The test results at a water inlet temperature of 50°C are shown in Figure 4-59.

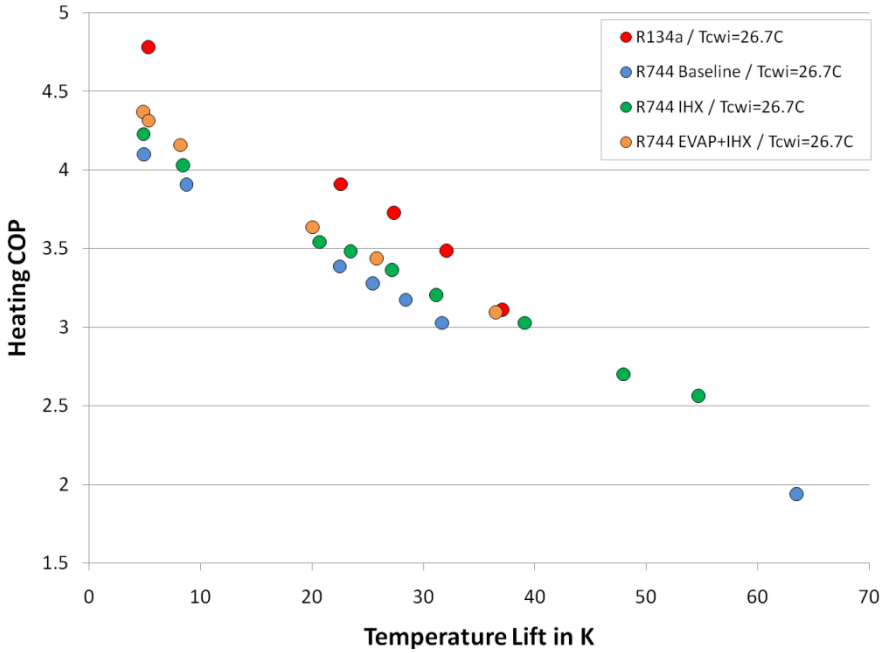

Figure 4-58: Heating COP versus water temperature lift at a water inlet temperature of 26.7°C

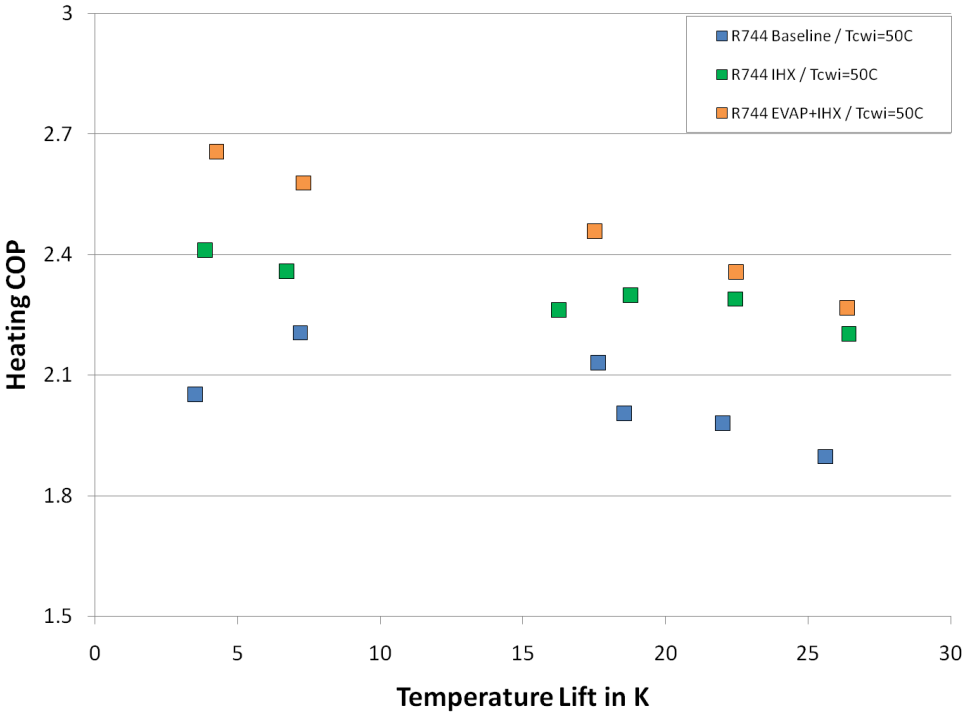

Figure 4-59: Heating COP versus water temperature lift at a water inlet temperature of 50°C

The enhanced evaporator system with IHX showed an improvement compared to the IHX system of 3% at lower water flow rates and 9% at higher water flow rates.

Figure 4-60 shows a comparison of all three conditions.

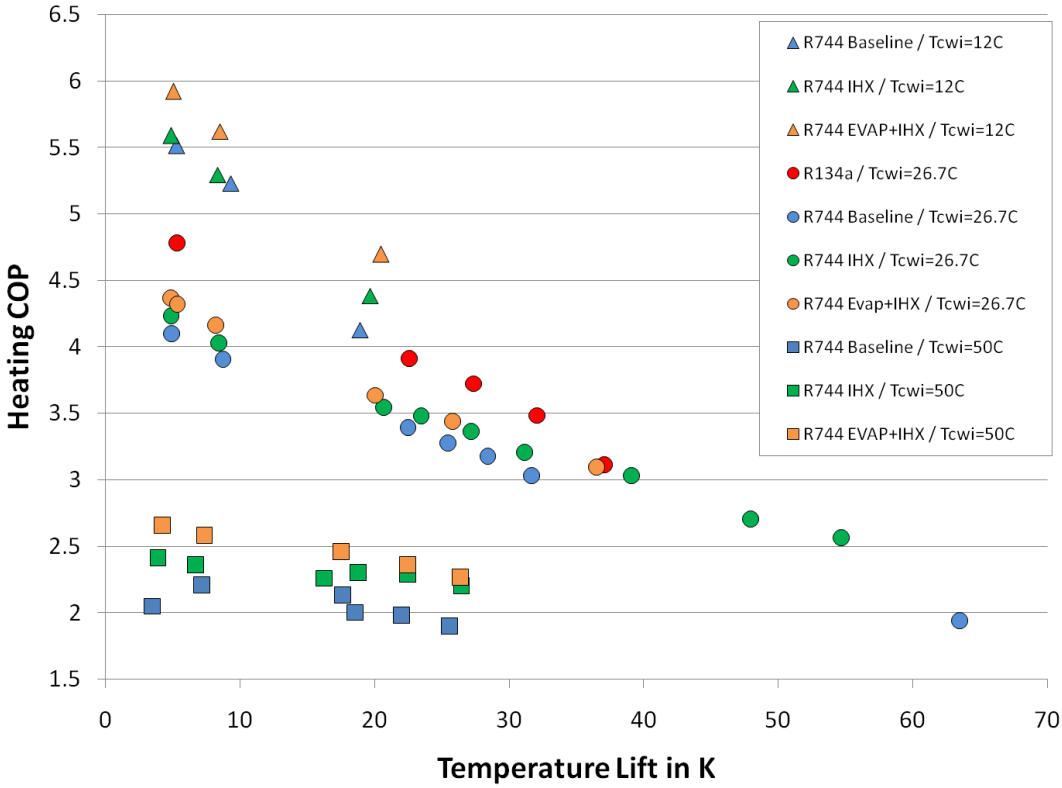

Figure 4-60: Comparison of heating COP versus temperature lift at investigated water inlet temperatures

Further tests at the rating water mass flow rate of 28 gallons per minute and various water and air inlet temperatures were done. In detail tests at an ambient temperature of 8°C and 12°C water inlet temperature as well as water inlet temperatures of 12°C , 26.7°C and 50°C at an ambient temperature of 26.7°C were accomplished. The test results are summarized in Figure 4-61 to Figure 4-64.

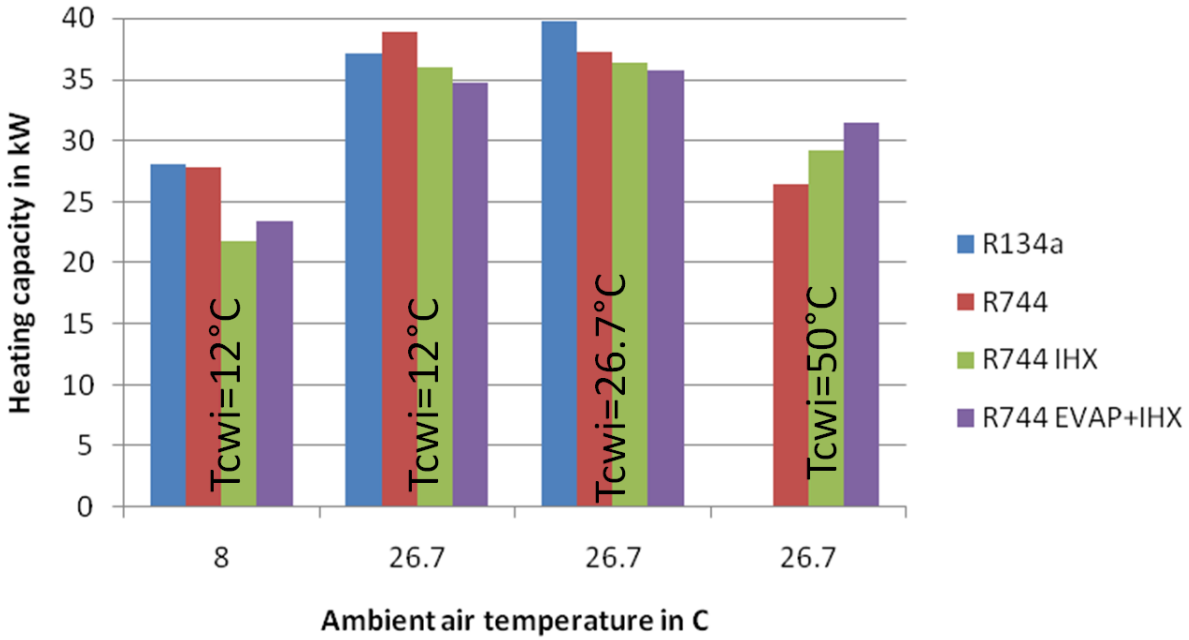

Figure 4-61: HPWH heating capacity at different ambient air and water inlet temperatures

The system performance of the HPWH is characterized by parameters like the heating capacity (Figure 4-61) the heating COP (Figure 4-62) as well as the combined COP (Figure 4-63) representing the combination of the useful heating and cooling capacities divided by the compressor power. Main aspect of the improvement of the system was the maximization of the heating COP.

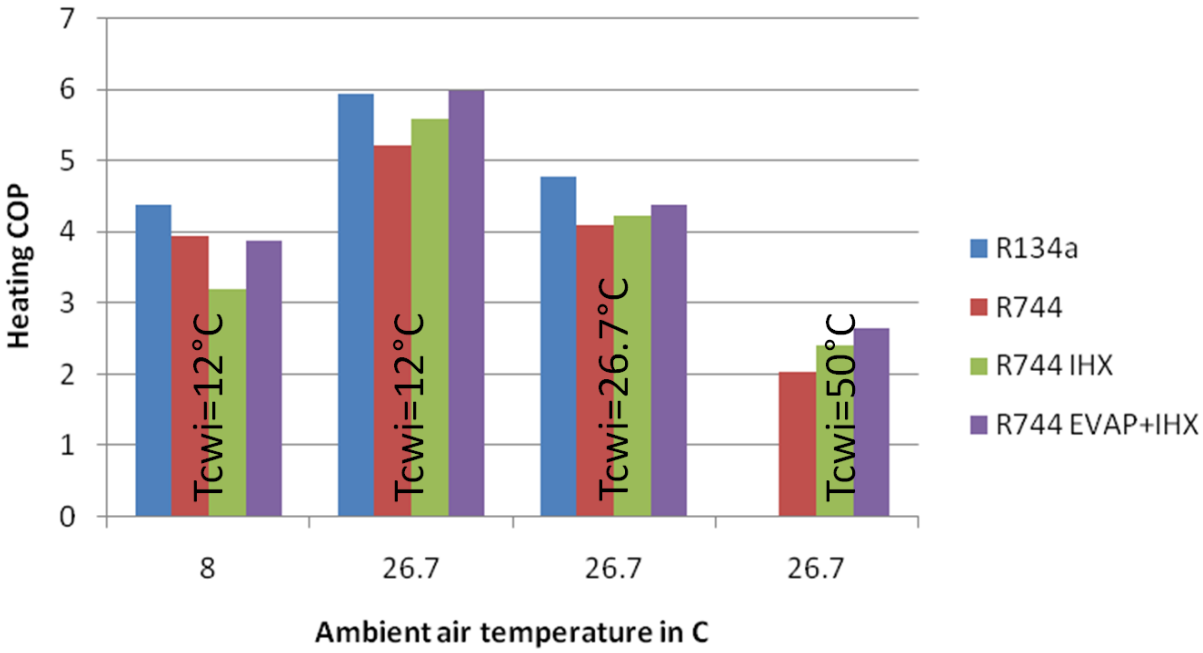

Figure 4-62: HPWH heating COP at different ambient air and water inlet temperatures

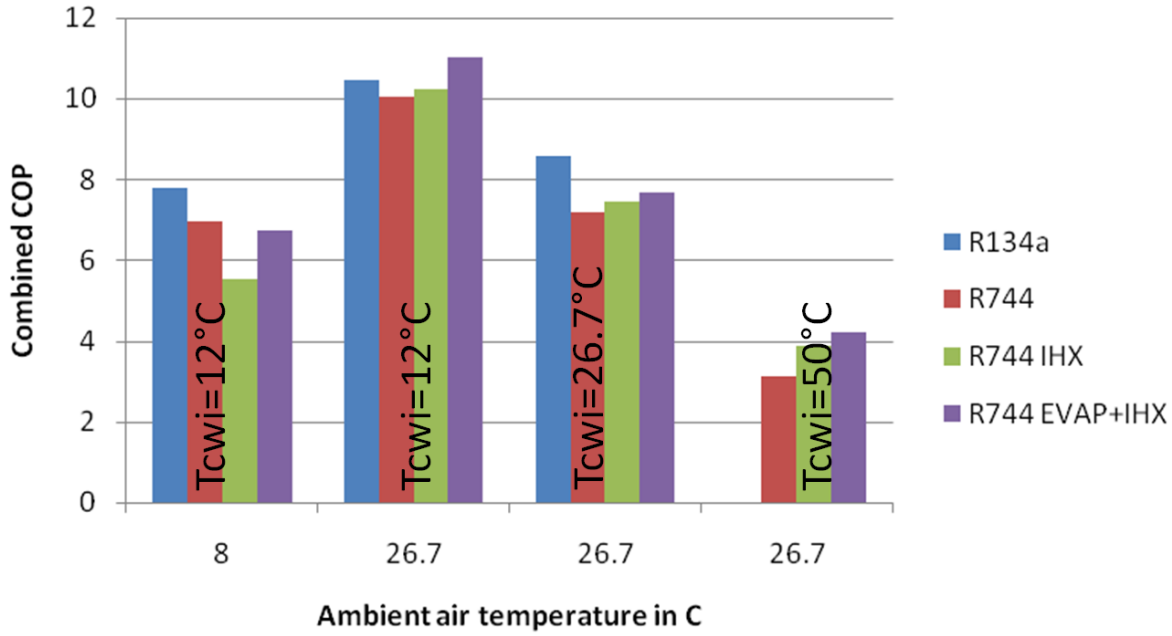

Figure 4-63: HPWH combined COP at different ambient air and water inlet temperatures

It was seen that in some conditions the heating capacity of the enhanced evaporator system with IHX (Figure 4-61: EVAP+IHX) was lower but at the same time the heating COP was higher compared to the other systems. The necessary compressor power was reduced due to a smaller evaporation approach temperature difference which increased the suction pressure of the compressor. Less power was needed for the compression process. The reduction in evaporator approach temperature difference is shown in Figure 4-64.

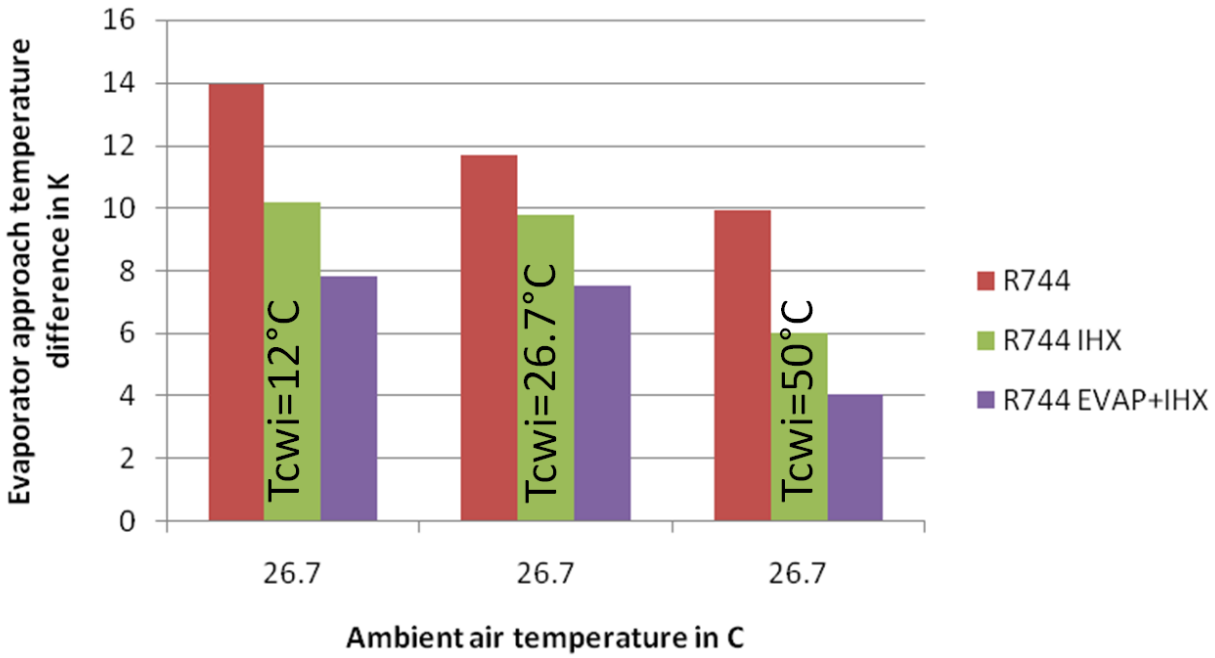

Figure 4-64: HPWH evaporator approach temperature differences at different ambient air and water inlet temperatures

As described earlier the relatively high pressure drop of the IHX had a negative effect on the system performance. In order to verify this influence and to be able to compare the possible improvement of the enhanced evaporator compared to the baseline system the IHX was isolated. This means the system schematic for the enhanced evaporator tests without IHX was the same as in the baseline system. Initial tests were done at a water inlet temperature of 12°C and an ambient air temperature of 26.7°C as well as at a water and air inlet temperature of 26.7°C. Both tests were accomplished at varied water flow rates in order to investigate the potential water temperature lifts. The initial results of the tests are shown in Figure 4-65 and Figure 4-66.

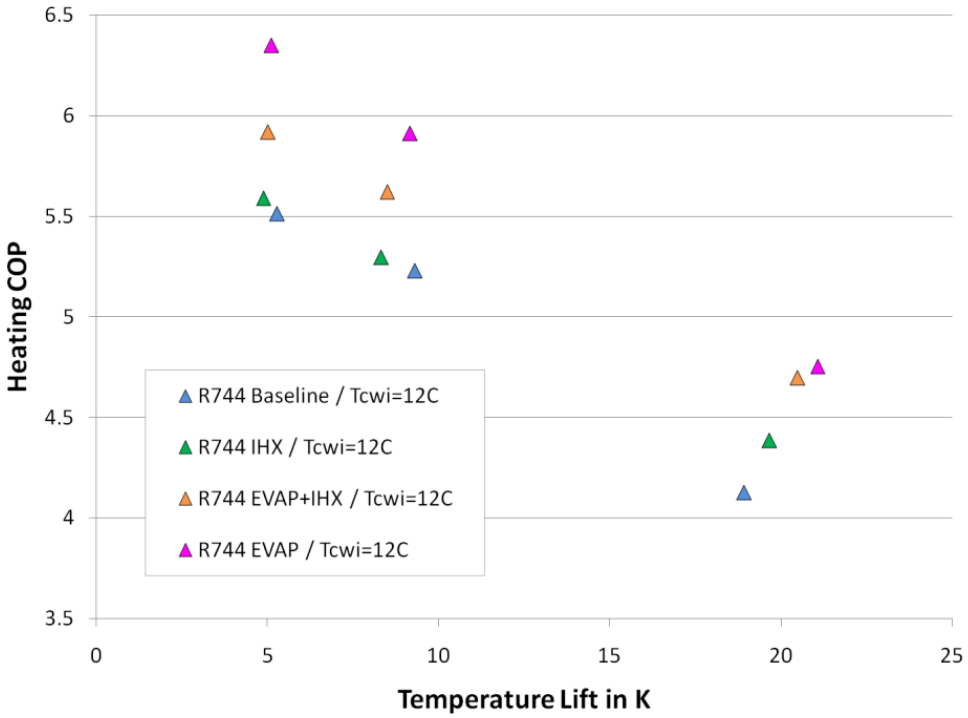

Figure 4-65: Comparison of heating COP versus temperature lift at a water and air inlet temperature of 12°C

It can be seen that higher maximum heating COP's were achieved with the enhanced evaporator system without IHX (Figure 4-65: EVAP) compared to the other HPWH development steps. Also higher temperature lifts were realized at this water inlet temperature of 12°C.

This situation changed when going to higher water inlet temperatures of 26.7°C (Figure 4-66). The EVAP system still provided a better heating COP at high water flow rates and low water temperature lifts. At higher water temperature lifts the EVAP performance declined more than the IHX systems. The IHX had a positive effect on the COP and damped the losses that occured with higher temperature differences.

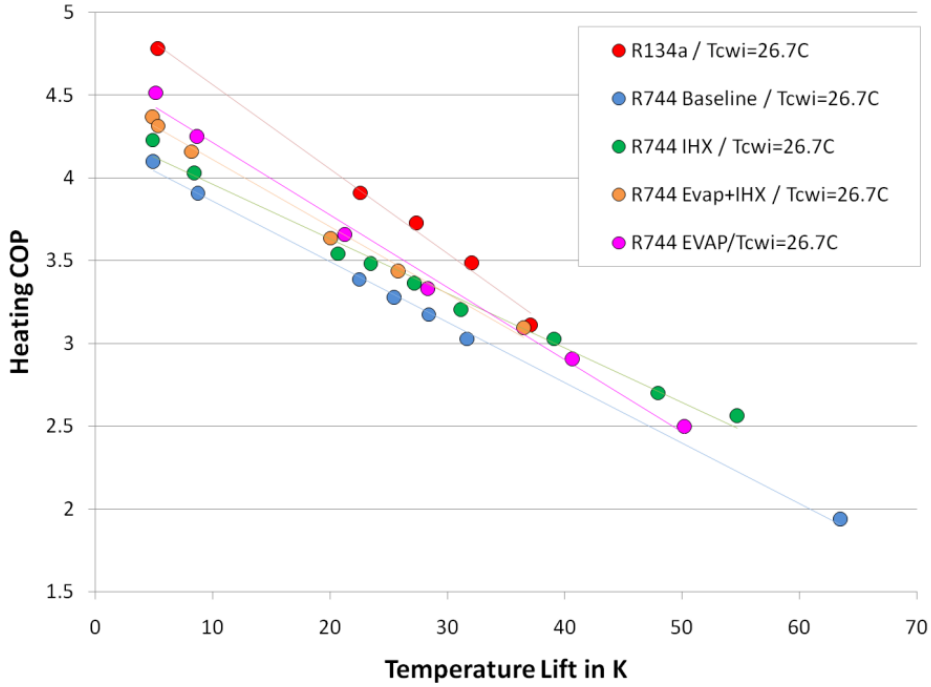

Figure 4-66: Comparison of heating COP versus temperature lift at a water and air inlet temperature of 26.7°C

First results of tests with the HPWH system with enhanced evaporator and without IHX were presented earlier. The tests were done at various water flow rates at an air inlet temperature of 26.7°C and water inlet temperatures of 12°C and 26.7°C. At these two conditions a trend of the enhanced evaporator system without IHX was seen. The improvement of this system compared to the other R744 HPWH decreased when increasing the water inlet temperature. Further tests were done at a water inlet temperature of 50°C. The results are shown in Figure 4-67.

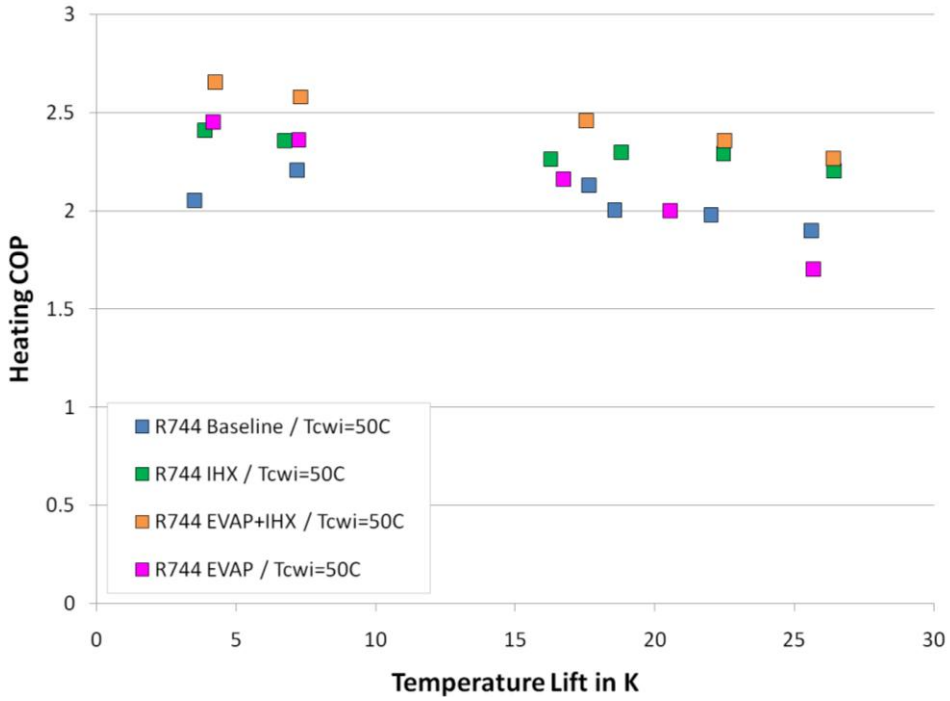

Figure 4-67: Heating COP versus temperature lift at a water inlet temperature of 50°C and an air inlet temperature of 26.7°C

It can be seen that the anticipated behavior from the previous tests is confirmed at a water inlet temperature of 50°C. The enhanced evaporator system no longer significantly outperforms the baseline and IHX systems. However, the IHX becomes more beneficial at higher water inlet temperatures and decreases the performance drop. This shows that the use of an internal heat exchanger assures a good performance over a wide range of water inlet temperatures. A comparison of the investigated water inlet temperatures of 12°C, 26.7°C and 50°C with varied water mass flow rates is shown in Figure 4-68.

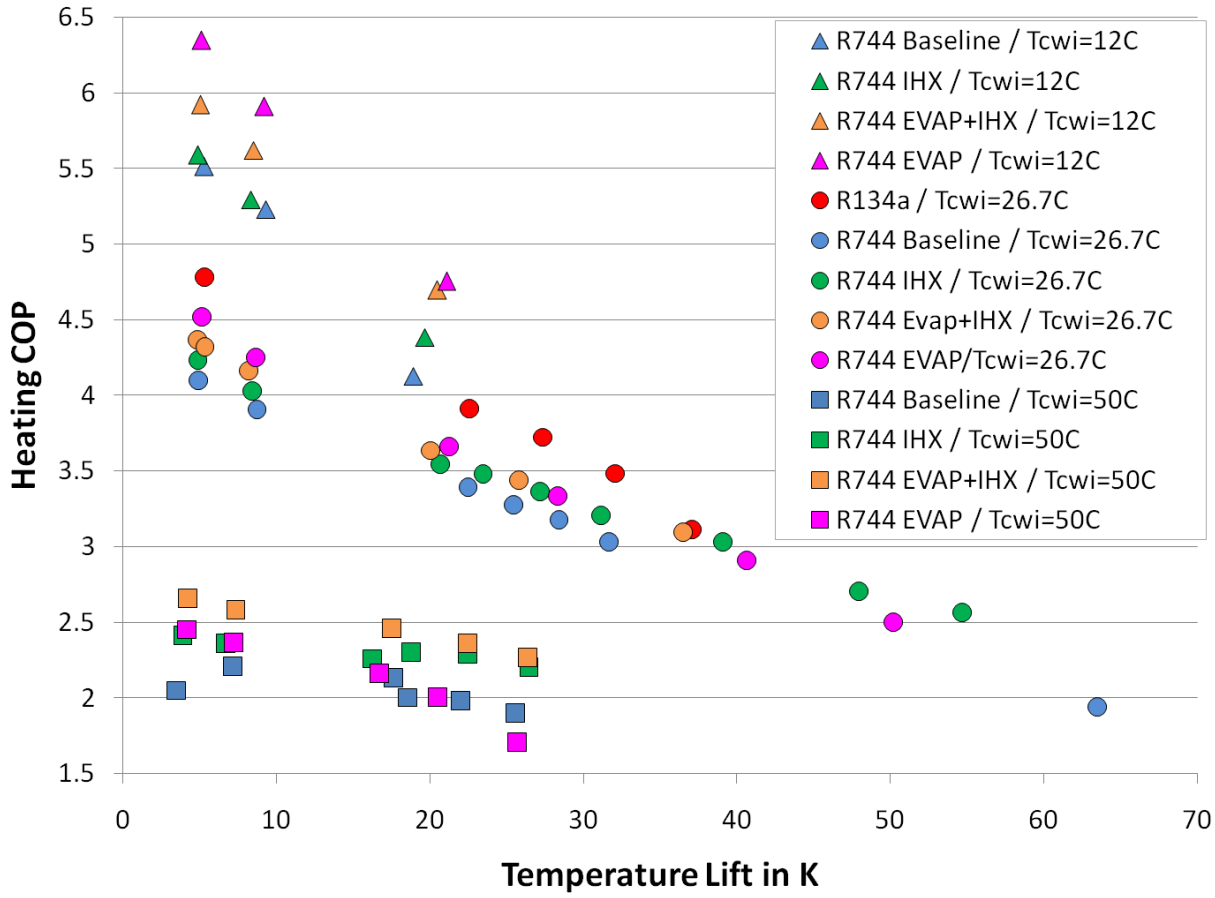

Figure 4-68: Comparison of heating COP versus temperature lift for various water inlet temperatures

Beside the investigation of varying water flow rates the comparison of different conditions for water and air temperature at the rating water mass flow rate of 28 gallons per minute helps to describe the influence of development stages on the HPWH performance. The results for heating COP (Figure 4-69), heating capacity (Figure 4-70), combined COP (Figure 4-71) and evaporator approach temperature difference (Figure 4-72) can be seen in the following figures.

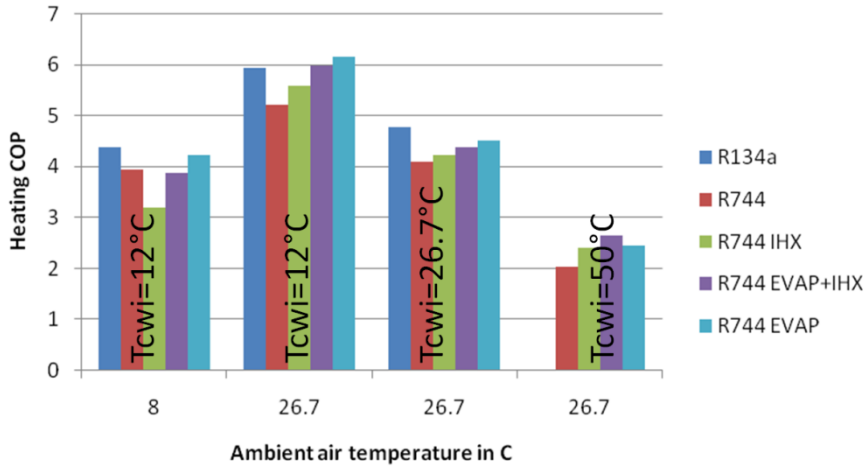

Figure 4-69: HPWH heating COP at different ambient air and water inlet temperatures

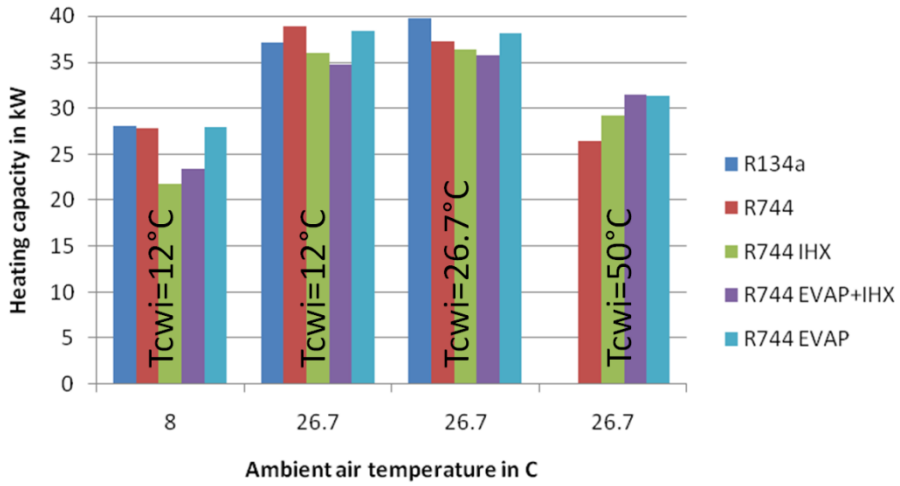

Figure 4-70: HPWH heating capacity at different ambient air and water inlet temperatures

As expected, the enhanced evaporator system without internal heat exchanger shows a higher heating COP compared to the other systems. This can be described with the elimination of the relatively high pressure drop in the IHX. The heating capacity is equal or even higher compared to the other R744 systems.

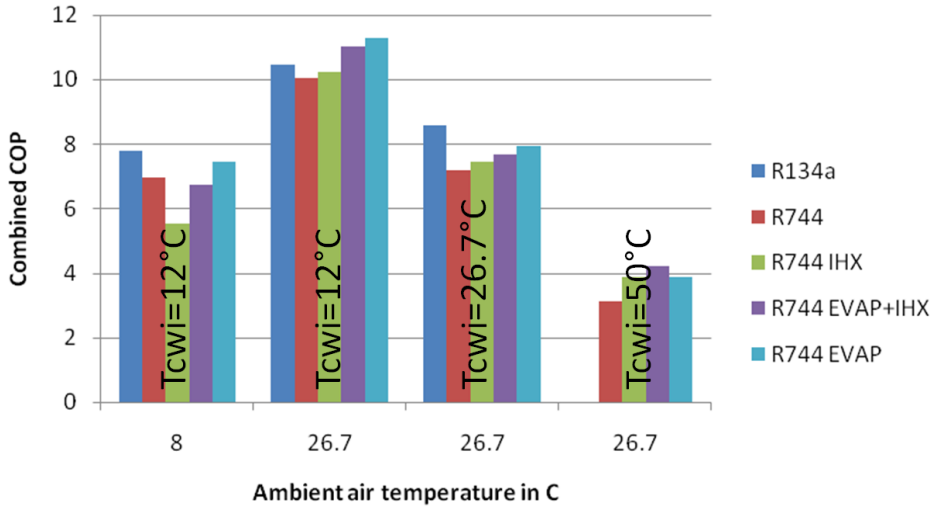

Figure 4-71: HPWH combined COP at different ambient air and water inlet temperatures

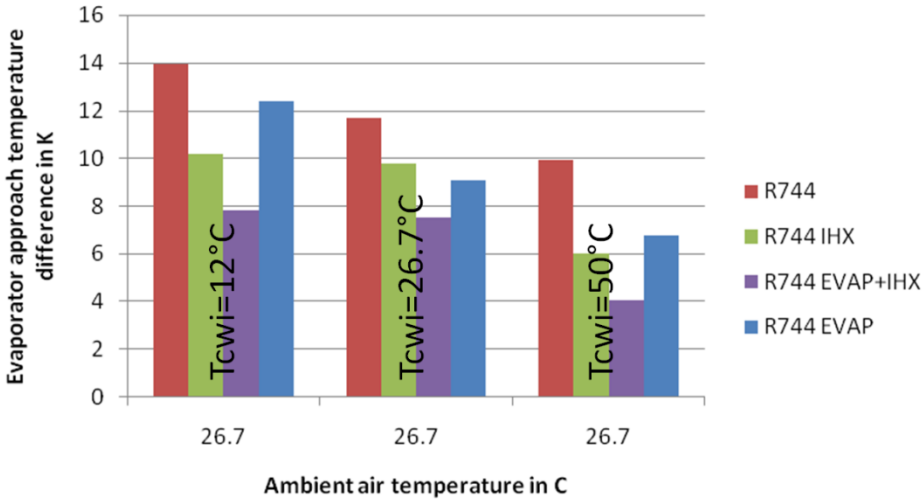

Figure 4-72: HPWH evaporator approach temperature difference at different ambient air and water inlet temperatures

A combined COP of almost 8 was reached for the rating condition of water and air inlet temperature of 26.7°C. Even higher values were possible for the same air inlet temperature and a water inlet temperature of 12°C. The evaporator approach temperature difference of the enhanced evaporator HPWH was lower compared to the baseline system due to the increased heat transfer area. The IHX systems showed the lowest evaporator approach temperature difference of the investigated HPWH.

4.4 Gas cooler

One step in the improvement process of the next generation HPWH was the minimization of the conduction losses in the gas cooler. This was achieved by using multiple gas coolers and therefore having several steps in transferring heat from refrigerant to water side. The proposed system schematic of the modified system consisting of the heat exchangers as well as additional valves to control the water flow is shown in Figure 4-73.

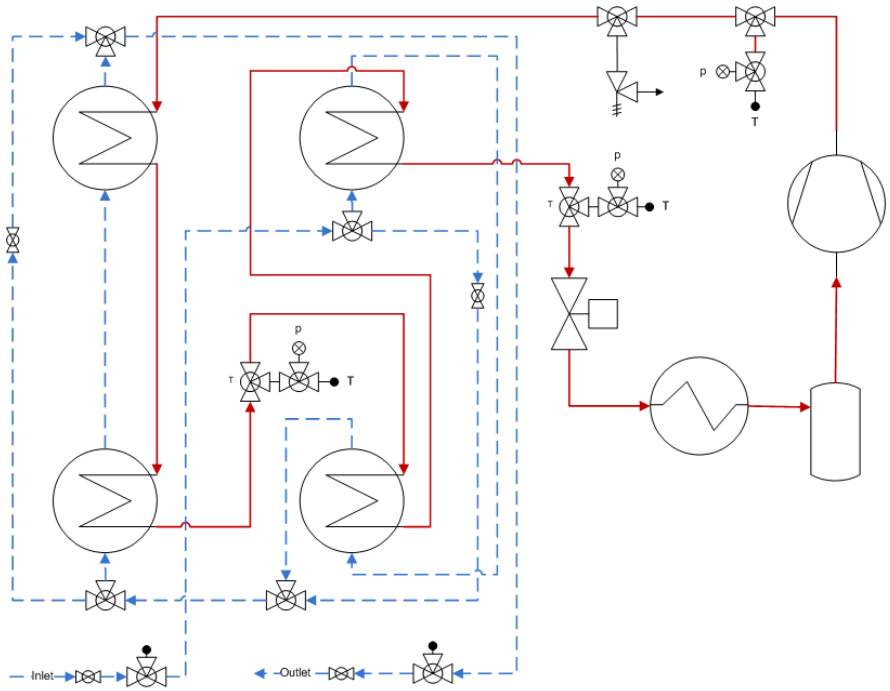

Figure 4-73: Multiple gas cooler schematic of water and refrigerant side

The modified HPWH with multiple gas coolers transferred heat from the refrigerant (Figure 4-73, red) to the water (Figure 4-73, blue) side. The two fluids were operated in counter flow in order to achieve a maximum in heat transfer. The water side had two additional globe valves which offered more control capabilities when operating the system. The bypasses of the first and second as well as the third and fourth heat exchanger enabled the adjustment of the flow through the gas coolers. With this the temperature difference between the two fluids was better matched and so the approach temperature was optimized. The CAD design of the gas cooler cart is shown in Figure 4-74.

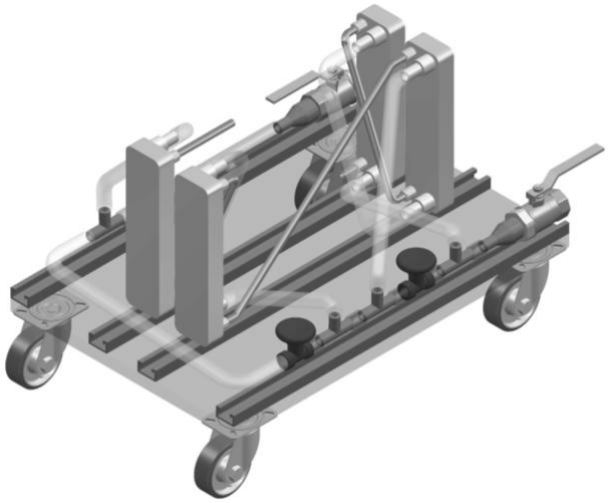

Figure 4-74: Grey scaled view of CAD design of multiple gas cooler cart

For the water lines braid-reinforced tubing was used. The refrigerant lines were done with stainless steel tubing to withstand the high pressures of up to 120 bar during operation. Compact brazed plate gas coolers were sourced for the multiple gas cooler assembly (Figure 4-75).

Figure 4-75: Brazed plate heat exchangers for gas cooler optimization

The implementation of the CAD model into the HPWH system visualized the orientation of the components towards each other which is shown in Figure 4-76.

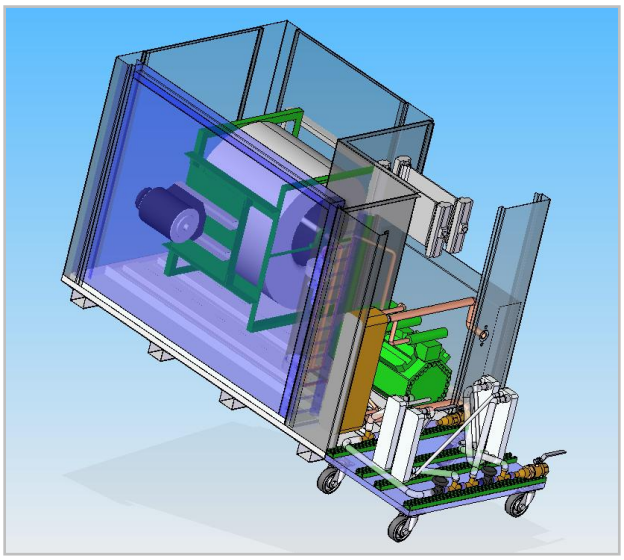

Figure 4-76: HPWH with gas cooler cart

The water lines were assembled using flexible braided reinforced tubing. Insulation was used to minimize possible heat losses to the environment. For the refrigerant lines stainless steel tubing was used because of the high pressure that was reached during operation in the gas cooler of the HPWH. The multiple gas cooler cart is shown in Figure 4-77 and Figure 4-78. Ball valves were used at the water inlet and outlet of the cart to separate it from the water cycle during installation. Also this made it easier to bleed air through the bleeder port of the water cycle. Two water globe valves were installed for a better control of the bypass of the first and second as well as the third and fourth gas cooler.

Figure 4-77: Multiple gas cooler cart

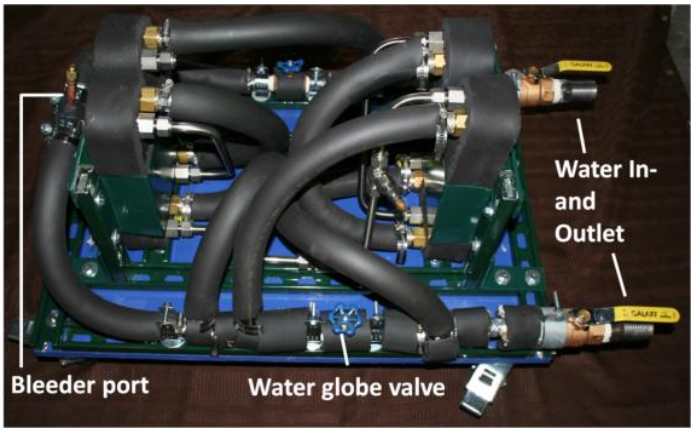

Figure 4-78: Water side components of multiple gas cooler cart

The analysis of the performance and effect of the multiple gas coolers on the HPWH system required additional information on the refrigerant side. Therefore the pressure and temperature after the second brazed plate heat exchanger gas cooler was recorded. With this information the gas cooling characteristic and behavior that was provided by this new component was better visualized. The calibration curve of the added pressure transducer is shown in Figure 4-79.

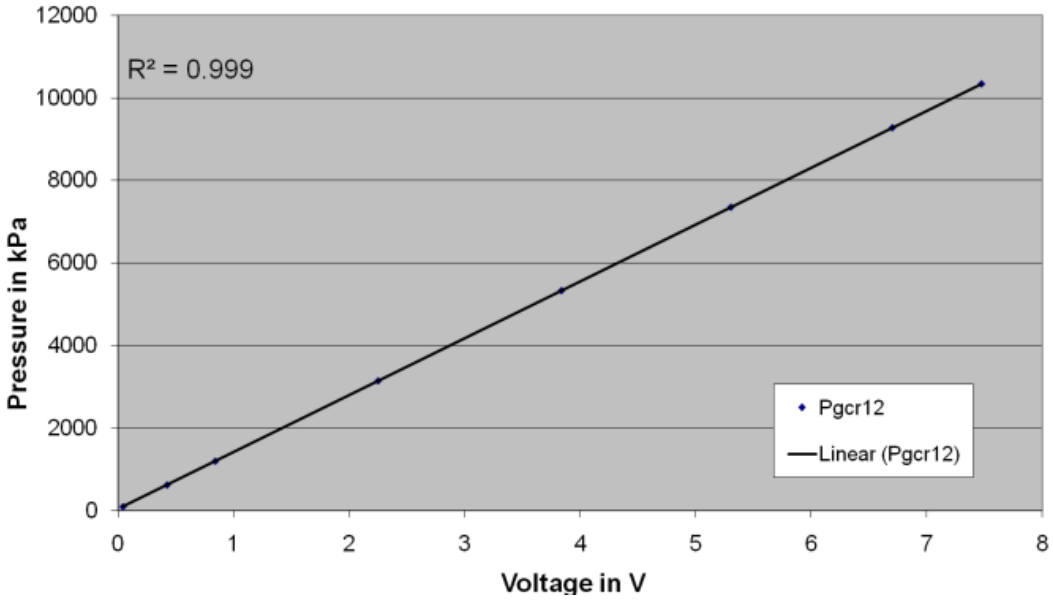

Figure 4-79: Calibration curve of additional gas cooler pressure transducer

Lower water mass flow rates were used for the analysis because of the higher pressure drop of the smaller multiple gas coolers compared to the single larger component with smaller pressure drop. The water side was set up in parallel in order to minimize the pressure drop and to be able to reach higher possible water flow rates. The investigated system schematics are shown in Figure 4-80 to Figure 4-82.

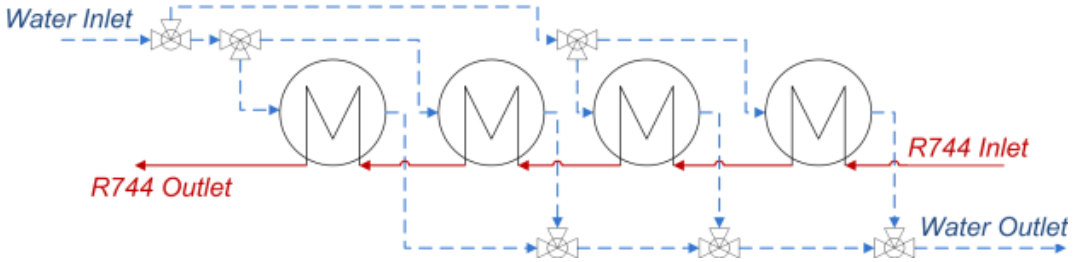

Figure 4-80: Water side in parallel and refrigerant side in series

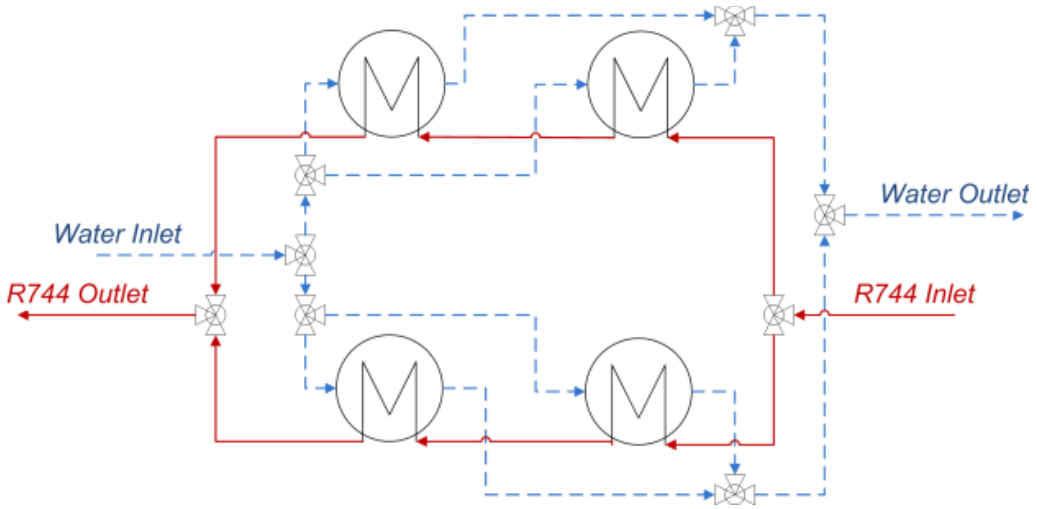

Figure 4-81: Water side in parallel and refrigerant side divided in two and two design

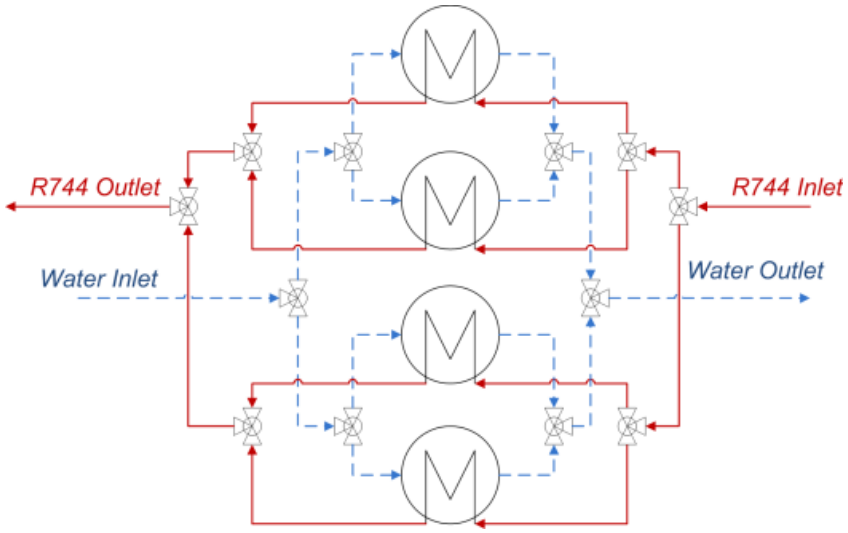

Figure 4-82: Water and refrigerant side in parallel

The refrigerant side was set up in three different configurations. In the first set up the refrigerant side was in series (Figure 4-80). Besides having the water side in parallel this configuration was investigated with the water side in series too. Even though lower flow rates were used for this approach due to the higher pressure drop, information and conclusions of the system performance were possible. The second system schematic was a two and two design of the refrigerant side (Figure 4-81). This means two heat exchangers in series were in parallel towards each other. The water side was in parallel. The third configuration was with both the

refrigerant and water side in parallel (Figure 4-82). This set up was expected to have the worst performance of the three designs due to the shortest heat exchanger length and the worst heat transfer characteristics. The HPWH system was modified for multiple gas cooler tests with adjustments to the refrigerant tubing, water lines and the installation of additional sensors for pressure and temperature. The installed multiple gas cooler cart with water and refrigerant side in series is shown in Figure 4-83.

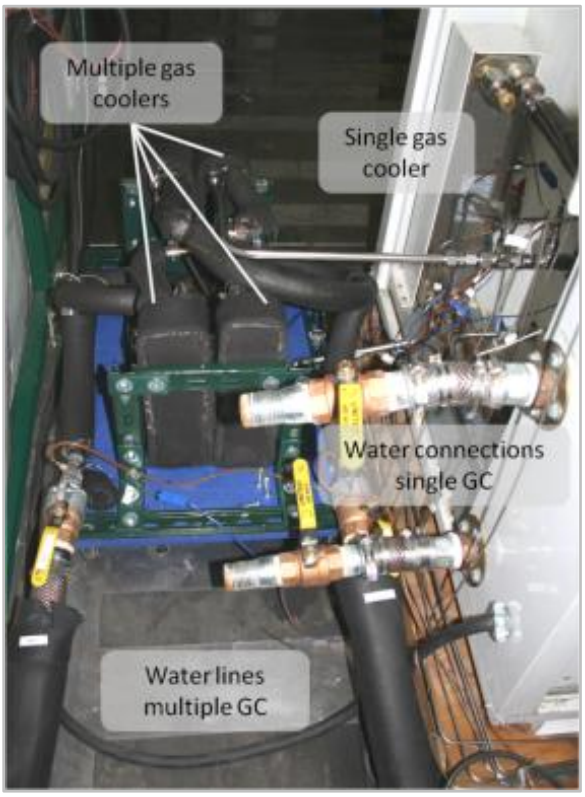

Figure 4-83: Multiple gas cooler cart connected to HPWH

Initial tests were done for both water and refrigerant side in series. The tests were done at a water and air inlet temperature of 26.7°C and various water mass flow rates. The situation in a pressure specific enthalpy diagram at a water mass flow rate of 150 g/s is shown in Figure 4-84.

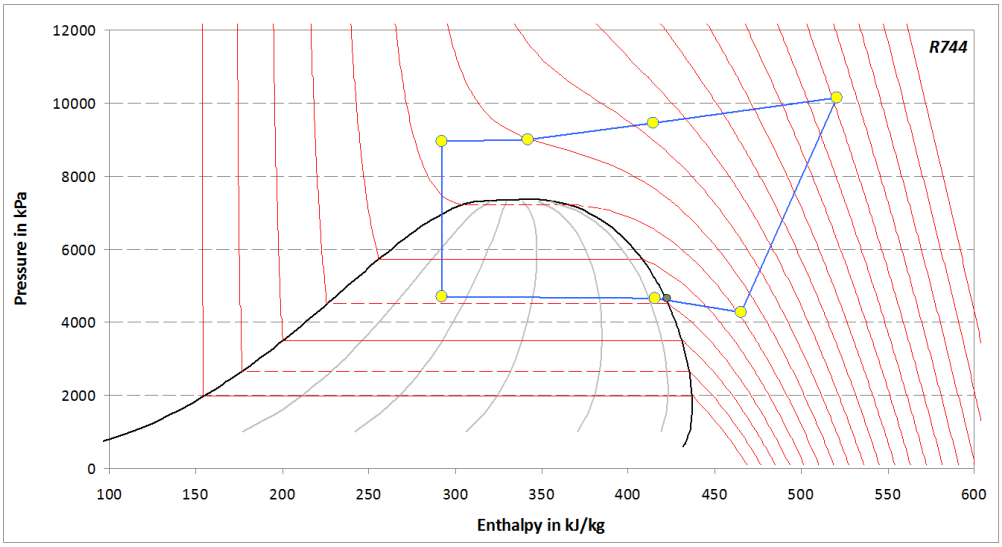

Figure 4-84: Cycle in ph-diagram of HPWH with multiple gas coolers

Even though the tests were not done for higher water mass flow rates the results showed a trend about capacities and COP's for higher flow rates was seen. A comparison of the test results with previous development stages is shown in Figure 4-85.

It can be seen that at the investigated low water mass flow rates very high water temperature lifts were achieved. At the highest water temperature lift a water outlet temperature of 92°C was reached. The trend for the heating COP showed better results compared to the other HPWH systems especially at high water temperature lifts where conduction effects are severe. A maximum improvement of 32% of the multiple gas cooler system over the baseline system can be reached at a water temperature lift of 63 K resulting in a water outlet temperature of 92°C.

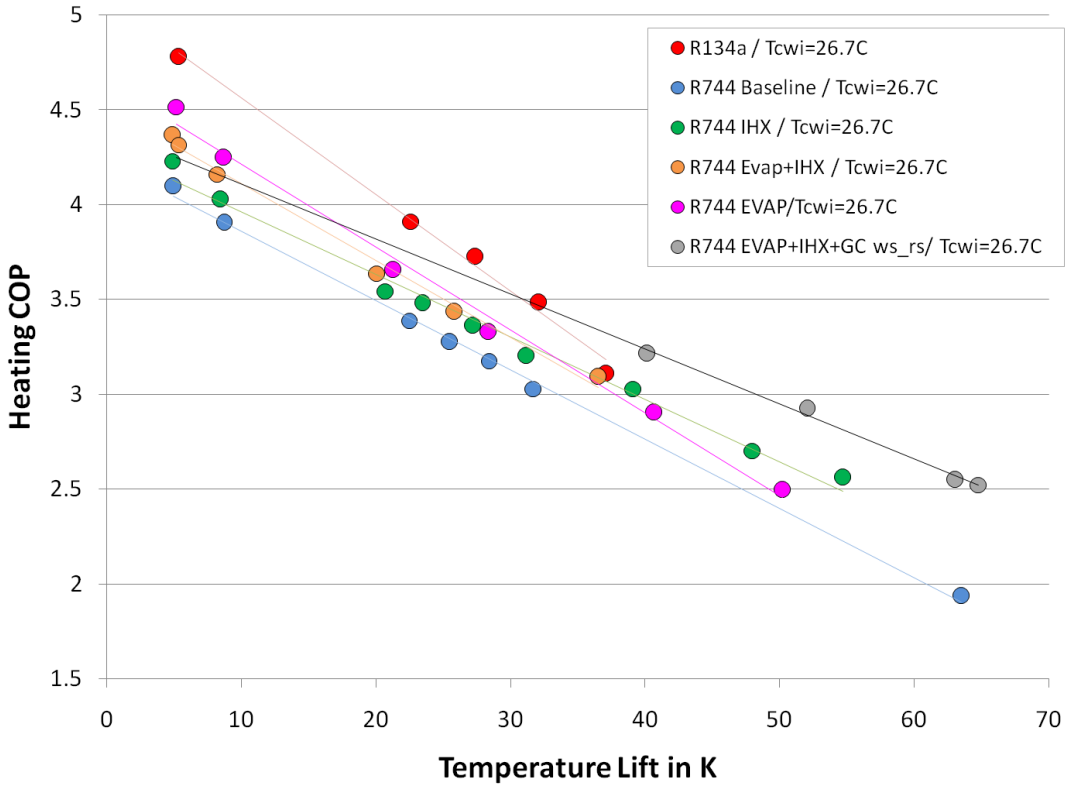

Figure 4-85: Heating COP versus temperature lift for various HPWH systems

Further tests were done with different flow set ups on the refrigerant side. The water side was kept at a parallel routing. The refrigerant side was investigated in series, two and two design, and in parallel routing. The different flow configurations are summarized in Table 4-3.

Table 4-3: Water and refrigerant side flow configurations

#	Water side	Refrigerant side	Abbreviation
1	Series	Series	WS/RS
2	Parallel	Series	WP/RS
3	Parallel	2 and 2	WP/2&2
4	Parallel	Parallel	WP/RP

A comparison of the pressure specific enthalpy diagrams for each step at water flow rate of 150 g/s and a water and air inlet temperature of 26.7°C is shown in Figure 4-86.

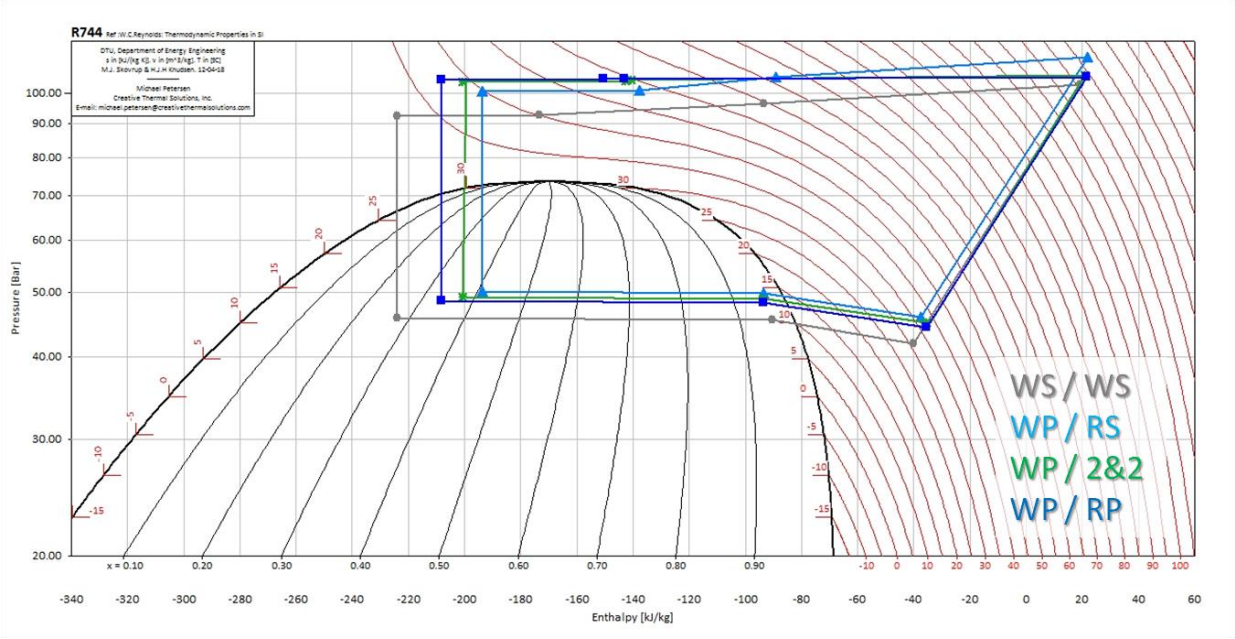

Figure 4-86: Logarithmic pressure specific enthalpy diagram of multiple gas cooler systems

The comparison of the different cycles showed several aspects. The water side had a big impact on the cycle which was seen when comparing the serial and parallel water side test points. The lower high side pressures were realized when a serial water side was used. The three parallel water side tests (Figure 4-86, WP) allow a comparison of the influence of the different refrigerant side configurations for example on the high side pressures, pressure drops and gas cooler exit temperatures. The reason of the different system behaviors can be best described when analyzing the system performance. The characterizing parameters are shown in Figure 4-87 to Figure 4-92.

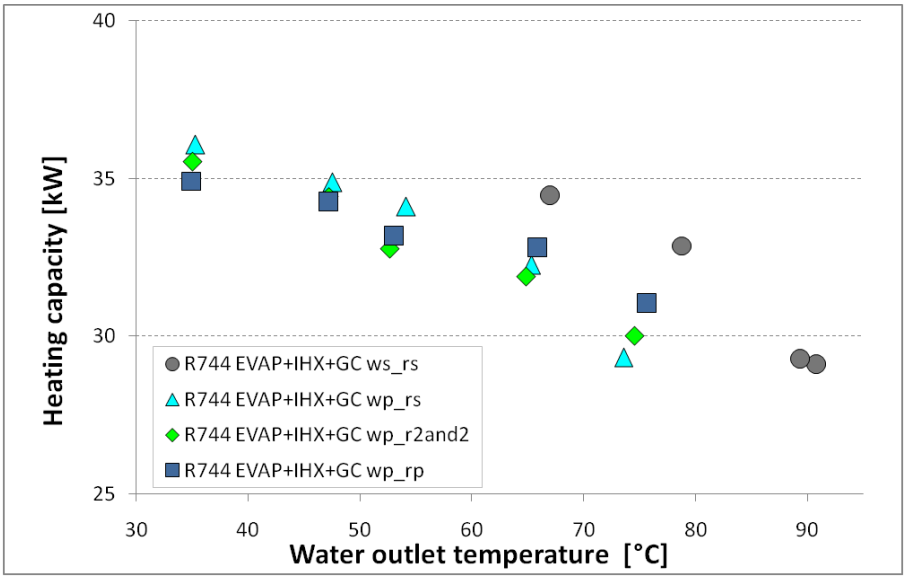

Figure 4-87: Heating capacity versus water outlet temperature

The heating capacity as the useful output of the heat pump water heater was determined on the water and refrigerant side. Figure 4-87 shows the heating capacity on the water side calculated by the water temperature lift, the specific heat and the water flow rate. As expected the configuration with both water and refrigerant side in series or counter flow showed the highest capacity values. All other configurations differed from the ideal counter flow heat exchanger and therefore showed lower capacities. The ratio between useful heating output and necessary HPWH power consumption is the heating COP (Figure 4-88). Combining both useful outputs of heating and cooling capacities divided by the necessary power consumption is the combined COP (Figure 4-89). Both parameters described the performance of the system whereas the heating COP was of main interest when heating up water. However the combined COP represented the overall performance of the system. It was seen that the ideal counter flow configuration showed the best performance. Theoretically it was expected that as the configuration differed more from the ideal counter flow set up the performance would have become worse. This behavior was not seen in the performance results shown in Figure 4-88 and Figure 4-89 as the system with parallel routing on water and refrigerant side showed better COP values at higher water temperature lifts.

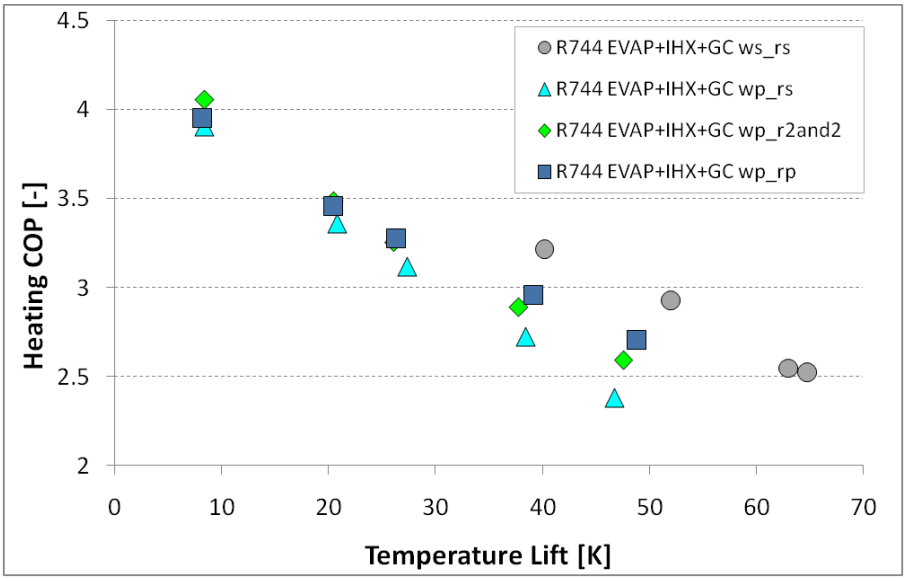

Figure 4-88: Heating COP versus water temperature lift

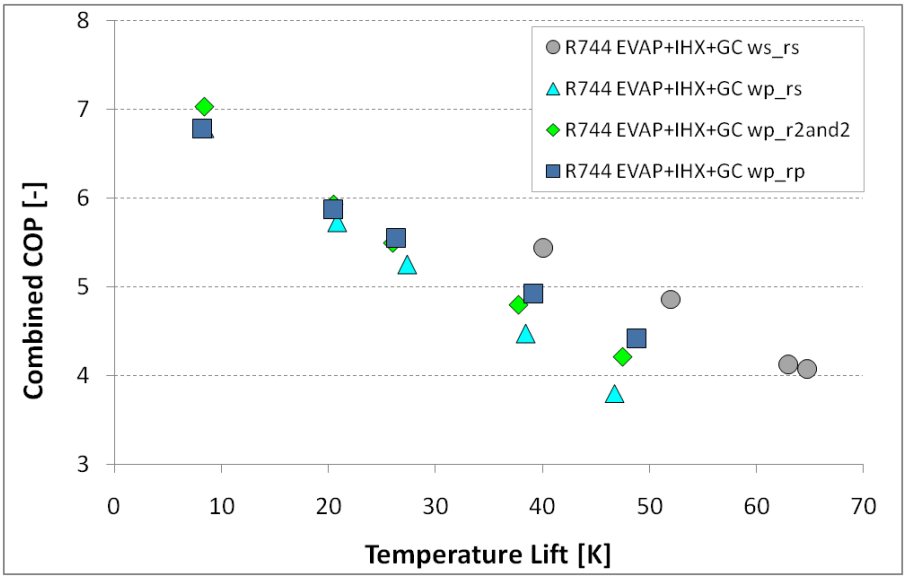

Figure 4-89: Combined COP versus water temperature lift

In order to determine the influence of different fluid routings on the system behavior component specific parameters had to be analyzed. One aspect was the approach temperature difference which is defined in equation (14).

$$T_{Approac\ h,GC} = T_{gcro} - T_{cwi} \qquad (14)$$

With: Tgcro Gas cooler outlet temperature
Tcwi Water inlet temperature

The approach temperature difference describes how close the heat exchanger refrigerant exit temperature approaches the coolants inlet temperature. An approach temperature difference of zero meaning the refrigerant outlet temperature equals the water inlet temperature cannot be achieved in real applications because this would be an ideal heat exchange without losses. The gas cooler approach temperature difference for the four gas cooler configurations is shown in Figure 4-90.

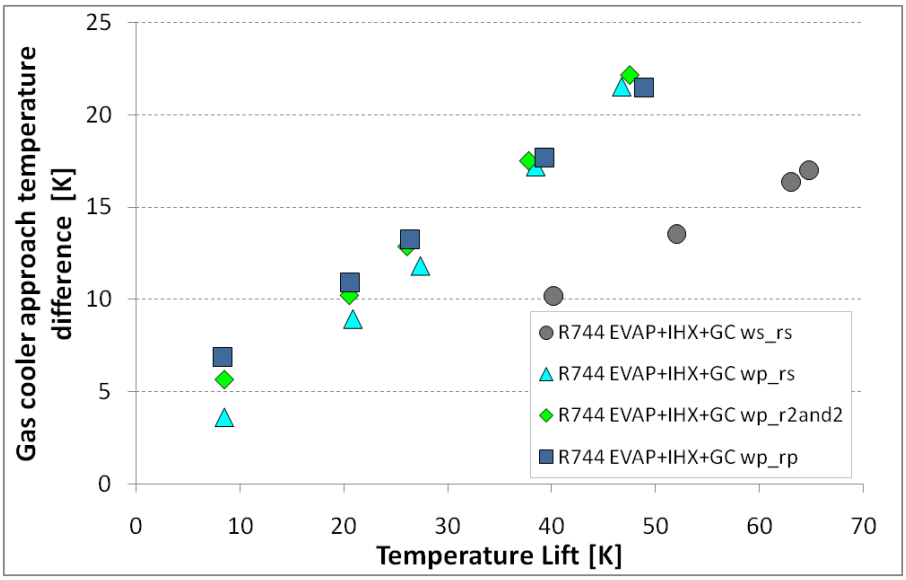

Figure 4-90: Gas cooler approach temperature difference versus water temperature lift

Especially at low water temperature lifts the expected performance development from serial to parallel refrigerant side approach temperatures was seen. The serial set up showed the performance of the three systems with parallel water side. Going to higher water temperature lifts the difference between the systems decreases and all three show almost the same performance. Another important characteristic is the logarithmic mean temperature difference (LMTD) which is defined in equation (2). The LMTD (Figure 4-91) specifies the average temperature difference between the two fluid streams and is also an indicator for the driving temperature gradient between the two fluids. However a low LMTD represents a good heat exchanger performance.

$$LMTD = \frac{(T_{gcro} - T_{cwi}) - (T_{cpro} - T_{cwo})}{\ln \frac{(T_{gcro} - T_{cwi})}{(T_{cpro} - T_{cwo})}} \quad (15)$$

With: Tcpro Compressor outlet temperature

Tcwo Water outlet temperature

The gas cooler LMTD confirmed the behavior that was seen for the approach temperature difference. At low water temperature lifts the counter flow configuration showed the lowest LMTD whereas the parallel set up had the largest LMTD.

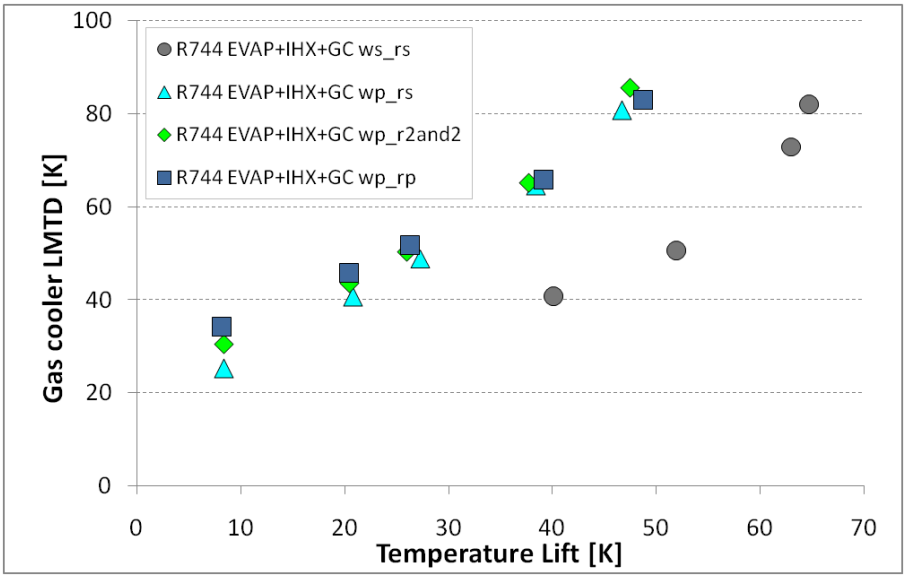

Figure 4-91: Gas cooler LMTD versus water temperature lift

The heating and combined COP described the overall system performance. When looking at the gas cooler itself a component efficiency that is a ratio between actual heating enthalpy difference and maximum enthalpy difference can be defined (16).

$$\varepsilon_{GC} = \frac{h_{cpro} - h_{gcro}}{h_{cpro} - [h = f(p_{gcro}, T_{cwi})]} \quad (16)$$

The maximum enthalpy difference was calculated at the gas cooler outlet pressure and water inlet temperature meaning ideal heat exchange or no approach temperature difference. The gas cooler efficiency is shown in Figure 4-92.

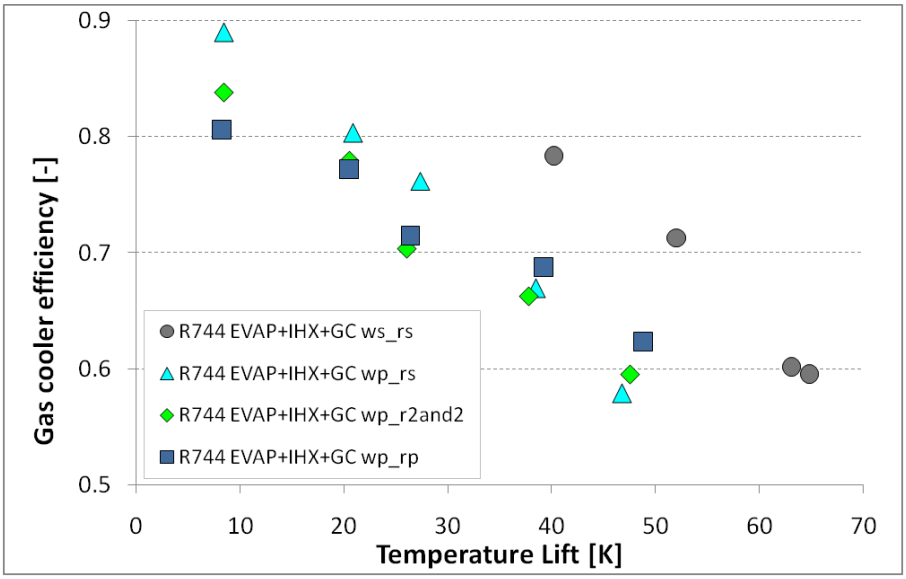

Figure 4-92: Gas cooler efficiency versus water temperature lift

It can be seen that the serial refrigerant configuration shows the best performance at lower water temperature lifts. Going to higher water temperature lifts the performance of the serial gas cooler drops and the parallel routing becomes more beneficial. The best performance can be achieved by the system with water and refrigerant side in series.

4.5 Ejector

The improvement of the expansion device is concentrating in reducing the throttling losses by using a two-phase ejector. The system schematic of the ejector cycle with IHX and the corresponding pressure specific enthalpy diagram are shown in Figure 4-93 and Figure 4-94.

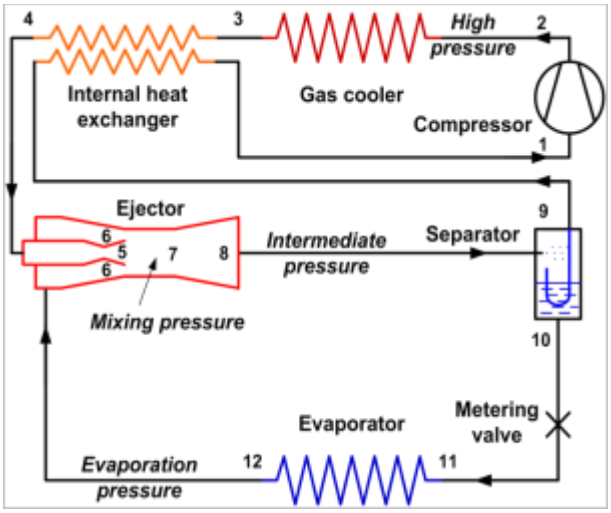

Figure 4-93: HPWH system schematic with ejector and IHX

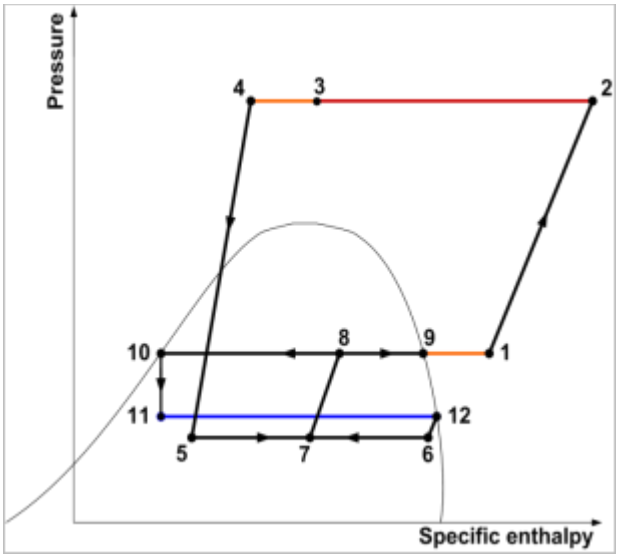

Figure 4-94: Pressure specific enthalpy diagram of HPWH system with ejector and IHX

An ejector can improve the system performance of the HPWH by recovering expansion work which minimizes the throttling losses that cannot be avoided when expanding the refrigerant from high pressure to low pressure. The ejector is beneficially influencing the system performance in different aspects. On the one hand the ejector reduces the compressor power by pre-compressing the refrigerant leaving the evaporator. On the other hand the ejector has a positive effect by providing liquid refrigerant to the evaporator. Due to the higher density the pressure drop is reduced through the evaporator. The liquid refrigerant is also improving the distribution in the evaporator which creates a more homogeneous temperature profile in the heat exchanger. Also the refrigerant side heat transfer coefficient is increased due to the better heat transfer characteristics of liquid compared to vapor. Finally a better isentropic efficiency can be achieved which results from the higher suction density of the refrigerant entering the compressor. The working principle of the ejector can be best described when looking at the qualitative pressure and velocity profiles.

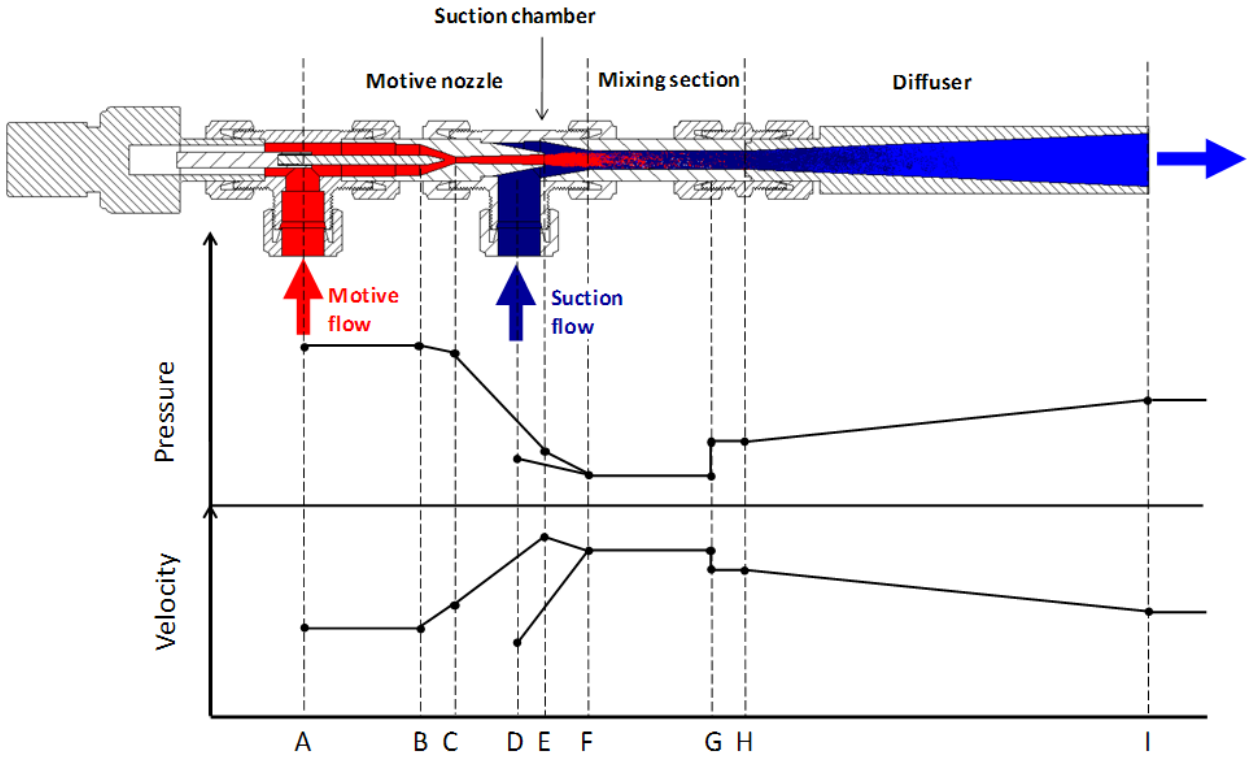

Figure 4-95: Qualitative trends of pressure and velocity in the ejector

Trends of pressure and velocity are qualitatively illustrated in Figure 4-95. The high pressure motive flow enters the converging-diverging motive nozzle (A) and undergoes a significant pressure drop. As the fluid expands in the diverging part of the motive nozzle (C) – (E) the velocity of the fluid can increase to values above supersonic speed. Therefore, the fluid gains kinetic energy that is transferred to the suction flow that enters the suction chamber (D). At the inlet to the mixing section the flows start to mix and their pressures and velocities equalize (F). Before the outlet of the mixing section (G) possible shock waves can cause a sharp decrease in velocity and a significant pressure rise. In the subsequent diffuser further compression is achieved with a reduction of velocity (H) – (I).

Several characteristics are used to evaluate the performance of the ejector at various conditions. The following set of equations defines the parameters for the ejector performance. Figure 4-96 graphically illustrates the ejector performance characteristic in a pressure-specific enthalpy diagram.

The mass entrainment ratio is the proportion of the suction mass flow rate to the motive mass flow rate as defined in Equation (1). Equation (2) defines the suction pressure ratio meaning the

ratio of the pressure at the diffuser outlet to the evaporator outlet pressure. A trade-off exists between the mass entrainment ratio and the suction pressure ratio. Either the ejector lifts a large amount of suction mass flow over a low pressure difference or vice versa. This can be controlled by means of the liquid metering valve upstream of the evaporator inlet.

$$\phi_{m,Ejector} = \frac{\dot{m}_{Suction}}{\dot{m}_{Motive}} \quad (17)$$

$$\pi_{s,Ejector} = \frac{p_{Diffuser\ ,out}}{p_{Evaporator\ ,out}} \quad (18)$$

The pressure lift of the ejector is defined in Equation (3) and expresses the difference from the diffuser outlet pressure to the evaporator outlet as indicated in Figure 4-96. The higher the pressure lift, the higher is the compressor inlet pressure which reduces the compressor power consumption and increases the COP. However, a high pressure lift reduces the suction mass flow rate and results in a lower cooling capacity which also reduces the COP. An optimum COP is a balance between a high pressure lift and a relatively large suction mass flow rate.

$$p_{Ejector\ ,lift} = p_{Diffuser\ ,out} - p_{Evaporator\ ,out} \quad (19)$$

The efficiency of the ejector is defined in Equation (4) and expresses the ratio of the work rate that is recovered by the ejector to the work rate potential. As shown in Figure 4-96, the work rate potential is the difference from isentropic expansion to isenthalpic expansion by the ejector from the ejector inlet pressure to the diffuser outlet pressure. The amount of work rate that the ejector actually recovers is an isentropic pressure lift of the suction mass flow rate from the evaporator outlet to the diffuser outlet pressure.

$$\eta_{Ejector} = \frac{\dot{W}_{recovered}}{\dot{W}_{potential}} \quad (20)$$

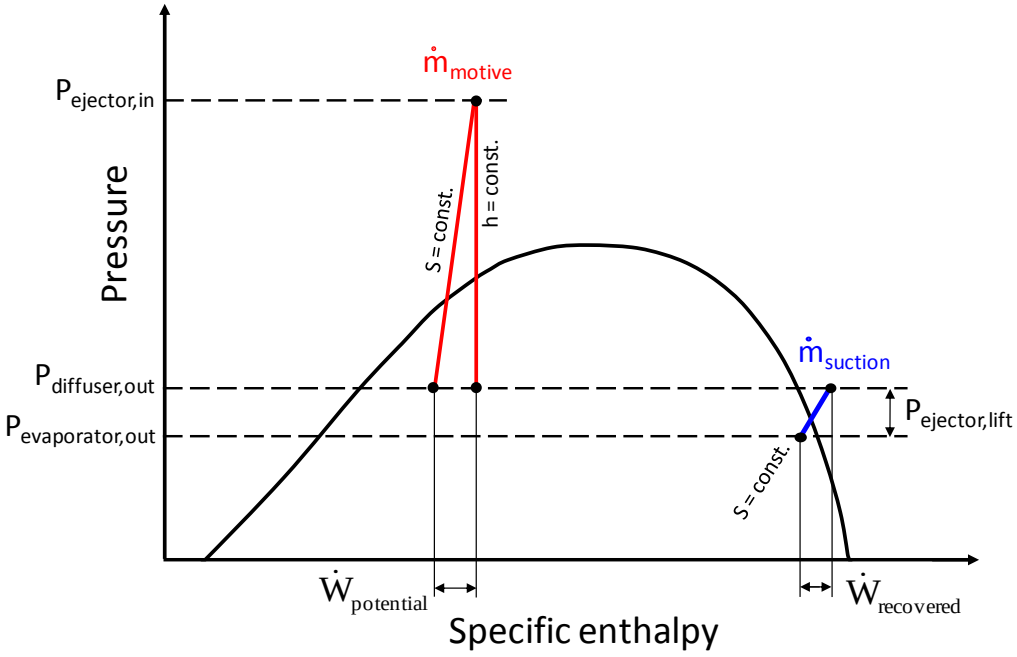

Figure 4-96: Ejector performance characteristics in a pressure-specific enthalpy diagram

Phase separator

The modification of the HPWH for ejector tests required additional components. A phase separator was used to separate the two-phase refrigerant flow coming from the ejector into its vapor and liquid fractions. A commercially available coalescing separator was sourced. The separator with its inlet, outlet and liquid ports as well as the port for the liquid level sensor is shown in Figure 4-97.

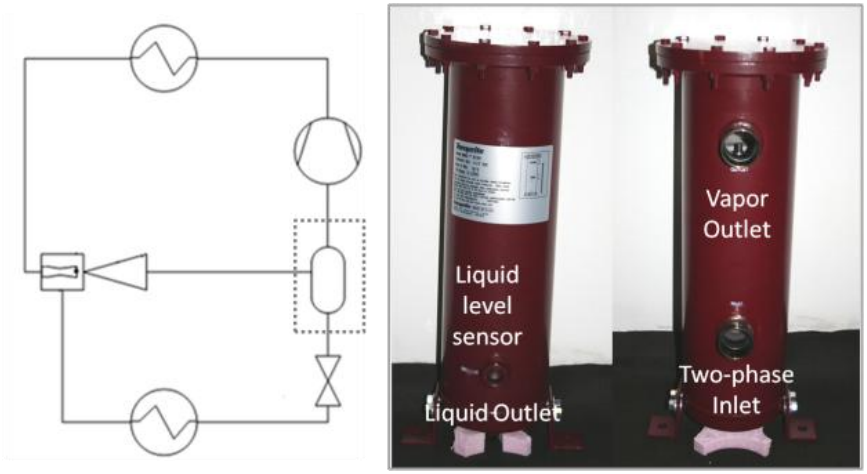

Figure 4-97: Phase separator

The working principle of the coalescing phase separator is illustrated in Figure 4-98. The two-phase inlet stream enters the filter element inside of the phase separator where it passes the cartridge from the inside to the outside. The filter cartridge consists of three layers. The droplets of the liquid phase of the stream wet the surface of the fine inner layer thus forming larger droplets. These large droplets continue moving through the cartridge and coalesce to bigger droplets as they travel through the coalescing layer. A pressure difference between the inside and outside of the filter element forces the large droplets through the mesh of the coarse outer layer. On the outside of the filter element gravity forces the formed droplets downwards where they are collected at the bottom of the vessel and build up a liquid level. The less dense gas flows upwards and is entrained through the vapor outlet.

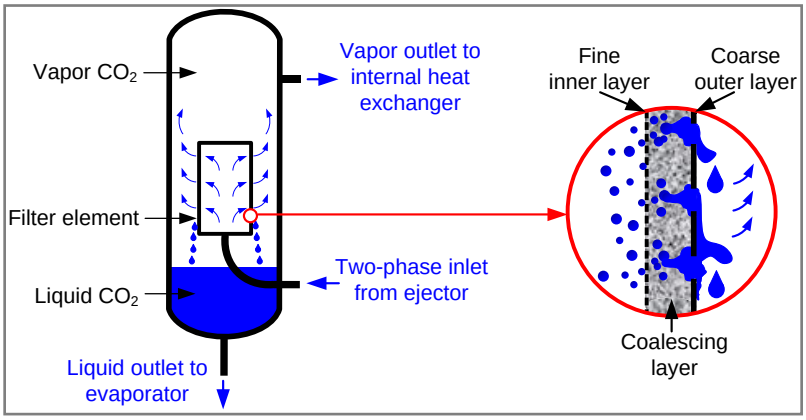

Figure 4-98: Schematic and working principle of a coalescing phase separator

A CO_2 liquid level sensor was used to monitor the height of the liquid column inside of the phase separator. A liquid volume of 1.26 l was reached when the sensor was activated.

Figure 4-99: CO_2 liquid level sensor

An important indicator of the phase separators performance is the separation efficiency (Equation (21)). The separation efficiency expresses the difference from the liquid mass flow

entering the phase separator to the remaining liquid that is contained in the vapor leaving the phase separator.

$$\eta_{Sep} = \frac{\dot{m}_{liquid\ ,in} - \dot{m}_{liquid\ ,entained\ \ ,vapor\ \ port}}{\dot{m}_{liquid\ ,in}} \qquad (21)$$

The integration of the stepper motor into the ejector design allowed a convenient and effective control of the ejector needle position. During operation the needle was moved axially into the throat which decreased the throat area. The relationship between axial needle movement, resulting throat area and the ejector opening is visualized in Figure 4-100.

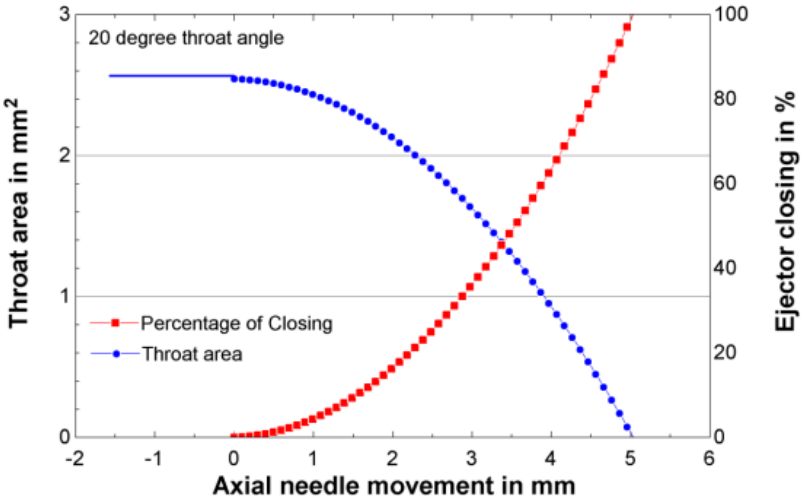

Figure 4-100: Throat area versus axial needle position

The relationship between those three parameters was calculated for a throat angle of 20 degrees. The percentage of the ejector closing was the relationship between the maximum throat area and the throat area which resulted from the needle position. Due to the circular shape of the needle and the throat area the resulting annulus area had an exponential influence on the ejector closing. This had to be considered when operating the ejector. For a small closing percentage no major influence on the throat area was seen. However when the ejector was closed further the influence became more evident.

It was seen that the throat area was constant until the needle entered the throat. Because of the size of the needle tip the area decreased immediately which resulted in a step. The following Figure 4-101 shows a detailed view of the influence of the needle tip.

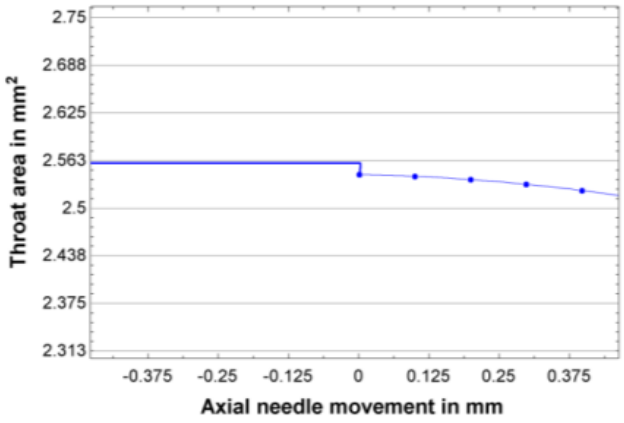

Figure 4-101: Throat area versus needle position (detailed view)

The phase separator and ejector assembly were included in the HPWH CAD design. This was done in order to design the tubing and the location of the components towards each other. An overview of the HPWH with phase separator and ejector as well as a detailed view is shown in Figure 4-102.

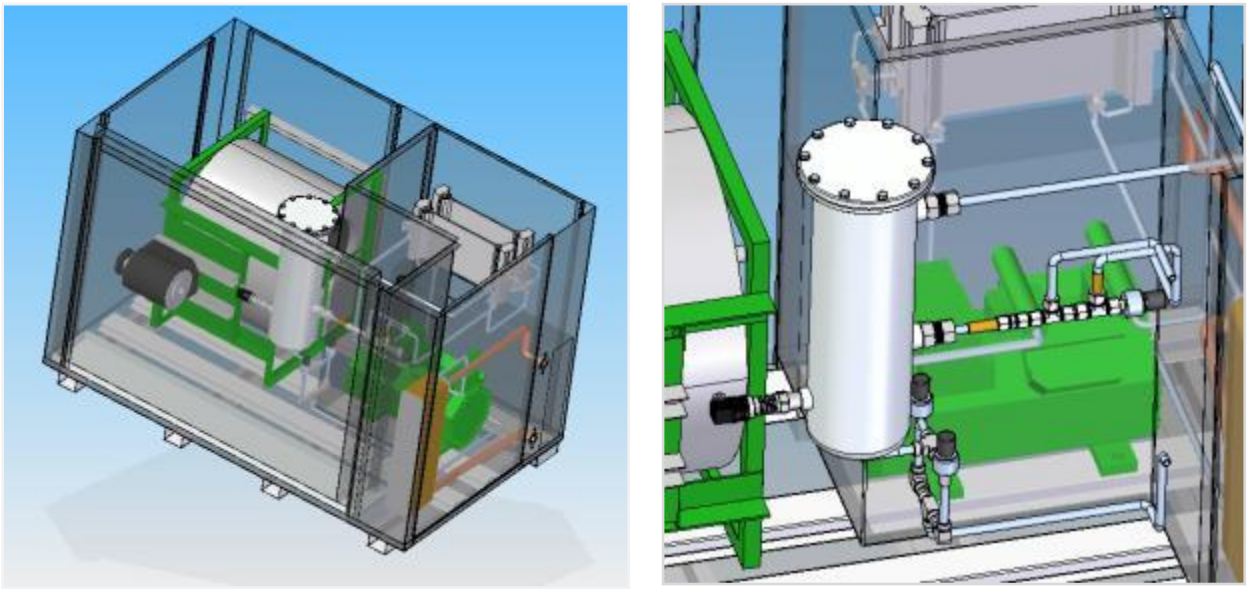

Figure 4-102: Ejector and phase separator in HPWH assembly and detailed view

A modified system schematic was necessary for ejector operation. The phase separator was mounted on brackets on the base plate of the HPWH. This ensured enough installation space for the liquid line that connected the evaporator. For shakedown tests the internal heat

exchanger (IHX) was used to ensure safe operation and enough superheat on the suction side of the compressor. The IHX was isolated for following steps of the project. For this only minor modifications on the suction side of the compressor and the discharge side of the gas cooler were necessary.

The shakedown tests of the heat pump water heater (HPWH) system with internal heat exchanger (IHX) and ejector were done with special interest on the functionality of the ejector. Other important aspects were the adjustment of charge, and metering valve to get experience of the liquid refrigerant level inside the phase separator and its response to different operating conditions. A steady liquid column inside the phase separator was desired in order to provide liquid refrigerant to the evaporator.

The following pressure specific enthalpy diagram of the shakedown test can be seen in Figure 4-103.

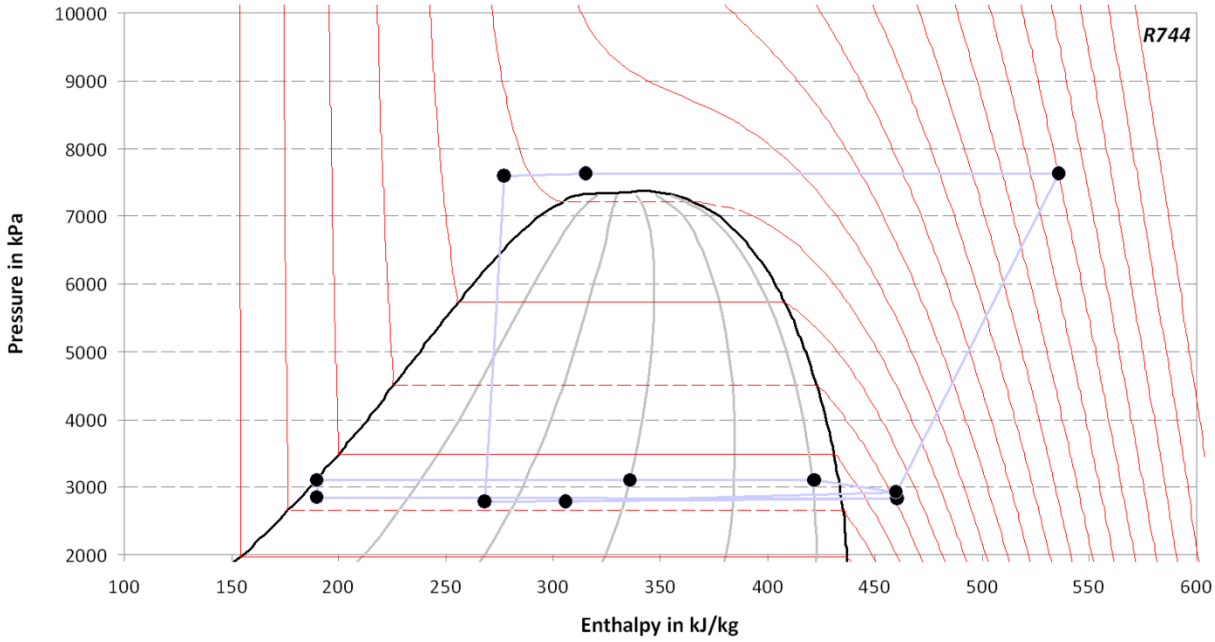

Figure 4-103: Pressure specific enthalpy diagram of a shakedown test ejector system with internal heat exchanger

In the development and improvement process of the R744 HPWH the use of an internal heat exchanger (IHX) was investigated. Positive effects on the system performance were seen and therefore better heating COP's were reached. However the IHX showed a relatively high

pressure drop which offset the improvement. Even better results could have been reached with a reduced pressure drop. This had an important impact especially for ejector systems. The ejector decreased the necessary compressor power by increasing the suction pressure. If an IHX with a high pressure drop would be used this benefit would be abolished. Therefore a minimum of pressure drop on the suction side was very important. That is why a new IHX design was sourced to obtain both good thermal as well as pressure drop characteristics. This brazed plate heat exchanger (BPHX) is shown in Figure 4-104.

Figure 4-104: Brazed plate internal heat exchanger

The BPHX was equipped with ½ inch male NPT connections on the low and high pressure side. Adapters going from ½ inch NPT to ½ inch Swagelok connections on the high pressure side and ½ NPT to 5/8 inch Swagelok on the low pressure side were used. The same system schematic that was used for the previous IHX set up was used. The tubing had to be modified though according to the smaller dimensions of the component.

The insufficient separation efficiency of the phase separator was identified earlier to have a negative influence on the operation behavior of the HPWH system without internal heat exchanger. As a first step in improving the separation efficiency a splash plate was installed inside of the filter element. This splash plate was anticipated to have a beneficial influence on the separation efficiency by reducing the speed of the refrigerant flow and rerouting it to better

utilize the coalescent filter. The test results for the set up with splash plate are shown in Figure 4-105 and Figure 4-106.

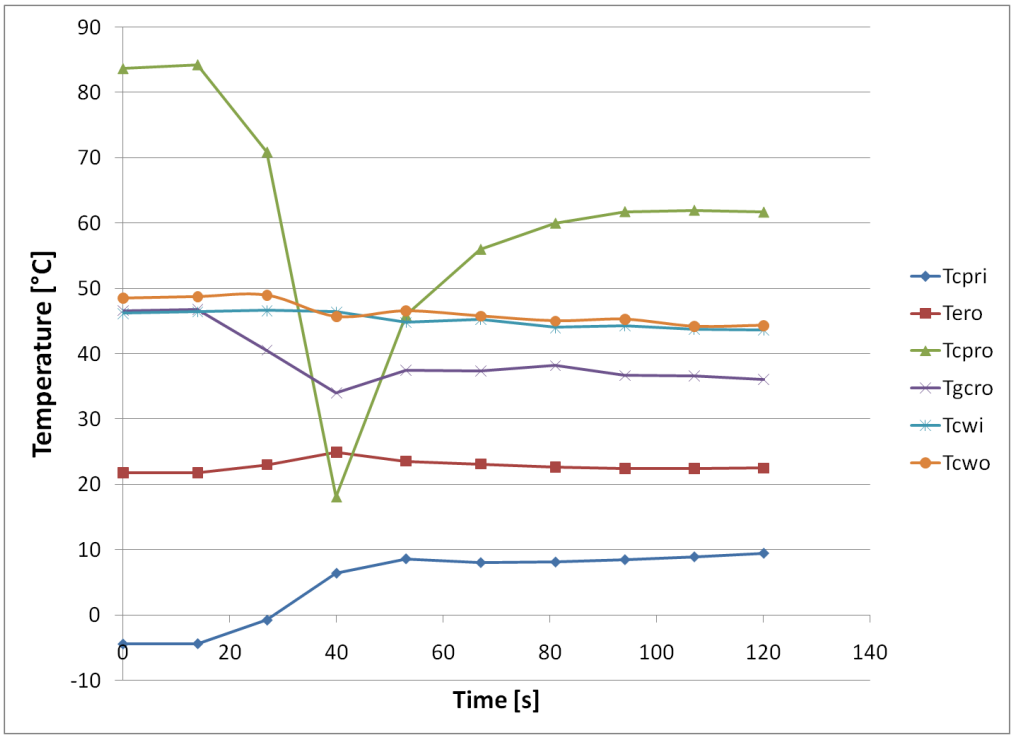

Figure 4-105: Transient temperatures for splash plate configuration

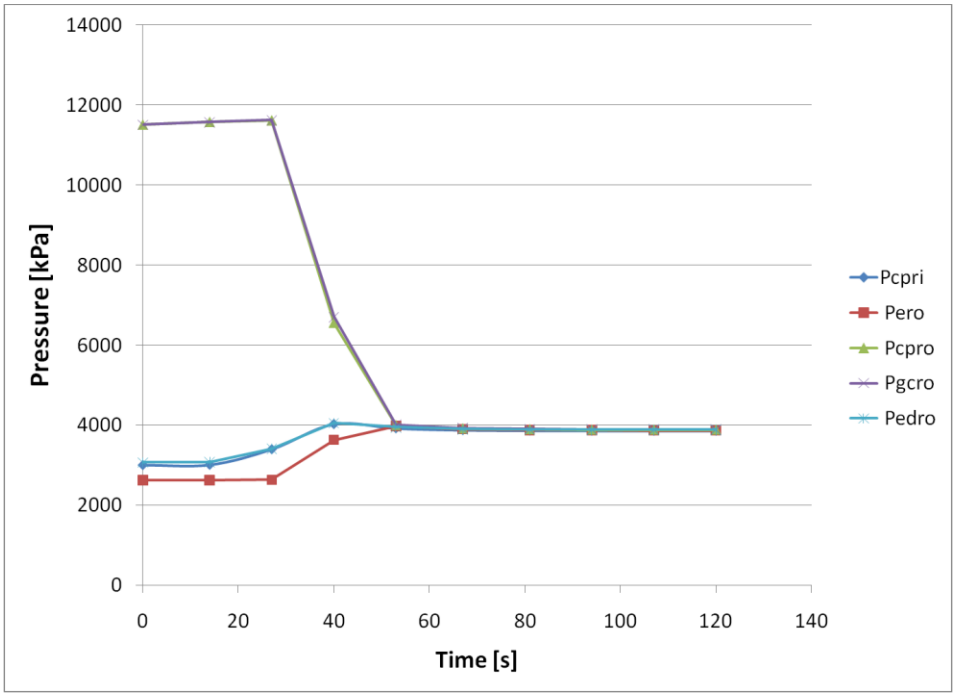

Figure 4-106: Transient pressures for splash plate configuration

The results of temperature and pressure versus time document the behavior that was seen when the liquid fraction of the suction refrigerant flow increased and finally shut down the compressor due to sudden pressure increase. This showed that no significant improvement was achieved with this solution.

As a second step a stacked filter configuration was used to improve the component performance. A schematic of the stacked filter configuration is shown in Figure 4-107.

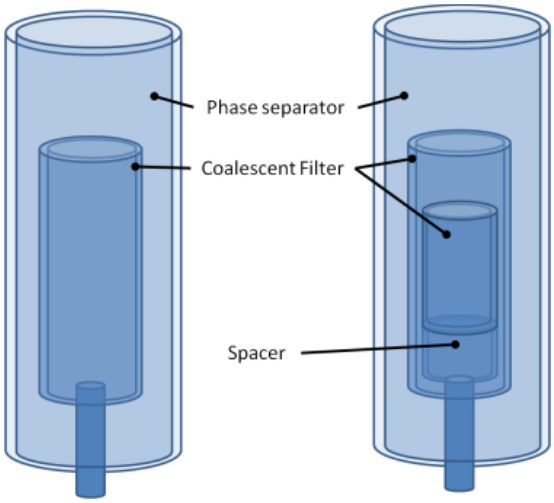

Figure 4-107: Conventional filter (left) and stacked filter separator (right)

A spacer for the stacked configuration was used to overcome the four leg adapter piece which holds the threaded rod. The spacer piece and the modified smaller coalescent filter are shown in Figure 4-108.

Figure 4-108: Large filter and small filter assembly with the spacer sleeve

Another option to improve the separation efficiency was to decrease the refrigerant flow rate to reduce the inlet velocity of the refrigerant flow which would have led to less turbulence inside the phase separator. The refrigerant flow rate was reduced by decreasing the compressor speed. In the baseline set up the compressor was running at 60 Hz. By using a various frequency drive (VFD) this frequency was reduced to lower values. The compressor was rated in a speed range of 30Hz and 83Hz. The installed VFD is shown in Figure 4-109.

Figure 4-109: Compressor VFD

The test results of the stacked filter configuration are shown in Figure 4-110 and Figure 4-111. The results for temperatures and pressures show the same behavior that was seen for the configuration with a splash plate. No significant improvement was observed. Consequently the compressor shut off. High separation efficiencies at various inlet conditions are very important for a stable operation when using a system without internal heat exchanger. This high separation efficiency could not be guaranteed with the current component. This shows that a stable operation can be easier guaranteed by using an internal heat exchanger which ensures superheated refrigerant on the suction side of the compressor.

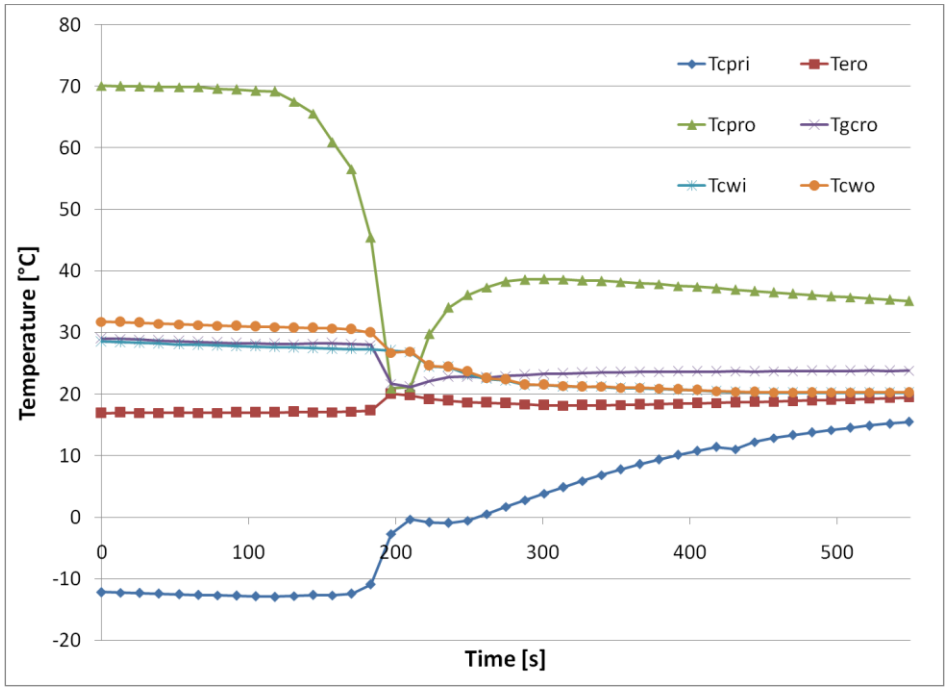

Figure 4-110: Transient temperatures for stacked filter configuration

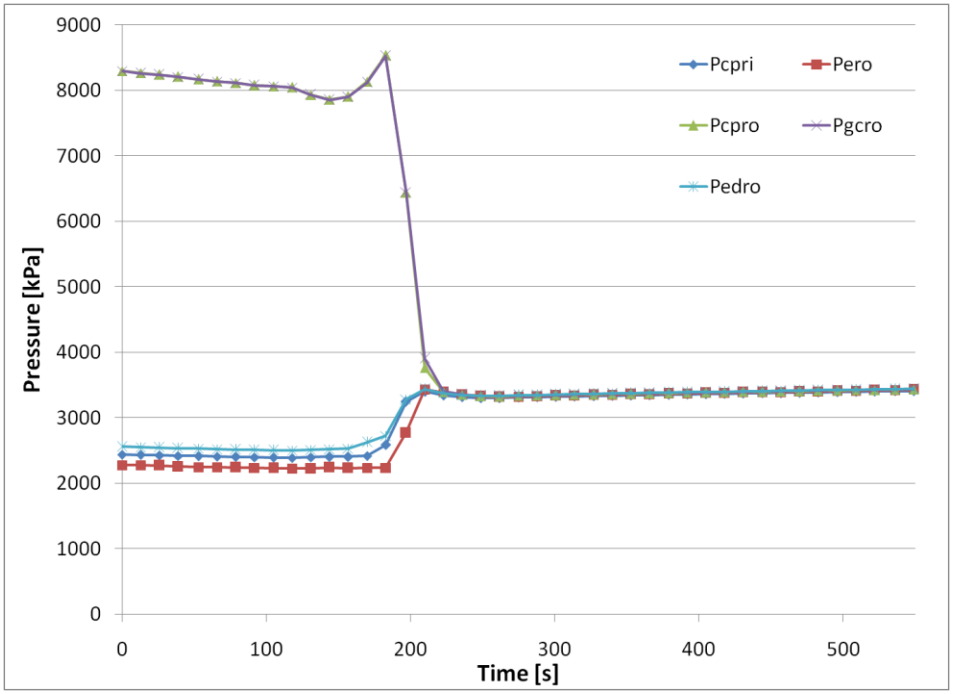

Figure 4-111: Transient pressures for stacked filter configuration

The importance of an internal heat exchanger with good heat transfer characteristics as well as a low pressure drop was pointed out earlier. A new brazed plate internal heat exchanger with a lower pressure drop was used to benefit from better pressure drop characteristics. This heat exchanger was prepared and installed in the HPWH. The installed component is shown in the following Figure 4-112 and Figure 4-113.

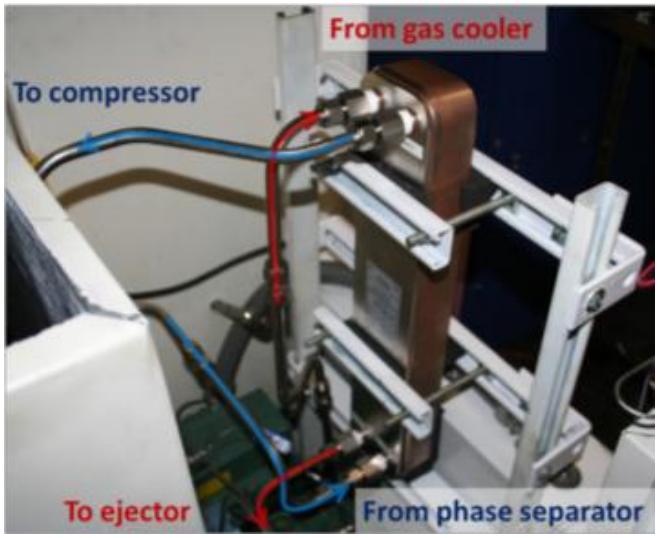

Figure 4-112: Brazed plate internal heat exchanger in HPWH

Figure 4-113: Side view of brazed plate internal heat exchanger

The installation was done using stainless steel tubing because of the high pressures that were reached during operation. The low and high pressure sides were set up in counter flow configuration. The flow configuration differed from the previous set up with microchannel tubes. There the refrigerant entered the heat exchanger headers on the high and low pressure side and was then distributed to the microchannel ports which crossed the IHX in one pass. The hot high pressure side was located between the two cool microchannel profiles. This design offered a good thermal performance but also had a relatively large pressure drop due to the small hydraulic diameters. The brazed plate design has a lower pressure drop due to a larger hydraulic diameter. It can be seen that the hot and cold fluid flow were distributed to the different plates which were set up in counter flow. This compact design combined good heat transfer characteristics with a low pressure drop. Better results for the ejector system were anticipated because the beneficial pressure lift that was created by the ejector was not offset as much as with the microchannel design.

Several system modifications were described that were done to improve the separation efficiency of the component. Another step in this process was the use of a larger phase separator which is shown in Figure 4-114.

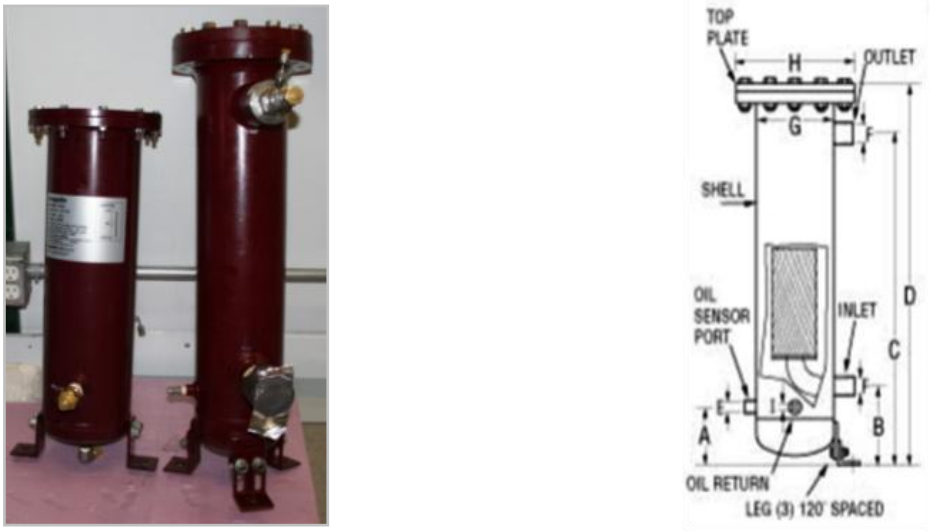

Figure 4-114: Comparison of smaller phase separator from previous investigations and new larger component

Table 4-4: Dimensions and working pressures of larger phase separator

Model	Max. Working	A	B	C	D	E	F	G	H	I
	Press.	Dim.	Dim.	Dim.	Dim.	Dim.	Dim.	Dim.	Dim.	Dim.
135A	130 bar	118 mm	152 mm	433 mm	545 mm	3/4" FPT	3/4" NPT	102mm	176mm	1/4" FPT
	1885 PSI	4.6"	6"	17"	21.4"			4.0"	6.9"	

The new phase separator had the same diameter as the smaller component but it's height as well as the distance between suction and discharge port was larger (Table 4-4). These two parameters positively affected the performance of the phase separator. First tests with the larger component were done at varying compressor speeds using a variable frequency drive (VFD). A comparison of property diagrams at 60 Hz and 47.5 Hz (Figure 4-115) shows the range the speed variation was done at.

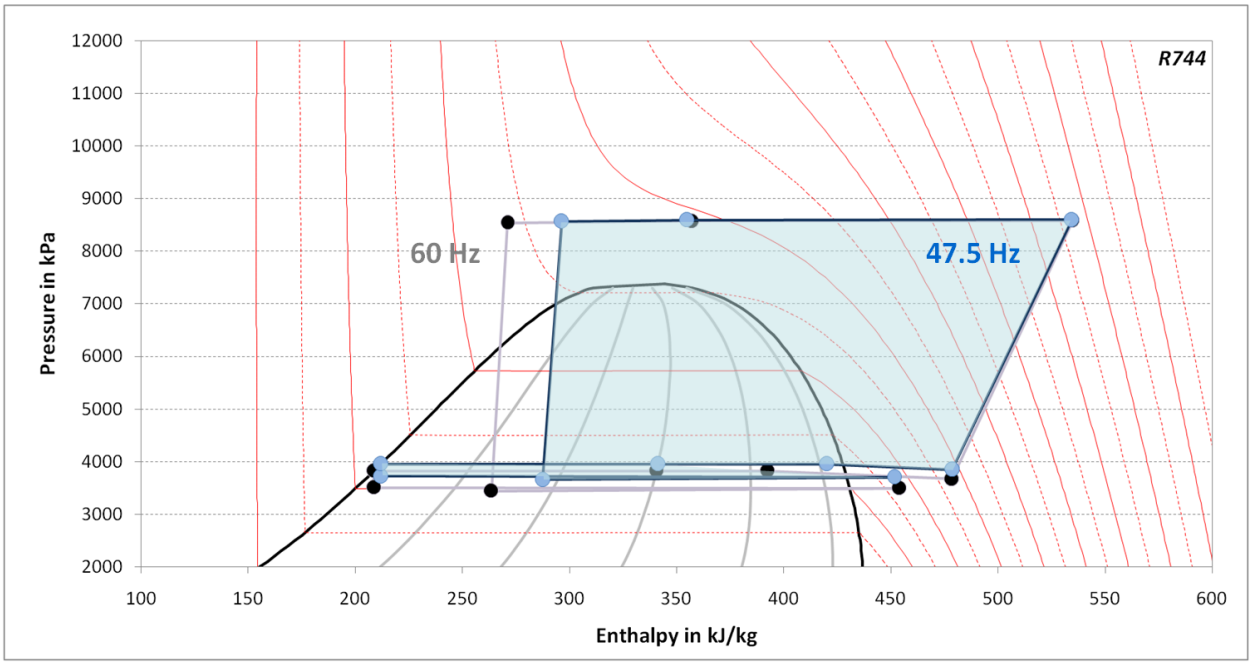

Figure 4-115: Comparison of HPWH cycles in ph-diagram at compressor speeds of 47.5 Hz and 60 Hz

The test results at an ambient air temperature of 26.7°C, a water inlet temperature of 37.8°C and a water mass flow rate of 28 gallons per minute are shown in Figure 4-116 and Figure 4-117.

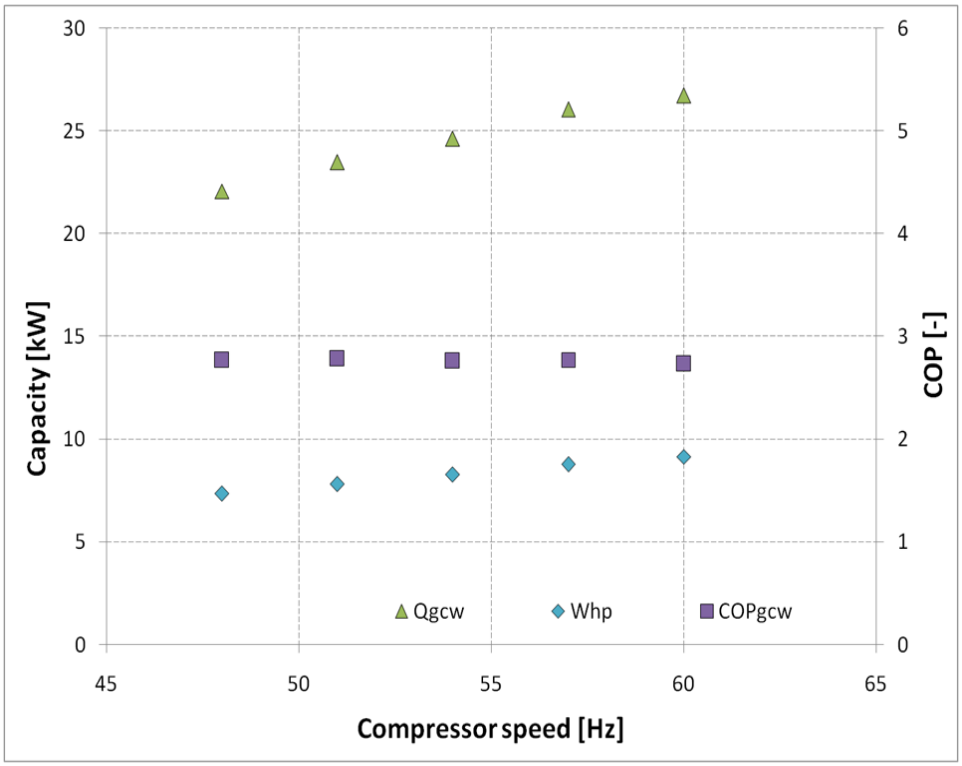

Figure 4-116: Heating capacity, heat pump power and heating COP at varying compressor speeds

Some important characteristics of the heat pump water heater (HPWH) like heating capacity, power consumption and heating COP are shown in Figure 4-116. It is shown that with decreasing compressor speed both heating capacity and power consumption decreased because of reduced refrigerant mass flow rate. Since both values showed the same trend the heating COP stayed at a constant level. To better understand the processes when reducing the compressor speed the refrigerant quality at the discharge of the ejector motive nozzle, the separation efficiency of the phase separator and the refrigerant mass flow rates on the motive and suction side were investigated (Figure 4-117).

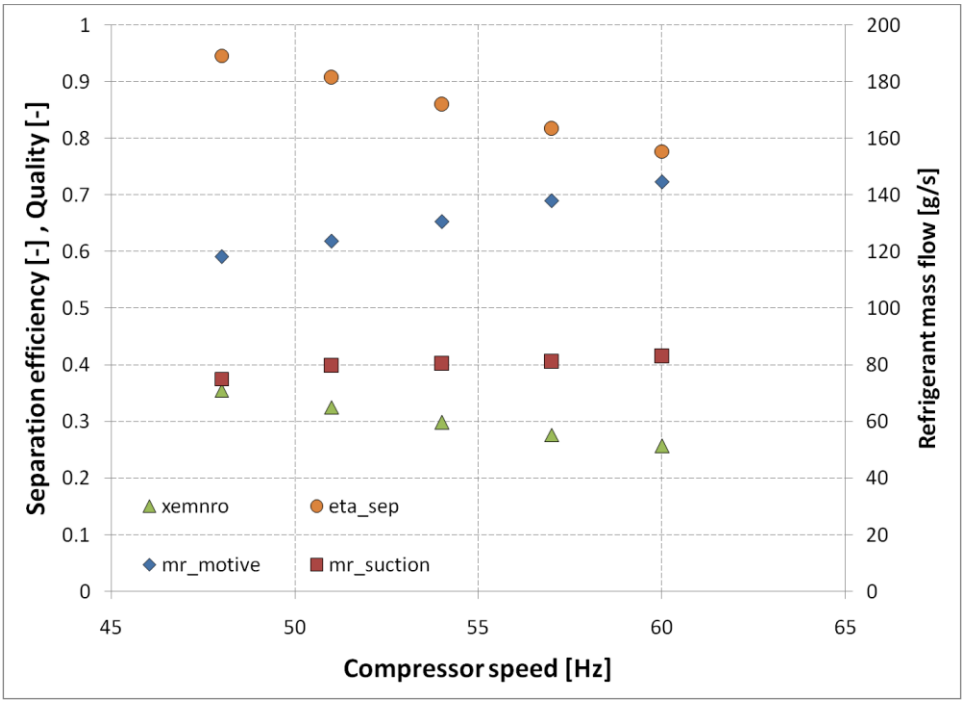

Figure 4-117: Separation efficiency, quality and refrigerant flow rate at varying compressor speeds

As expected the refrigerant mass flow rates on the suction and motive side decreased at lower compressor speeds. However the gradient was much steeper on the motive side compared to the suction side. A big improvement was seen for the separation efficiency. It improved from 78% at a compressor speed of 60 Hz to 95% at 47.5 Hz. This good separation efficiency was expected to be high enough for a stable operation of the compressor.

With the obtained data the main influencing parameters on the separation efficiency were identified as follows.

Phase separator refrigerant inlet velocity

The refrigerant velocity was determined by the mass flow rate that was supplied by the compressor of the system. Even though the refrigerant flow expanded when it entered the phase separator its velocity was still large. Larger velocities led to lower separation efficiencies compared to lower speeds because the coalescent effect became worse. More liquid particles were sucked to the vapor port.

Phase separator coalescent filter design

The coalescent filter separated the liquid particles of the refrigerant flow and combined them to bigger droplets while passing the filter. The separation effect was improved when reducing the pore size of the filter material. However the tradeoff was an increasing pressure drop.

Phase separator design

The separation efficiency was beneficially affected by a proper design and geometry of the phase separator. A larger volume led to better separation between liquid and vapor fraction due to less potential of liquid refrigerant to leave the component. The distance between the inlet and outlet of the phase separator also affected the separation efficiency which was observed in the larger component.

Beside these more apparent parameters the refrigerant inlet condition was an important characteristic which had to be considered. The internal heat exchanger outlet condition on the high pressure side determined the ejector motive nozzle outlet quality. This relationship is described in Figure 4-118 which shows the separation efficiency as a function of the motive nozzle outlet quality.

The linear trend shown by the dotted line describes the observed behavior of the system. With increasing ejector outlet quality increasing separation efficiency was seen. The data points that showed a differing behavior from the trend can be explained by the lower inlet velocities that were achieved by reducing the compressor speed.

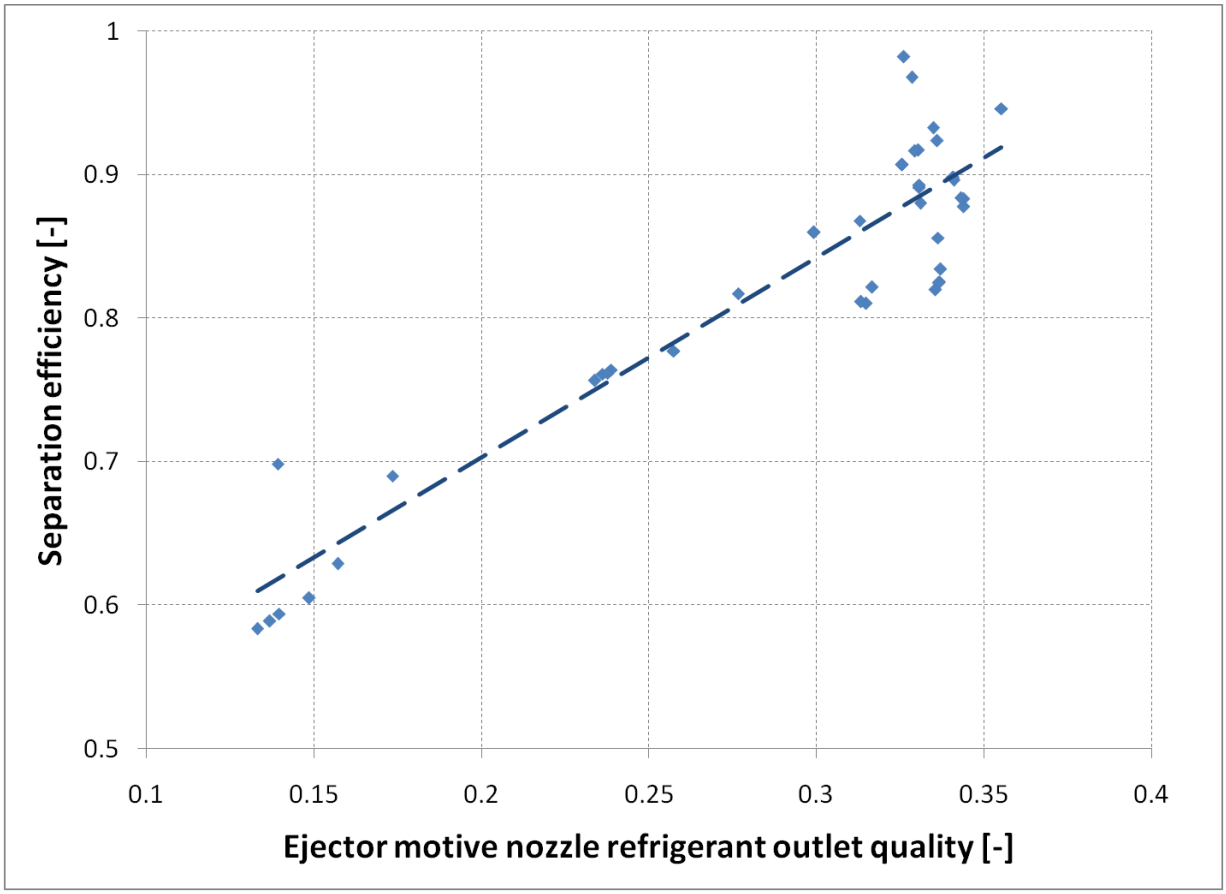

Figure 4-118: Phase separator separation efficiency versus ejector motive nozzle refrigerant outlet quality

The beneficial influence of the ejector motive nozzle outlet quality on the separation efficiency was even better utilized when running the system without IHX. The IHX transferred heat from the hot refrigerant leaving the gas cooler to the cool suction side leading to more sub cooling on the high pressure side and more superheat on the low pressure side. Without the IHX the ejector motive nozzle outlet quality was higher which helped to receive better separation efficiencies. That is why ball valves were used to switch between IHX and no IHX operation. The IHX with the bypass ball valve are shown in Figure 4-119.

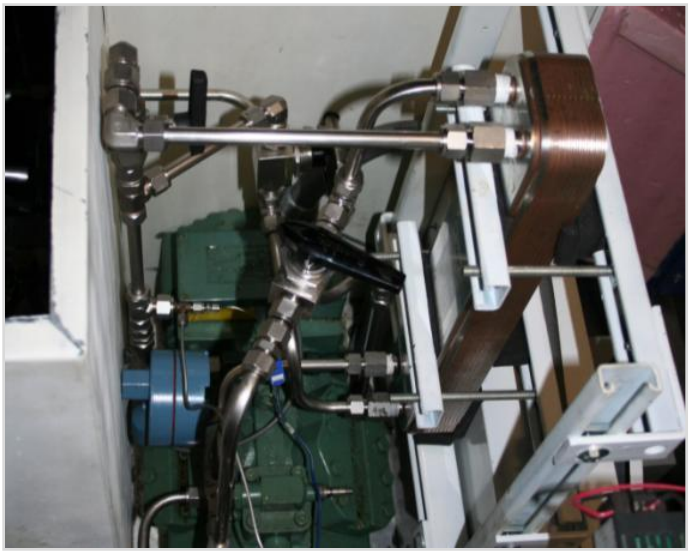

Figure 4-119: IHX with bypass ball valves

The tests were done at an ambient temperature of 26.7°C a water mass flow rate of 1760 g/s and water inlet temperatures of 37.8°C and 50°C. The system was started with full IHX and brought to steady state condition. After taking data the system was gradually switched to operation without IHX and then brought to steady state again to record data. The resulting ph-diagrams for the 37.8°C water inlet condition with (Figure 4-120) and without IHX (Figure 4-121) as well as for the 50°C water inlet condition for IHX (Figure 4-122) and without IHX (Figure 4-123) show the resulting cycles. Figure 4-124 and Figure 4-125 show the obtained performance data.

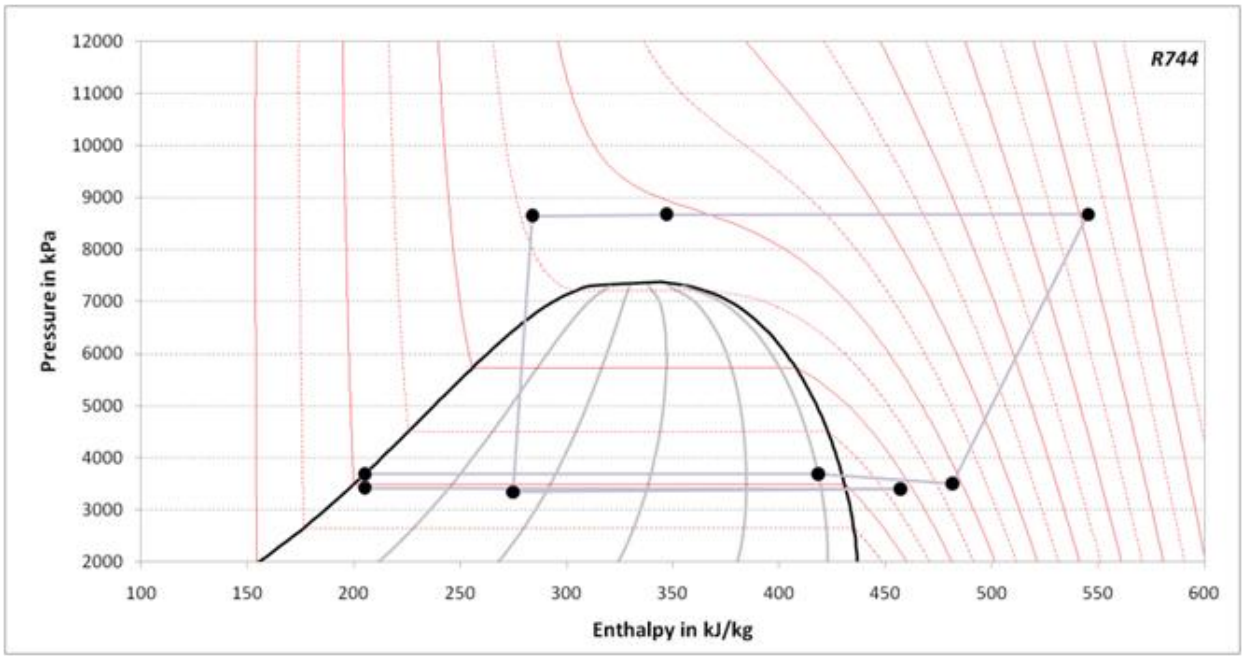

Figure 4-120: Pressure specific enthalpy diagram of IHX system for a water inlet temperature of 37.8°C

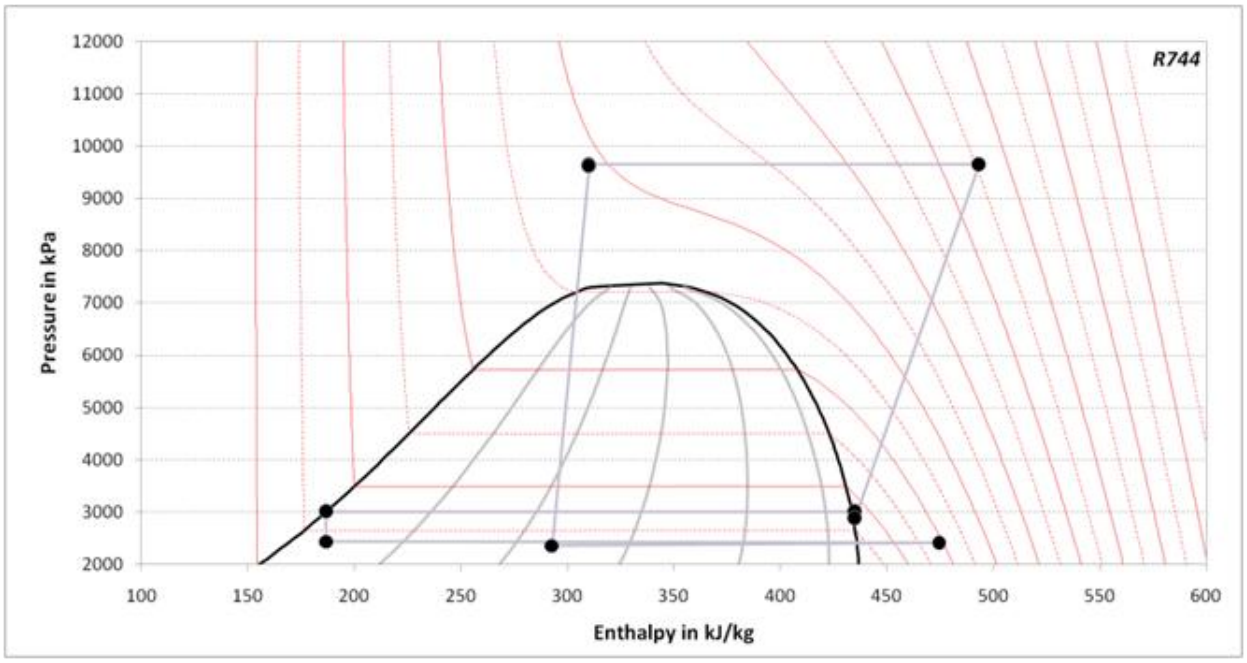

Figure 4-121: Pressure specific enthalpy diagram of system w/o IHX for a water inlet temperature of 37.8°C

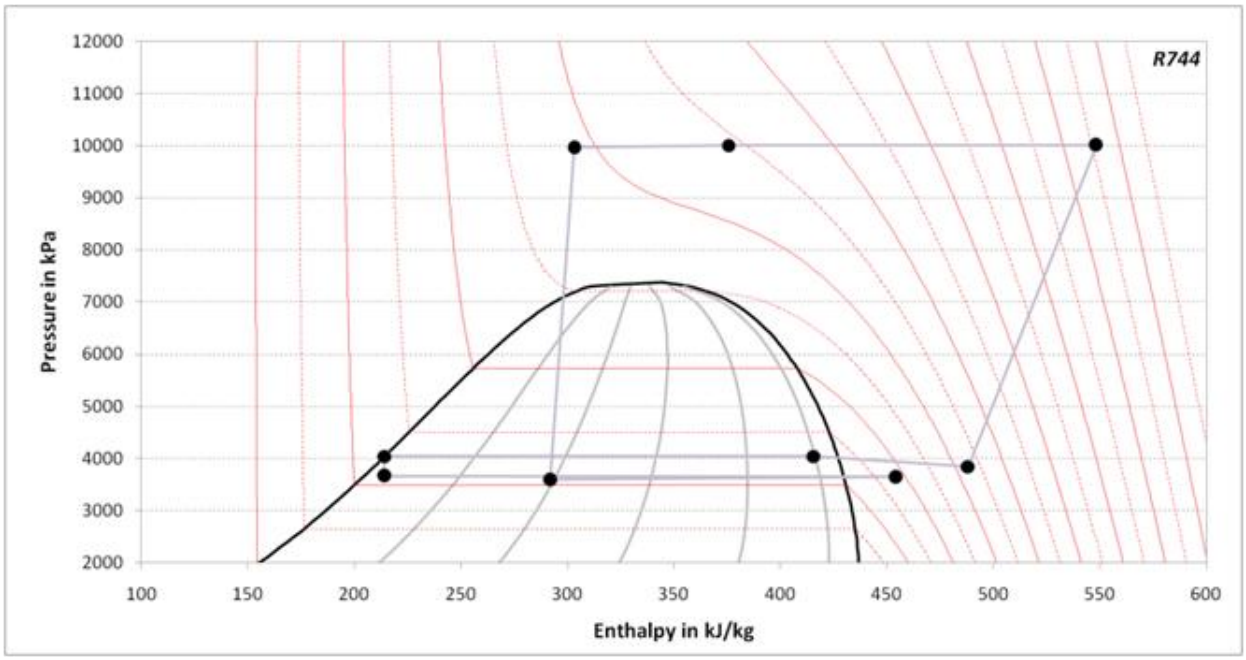

Figure 4-122: Pressure specific enthalpy diagram of IHX system for a water inlet temperature of 50°C

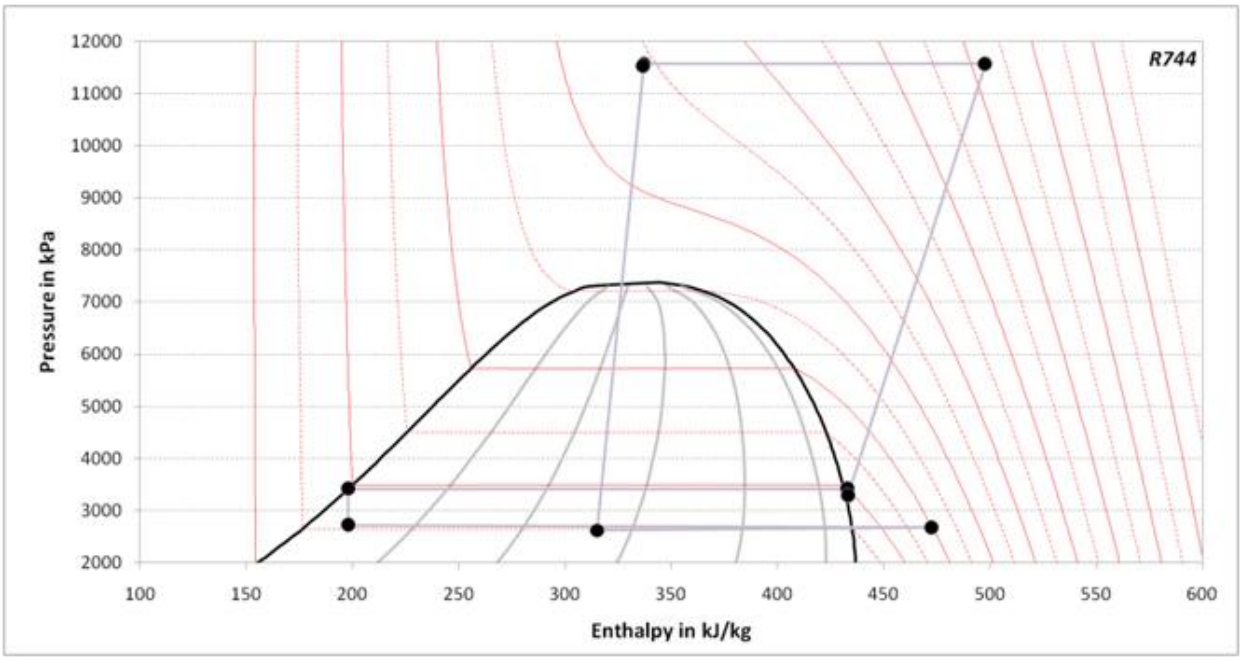

Figure 4-123: Pressure specific enthalpy diagram of system w/o IHX for a water inlet temperature of 50°C

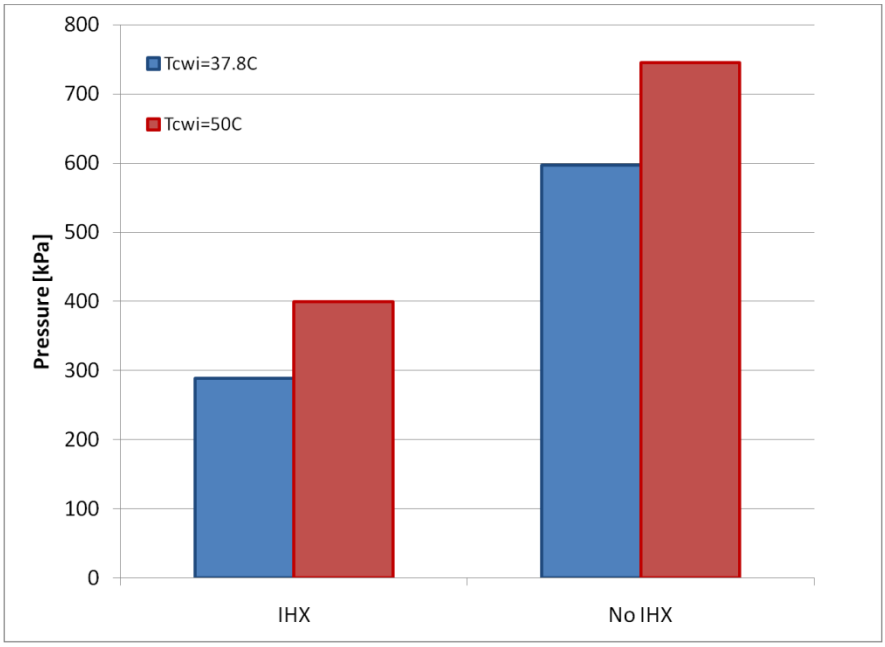

Figure 4-124: Ejector pressure lift for cycle with and without IHX

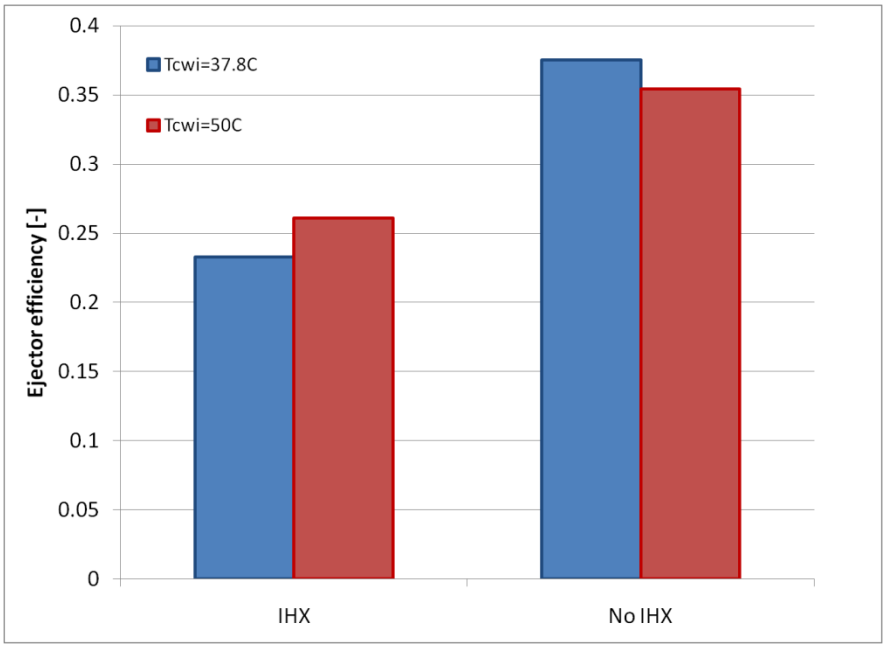

Figure 4-125: Ejector efficiency for cycle with and without IHX

The cycle property diagrams show for water inlet temperatures of 37.8°C (Figure 4-120 and Figure 4-121) and 50°C (Figure 4-122 and Figure 4-123) the same behavior for IHX and no IHX

operation. Higher high side pressures were seen for the systems without IHX. For the lower temperature a difference of approximately 10 bar and for the higher water inlet temperature an increase of 15 bar for the systems without IHX were observed. These higher pressures offered a larger throttling loss recovery potential for the ejector. The recorded pressure lifts that almost doubled for both temperatures (Figure 4-123) confirmed this. The improved operating condition had a beneficial effect on the ejector effectiveness which increased from approximately 25% to 35%. The initial tests were performed to verify the functionality of the ejector. This was done at different starting points of 8000 kPa and 9000 kPa. These starting points were used with fully open ejector while adjusting the water inlet temperature. For all tests a steady liquid column signal in the phase separator was maintained to provide liquid refrigerant to the evaporator. After this starting point the ejector needle was stepwise closed to a maximum ejector closing of 65% which decreased the throat area. The variation of the pressure on the ejector inlet on the motive and suction side between 0% and 70 % closing are shown in Figure 4-126.

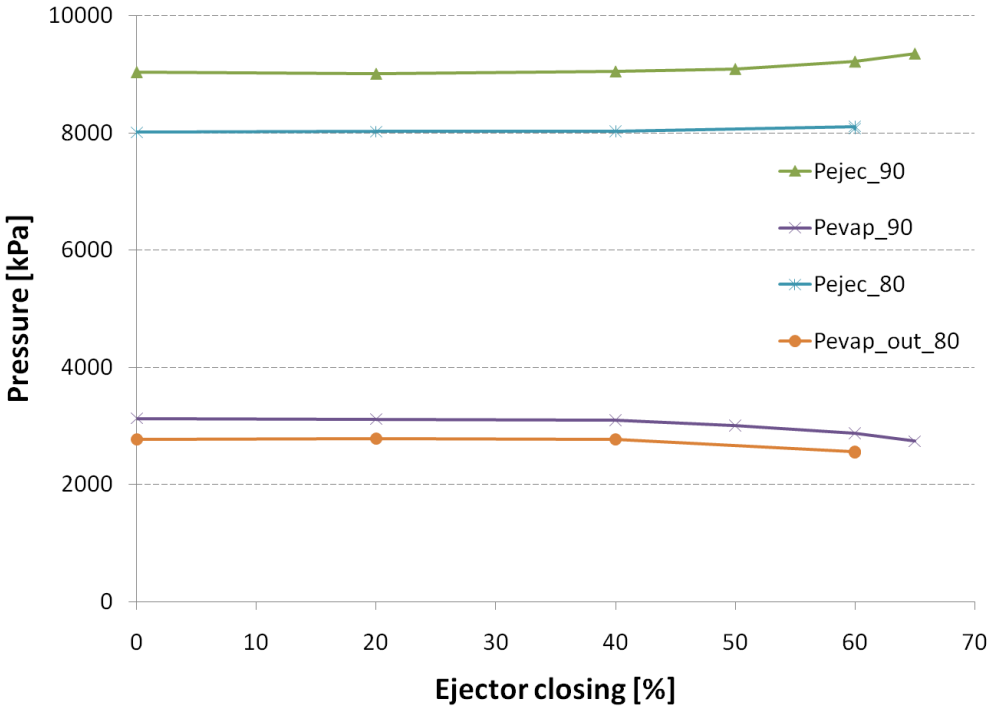

Figure 4-126: Pressure versus ejector closing

The ejector inlet on the high pressure motive flow was located after the IHX. The low pressure suction flow was coming from the evaporator outlet. It was seen that the high side pressure increased for both starting points of 8000 kPa and 9000 kPa while closing the ejector. The low

side pressure decreased at the same time. The steepest pressure gradient for low and high pressure side was seen at high closing percentages. This can be described with the closing characteristics of the ejector.

Beside the changing pressure levels ejector characterizing parameters like the potential of expansion work recovery and the efficiency of the ejector were investigated. The potential work that can be recovered is defined in equation (22).

$$W_{pot} = \dot{m}_{r,motive} \cdot \left(h_{emnri} - h(p_{edro}, s_{emnri})\right) \tag{22}$$

The actual recovered work is defined in equation (23).

$$W_{rec} = \dot{m}_{r,suction} \cdot \left(h(p_{edro}, s_{ero}) - h(p_{ero}, T_{ero})\right) \tag{23}$$

The ejector efficiency is calculated as the ratio of recovered work and maximum potential recovery work as defined in equation (24).

$$\eta_{ejec} = \frac{W_{rec}}{W_{pot}} \tag{24}$$

The results for the described parameters are shown in Figure 4-127.

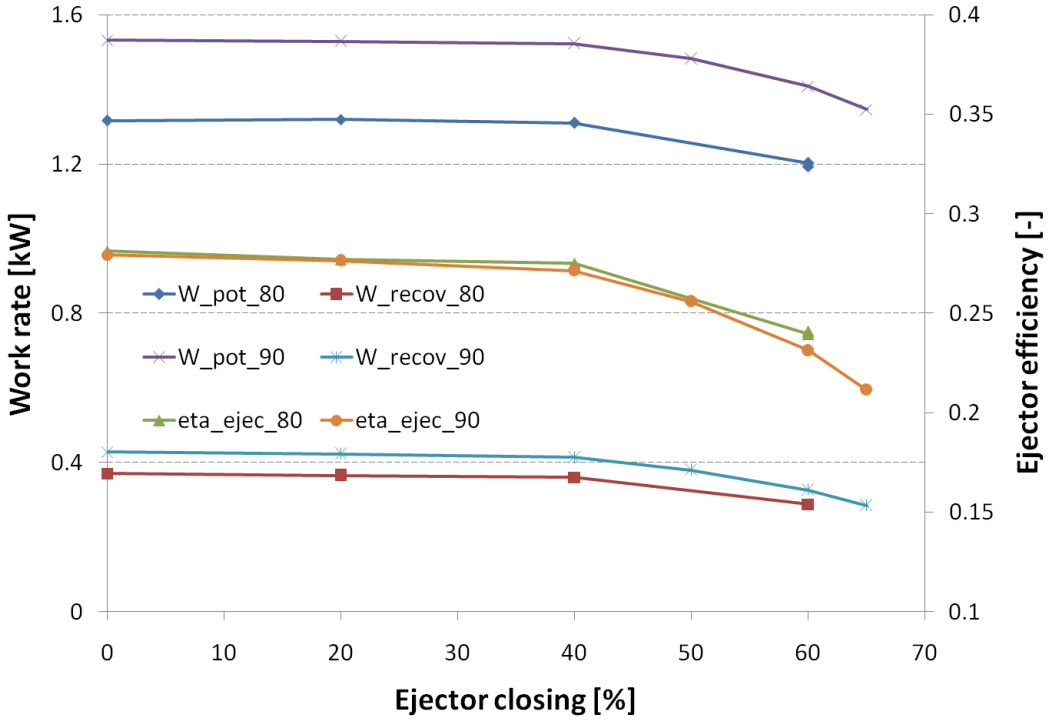

Figure 4-127: Work rate and ejector efficiency versus ejector closing

The mass flow rates for motive and suction flow were another interesting aspect that had to be taken into account for the ejector evaluation. The results are shown in Figure 4-128.

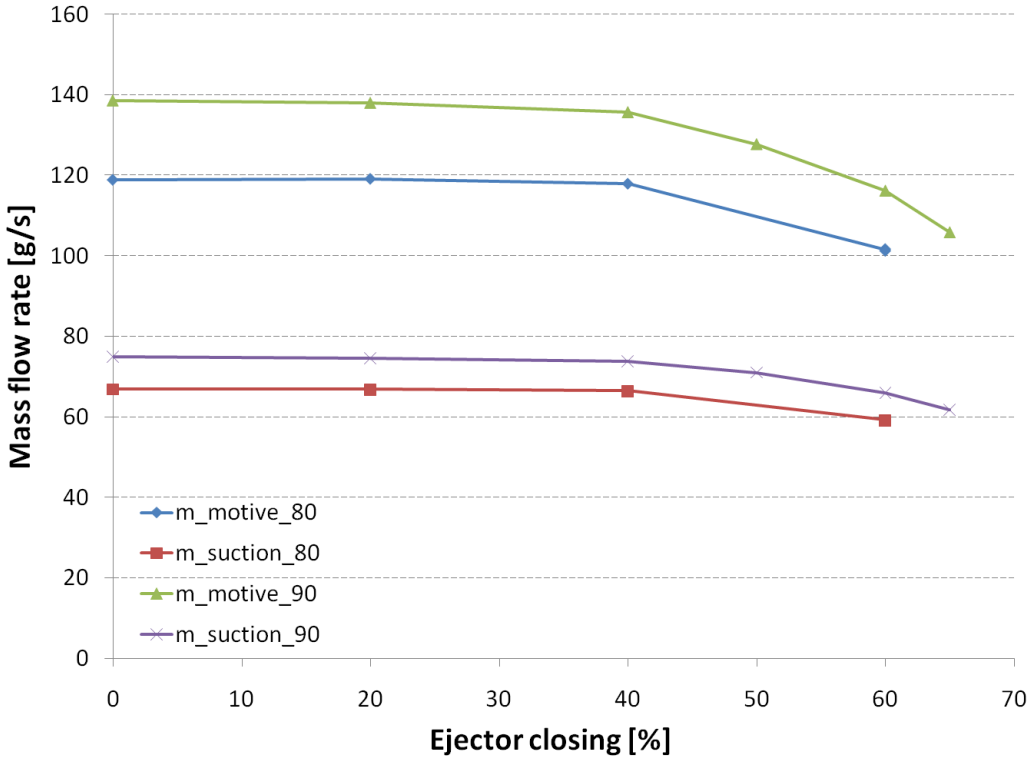

Figure 4-128: Refrigerant mass flow rate versus ejector closing

As expected the flow rates decreased for both pressure levels with increasing ejector throat closing. This decrease in refrigerant flow rates had a direct effect on the possible capacities that were achieved. The combined COP included both useful capacity outputs of heating and cooling divided by the HPWH power consumption (Figure 4-129).

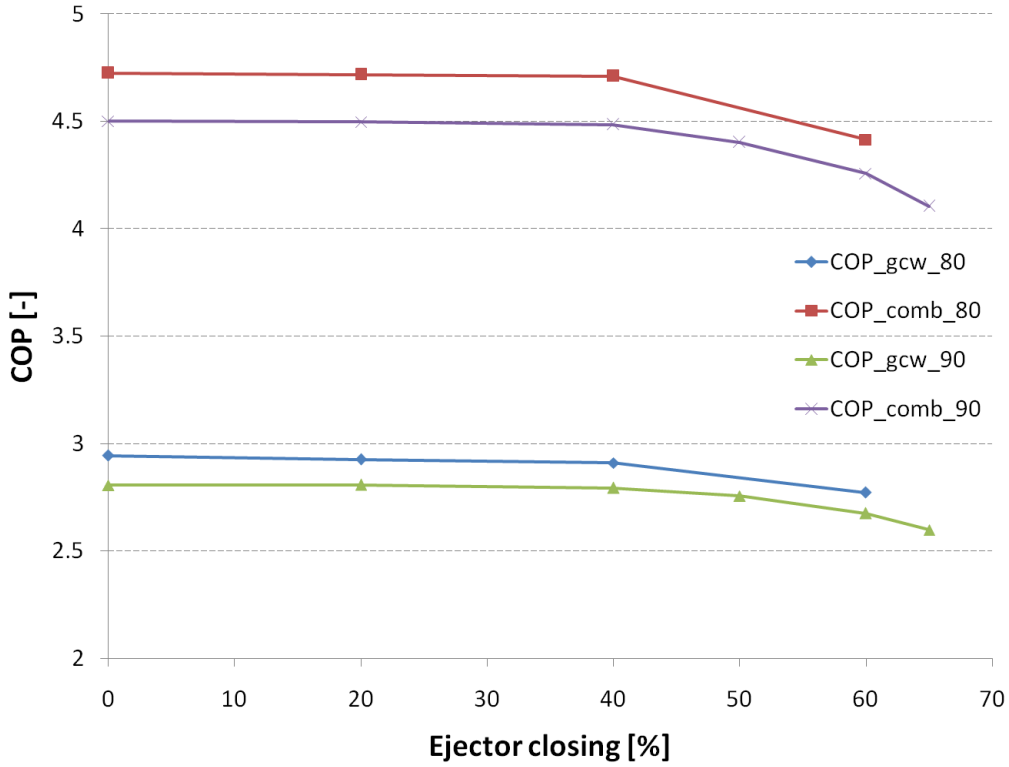

Figure 4-129: COP versus ejector closing

The same qualitative trends that were seen for pressures, flow rates and ejector characteristics were seen for the COP's. Maximum COP's of 2.95 and 4.65 for heating and combined values respectively were reached at maximum opening of the ejector with decreasing values for decreasing throat area.

The mass entrainment ratio is the ratio of suction and motive refrigerant mass flow is another parameter that was used to investigate the ejector performance. It is defined in equation (25).

$$\Phi_{ejec} = \frac{\dot{m}_{r,suction}}{\dot{m}_{r,motive}} \qquad (25)$$

The achievable pressure lift that can be realized with the ejector which is the difference between ejector diffuser discharge pressure and evaporator outlet pressure is defined in equation (26).

$$p_{lift} = p_{edro} - p_{ero} \qquad (26)$$

This represents the precompression that was saved for the compression process. It reduced the necessary compressor power and therefore had a positive effect on the system performance. The results of the pressure lift can be seen in Figure 4-130.

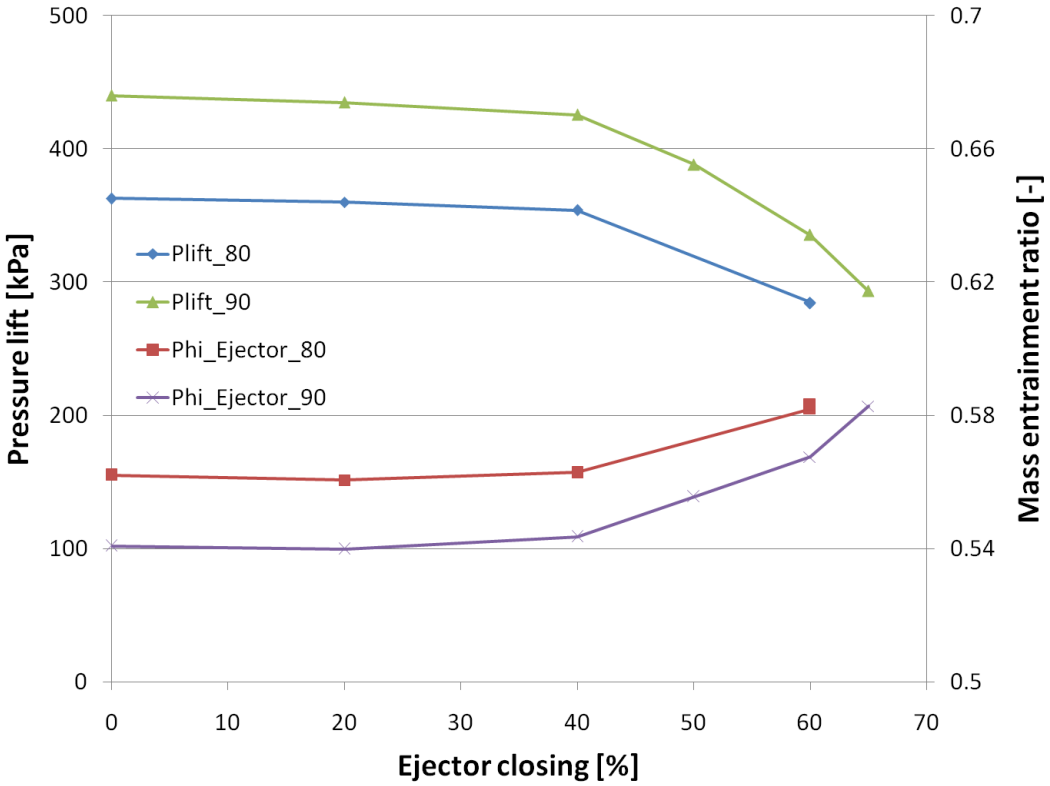

Figure 4-130: Pressure lift versus ejector closing

The decreasing pressure lift and therefore decreasing compressor power reduction confirmed the development of COP. While a decreasing pressure lift was seen the mass entrainment ratio increased because of increasing mass flow acceleration. More suction refrigerant mass flow per motive refrigerant mass flow was entrained.

The HPWH ejector test results that were obtained were compared to previous measurements. The qualitative behavior of the HPWH ejector coincided well with those reference results. The functionality of the ejector was therefore confirmed.

The relatively high pressure drop of the microchannel IHX was described to have a negative influence on the possible savings that can be reached by using an ejector. Therefore after confirming the functionality of the ejector experiments without IHX were the next step. The operation without IHX required a high separation efficiency of the phase separator of the system. The phase separator divided the liquid and vapor fractions of the refrigerant mass flow

after the ejector diffuser. Ideally the refrigerant flow going from the phase separator to the evaporator had a quality of 0 meaning saturated liquid entered the evaporator. The motive flow going to the compressor had a quality of 1 or saturated vapor. This would ensure that no liquid refrigerant droplets would enter the compressor which could potentially damage it due to their incompressibility. In realty the phase separator had a non-ideal separation efficiency below 1 which means liquid refrigerant got to the compressor. For small amounts of liquid refrigerant and separation efficiencies close to one no problems during operation were expected.

After separating the IHX from the system initial tests were done. During shakedown low separation efficiencies were observed and therefore liquid refrigerant was sent to the compressor. As a result the high pressure switch was triggered and the compressor shut off. The resulting time dependent development of temperatures and pressures during compressor shut off are shown in Figure 4-131 and Figure 4-132.

It can be seen how the increasing liquid refrigerant fraction of the refrigerant flow entering the compressor affected the operation. The suction density increased gradually due to the increasing liquid refrigerant fraction which caused an increase in flow rate. At the same time the high side pressure increased and the compressor discharge temperature decreased. The compressor outlet condition basically moved to a higher pressure and smaller specific enthalpy values in the pressure specific enthalpy diagram. Finally the pressure increased to the high pressure cut out pressure which shut off the compressor. The pressure levels equalized and the refrigerant flow dropped to zero.

In order to investigate the reason for the compressor shut off the pressure specific enthalpy diagram was used which is shown in Figure 4-133.

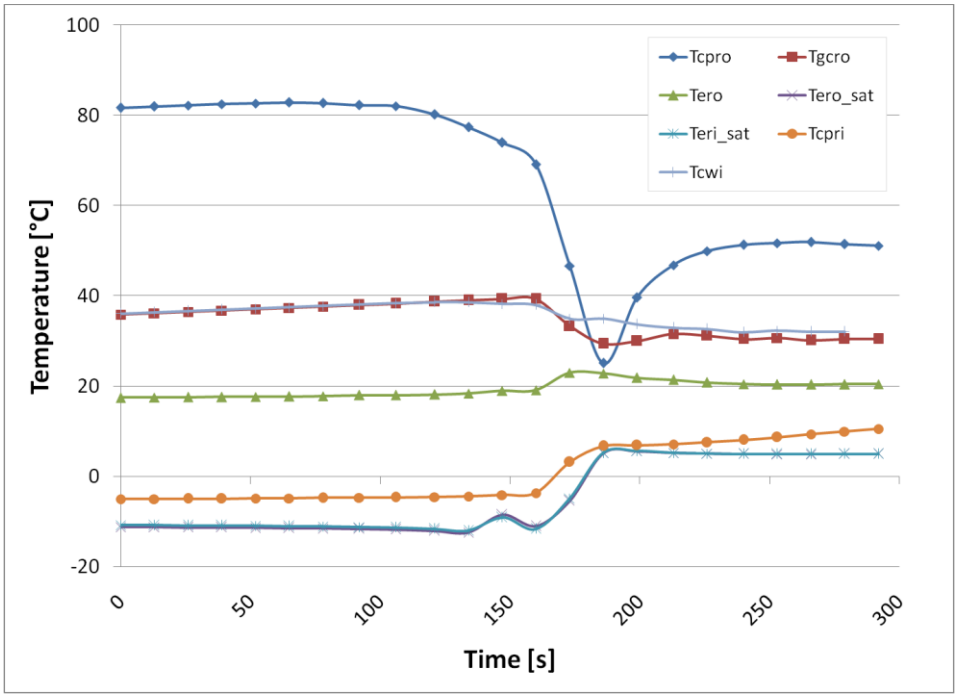

Figure 4-131: Temperature development during compressor shut off

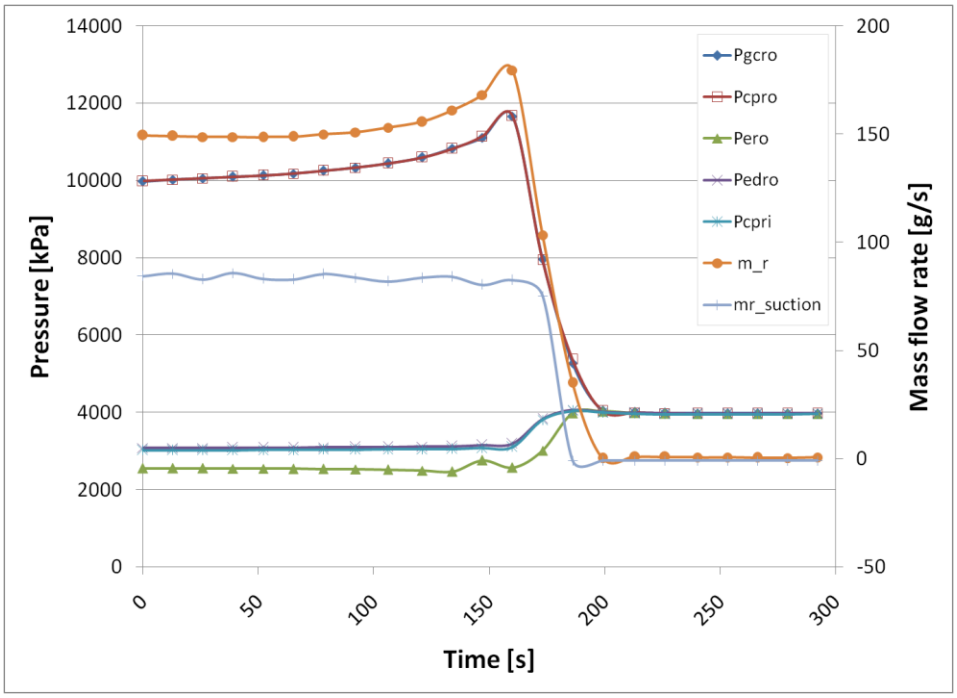

Figure 4-132: Pressure development during compressor shut off

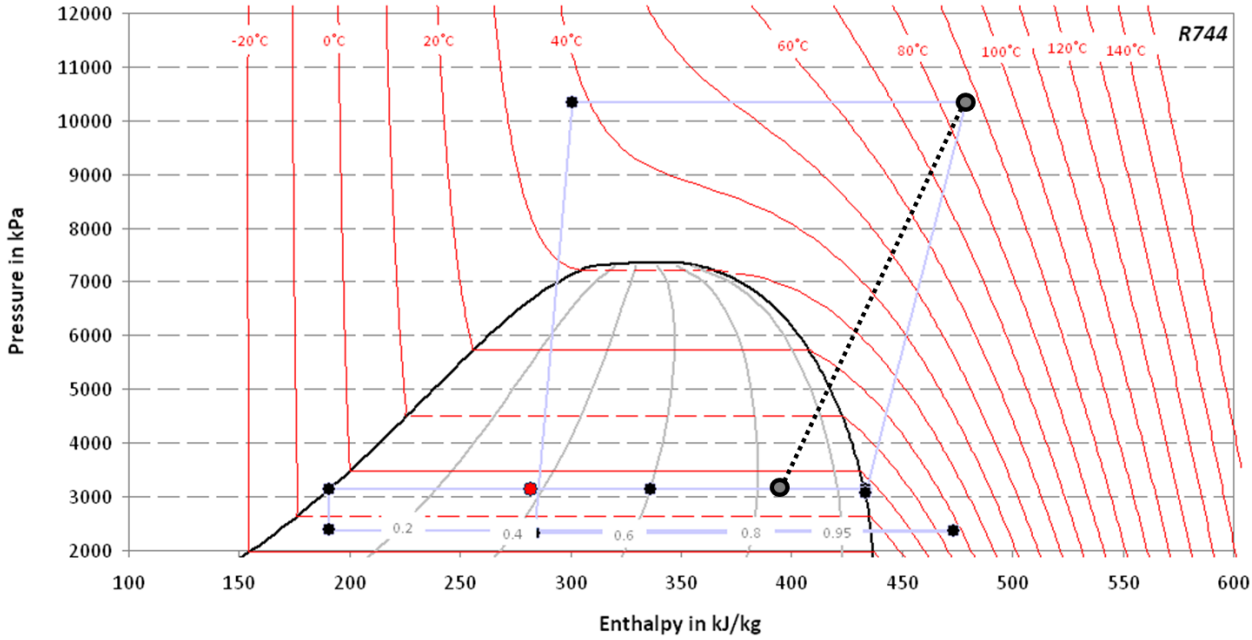

Figure 4-133: Suction quality based on isentropic efficiency of compressor

The observed cycle in the ph-diagram had a saturated compressor inlet condition. An online calculation backwards into the dome was not possible without an internal heat exchanger. Therefore earlier results were used to include the isentropic efficiency of the compressor to get an idea of the suction state. It can be seen that a compressor inlet quality of approximately 85% was reached. This means a relatively large amount of liquid entered the compressor which finally led to the shut off.

A more stable operation would have been achieved by improving the separation efficiency. In order to do that as a first step the phase separator was opened and a splash plate was installed which is shown in Figure 4-134 and Figure 4-135.

Figure 4-134: Opened phase separator without splash plate

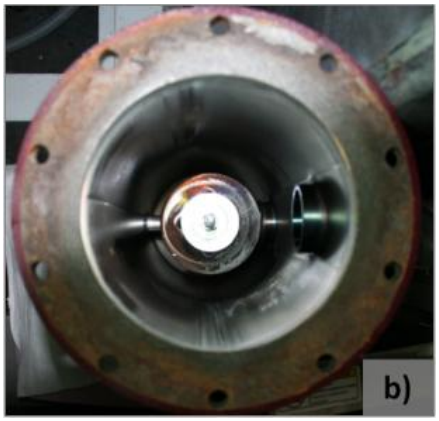

Figure 4-135: Opened phase separator with splash plate

The splash plate was installed on top of the four leg inlet adapter which held the coalescent filter. The splash plate decreased the refrigerant velocity and rerouted it. The initial and changed flow paths are shown in a schematic in Figure 4-136.

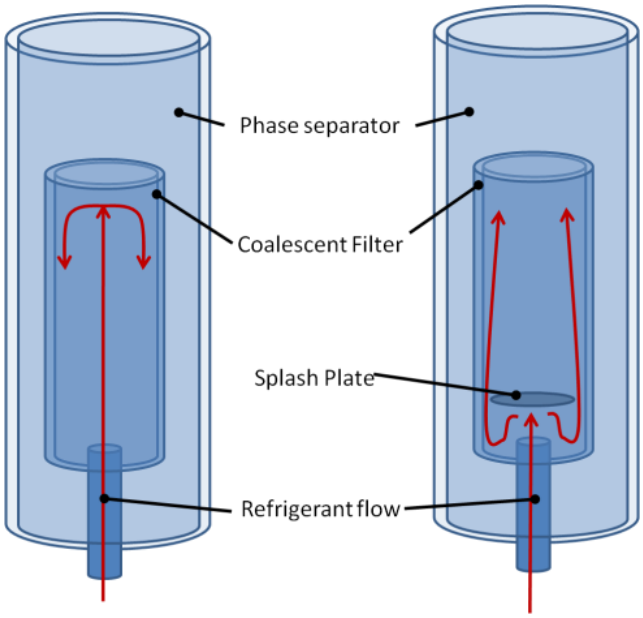

Figure 4-136: Refrigerant flow path without and with splash plate

Tests with and without IHX were conducted which showed the different recovery potential with the ejector depending on the high side pressure. The HPWH system was changed back to a DX layout with enhanced IHX in order to allow a comparison with the ejector system. For this the ejector test conditions at the evaporator outlet for pressure and temperature as well as the

heating capacity was matched. In order to consider the influence of the high side pressure which can be significant in R744 systems the gas cooler outlet condition for temperature and pressure as well as heating capacity were matched. These two matched conditions were conducted for water inlet temperatures of 37.8°C and 48°C at an ambient air temperature of 26.7°C and rating water flow rate of 28 gallons per minute. The matched ejector conditions for the high and low pressure side can be best demonstrated by the three cycles in the pressure – specific enthalpy diagrams (Figure 4-137, Figure 4-138).

For both figures the red and blue cycles represent the DX systems and the grey cycle shows the ejector system state points. The red cycles matched the gas cooler outlet condition and the blue cycles matched the evaporator outlet condition. It was seen that for both water inlet temperatures it was possible to get a good match of the ejector conditions. The performance characterizing parameters of the ejector system and the heating COP's of the three systems are shown in Figure 4-139 and Figure 4-140 respectively.

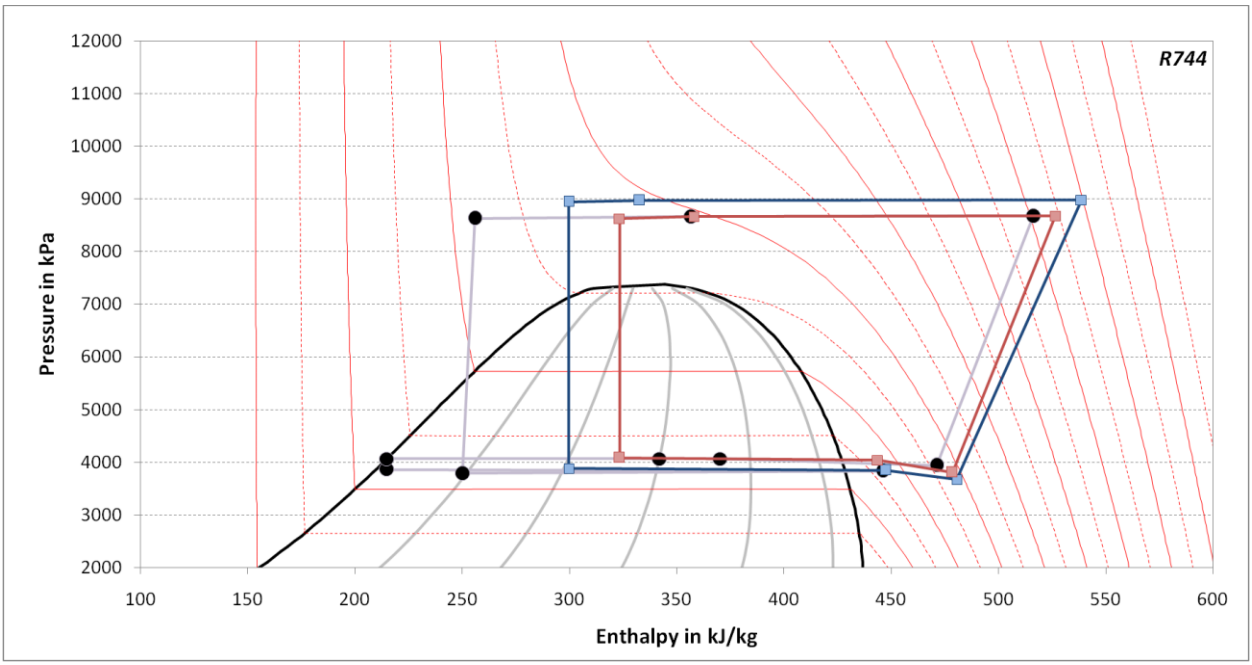

Figure 4-137: Pressure- specific enthalpy diagram of ejector test condition match with DX enhanced IHX system at a water inlet temperature of 37.8°C

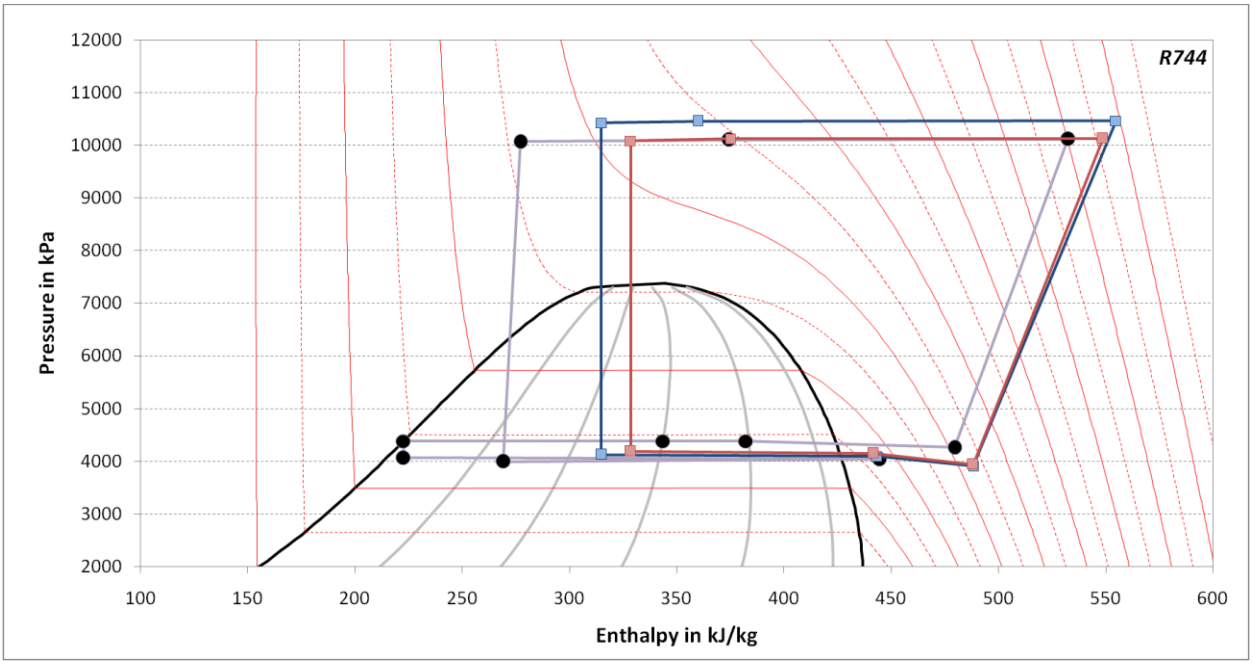

Figure 4-138: Pressure- specific enthalpy diagram of ejector test condition match with DX enhanced IHX system at a water inlet temperature of 48°C

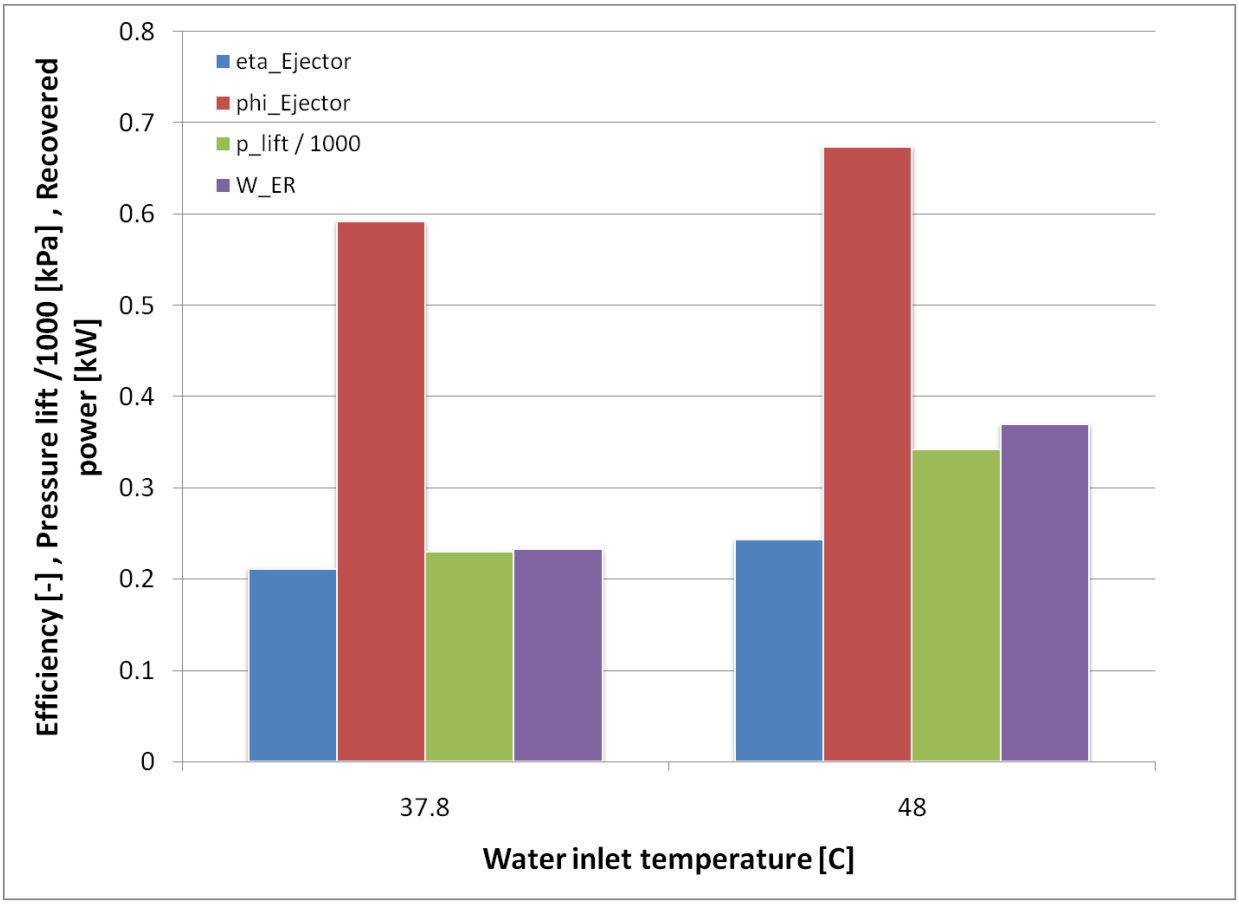

Figure 4-139: Characteristic ejector parameters at different water inlet temperatures

The characteristic parameters of the ejector system benefitted from increasing water inlet temperature. This was because of the increasing high side pressure which was seen in the pressure- specific enthalpy diagrams (Figure 4-137, Figure 4-138). A larger high side pressure offered more recovery potential in the ejector. This relationship was seen in all four investigated aspects. The ejector efficiency as well as the entrainment ratio increased from 21% to 24% and 58% to 67% respectively. Also the pressure lift and recovered power increased from 230 kPa to 340 kPa and 0.24 kW to 0.36 kW respectively. These good performance characteristics of the ejector had a beneficial influence on the whole cycle performance which was seen in the heating COP of the system in comparison with the DX system (Figure 4-140).

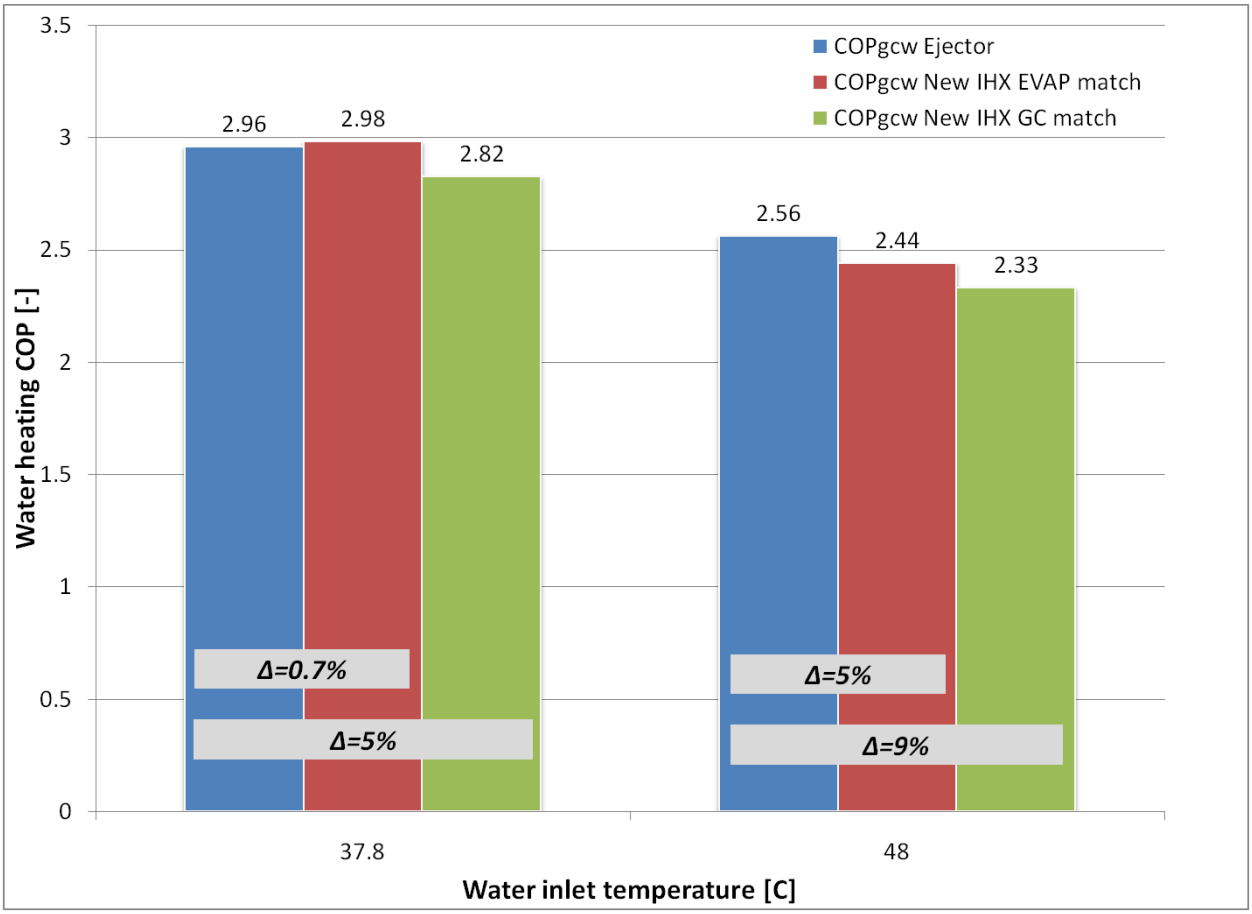

Figure 4-140: Comparison of water heating COP's for ejector and DX enhanced IHX system

The comparison of the water heating COP's confirmed the trend that was seen for the ejector characterizing parameters. At the lower water inlet temperature there was basically no difference between the ejector system and the DX system match on the evaporator outlet. This changed when the gas cooler outlet was matched by the DX system. This led to a 5% better ejector system compared to the DX system. The ejector performance improved even more when increasing the water inlet temperature. The difference between ejector system and evaporator outlet match was 5% and even 9% for the gas cooler exit match.

These good ejector performance results compared to a DX system were even offset because of the fact that an ejector condition with low separation efficiency was used. This was done because of the relatively moderate pressure levels on the high and low pressure side. These conditions were well suited for the comparison but did not reflect the full performance of the ejector. Even better ejector efficiencies were seen for smaller degrees of opening of the

metering valve. This means even better results can be expected for the ejector system at these optimized conditions compared to the DX system.

4.6 High efficiency Interior Permanent Magnet (IPM) compressor motor

Part of the project is to look at various ways that a next generation R744 HPWH system could be improved. The development of a higher efficiency Interior Permanent Magnet (IPM) compressor motor was part of the development of the next generation HPWH.

Many current R744 compressors use grid connected induction machines. While using a grid connected line fed induction machine avoids the cost of a variable frequency drive, it limits the compressor operation to a relatively small speed and capacity range. A variable frequency drive can be used in conjunction with an induction machine to allow the compressor to operate over a large capacity range by changing speeds. However, the efficiency of the induction machine falls off substantially if it is not operated near its rated operating point.

An alternative electric motor which generally offers higher efficiency than an induction machine across a range of operating conditions is the interior permanent magnet (IPM) motor. IPM motors are a configuration of a permanent magnet AC synchronous machine with the permanent magnets embedded below the rotor surface. One downside of IPM motors is that they must be used with a current regulated variable frequency drive. The design of IPM motors has been extensively researched for the last decade but remains complex. Although higher in cost, IPM motors have seen extensive deployment in hybrid electric vehicles and are beginning to gain traction in other markets as costs come down and the value proposition starts to make sense.

The R744 compressor used in the baseline R744 experimental system had a speed range of 30 to 70Hz. It used a line fed induction machine nominally rated for 10 hp. The torque and output power of the induction machine were estimated to determine the design requirements of the IPM motor (

Table 4-6).

Table 4-5: Four Pole 50 Hz Induction Machine Torque Output Assuming a 12,500 W Power Input

	Efficiency						
Slip	0.8	0.82	0.84	0.86	0.88	0.9	0.92
0.01	64.3	66.0	67.5	69.1	70.7	72.3	74.0
0.015	64.6	66.2	67.9	69.5	71.1	72.7	74.3
0.02	65.0	66.6	68.2	69.8	71.5	73.1	74.7
0.025	65.3	66.9	68.6	70.2	71.8	73.5	75.1
0.03	65.6	67.3	68.9	70.6	72.2	73.8	75.5
0.035	66.0	67.6	69.3	70.9	72.6	74.2	75.9
0.04	66.3	68.0	69.6	71.3	72.9	74.6	76.3

Table 4-6: Four Pole Induction Machine Power Output as a Function of Operating Speed

	Shaft Output Power						
	(a) Compressor Speed 1500 RPM						
Pout (W)	10000	10250	10500	10750	11000	11250	11500
Pout (hp)	13.40	13.74	14.08	14.41	14.75	15.08	15.42
	(b) Compressor Speed 1800 RPM						
Pout (W)	12000	12300	12600	12900	13200	13500	13800
Pout (hp)	16.09	16.49	16.89	17.29	17.69	18.10	18.50
	(c) Compressor Speed 2100 RPM						
Pout (W)	14000	14350	14700	15050	15400	15750	16100
Pout (hp)	18.77	19.24	19.71	20.17	20.64	21.11	21.58

Because of the uncertainty in exact torque and power output levels required, values on the higher side of the estimated levels were used to ensure operation of the compressor. Additionally, because many of the components in the heat pump water heater system were sized for a capacity achievable with the 60 Hz grid fed induction machine the IPM was sized to 13.4 kW (18 hp) see

Table 4-6 c). This power output level also worked well with the axial length available in the compressor housing while allowing the IPM to maintain a high efficiency.

Multi-objective Differential Evolution Finite Element Analysis (FEA)-based optimization considering a total of *22,500* candidate designs has been performed. The optimization

procedure is described in [*IEMDC 2011*][1]. Three motor topologies have been considered in the optimization. Significant performance variations are observed from the results shown in Figure 4-141. Depicted in Figure 4-142 are the objectives corresponding to the candidate designs that satisfy the design constraints. *Best compromise* designs corresponding to every topology are selected and corresponding objectives are plotted in Figure 4-141 and Figure 4-142. The cross-sections of optimized machines and relevant performance criteria are provided in Figure 4-141 and Figure 4-142 respectively.

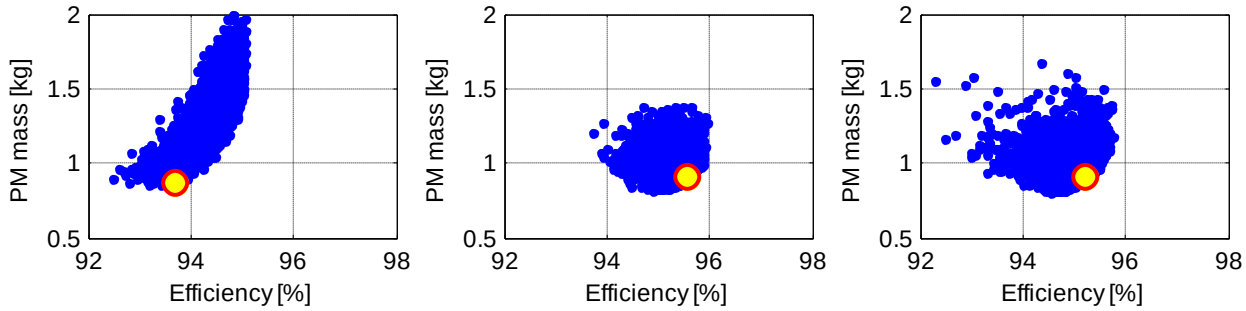

Figure 4-141: Design objectives corresponding to all 22,500 candidate designs evaluated during optimization. Also shown are the selected best compromise designs corresponding to every topology.

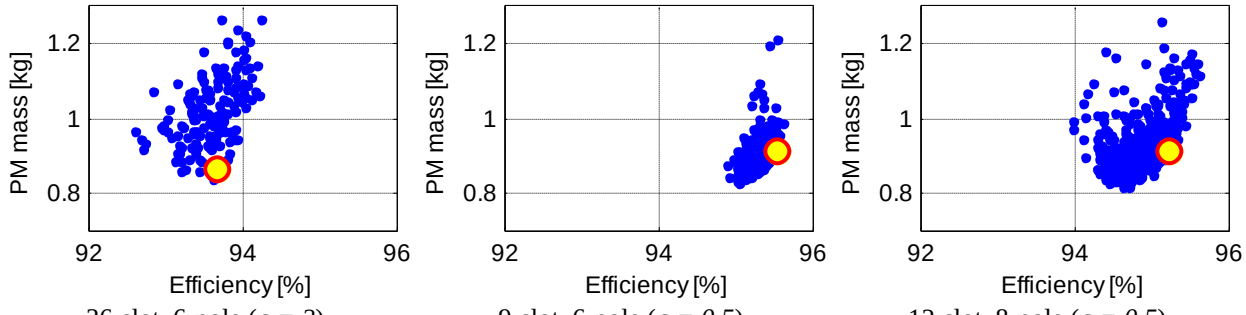

Figure 4-142: Design objectives corresponding only to motors satisfying the design constraints. Also shown are the selected best compromise designs corresponding to every topology.

1 [1] G. Y. Sizov, D. M. Ionel, N.A.O. Demerdash, "Multi-Objective Optimization of PM AC Machines Using Computationally Efficient - FEA and Differential Evolution," Procs. of International Electric Machines and Drives Conference IEEE-IEMDC 2011, Niagara Falls, Canada, May 2011.

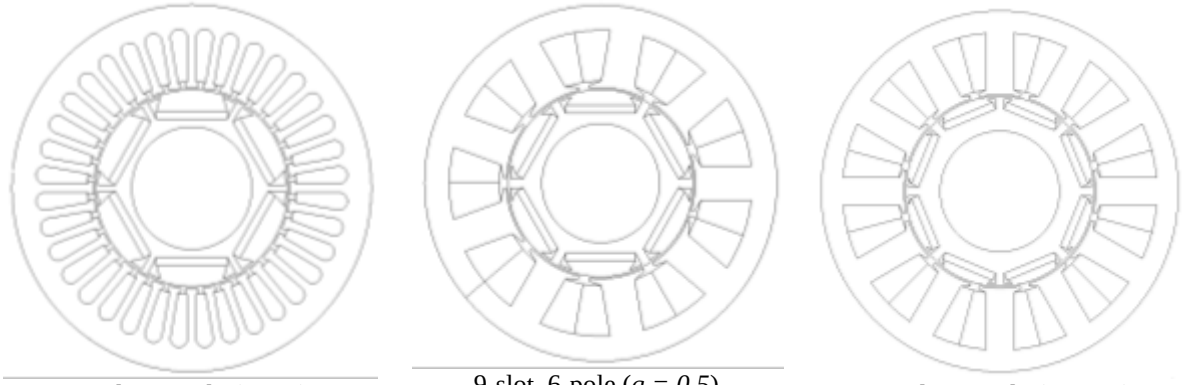

36-slot, 6-pole ($q = 2$) 9-slot, 6-pole ($q = 0.5$) 12-slot, 8-pole ($q = 0.5$)

Figure 4-143: Cross-Sections of Optimized Motors

Table 4-7: Performance Parameters

	36-slot, 6-pole ($q = 2$)	9-slot, 6-pole ($q = 0.5$)	12-slot, 8-pole ($q = 0.5$)
Estimated Efficiency [%]	93.8	95.6	95.2
PM mass [kg]	0.892	0.912	0.909
Torque ripple [%]	28.95 (5.5 skewed)	9.6	9.7
Stack length [mm]	126.1	133.0	131.2
Saliency L_q/L_d	2.02	1.804	1.72

Optimized motor designs shown in Figure 4-142 were used for evaluation An increase of 6 to 13 percent in motor efficiency was expected compared to the induction motor currently used in the compressor. Because the IPM machine must be used with a variable frequency drive (~95% efficiency or higher) the system efficiency at the rated operating point would be 1 to 8 percent higher. In addition, unlike the induction motor, at relatively low speed/capacity operation, the system maintains high efficiency.

The three optimized designs all meet the design requirements. The choice between the two stator types, i.e. the integer-slot (36-slot, 6-pole with q = 2 slots/pole/phase) and the fractional-slot (9-slot, 6-pole with q = 0.5 slots/pole/phase or 12-slot, 8-pole with q = 0.5 slots/pole/phase) was dictated by the capabilities of the ac drive that will be used to supply and control the motor. When the drive was considered the integer slot motor appeared as an “easier” motor to control

due to a more sinusoidal back-emf waveform, when compared to the fractional slot machines (see Figure 4-144). The quality of the motor control and the motor efficiency are dependent on the ability of the A.C. drive to regulate to sinusoidal currents, and hence are related to the current-regulator's bandwidth. In this regard, the fractional slot motors have higher back-emf harmonic content that may pose challenges to the commercially available, general purpose drive (Yaskawa A1000). On the other hand, the more aggressive fractional slot motor designs have a potential for improved operating efficiency due to reduced copper losses.

The final prototype must operate in a hermetically sealed compressor environment without position and speed feedback sensors. The Yaskawa A1000 drive advertises a sensor-less speed and torque control feature when used with an interior permanent magnet machine. However the exact sensor-less control method and capabilities of the Yaskawa A1000 drive is unknown. The impact of the increased back-emf waveform harmonics of the fractional slot designs is also unknown.

Because of the unknown current regulator bandwidth and sensor-less control capabilities of the Yaskawa A1000 drive, it was decided to use a hybrid rotor design that can operate with both integer slot and fractional slot stator designs (6 pole, 36-slot and 9-slot). Using a common rotor that can operate with the two different stator types should reduce the risk that the motor would be incompatible with the drive for sensor-less operation. It is expected that using a common rotor will allow to prototyping both machine types at minimal extra cost. The final proposed motor will be selected for pressing into the compressor after thorough dynamometer lab testing is completed. This will allow for possible efficiency variations due motor-drive interaction that have not been considered in the design and optimization process.

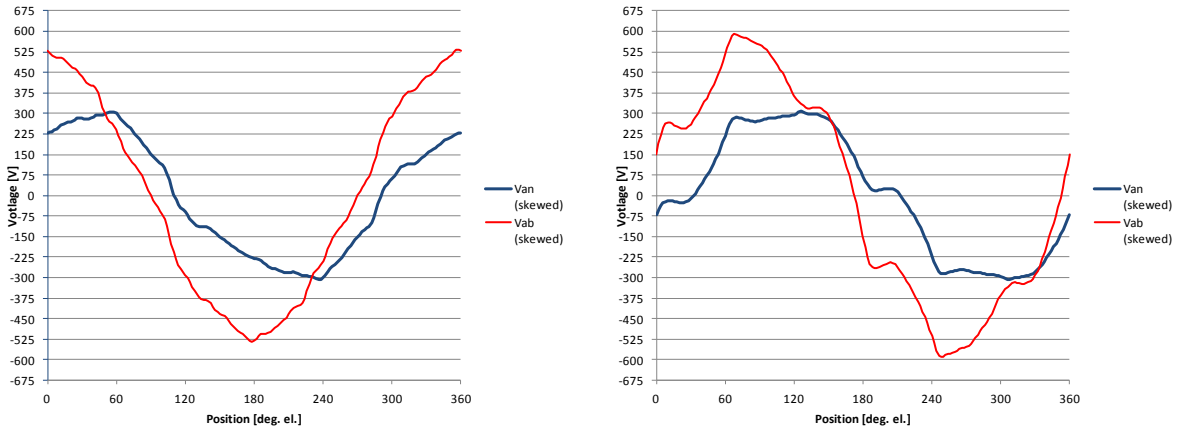

36-slot, 6pole 9-slot, 6-pole

Figure 4-144: Induced line and phase voltages at rated-load with step skewed rotors (10 $^{o}_{Mech}$ equivalent)

A common rotor was designed by tweaking the optimized rotor designs for the 36 slot and 9 slot machines. As can be seen in Figure 7.3 the optimized rotor designs of the 36 slot and 9 slot machines are relatively similar. The final 6 pole designs with a common rotor are shown in Figure 4-145. To reduce the torque ripple of the 36 slot machine a 5º mechanical step skew was added to the rotor. The 5º mechanical step skew approximates a continuous skew of 10º mechanical degrees. The step skew has a relatively small impact when combined with the 9 slot stator because of the width stator tooth tips.

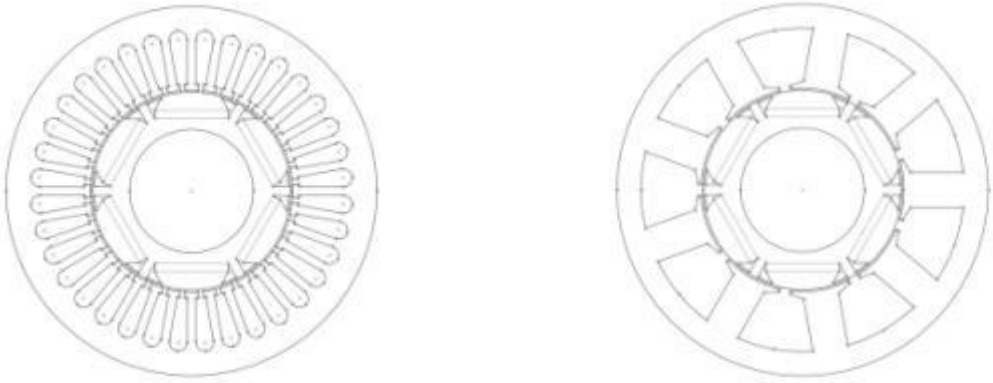

(a) 36 Slot 6 Pole Design (b) 9 Slot 6 Pole Design

Figure 4-145: Final 6 pole designs using a common rotor.

Initial Analysis of 6 Pole Optimized Designs with Common Rotor

Initial analysis of the performance of the two 6 pole optimized designs with a common rotor was carried out before final lamination and winding designs were completed. The torque versus current angle and maximum torque per ampere (MTPA) operating point for both designs is shown in Figure 4-146. The MTPA current angle of the 36 slot 6 pole machine (123º) is slightly higher than the 9 slot 6 pole design (119º). Both motors appear to meet the 71 Nm torque output design requirement.

The efficiency maps of both designs using the common rotor were also calculated, Figure 4-147. The efficiency maps do not account for rotor and permanent magnet core losses which should be relatively low in interior permanent magnet machines. The estimated efficiency of the two designs with the common rotor at the rated operating point is indicated by a black dot. The 9 slot 6 pole machine is predicted to be 1.5 % more efficient than the 36 slot 6 pole design. The 9 slot 6 pole machine is likely to have higher rotor and permanent magnet core losses than the 36 slot 6 pole machine so the efficiency difference will likely shrink.

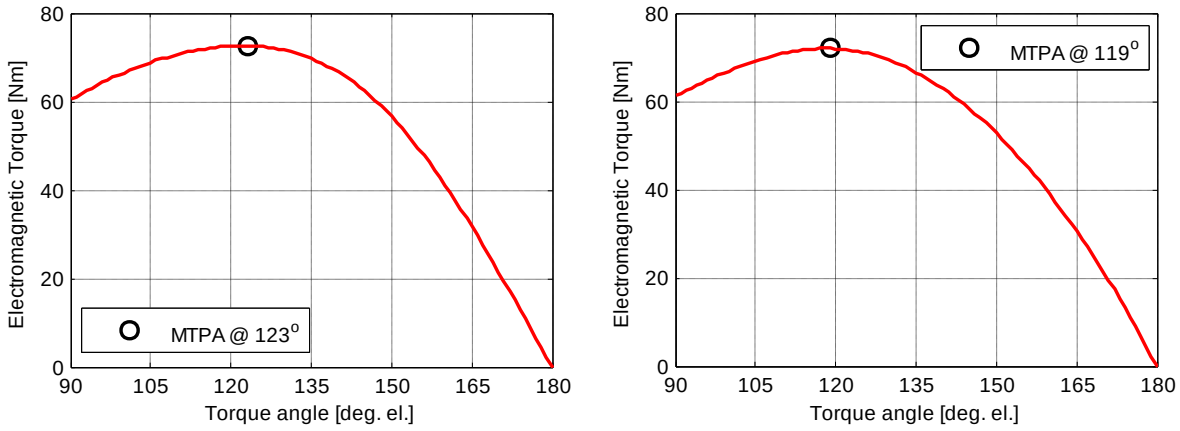

(a) 36 Slot 6 Pole Design (b) 9 Slot 6 Pole Design

Figure 4-146: Static finite element solution results to calculate the maximum torque per ampere (MTPA) torque angle relative to the magnetic flux axis (d-axis) at the design current densities of for the two stator types with the common rotor (36/6 6 A/m^2, 9/6 6.25 A/m^2).

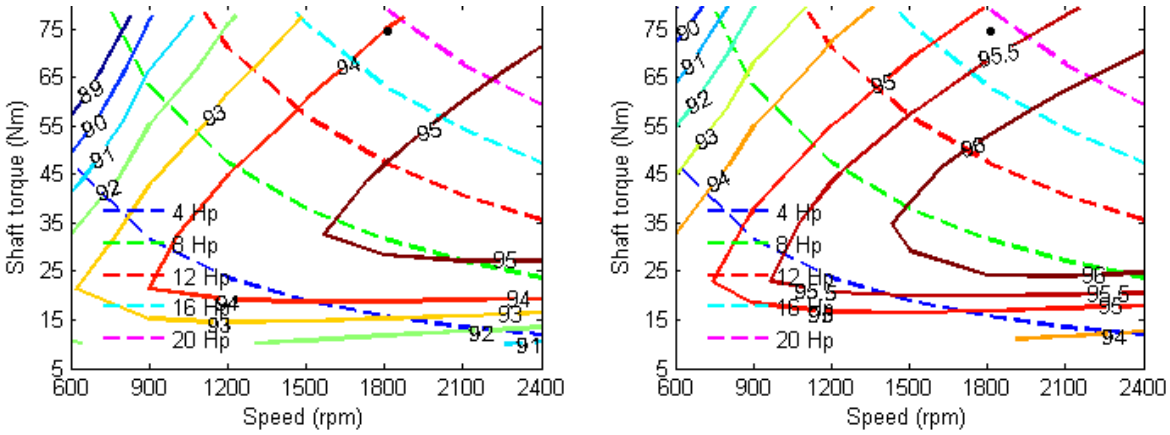

(a) 36 Slot 6 Pole Design (b) 9 Slot 6 Pole Design

Figure 4-147: Estimated efficiency maps of prototype IPM motors with common rotor at the MTPA current angle. The design rated operating point is indicated by the black dot. Efficiency calculations do not include rotor or permanent magnet core losses.

Final Lamination Design

The final stator lamination designs are shown in Figure 4-148 and the final common rotor design is shown in Figure 4-149. Flats were added to the stator outer diameter to approximate the flats in the induction machine lamination currently used in the 4MTC-10K compressor. By matching the flats, the press force necessary for inserting the permanent magnet stator stack should roughly approximate that of the induction machine. The flats may also aid oil circulation in the compressor. The laminations are stamped with a larger stator outer diameter than the final press dimension. To dimensional control over the entire stator stack and ensure a smooth press into the compressor housing 0.25 mm will be ground from the stator stack after winding and varnishing. To avoid grinding away the weld holding the laminations together, four small depressions were added to the stator outer diameter to contain the weld beads. To ensure accurate laser cutting radiuses, several features were added to the final common rotor lamination design including six bolt holes for retaining the lamination stack. The bolt holes and key slot are offset to allow step skewing of the rotor stack. Magnet retention bumps were added to the q-axis bridges. The thickness of the magnet and magnet slot thickness were also increased to account for the clearance air gaps around the magnets.

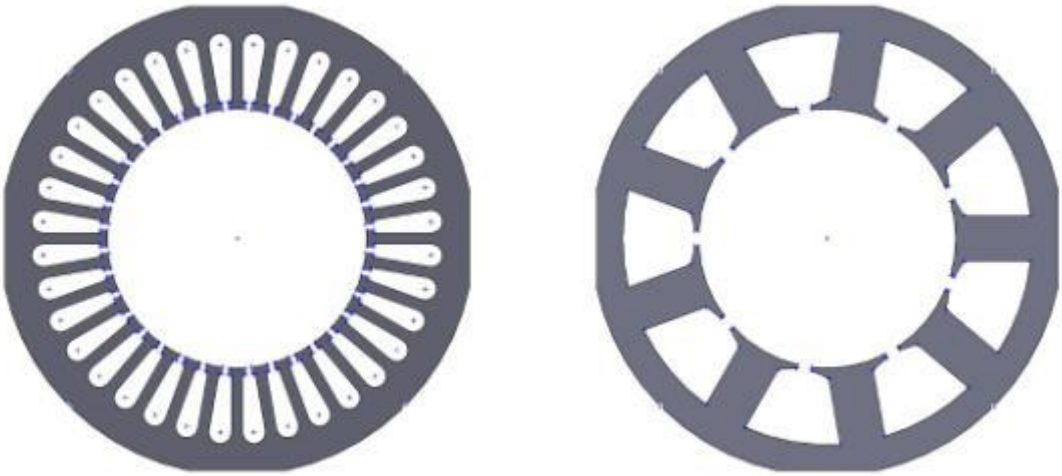

(a) 36 Slot 6 Pole Design (b) 9 Slot 6 Pole Design

Figure 4-148: Final stator lamination designs

Figure 4-149: Final common rotor lamination design.

Winding Design

The winding designs selected for the interior permanent magnet machine prototypes are shown in Figure 4-150. The number of turns was selected to leave sufficient voltage margin for the voltage drop on the end windings and to allow the drive to operate under low voltage conditions, Table 4-8. Magnet wire grade and insulation materials were selected to be CO_2 and oil compatible.

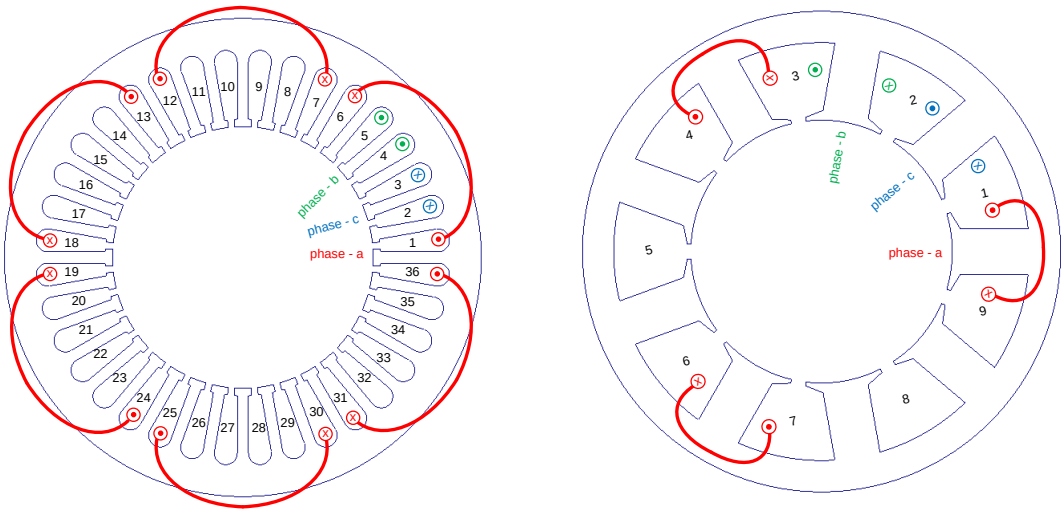

(a) 36 Slot 6 Pole Design (b) 9 Slot 6 Pole Design

Figure 4-150: Winding patterns for the 36 slot 6 pole and 9 slot 6 pole stators. Phases B and C continue in the same pattern as phase A

Table 4-8: Winding Design Properties

	(a) 36 Slot 6 Pole Design	(b) 9 Slot 6 Pole Design
Coils per Phase	6	3
Parallel Paths	None (All series connected)	None (All series connected)
Turns per Coil	21	39
Strands in Hand	4	4
Wire Size	17 AWG	16.5 AWG
Coil Pitch	5	1
Est. L-n Resistance at 20 ºC	0.350 Ω	0.176 Ω
Materials	CO_2 and oil compatible	CO_2 and oil compatible

Detailed Analysis of 6 Pole Optimized Designs with Common Rotor

To predict in more detail the performance of the final lamination designs and windings, nonlinear time stepping finite element analysis was carried out for both the 36 slot 6 pole and 9 slot 6 pole designs with the common rotor. Second order elements were used to improve the torque and voltage waveform predications. The behavior of the machines was examined under a number of operating conditions including open-circuit, rated current with a current angle of 90 degrees, and rated current at the MTPA current angle. Calculated quantities include the electromagnetic

torque, shaft torque, torque ripple, line to neutral voltage, line to line voltage, copper and core losses, power, power factor, and efficiency. Table 4-9 displays the results for the 36 slot 6 pole common rotor design and Table 4-10 displays the results for the 9 slot 6 pole common rotor design.

Table 4-9: Summary of Time Stepping Results for the Common Rotor, 36 Slot 6 Pole Design

	Open-Circuit		**Rated-Current (90deg)**		**Rated-Current (MTPA)**	
	non-skewed	*skewed (1 sp)*	*non-skewed*	*skewed (1 sp)*	*non-skewed*	*skewed (1 sp)*
Terminal Current						
Input current [Arms]	0	0		**24.1**	**24.1**	**24.1**
Torque Angle [deg. el.]	N/A	N/A		90	123	123
Input Frequency [Hz]	90	90		90	90	90
Torque and Speed						
Tem avg. [Nm]	0.0	0.0		61.3	73.5	72.6
Tsh avg. [Nm]	-0.7	-0.7		60.0	72.4	71.5
Tripple [%]	3.3	1.7		8.1	21.7	7.6
Speed [r/min]	1800.0	1800.0		1800.0	1800.0	1800.0
Motor Voltage (Induced)						
Van peak [Vpk]	258.7	233.8		332.4	348.8	313.1
Van fund [Vpk]	254.3	251.4		345.0	299.7	296.3
Van rms [Vrms]	181.0	179.0		247.0	213.8	211.3
Vab peak [Vpk]	516.9	462.1		**610.7**	566.0	545.0
Vab fund [Vpk]	440.5	435.5		597.6	519.0	513.1
Vab rms [Vrms]	313.5	310.0		427.7	370.3	366.1
Powers, Losses and Efficiencies						
Copper [W]	0.0	0.0		610.6	610.6	610.6
Stator Core [W]	128.3	128.3		228.7	185.7	185.5
Rotor Core [W]	6.1	6.1		16.2	13.7	13.7
PM Eddy 2-D [W]	0.0	0.0		1.1	0.8	0.7
Electromagnetic Power [kW]	0.00	0.00		11.55	13.85	13.68

Input Power [kW]	0.00	0.00		12.16	14.46	14.29
Shaft Power [kW]	-0.13	-0.13		11.30	13.65	13.48
Power Factor [pu]				0.67	0.91	0.91
Efficiency [%]	N/A	N/A		93.0	94.4	94.3

Notes:
1. Time-stepping FE with 2nd order elements (current-driven, 180 samples per el. cycle)
2. PM: VACODYM 677HR @ 20 deg. C
3. Copper: @ 20 deg. C
4. Core losses calculated using AK M19-26Ga (x2 scaling factor)
5. Efficiency calculation does not include friction and windage losses

Table 4-10: Summary of Time Stepping Results for the Common Rotor, 9 Slot 6 Pole Design

	Open-Circuit		**Rated-Current (90deg)**		**Rated-Current (MTPA)**	
	non-skewed	*skewed (1 sp)*	*non-skewed*	*skewed (1 sp)*	*non-skewed*	*skewed (1 sp)*
Terminal Current						
Input current [Arms]	0	0		**28.0**	**28.0**	**28.0**
Torque Angle [deg. el.]	N/A	N/A		90	119	119
Input Frequency [Hz]	90	90		90	90	90
Torque and Speed						
Tem avg. [Nm]	0.0	0.0		60.6	71.8	70.8
Tsh avg. [Nm]	-0.7	-0.7		58.8	70.1	69.2
Tripple [%]	1.8	1.1		8.1	8.9	6.6
Speed [r/min]	1800.0	1800.0		1800.0	1800.0	1800.0
Motor Voltage (Induced)						
Van peak [Vpk]	233.4	231.7		316.3	272.2	271.3
Van fund [Vpk]	221.5	219.0		313.2	273.0	269.9
Van rms [Vrms]	157.5	155.7		224.3	195.8	193.6
Vab peak [Vpk]	366.5	362.5		**625.9**	497.4	498.0
Vab fund [Vpk]	383.7	379.3		542.4	472.8	467.5
Vab rms [Vrms]	272.7	269.6		388.4	339.1	335.2
Powers, Losses and Efficiencies						

Copper [W]	0.0	0.0		414.8	414.8	414.8
Stator Core [W]	122.4	122.4		235.8	188.1	186.7
Rotor Core [W]	7.9	7.9		39.3	40.3	38.8
PM Eddy 2-D [W]	0.2	0.2		64.6	77.1	77.1
Electromagnetic Power [kW]	0.00	0.00		11.43	13.53	13.34
Input Power [kW]	0.00	0.00		11.84	13.94	13.75
Shaft Power [kW]	-0.13	-0.13		11.09	13.22	13.04
Power Factor [pu]				0.62	0.84	0.84
Efficiency [%]	N/A	N/A		93.6	94.8	94.8

Notes:
1. Time-stepping FE with 2nd order elements (current-driven, 180 samples per el. cycle)
2. PM: VACODYM 677HR @ 20 deg. C
3. Copper: @ 20 deg. C
4. Core losses calculated using AK M19-26Ga (x2 scaling factor)
5. Efficiency calculation does not include friction and windage losses

The 36 slot 6 pole machine produced a slightly higher average torque at rated operating conditions than the 9 slot 6 pole machine. If the drive cannot control the torque angle properly and reverts to controlling the stator current angle at 90 degrees the drive will run out of voltage before the rated speed can be reached for both machine designs. The detailed efficiency calculation predicts a much smaller efficiency difference than the initial design analysis did. The core losses in the rotor and magnets are higher in the 9 slot 6 pole design than the 36 slot 6 pole machine because of increased armature reaction harmonic content. This counteracts the reduced copper losses in the 9 slot 6 pole design. This analysis has not considered the effect of copper losses in the end turns for which the 9 slot 6 pole design should have an advantage. The fundamental power factor is slightly higher in the 36 slot 6 pole design than in the 9 slot 6 pole design. This could allow the use of a reduced kVA rating inverter when paired with the 36 slot 6 pole design.

The cogging torque waveforms for both designs with the common rotor are shown in Figure 4-151. Step skewing the rotor by 5 mechanical degrees which approximates a continuous electrical skew of 10 electrical degrees or 1 slot pitch has a large impact on the cogging torque

in the 36 slot 6 pole design, Figure 4-151 (a). While the cogging torque reduction because of the skewed common rotor in the 9 slot 6 design is rather minor, its cogging torque was already smaller than in the 36 slot 6 pole design.

The electromagnetic torque ripple at rated current for both designs is shown in Figure 4-152 and Figure 4-153. In Figure 4-152 the current angle is 90 degrees and in Figure 4-153 at the MTPA current angle for each design. With the skewed rotor the torque ripple with a current angle of 90 degrees is roughly equivalent for both machine designs. The frequency content of the 36 slot 6 pole machine is higher and will be filtered to a greater extent by the system inertia. As can be seen in Figure 4-153 if the common rotor was not skewed the torque ripple of the 36 slot 6 pole machine would be substantially higher the than 9 slot 6 pole machine at their MTPA rated operating points. With the skewed rotor the torque ripple is still slightly smaller with the 9 slot 6 pole machine though of lower frequency content.

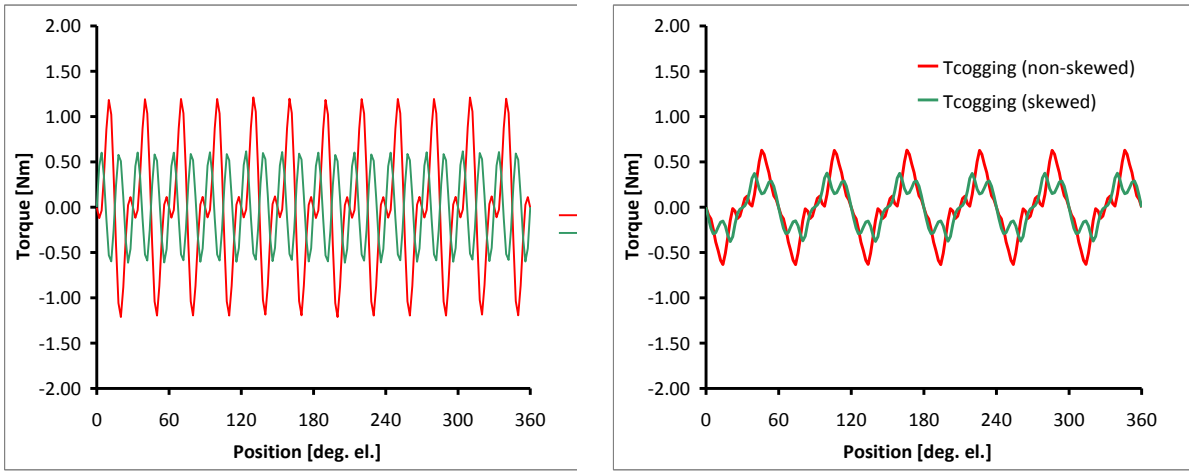

(a) 36 Slot 6 Pole Design

(b) 9 Slot 6 Pole Design

Figure 4-151: Estimated cogging torque from time stepping finite element simulations for the two stator designs and common rotor.

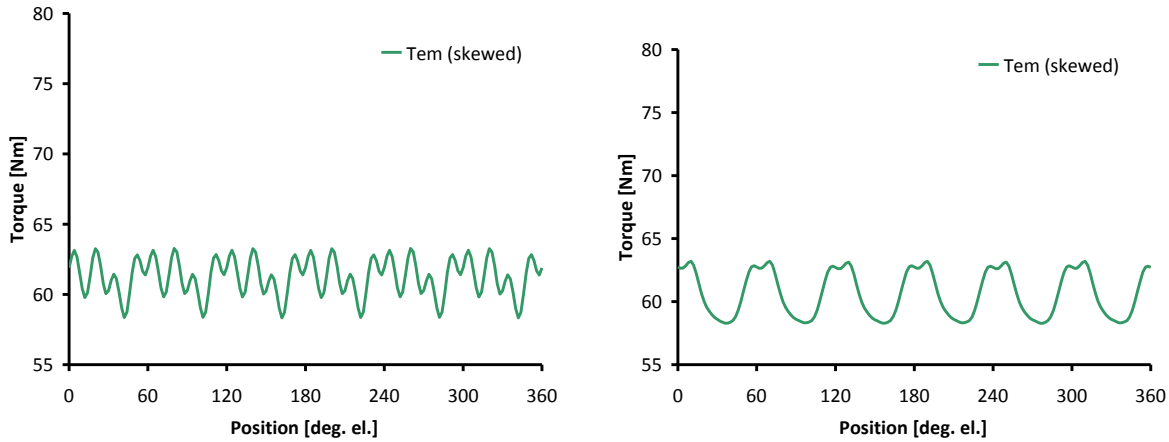

(a) 36 Slot 6 Pole Design (b) 9 Slot 6 Pole Design

Figure 4-152: Estimated torque waveforms from time stepping finite element simulations for the two stator designs and common rotor operating at their design currents and a torque angle of 90 degrees electrical

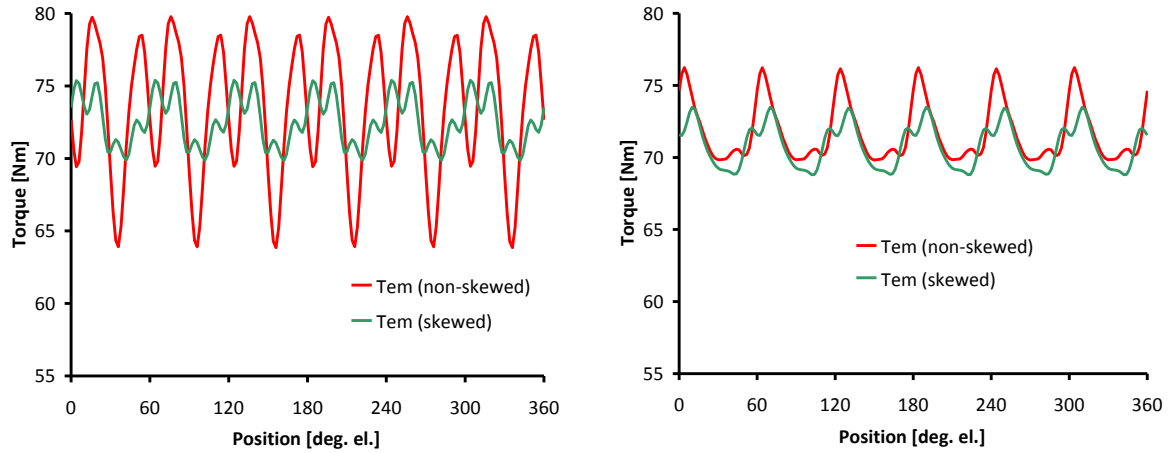

(a) 36 Slot 6 Pole Design (b) 9 Slot 6 Pole Design

Figure 4-153: Estimated torque waveforms from time stepping finite element simulations for the two stator designs and common rotor operating at their design currents and their maximum torque per ampere (MTPA) torque angle.

The active conductor voltage waveforms for the two designs with the common rotor are shown in Figure 4-154 to Figure 4-156 for open circuit conditions, rated current and a current angle of 90 degrees, and rated current at the MTPA current angle. All voltage waveforms do not include

the voltage drop across the end turns. The harmonic content of the 9 slot 6 pole design is substantially higher for all operating conditions. The harmonic content may make it more difficult for the drive to regulate the phase currents to perfect sinusoids. As mentioned above if the drive does not advance the current angle it may run out of voltage before reaching the rated speed of 1800 RPM. This can be seen in Figure 4-155.

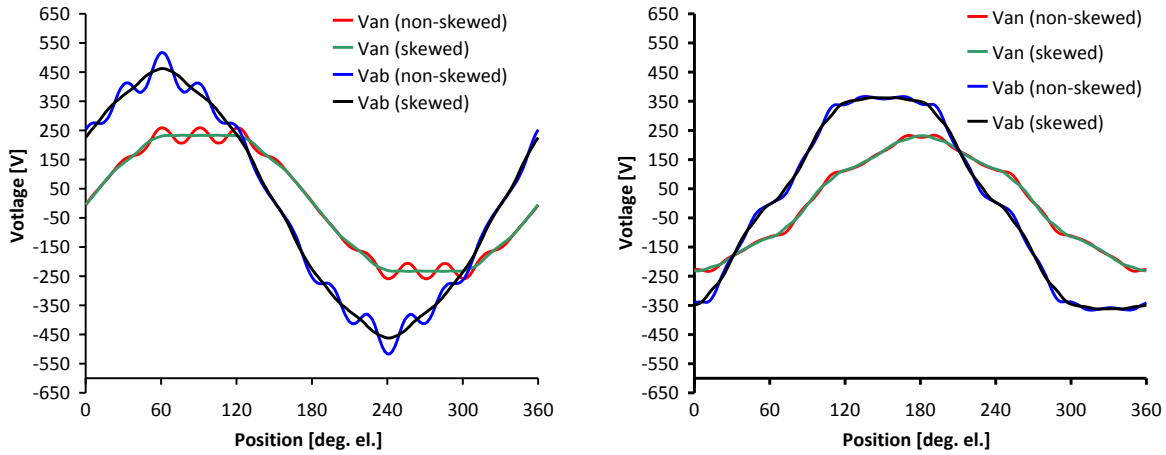

(a) 36 Slot 6 Pole Design (b) 9 Slot 6 Pole Design

Figure 4-154: Open circuit voltage waveforms calculated using time stepping nonlinear finite element analysis. End turn voltage drops are not included in the results.

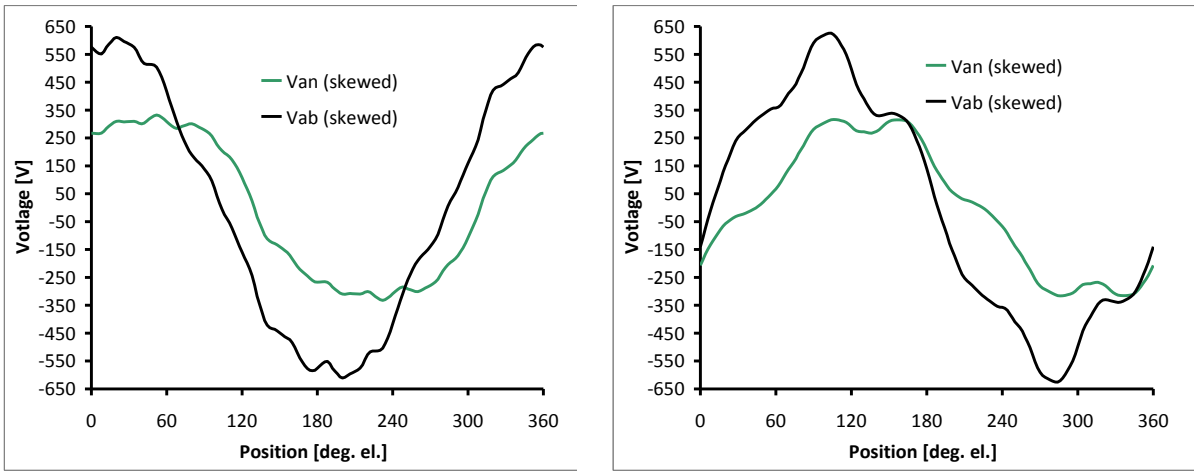

(a) 36 Slot 6 Pole Design (b) 9 Slot 6 Pole Design

Figure 4-155: Voltage waveforms at the design current and torque angle of 90º calculated using time stepping nonlinear finite element analysis. End turn voltage drops are not included in the results.

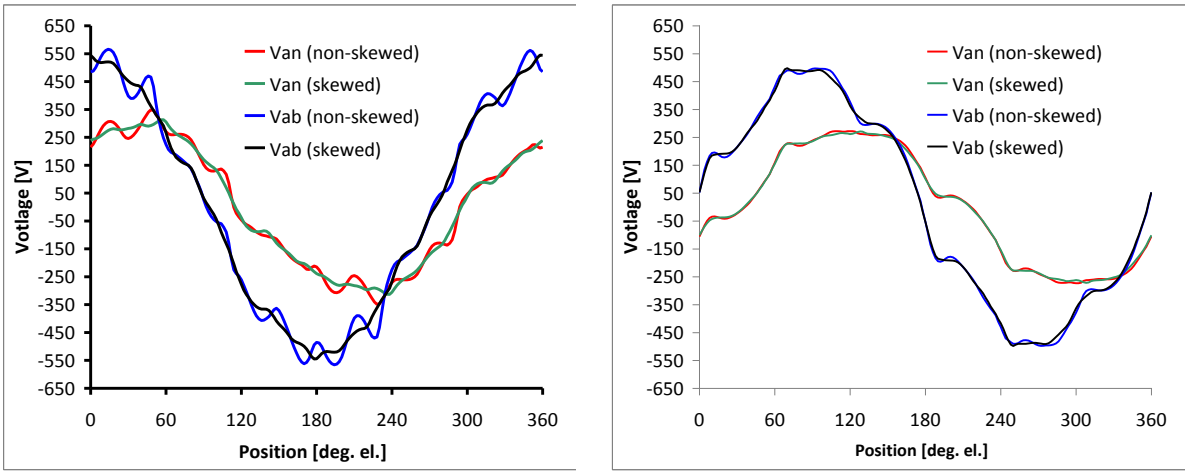

(a) 36 Slot 6 Pole Design (MTPA = 123º)

(b) 9 Slot 6 Pole Design (MTPA = 119º)

Figure 4-156: Maximum torque per ampere voltage waveforms calculated using time stepping nonlinear finite element analysis. End turn voltage drops are not included in the results.

Prototype Construction

The laser cut laminations for both the 36 slot 6 pole and 9 slot 6 pole stators have been received, Figure 4-157. The laser cut common rotor laminations were also received, Figure 4-158. All laminations were cut from AK M19 26 Ga steel as per the design specifications. The tolerances on laminations appear to be well within the design specifications. Currently the stator laminations have been sent out for winding and varnishing.

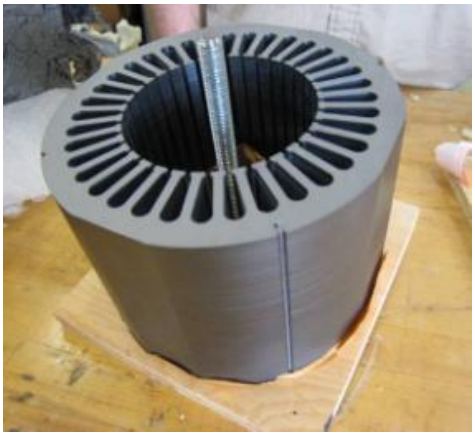

(a) 36 Slot 6 Pole Stator

(b) 9 Slot 6 Pole Stator

Figure 4-157: Laser cut and welded stator stacks

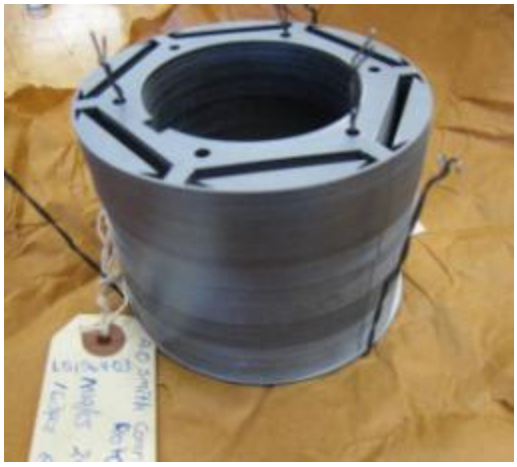

Figure 4-158: Laser cut common rotor laminations.

Mechanical Design

An approximate cross-section of the mechanical situation in the Bitzer 4MTC-10K transcritical R744 compressor is shown in Figure 4-159. This cross-section shows the induction machine rotor which is cantilevered. The rotor also has a counter bore on both ends. The bearing support for the cantilevered rotor reduces the area available for stator end turns. Overall there is limited room for both the lamination stacks and end turns for the PM motor. The bearing support and counter bores in the rotor present difficulties for the mechanical design of the internal permanent magnet rotor.

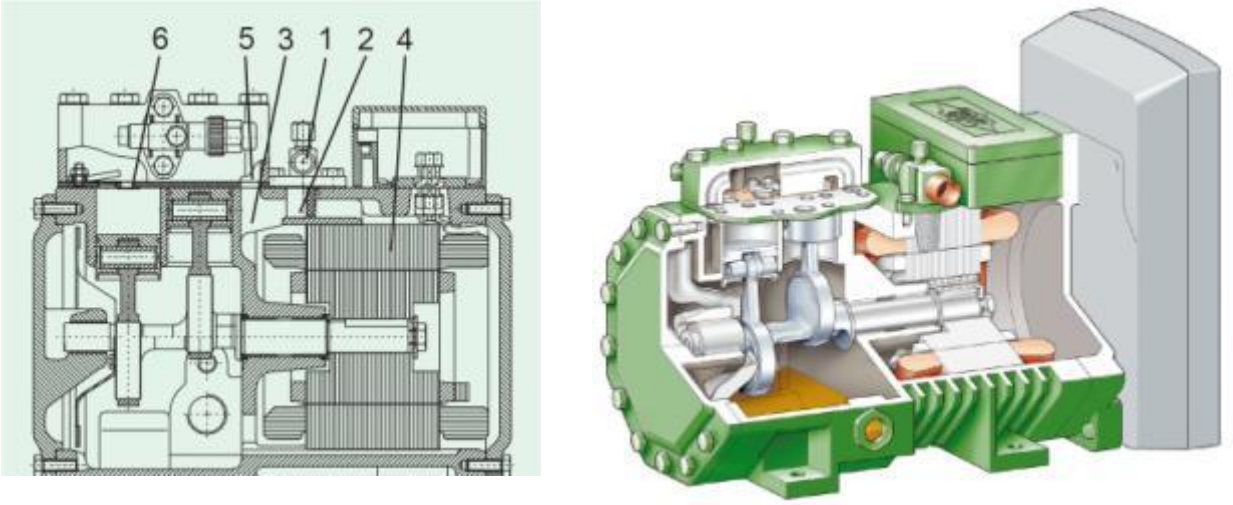

Figure 4-159: Section view of Bitzer compressor showing cantilevered rotor with counter bore (Source Bitzer compressor online documentation).

To test the common permanent magnet rotor design in a dynamometer and use the same rotor in a sample compressor, a shaft adapter, opposite lead end clamp ring, were designed. The shaft adapter and opposite lead end clamp ring are shown with several laminations in Figure 4-160. The shaft adapter by itself is shown in Figure 4-161. The shaft adapter allows a single lamination design to be used the entire length of the permanent magnet rotor unlike in the induction machine. The rotor lamination inner diameter is the same as that in the induction machine counter bore currently used in the production 4MTC-10K compressor. The counter bore laminations are held into place with the opposite lead end clamp ring, six threaded rods, and magnets. A planned epoxy encapsulant in the magnet slots should add strength to the structural integrity of the counter bore laminations.

Figure 4-160: Shaft adapter, opposite lead end clamp ring, and several laminations.

Figure 4-161: Rotor shaft adapter with a single lamination

To measure the efficiency and verify the sensor-less operation of the two stator designs with the common rotor, dynamometer testing is necessary. The overall design of the canister, end plates, shaft, and shaft adapter for dynamometer testing is shown in Figure 4-162 through Figure 4-165. The use of the shaft adapter allows the common rotor to be transferred to the compressor without extensive disassembly or modification.

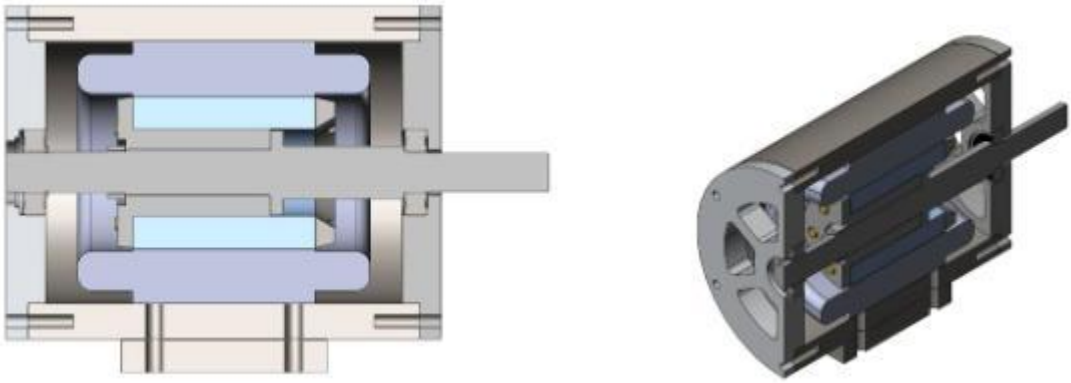

Figure 4-162: Mechanical design of canister, shaft adapter, and shaft for dynamometer testing and evaluation of the sensor-less control performance with the two stator designs and common rotor.

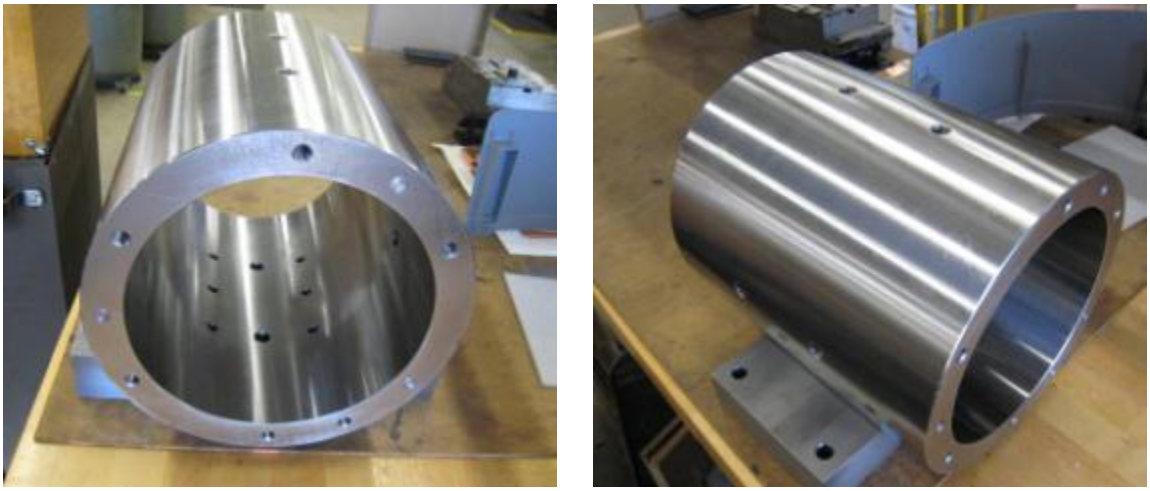

Figure 4-163: Canister for dynamometer testing and evaluation of sensor-less control performance with the two stator designs and common rotor.

Figure 4-164: Canister End Plates

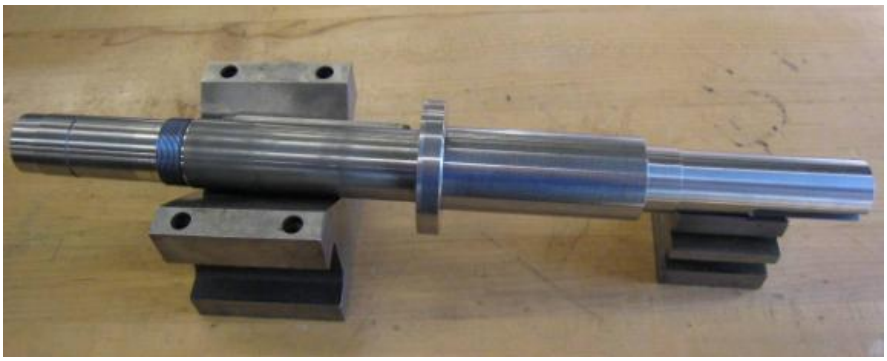

Figure 4-165: Shaft for Dyne Testing

If the rotor is not inserted concentric to the stator bore, the magnetic forces due to the permanent magnets will try to pull the rotor to the closer stator side. To keep the rotor aligned with the stator bore, a centering horn is used, Figure 4-166. The rotor shaft is held in the chuck of a lathe with the canister mounted to the lathe slide. The centering horn passes through the canister endplate to support the end of the rotor shaft not mounted in the lathe chuck. The lathe slide is advanced until the rotor is inserted into the stator and the end plates bolted into place.

Figure 4-166: Rotor Insertion Centering Horn

Light Load Dynamometer Testing

Both the 9 slot 6 pole and 36 slot 6 pole stators with the common interior permanent magnet (IPM) rotor were tested under light load conditions at A.O. Smith to verify the correct insertion of the magnets and measure the back-emf, friction and windage losses, open circuit core losses, and light load efficiency and sensorless operation.

Three operating modes are available in the Yaskawa A1000 drive for permanent magnet motors: open loop vector control for PM motors, advanced open loop vector control for PM motors, and closed loop vector control for PM motors. The closed loop vector control mode requires and encoder. In the compressor, operation without an encoder is necessary. A relatively large speed range and the ability to startup against large torque loads is also desirable for operation in the compressor. The advanced open loop control mode can utilize a high frequency injection sensorless control method a low speeds which should provide greater starting torque capability and better rotor position estimation. For both the light load and full load dynamometer testing the advanced open loop vector control mode for PM motors was used.

In addition to the drive control mode motor parameter estimates are needed by the drive for proper operation. The Yaskawa A1000 drive has a stationary auto-tuning procedure with an adjustable current excitation level that defaults at 30 percent of the rated current. At light loads the auto-tuning determined parameters, primarily L_d, L_q, and K_e, at the default current level appeared give good sensorless control performance and very good efficiency. It was found that during full load dynamometer testing the motor parameters and drive controller gains needed to be hand tuned for stability and optimum performance.

The Yaskawa A1000 drive also has a feature which it calls “Energy Saver”. This feature is not well documented in the drives technical manual but appears to slowly vary the direct axis

current to minimize the power input to the drive while maintaining the required commanded speed. This setting had minimal impact on the light load efficiencies and a measurable impact with larger torque loads. Unfortunately, under larger loads it also seemed to cause instability.

Light Load Dynamometer Setup

The light load dynamometer at A.O. Smith is shown in Figure 4-167 and Figure 4-168. The motor under test is housed in the metallic cylinder and the load motor is a 3 Hp induction machine driven by a 3 Hp Baldor vector drive. Cooling is provided by 3 grey Dayton blowers. Torque and speed measurements are collected by a 100 Lb-In Himmelstein Torque Meter and Himmelstein 700 series conditioning box. The Himmelstein Torque Meter was calibrated with dead weights. Input to the drive was measured with a Yokogawa WT 1600 power analyzer and two Yokogawa PZ4000 power analyzers were connected on the output of the drive. One of the PZ4000 analyzers was run in normal mode while the other was run in harmonic mode. Both analyzers were triggered simultaneously to ensure analysis of the same data. Because the two motor design current ratings are higher than the current limit for the PZ4000 power analyzers a custom made current sense box with closed loop nulling Hall Effect LEM current sensors was fed into the PZ4000 power analyzers. Analog torque and speed data was also simultaneous sampled by the PZ4000 in normal mode from the Himmelstein signal conditioning box.

Measurements of the motor winding temperatures were made using thermocouples embedded in the winding and behind the slot insulation. The thermocouples were connected to a Stanford Research thermocouple reader. Data collected and calculations performed by the power analyzers were imported into an Excel spreadsheet using a custom made LabView program communicating with the power analyzers and thermocouple reader via GPIB. Torque and speed data was also collected directly in LabView via a serial link to the Himmelstein signal conditioning box.

Figure 4-167: Light load dynamometer set up

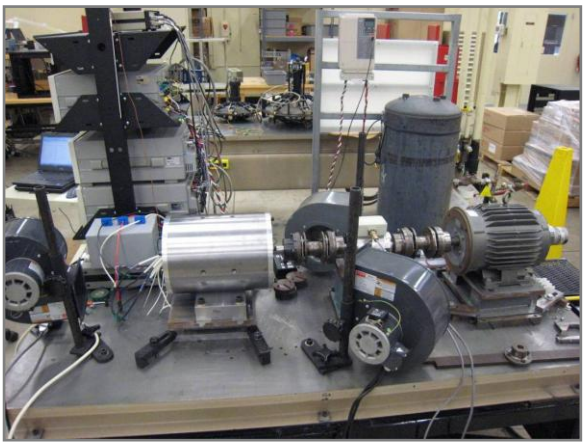

Figure 4-168: Light load dynamometer setup alternative view

Light Load Dynamometer Test Results

The friction and windage losses were estimated using the 36 slot 6 pole stator and a dummy steel slug of the same diameter as the rotor, Figure 4-169. The open circuit core losses were also measured for both stators, Figure 4-170. The open circuit core losses for the 9 slot 6 pole design are lower than for the 36 slot 6 pole design. The finite element analysis (FEA) prediction of the open circuit core losses are substantially higher than the measured values, Figure 4-170. This is likely due to the 2 times scaling value which is somewhat arbitrarily used. The FEA predicted open circuit core losses are essentially identical for both designs. It is unclear why the measured values differ. Under load the losses of the 9 slot 6 pole design are predicted to be higher than the 36 slot 6 pole design because of increased airgap armature reaction harmonics.

The open circuit back-emfs were experimentally measured and compared to FEA predicted waveforms, Figure 4-171. The measured and predicted waveforms very closely match for both stator types. This also indicates that the magnets were inserted properly.

The light load dynamometer motor, drive, and efficiency results for both stator designs with the common rotor are shown in Figure 4-172 and Figure 4-173. For both machines the motor, drive, and system efficiency are very high for light load conditions. The drive sensorless control algorithm seemed to handle light load torque transients without a problem.

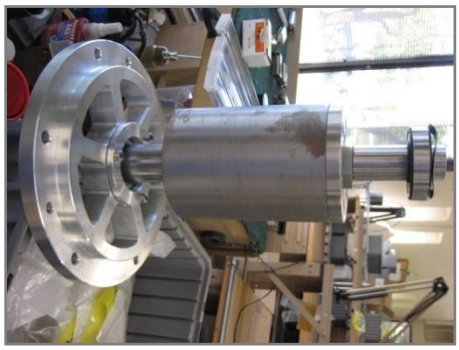

Figure 4-169: Steel slug for measuring friction and windage losses

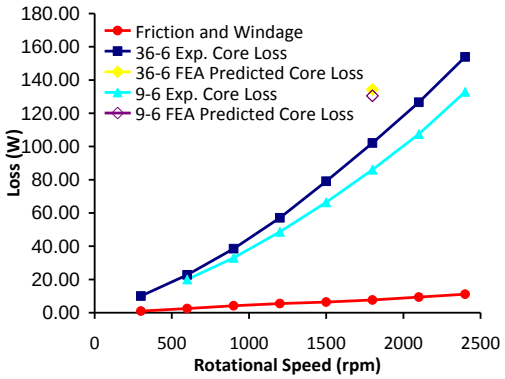

Figure 4-170: Measured and predicted open circuit losses including friction and windage and open circuit core losses

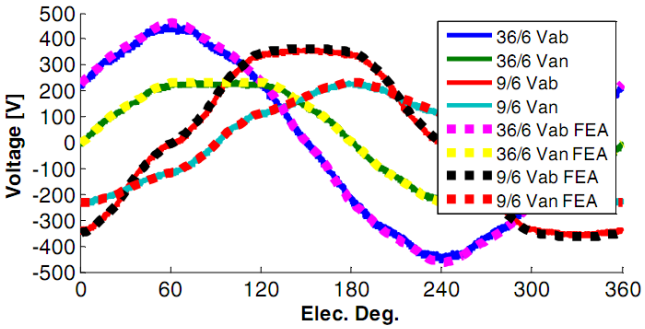

Figure 4-171: Experimentally measured open circuit back-emfs at 1800 rpm with comparison to time stepping FEA results

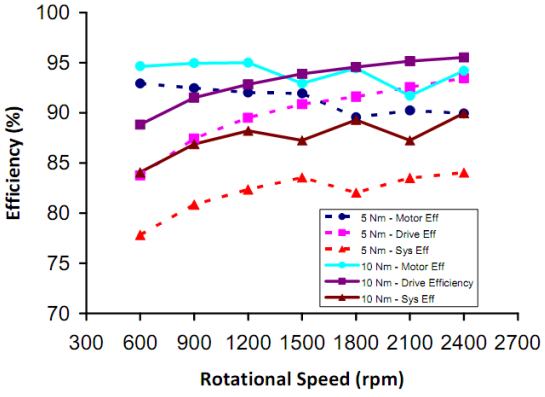

Figure 4-172: 9 slot 6 pole light load dynamometer measured motor, drive, and system efficiency

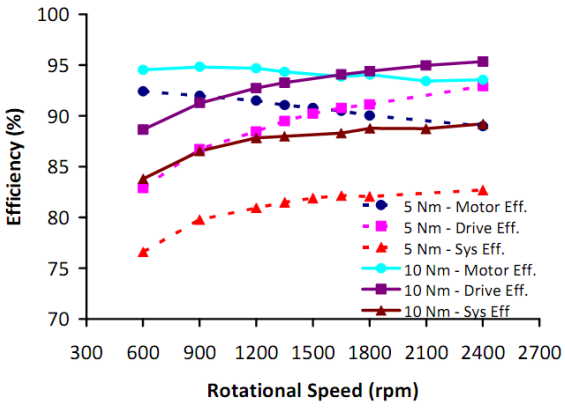

Figure 4-173: 36 slot 6 pole light load dynamometer measured motor, drive, and system efficiency

Full Load Dynamometer Setup

Because the dynamometer available at A.O. Smith was too small to operate the prototype motors at their rated operating point, a 50 Hp dynamometer was rented at an outside company, Dyne Systems Inc. The full load dynamometer setup is shown in Figure 4-174, Figure 4-175 and Figure 4-176. The load motor was a 50 Hp ABB induction machine connected to an ABB regenerative drive. The load motor and drive were controlled using a Dyne Systems Interlock V controller. This allowed the load motor to be operated in either torque or speed mode with over-speed and torque limits. The drive tuning and efficiency measurements were carried out with the Yaskawa A1000 drive in speed mode and the load ABB drive and Dyne Systems Interlok V controller in torque mode.

The same experimental measurement equipment was used as for the light load dynamometer testing except for the torque meter and speed measurement. Torque was measured using an HBM T40 1000 Nm torque meter. The range of this torque meter is much higher than needed for the rated torque of the prototype motors, 70 Nm. The torque meter is specified to have an accuracy of 0.5% over its full range. The speed measurement is from a dual encoder mounted on the load motor.

The torque meter provides an analog output to the Interlock V controller which is normally scaled 10 V = 1000 Nm. The torque and speed signals were then retransmitted by the Interlock V in both analog and serial forms. The analog outputs were connected to the motor module of the Yokogawa PZ4000 operating in normal mode and a serial link connected to the LabView data collection program. With the default scaling at full load the analog output from the torque meter is only 0.7 V. At lower torque values such as 10 Nm the torque meter output voltage reading of 0.10 V is quite susceptible to noise, and offsets introduced during analog to digital and digital to analog conversions. To improve the signal to noise ratio an additional signal conditioning model, HBM TIM, was used to rescale the voltage signal from the torque meter to 10V = 100 Nm for the dyne testing of the 36 slot 6 pole machine.

The torque meter or the analog to digital interface of the dyne controller also seemed to have an approximately 0.5 Nm offset. In the forward direction at 1800 RPM a torque of 1.5 Nm was measured. In the reverse direction at 1800 RPM a torque of 0.5 Nm was measured. The direction of rotation should not have any impact on the torque value. An offset of 0.3 V in the forward rotation direction was also corrected for.

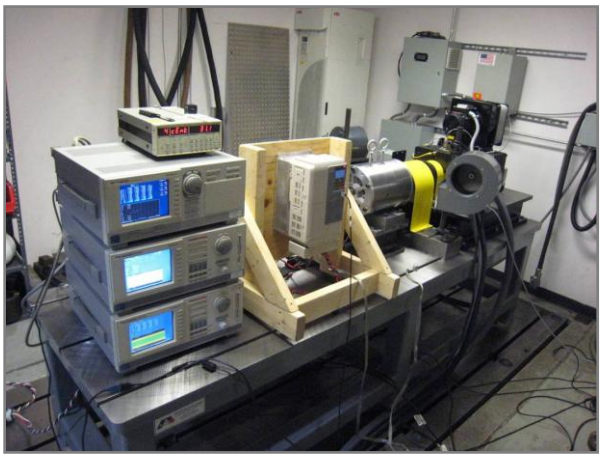

Figure 4-174: Full load dynamometer with data acquisition equipment

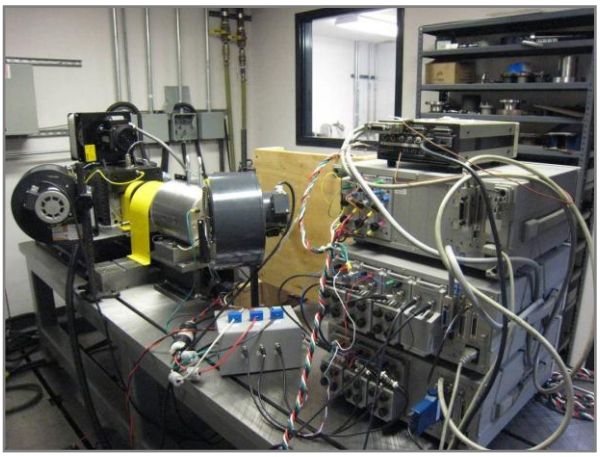

Figure 4-175: Full load dynamometer with data acquisition equipment reverse side

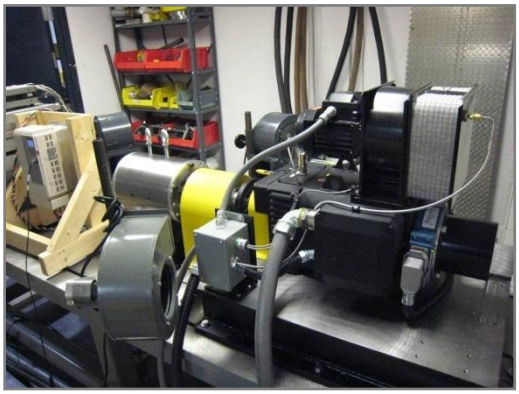

Figure 4-176: Full load dynamometer cooling setup

System Tuning

In the light load dyne testing the stationary auto-tuning with 30% of the rated current was found result in satisfactory if not very good performance with both motor designs. While the stationary auto-tuned parameters were used as a starting point considerable tuning was necessary to operate both motor designs stably at their rated operating points. The tuning primarily consisted of hand tuning the L_d, L_q, K_e, sensorless PLL gain, ASR proportional gain, and energy saver parameters. Tuning was carried out by setting the drive parameters and then ramping up the load torque till the drive tripped or rated operation was achieved. Once the rated operation was achieved the output current, motor, drive, and system efficiencies were observed and compared to FEA predicted values.

As the common rotor is has a interior or buried permanent magnet both motor designs require d-axis current, I_d, for reluctance torque production. The stator core losses are also reduced at high speed by bucking the magnet flux. The amount of I_d current ideally varies with torque and speed. At low torque and speed no Id is needed. It appears that the Energy Saver feature of the Yaskawa drive attempts to vary the I_d current to minimize the energy input to the drive. However for both machine designs the drive was not consistently found to be stable with the energy saver feature enabled. After considerable time spent tuning other drive parameters to try to achieve more stable operation the feature was disabled. Without the energy saver feature enabled the I_d current was tuned for the rated operating point. At other operating points the I_d current is not necessarily at its optimum value.

The stationary auto-tuning procedure was found to overestimate the back-emf constant, K_e, of the motors. During the tuning process it was found that stable operation was much more likely by reducing the back-emf constant to that predicted by the FEA analysis. The stator resistance parameter was also changed to that measured offline with a 4 wire meter. It appears that by varying the L_d, L_q, and K_e parameters the drive could be tricked into estimating the d-axis position ahead of its true location. This results in d-axis current which as mentioned above is desirable for optimum operation of interior permanent magnet machines. By monitoring the drive output current, machine, drive, and system efficiencies, the drive parameters were hand tuned to result in drive output currents and efficiencies close to the FEA predicted values at the rated operating point. Ideally in a production system the drive would be programmed to vary the I_d current with the system operating point. This is price for using an off the shelf general purpose drive. The default value, 1, for the sensorless PLL gain appeared to result in too much noise in the rotor position estimate. For both motor designs it was necessary to reduce this parameter setting. A range of values between 0.1 and 0.75 was tried. The tradeoff for the reduced gain is a longer time for the PLL to respond to disturbances. The default speed controller proportional gain, ASR P1 and P2, also seemed to be overturned for both motor designs and resulting in noise in the current command. The final tuning values for the two motor designs are listed in

Table 4-11 and Table 4-12.

Table 4-11: 9 slot 6 pole drive parameters

Drive Parameter	Value
Energy Saver	0
Rs (Ohms)	0.206
Ld (mH)	12.00
Lq (mH)	15.46
Ke (mV sec/rad)	142.0
PLL Gain	0.50
ASR P Gain (s)	5.00

Table 4-12: 36 slot 6 pole drive parameters

Drive Parameter	Value
Energy Saver	0
Rs (Ohms)	0.270
Ld (mH)	7.90
Lq (mH)	17.36
Ke (mV sec/rad)	172.2
PLL Gain	0.75
ASR P Gain (s)	5.00

Full Load Dynamometer Test Results

The motor, drive, and system efficiency maps are shown in the following section for both the 9 slot 6 pole and 36 slot 6 pole designs. The efficiency maps for the 9 slot 6 pole design are up to the design rated operating speed of 1800 RPM while for the 36 slot 6 pole design the efficiency maps are extended up to a speed of 2100 RPM. It was more difficult to tune and operate stably the 9 slot 6 pole design. Because of time limitations higher speeds than 1800 RPM were not tested.

The motor and system efficiency maps are shown for calculations using the torque values collected via a serial link from the dyne controller but corrected for the torque meter offset as

discussed in the previous section. The same efficiency maps are also shown using calculations from torque values transmitted and sampled by the PZ4000 power analyzer and corrected for the torque offset. The torque is not used in the drive efficiency calculation so only one map is shown for each machine design.

Both machine designs are highly efficient with motor and system efficiency seeming to be slightly higher for the 36 slot 6 pole machine. The 36 slot 6 pole machine also appeared to be more stable over a wider range of drive parameters. It was also possible to operate the machine above the design base speed of 1800 RPM. This would enable higher capacity operation of the compressor to be explored. Primarily, because of the perceived stability advantage of the 36 slot 6 pole design it was decided to test this motor in the Bitzer transcritical CO_2 compressor.

9 Slot 6 Pole Motor with Common IPM Rotor

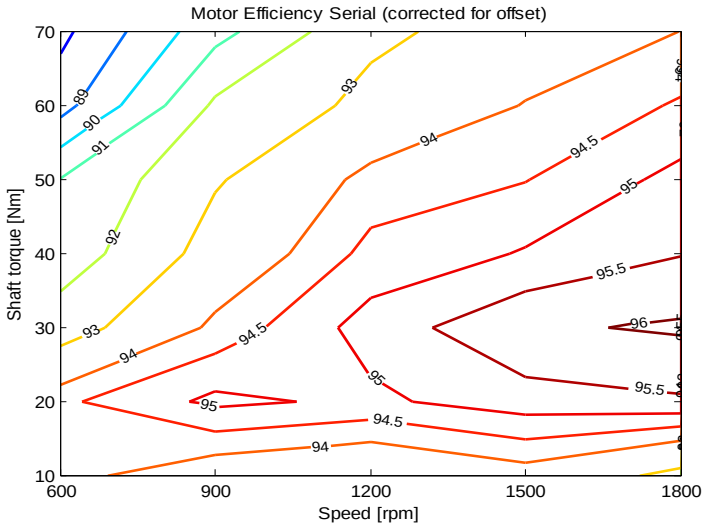

Figure 4-177: 9 slot 6 pole motor efficiency calculated using a serial link torque output from the dynamometer controller. The output torque readings were corrected for an offset in the output torque measurement

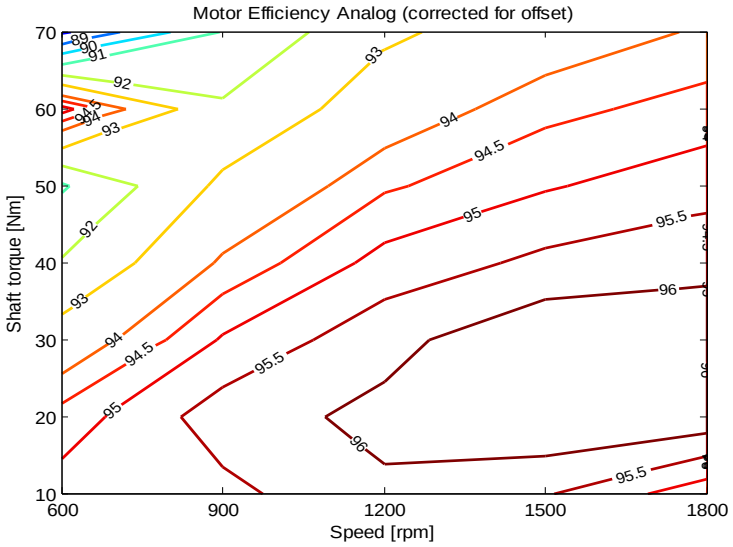

Figure 4-178: 9 slot 6 pole motor efficiency calculated using an analog output from the dynamometer controller and sampled by the motor module in a Yokogawa PZ4000 power analyzer (10 V = 1000 Nm). The output torque readings were corrected for an offset in the output torque measurement.

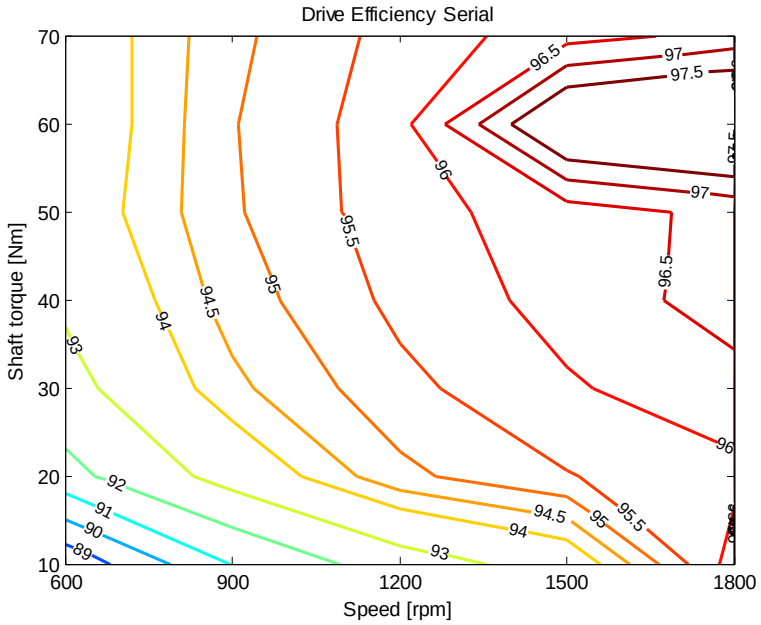

Figure 4-179: Measured Yaskawa A1000 drive efficiency when operating the 9 slot 6 pole motor.

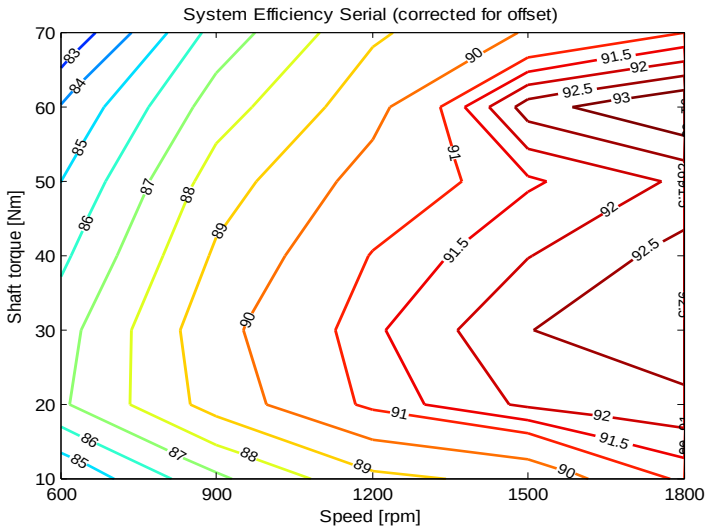

Figure 4-180: Measured system efficiency with the 9 slot 6 pole motor using a serial link torque output from the dynamometer controller. The output torque readings were corrected for an offset in the output torque measurement.

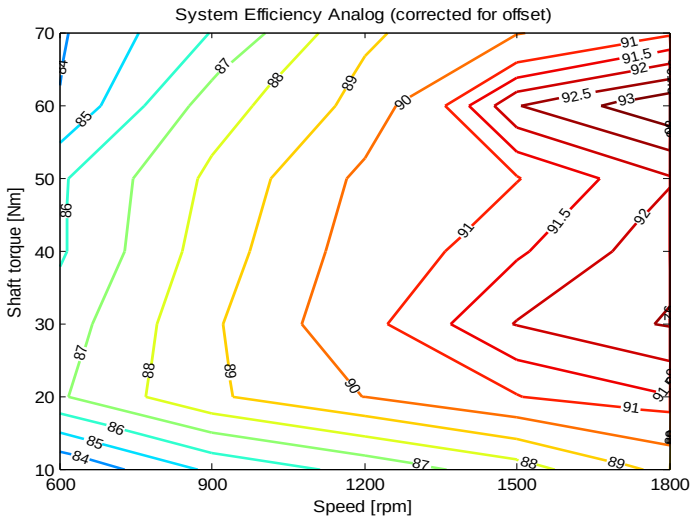

Figure 4-181: Measured system efficiency with the 9 slot 6 pole motor using an analog output from the dynamometer controller and sampled by the motor module in a Yokogawa PZ4000 power analyzer (10 V = 1000 Nm). The output torque readings were corrected for an offset in the output torque measurement.

36 Slot 6 Pole Motor with Common IPM Rotor

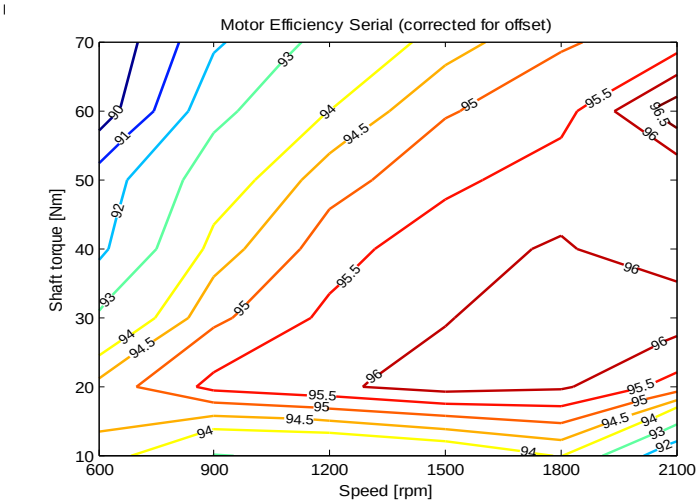

Figure 4-182: 36 slot 6 pole motor efficiency calculated using a serial link torque output from the dynamometer controller. The output torque readings were corrected for an offset in the output torque measurement.

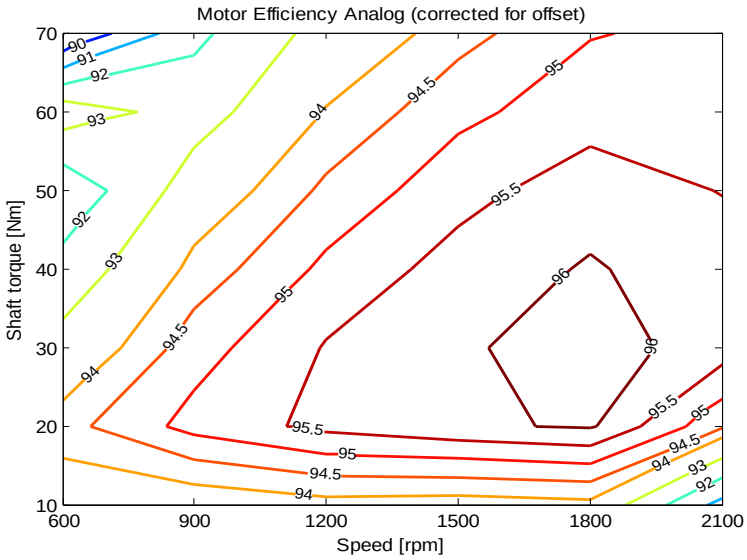

Figure 4-183: 36 slot 6 pole motor efficiency calculated using an analog output from the HBM T40 TIM and sampled by the motor module in a Yokogawa PZ4000 power analyzer (10 V = 100 Nm). The output torque readings were corrected for an offset in the output torque measurement.

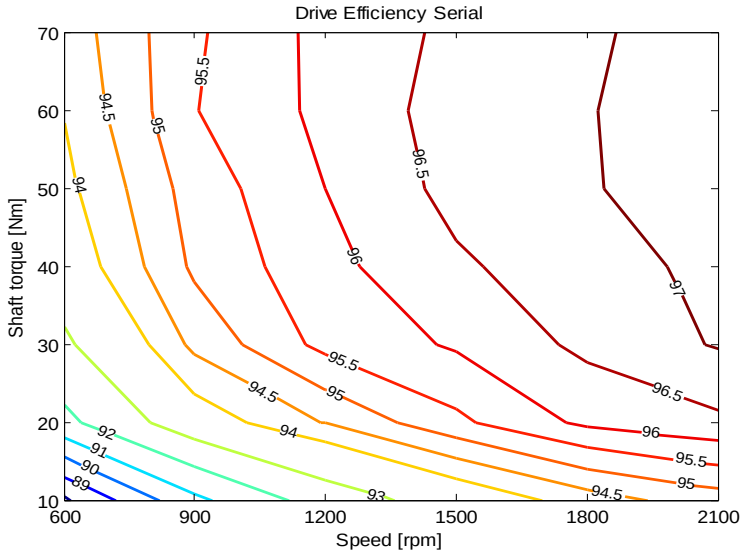

Figure 4-184: Measured Yaskawa A1000 drive efficiency when operating the 9 slot 6 pole motor.

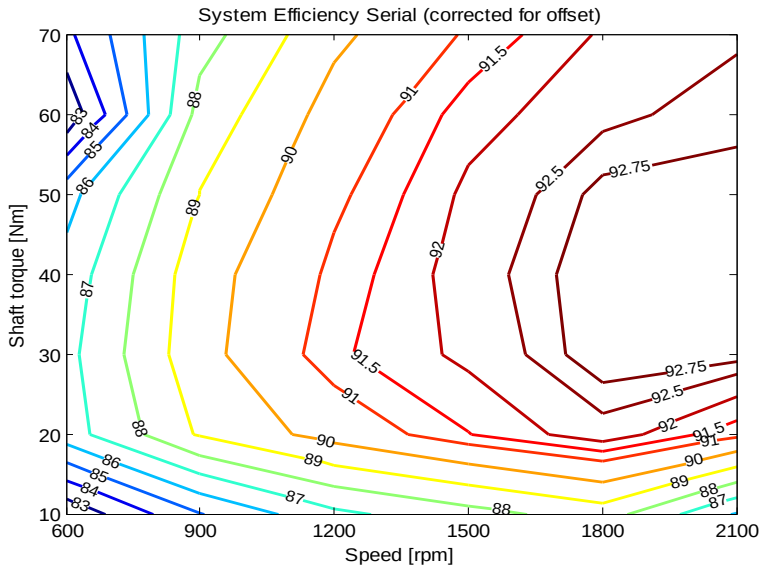

Figure 4-185: Measured system efficiency with the 36 slot 6 pole motor using a serial link torque output from the dynamometer controller. The output torque readings were corrected for an offset in the output torque measurement.

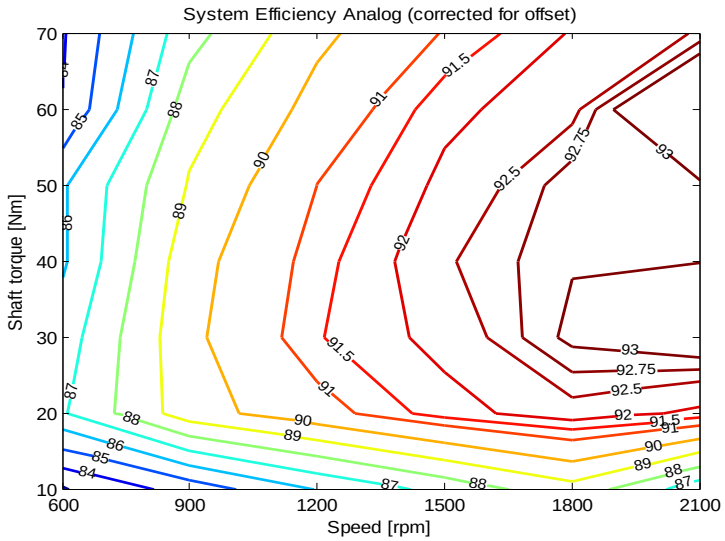

Figure 4-186: Measured system efficiency with the 36 slot 6 pole motor using an analog output from the HBM T40 TIM and sampled by the motor module in a Yokogawa PZ4000 power analyzer (10 V = 100 Nm). The output torque readings were corrected for an offset in the output torque measurement.

Extraction of Induction Machine from the Compressor

To extract the stock induction machine from the Bitzer transcritical CO_2 4MTC-10K-40S compressor the end bell and connection terminal blocks were removed. This allowed access to the induction machine rotor and stator. The aluminum squirrel cage rotor was removed from the compressor by removing a holding nut from the end of the cantilevered shaft, Figure 4-187. To remove the pressed in stator was a much more involved process.

Because the stator was likely pressed in with several thousand pounds of force spectra line was laced through the stator end turns and a steel pulling ring, Figure 4-188. Bolts to support a backing plate were screwed into the compressor end manifold, Figure 4-189, and the backing plate held into place with nuts. The central bolt used to pull the stator was turned with a custom made nut driver. The partially extracted induction machine stator is shown in Figure 4-190.

Figure 4-187: Stock induction machine rotor and holding nut.

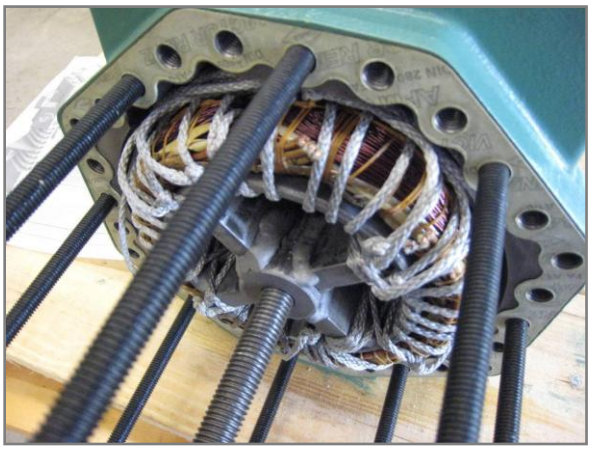

Figure 4-188: Spectra lines laced through induction machine end turns and backing bolts

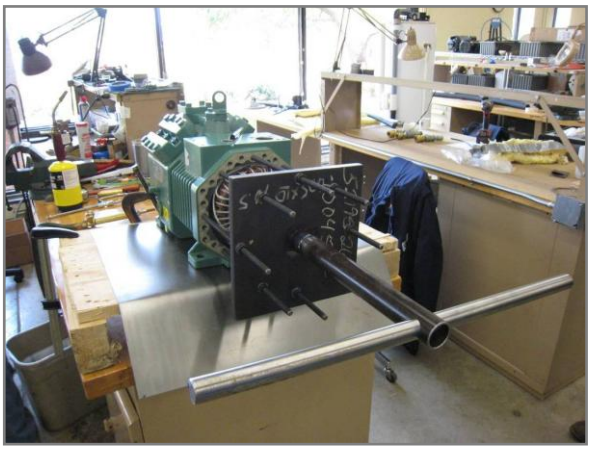

Figure 4-189: Back bolts and plate with large custom made nut driver.

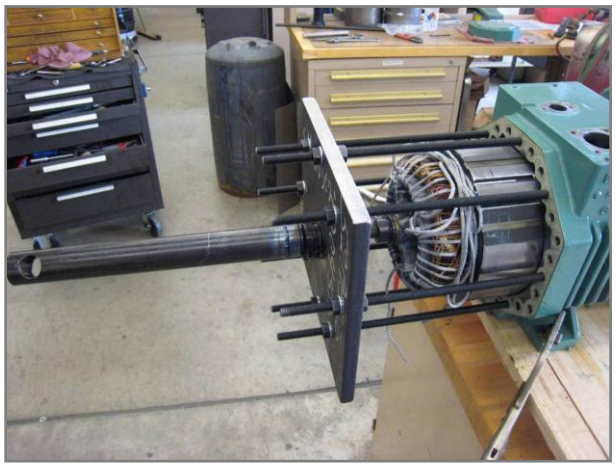

Figure 4-190: Partially extracted induction machine stator

Insertion of 36 Slot 6 Pole Stator into Compressor

To press in the 36 slot 6 pole stator, a similar process was used as to extract the stock induction machine. Because the stator stack length is not exactly the same as in the stock induction machine a spacing ring was machined to fit in the compressor bore, Figure 4-191 and Figure 4-192. A pressing ring was created out of rolled sheet steel, Figure 4-193. Bolts were screwed into the compressor end manifold with a backing plate used to press the stator into the compressor bore, Figure 4-194. The fully inserted stator is shown in Figure 4-195.

Figure 4-191: Compressor, 36 slot 6 pole stator and spacing ring readied for insertion

Figure 4-192: Spacing ring installed in compressor bore

Figure 4-193: Pressing ring installed on stator

Figure 4-194: Partially pressed in 36 slot 6 pole stator

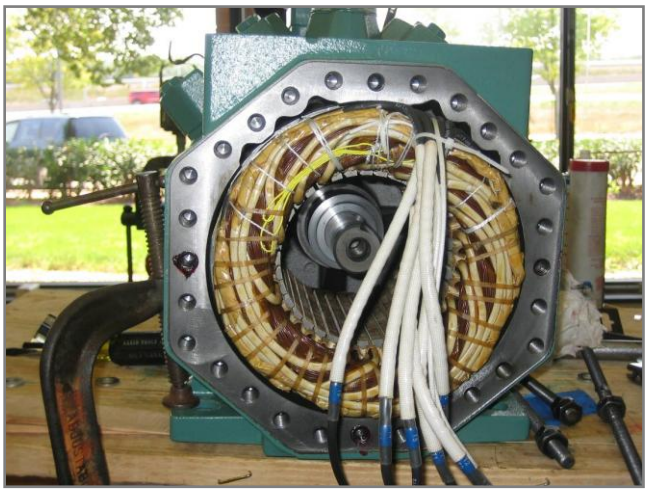

Figure 4-195: Fully inserted 36 slot 6 pole stator with lead not yet connected to terminal box

The fabrication and insertion of the interior permanent magnet (IPM) motor into the compressor are finished and the enhanced component arrived at CTS (Figure 4-196 and Figure 4-197). The only apparent difference between the modified compressor with IPM motor and a regular unmodified compressor are the new black bolts of the motor cap (Figure 4-196). Before shipping the compressor was leak checked and shipped with a nitrogen charge of 60 PSI. The suction and discharge ports had to be prepared for installation with 5/8 inch and 1/2 inch Swagelok male connections. Close attention was paid to the distances of these connections to verify the same geometry as in the baseline compressor to facilitate installation. The opened suction port is shown in Figure 4-198. The initial oil charge of 2 liters was drained for the motor installation. Since it was exposed to the ambient and due to its hygroscopic behavior the oil was discarded and not reused. New refrigeration oil was used for the compressor. Two liters of C85E which is recommended by the compressor manufacturer were used. The right amount was confirmed by watching the sight glass and the oil level indicator (Figure 4-199).

Figure 4-196: Compressor after arrival (motor side)

Figure 4-197: Compressor after arrival (crankcase side)

Figure 4-198: Compressor suction port

Figure 4-199: Compressor with suction and discharge port after addition of oil

The last step in the evapuation of the next generation heat pump water heater is the comparison of the compressor with interior permanent magnet (IPM) motor to the compressor with induction machine. For this, tests at rating water mass flow rate and different gas cooler water inlet temperatures were done at matched compressor suction pressures and temperatures as well as heating capacities. For both investigated direct expansion systems the enhanced evaporator and internal heat exchanger was used. The well matched conditions on the suction side of the compressor are documented in Figure 4-200 with a comparison of pressure and temperature.

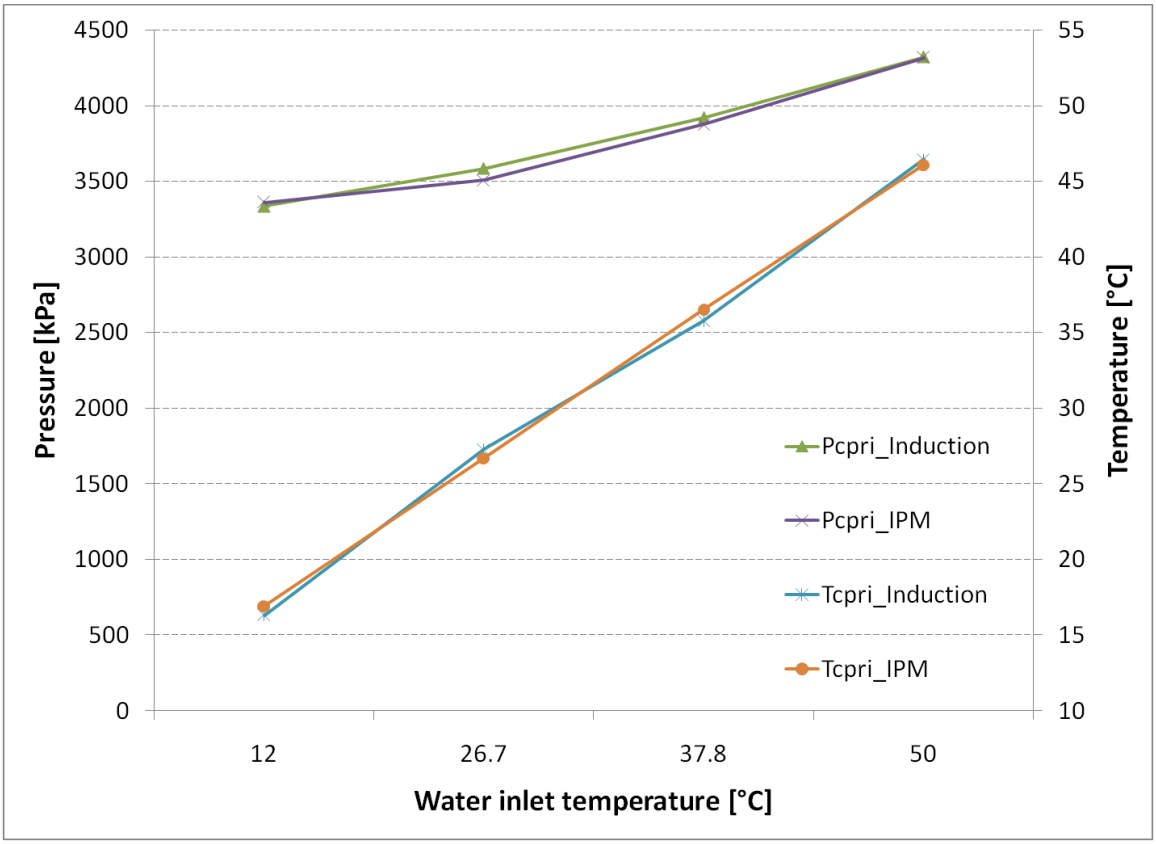

Figure 4-200: Compressor refrigerant suction pressure and temperature for different gas cooler water inlet temperatures

The following Figures (Figure 4-201 to Figure 4-204) show a comparison of the investigated cycles in pressure specific enthalpy diagrams.

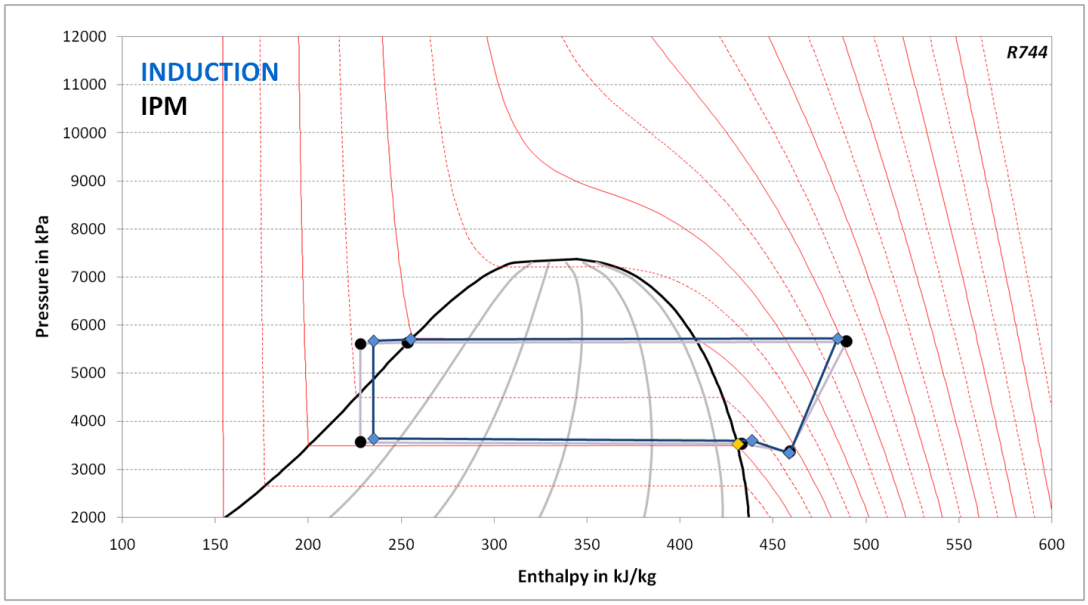

Figure 4-201: Cycle comparison in pressure specific enthalpy diagram of induction machine and IPM motor at an ambient temperature of 26.7°C, a water inlet temperature of 12°C and a water flow rate of 28 gallons per minute

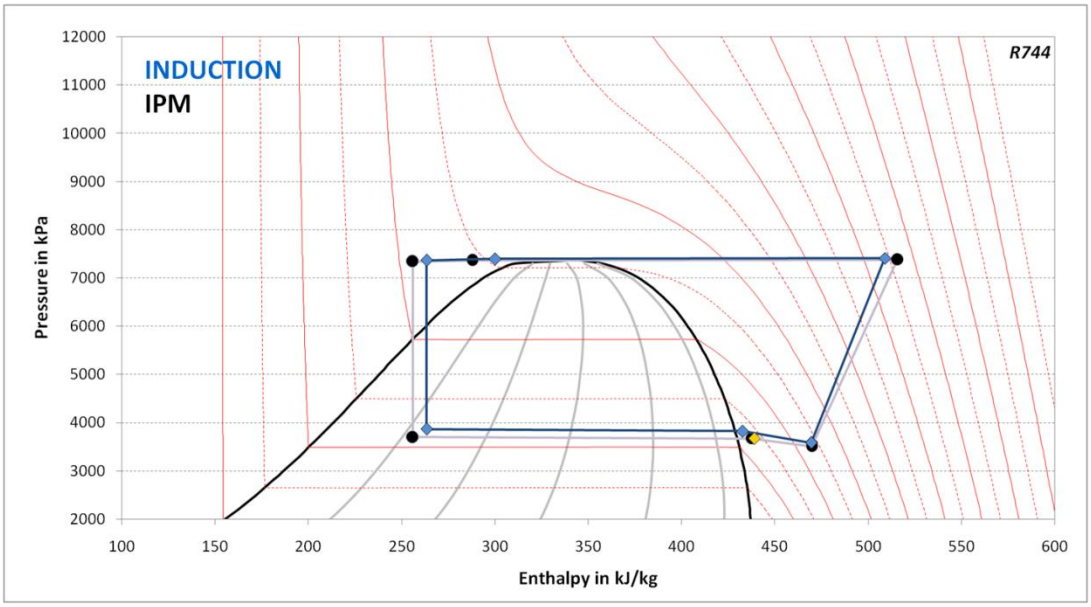

Figure 4-202: Cycle comparison in pressure specific enthalpy diagram of induction machine and IPM motor at an ambient and water inlet temperature of 26.7°C and water flow rate of 28 gallons per minute

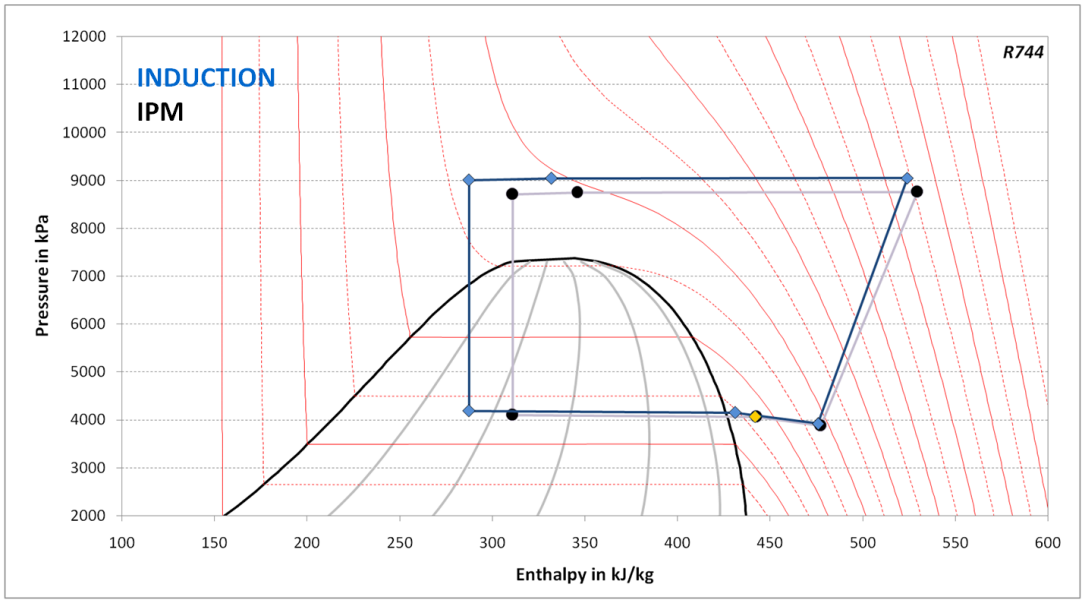

Figure 4-203: Cycle comparison in pressure specific enthalpy diagram of induction machine and IPM motor at an ambient temperature of 26.7°C, a water inlet temperature of 37.8°C and a water flow rate of 28 gallons per minute

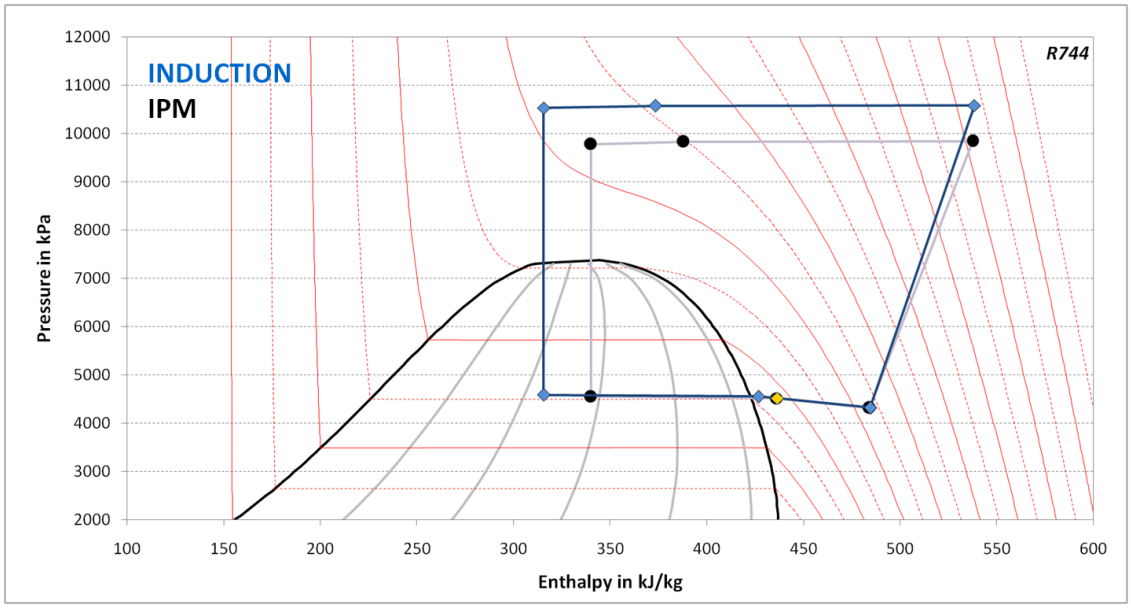

Figure 4-204: Cycle comparison in pressure specific enthalpy diagram of induction machine and IPM motor at an ambient temperature of 26.7°C, a water inlet temperature of 50°C and a water flow rate of 28 gallons per minute

The property diagrams of the two cycles show the good match on the suction side for each condition. The compression process shows for all test conditions the steeper curve for the system with induction machine which indicates a more efficient compression process. However this property diagram comparison does not take the actual compressor power including losses into account. The isentropic efficiency versus pressure ratio in Figure 4-205 provides better information. The increasing pressure ratio corresponded to the increasing water inlet temperature.

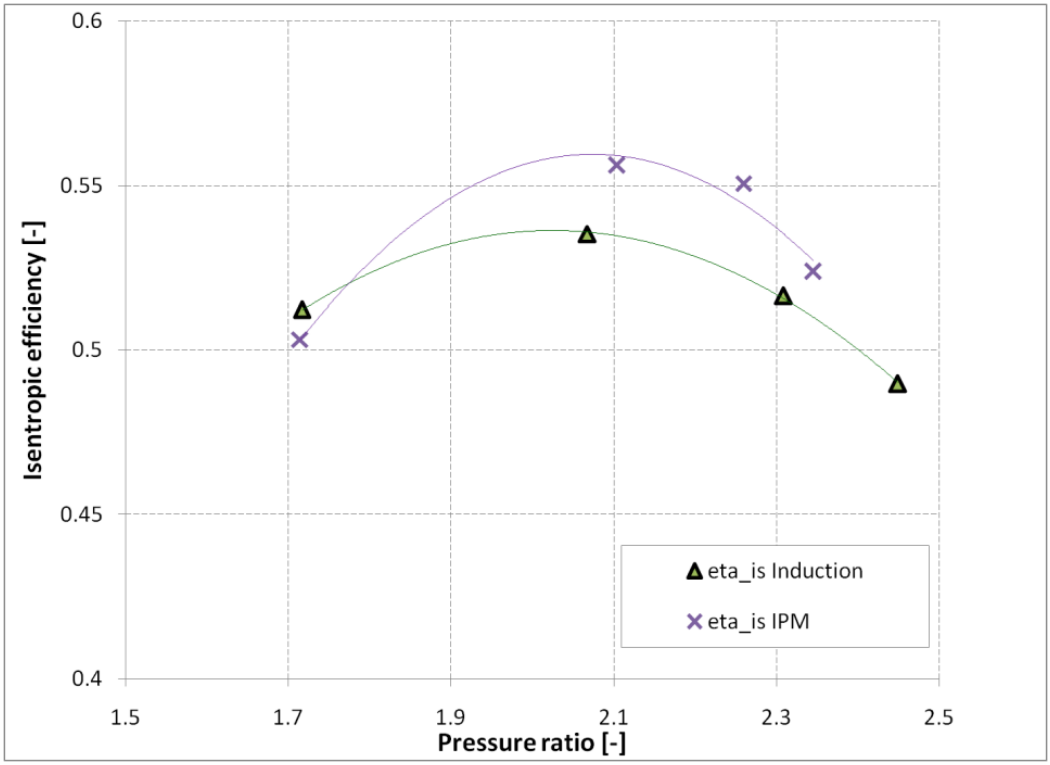

Figure 4-205: Compressor isentropic efficiency versus pressure ratio for induction machine and IPM motor

It can be seen that the IPM motor showed a better isentropic efficiency above 12°C water inlet temperature at a pressure ratio of approximately 1.7. The effect on the overall system performance was investigated when comparing the heating COP for the two systems (Figure 4-206). It was seen that both systems showed comparable performance. For 12°C (+0.2%), 37.8°C (-2%) and 50°C (+2%) the relative difference between IPM and induction machine was within the measurement uncertainty. Only for a water inlet temperature of 26.7°C a 6.3% larger heating COP was seen.

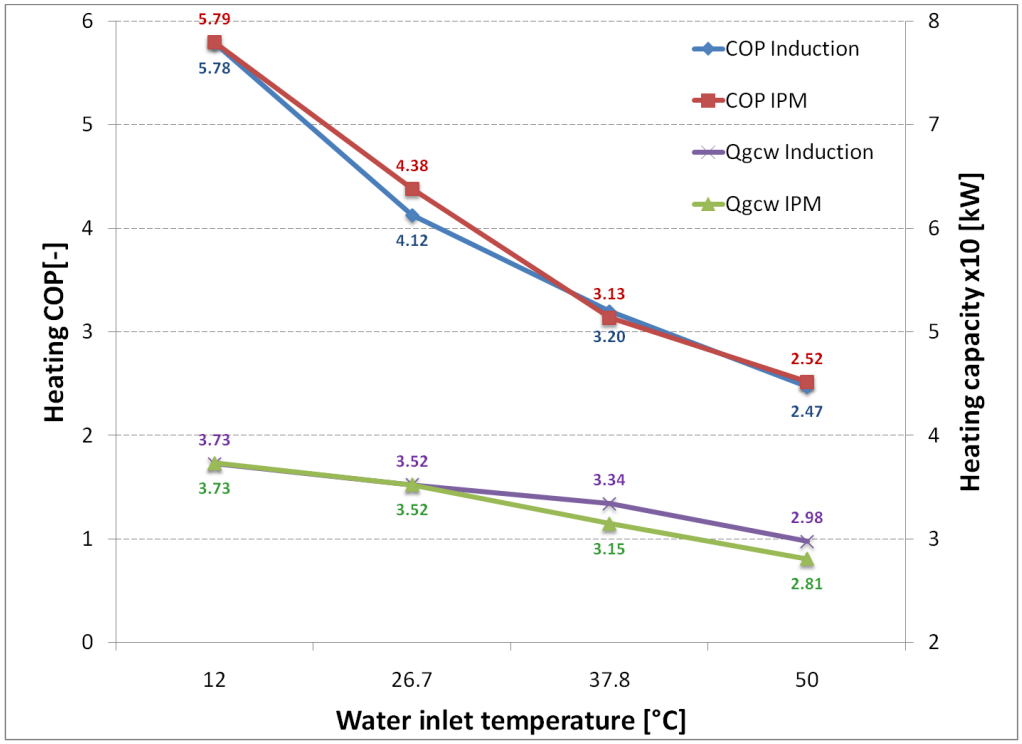

Figure 4-206: Water heating COP and heating capacity for induction machine and IPM motor at various gas cooler water inlet temperatures for an ambient temperature of 26.7°C and a water flow rate of 28 gallons per minute

The use of an IPM motor for the next generation HPWH was anticipated to provide potential performance improvement of 1 to 8%. The comparison of the heating COP's of the induction machine and IPM motor system showed a maximum improvement of 6.3% at a water inlet temperature of 26.7°C. However comparable results were observed for the other investigated conditions.